A Flow-Reactor Investigation of Two Chemical Kinetic Systems: Hydrocarbon Fuels and Methyltrichlorosilane/Hydrogen Mixtures

---

A Dissertation
Presented to the Faculty of the
School of Engineering and Applied Science
University of Virginia

In Partial Fulfillment
of the Requirements for the Degree of
Doctor of Philosophy in
Mechanical and Aerospace Engineering

by
Khanh H. Dang

August 2020

Approval Sheet

This dissertation is submitted in partial fulfillment of the requirements for the degree of Doctor of Philosophy in Mechanical and Aerospace Engineering

Khanh H. Dang

This dissertation has been read and approved by the Examining Committee:

Prof. Eric Loth, Committee Chairman

Prof. Harsha K. Chelliah, Dissertation Advisor

Prof. Haibo Dong

Prof. Elizabeth J. Opila

Dr. Chong Cha

Accepted for the School of Engineering and Applied Science:

Craig H. Benson, Dean, School of Engineering and Applied Science

August 2020

Abstract

The design of future jet engines has to meet the requirements of lower pollutant emission and higher efficiency. One of the main pollutants is soot particulates, whose emission not only affects the global climate and human well-being, but also indicates an inefficient combustion process. As a result, minimizing soot formation in jet engines can reduce both the economic and social costs of transportation. In addition to minimizing soot formation, the overall efficiency of jet engines can be improved by replacing the current metal super-alloy materials with ceramic matrix composites (CMCs), particularly silicon carbide matrix/silicon carbide fiber ($\mathrm{SiC}_m/\mathrm{SiC}_f$) composites. $\mathrm{SiC}_m/\mathrm{SiC}_f$ composites offer similar, if not better, maximum service temperature to the metal alloys, but only at one-third of the weight. Employing the composites will increase 1) the combustion efficiency with higher allowable flame temperature, 2) the engine thrust with smaller air flow diverted for cooling, and 3) the fuel mileage with lighter engines.

However, there exists a number of challenges that hinder the achievement of minimal soot formation and cost-effective production of $\mathrm{SiC}_m/\mathrm{SiC}_f$ composites. The processes of soot formation and $\mathrm{SiC}_m/\mathrm{SiC}_f$ composite fabrication have one step in common: the production of important gas phase precursors from decomposition of the parent fuel or reactants. Numerous research efforts have been dedicated to studying the gas phase chemistry during these two processes. Such efforts have resulted in a large number of detailed chemical kinetic models whose purpose is to predict the

soot formation and SiC_m/SiC_f composite fabrication processes in CFD simulations. Unfortunately, the models are still facing two major limitations: 1) significant uncertainties in reaction rate coefficients incorporated in the models and 2) huge numbers of species and reactions that render the models impractical for complex CFD simulations. In order to overcome these two limitations, there exists a need for fundamental experimental data to 1) validate and optimize the models to minimize the reaction rate coefficient uncertainties, and 2) reduce the model size while preserving their performance for practical CFD simulations of soot formation and SiC_m/SiC_f composite fabrication processes.

Recognizing this need for experimental data, the Reacting Flow Laboratory (RFL) at the University of Virginia (UVa) has constructed and verified an excellent analytical system for chemical kinetic studies. The main component of the analytical system is a microflow tube reactor (MFTR) whose design was demonstrated to be able to eliminate the problems associated with defining the initial conditions and minimize typical non-idealities encountered by flow reactors. An additional advantage of the MFTR is that it can be paired with different diagnostic tools, such as: gas chromatography (GC), gas chromatography/mass spectrometry (GM/MS), molecular beam mass spectrometry (MBMS), and scanning mobility particle sizer (SMPS), to quantify stable and radical gaseous species, and solid products during thermal and oxidative decomposition of hydrocarbon fuels or other chemicals of interest.

This thesis work employed the established analytical system to study thermal decomposition (pyrolysis) of three different hydrocarbon fuels: ethylene (C_2H_4), n-dodecane ($nC_{12}H_{26}$), and Jet A (POSF 10325). The objectives were to investigate the effects of temperature, residence time and fuel chemical composition on the formation of soot precursors in the gas phase. In addition, the three fuels were selected to have progressively complex chemical composition. Ethylene is the smallest alkene species (straight chain hydrocarbons with one C-C double bond). n-Dodecane is a normal alkane species (straight chain hydrocarbons with only C-C single bond). And Jet A is a commercial aviation fuel that contains thousands of hydrocarbon species. Thus, the three fuels provided a comprehensive test of detailed chemical kinetic models. The detailed models were constructed in a hierarchical manner. Starting with a base model of small hydrocarbon species (C_1-C_4), larger species with their own sets of reactions were appended to the base model to form a final detailed model. Comparing the experimental data of the three fuels with predictions by the models helped isolate which module of the model needed to be improved. Besides traditional chemical kinetic models, the experimental data were also used to test a new concept in modeling real jet fuels: the Hybrid Chemistry (HyChem) approach. This approach considers combustion of jet fuels as a two step process. The fuel initially undergoes thermal or oxidative decomposition to produce about ten products, which then get oxidized to form the final combustion products such as CO_2 and H_2O. At high temperature conditions of practical engines, the pyrolysis step is sufficiently fast to be assumed instantaneous, whereas the oxidation step is the rate-limiting step. Thus, the combustion of jet fuels can be viewed as the oxidation of their pyrolysis products. The HyChem approach models the pyrolysis process with seven reactions, whose rate coefficients and species stoichiometric coefficients were determined experimentally, whereas the oxidation step is modeled by a detailed foundational chemical kinetic model. Given the importance of the pyrolysis step in representing the chemical composition of a jet fuel, it needs to be thoroughly examined in order to ensure that the HyChem approach can accurately model the jet fuel combustion. Comparing the data of Jet A pyrolysis to predictions by the HyChem model showed that the model reasonably captured most of the data. However, both the seven pyrolysis reactions and the detailed foundational model in the HyChem model still need to be further improved in order to accurately predict the evolution of ethane (C_2H_6), propadiene (aC_3H_4), propyne (pC_3H_4), 1,3-butadiene (C_4H_6), benzene (C_6H_6), and

toluene (C_7H_8).

In addition to pyrolysis of hydrocarbon fuels, this thesis work also employed the analytical system to investigate species transport and chemical kinetics during silicon carbide (SiC) deposition from pyrolysis of methyltrichlorosilane/hydrogen (MTS/H_2) mixtures. First of all, the effects of experimental conditions such as temperature, total flow rate and pressure on the deposition rate, morphology and preferred crystal orientation of SiC on quartz substrates were investigated in a hot-walled flow reactor. The analysis showed that the SiC deposition was controlled by either chemical kinetics or species transport depending on the experimental conditions. At normal atmospheric pressure (1 atm), increasing either temperature or initial MTS concentration transitioned SiC deposition from being controlled by chemical kinetics to being controlled by species transport. On the other hand, reduced pressure condition (0.5 atm) extended the transition conditions to higher values, i.e., higher temperature or higher initial MTS concentration. The morphology and preferred crystal orientation of the SiC deposits also changed in accordance with the deposition controlling regime. Furthermore, the experimental results were able to capture the reactant depletion effect typically encountered in hot-walled flow reactors similar to the UVa premixed microflow tube reactor (PMFTR). Either increasing total flow rate or decreasing total pressure helped mitigate the reactant depletion effect.

Besides SiC deposition on quartz substrates, the formation of SiC precursors in the gas phase during pyrolysis of MTS/H_2 mixtures was also investigated over a wide range of temperature and nominal residence time at normal atmospheric pressure (1 atm). Four species: MTS, methane (CH_4), trichlorosilane (CH_3SiCl_3), and silicon tetrachloride ($SiCl_4$), were quantified by GC. The measured data were compared to predictions by the Ge et al. model. The results of the comparison showed that the reactivity of the MTS/H_2 mixture predicted by Ge et al. model was much slower than that shown by the experimental data. Therefore, modification of the model was attempted with the data serving as the benchmark. Sensitivity and reaction pathway analyses were conducted to determine the most important reactions to the evolution of the four detected species. Then, the reaction rate parameters (pre-exponential factors and activation energies) were modified until minimum error between model predictions and data was reached. The modified model was able to reasonably capture the experimental data over the considered experimental conditions, but further studies are still needed to improve its predictability of the Si-containing products. Nevertheless, an attempt to reduce the dimension of the modified Ge et al. model was carried out. The result was a skeletal model that preserved the performance of the detailed optimized model but with half the size (23 vs. 47 species and 57 vs. 112 reactions).

Acknowledgements

First and foremost, I would like to express my sincere gratitude to my advisor, Prof. Harsha Chelliah. The knowledge and wonderful experience that I have today are all thanks to you. You were the one who really believed in me and allowed me an opportunity to pursue this Ph.D. degree. Throughout my Ph.D. studies, you've always been there to guide me through a great number of obstacles. I honestly hope that I have made you proud as one of your students and that you don't have any regret giving me a chance to work with you.

To my committee, thank you for your patience and guidance since my Ph.D. qualifying exam to the completion of my thesis. Prof. Loth, you have known me since my years as an undergraduate student at the University of Virginia (UVa). I learned from you my first experience in conducting scientific research. Without that foundation, I don't think I would be able to complete my degree. Prof. Dong, you have taught me in two classes: Thermodynamics and Computational Fluid Dynamics (CFD). Throughout the time that I got to interact with you, you have shown me that you really cared about your students. I could not find a better teacher anywhere else. Prof. Opila, you have always answered all the questions that I had for you. As I started my research on silicon carbide, I learned a great deal from your papers. The dedication that you have shown in your papers has been the guide for me to write my research papers and this thesis. In addition, I would like to thank you for your hard work at organizing meetings between UVa students and Rolls Royce. Dr. Cha, you have given me an opportunity to learn something new with the silicon carbide project. It was challenging but I have grown a lot as a researcher because of it. I hope that the results of my experiment will greatly help you with your project.

I also want to thank Scott Rorrer and Richard Roberts. You have helped me take good care of my laboratory. Whenever something broke down, I always turned to you for help, and you have never failed to show up. My colleagues and I are very fortunate to have you as our guys. In addition, I would like to thank Richard White at the Nanoscale Materials Characterization Facility (NMCF) at UVA. Thank you for training me to use all the tools that I needed for my research and for always teasing me when I needed your help. I always enjoyed your humor. You are that teacher who looks very serious but is very fun to be around. Prof. Dedic, I am not forgetting you. Although I have only known you for a short period of time, you have been my great inspiration. And thank you for allowing me to participate in your group meetings to practice my presentation skills.

To my friends and colleagues: Dr. Ujuma Shrestha, Dr. Greg Simms, and Dr. Andreas Rauch, I cannot thank you all enough. You've made my time in the lab so much more enjoyable. Dr. Shrestha, you were like a big sister to me when you were in the lab. You taught me a lot of things. You never got angry when I made a mistake or almost ruined your experiment. Dr. Simms, you are my big brother and friend at the same time. You are special because you not only helped with research but also played basketball with me. Dr. Rauch, you are such a good friend that I will treasure for the rest of my life. Whenever I needed help with CFD, you went above and beyond to help me. Wherever we end up in the future, I hope that we can keep in touch.

Last but not least, I would like to say thank to the two most important people in my life. To my wife, Huyen, thank you for having always been by my side. You are my constant source of joy that gets me through all difficult times. Thank you for coming into my life. It has becomes more colorful since you arrived. And to my mother, thank you for giving birth to me. You made everything possible. Thank you for raising me to become a decent man. Thank you for trying your hardest to find a way for me to come to the United States to have a better life. Without you, I could never have been able to study or to meet Huyen. Thank you for everything, mom!

Contents

List of Figures

List of Tables

List of Symbols and Abbreviations

Abbreviations

CARD	Computer Aided Reaction/Reactor Design
CARS	Coherent anti-Stokes Raman Spectroscopy
CFD	Computational Fluid Dynamics
CVD	Chemical Vapor Deposition
CVI	Chemical Vapor Infiltration
DCN	Derived Cetane Number
FID	Flame Ionization Detector
GC	Gas Chromatography
GC/MS	Gas Chromatography/Mass Spectrometry
HACA	Hydrogen Abstraction Carbon Addition
HPST	High Pressure Single Pulse Shock Tube
ID	Inner Diameter
JSR	Jet Stirred Reactor
LII	Laser Induced Incandescence
ICDD	International Center for Diffraction Data
MBMS	Molecular Beam Mass Spectrometry
MFTR	Microflow Tube Reactor
MI	Melt Infiltration
MTS	Methyl-trichloro-silane - CH_3SiCl_3
NTC	Negative Temperature Coefficient
PAH	Polycyclic Aromatic Hydrocarbon
PID	Proportional Integral Derivative
PIP	Polymer Infiltration and Pyrolysis
PFR	Plug Flow Reactor
PLIF	Planar Laser Induced Fluorescence
PMFTR	Premixed Microflow Tube Reactor
RFL	Reacting Flow Laboratory
SCCM	Standard Cubic Centimeter per Minute
SEM	Scanning Electron Microscopy
SMPS	Scanning Mobility Particle Sizer
TCD	Thermal Conductivity Detector
UVA	University of Virginia
VPFR	Variable Pressure Flow Reactor
XRD	X-ray Diffraction

Symbols

a	Thermal conductivity
A	Reactor cross sectional area
A_f	Pre-exponential factor
c_p	Mass-averaged heat capacity
Da	Damköhler number
D_{ij}	Binary species diffusion coefficient
$D_{multi,i}$	Multicomponent diffusion coefficient of species i
E_a	Activation energy
G	Effective species diffusion with Taylor-Aris dispersion
I_{hkl}	Intensity of the (hkl) peak from XRD data
$I_{0,hkl}$	Standard intensity from ICDD
J_i	Species flux of species i
k	Reaction rate coefficient
k_b	Boltzmann constant
l	Reactor length
n	Overall reaction order
$\dot{n}_i$	Mole flow rate of species i
$\dot{m}$	Mass flow rate
M_i	Molecular weight of species i
p	Pressure
Pe_i	Mass transfer Peclet number of species i
Pe_{th}	Thermal transfer Peclet number
p_k	Multiplier of rate coefficient of reaction k
q_i	Volume flow rate of species i
r	reactor radius
R	Dimensionless reactor radial coordinate
R_i	Specific gas constant
R_u	Universal gas constant
$S_{i,k}$	Sensitivity coefficient of species i w.r.t. reaction k
t_{res}	Residence time
T	Temperature
TC_{hkl}	Texture coefficient
u	Velocity
u_{total}	Total uncertainty
u_{cal}	Calibration uncertainty
u_{exp}	Experimental uncertainty
U	Dimensionless velocity
U_{pl}	Plug flow velocity
V	Reactor volume
X_i	Mole fraction of species i
Y_i	Mass fraction of species i
z	Reactor axial coordinate

Z	Dimensionless reactor axial coordinate

Greek Symbols

α	Ratio of $X_{H_2,0}$ to $X_{MTS,0}$
ϵ	Ratio of the reactor diameter to its length
ε	characteristic Lennard-Jones energy
ρ	Density
σ_x	Error in a measured quantity x
σ_{ij}	Collision diameter between species i and j
σ	Characteristic Lennard-Jones length
$\tau_{c,L}$	Characteristic convection time in axial direction
$\tau_{c,R}$	Characteristic convection time in radial direction
$\tau_{sd,R}$	Characteristic diffusion time in radial direction
τ_k	Characteristic reaction time
τ_{td}	Characteristic thermal diffusion time
$\dot{\omega}_i$	Consumption or production of species i
$\widehat{\dot{\omega}}_i$	Dimensionless consumption or production of species i
ψ	Intermolecular energy between two species
ωQ	Overall heat release
Ω_D	Diffusion collision integral

Chapter 1

Introduction

According to the International Civil Aviation Organization - ICAO, commercial aircraft transports more than 10 million passengers and USD 18 billion worth of goods everyday, and this high demand for air transport will increase by an average of 4.3% annually over the next 20 years [1]. Such strong increase in air traffic activity raises an issue of sustainability. At a time of global concern over climate change, designing of the next generation of commercial aircraft, especially their gas turbine engines, to have less impact on the environment becomes more important. Lessening the impact on the environment means reduced pollutant emissions from commercial aviation, which requires more efficient gas turbine engines that burn less fuel. There have been efforts to integrate electricity to aid or replace current propulsion methods, e.g., NASA's work on the all-electric X-57 Maxwell. However, at large aircraft level, the modern gas turbine engines powered by the combustion of liquid hydrocarbon fuels will remain the dominant mode for a foreseeable future. The relevance of the gas turbine engines merits extensive research efforts on new technologies such as advanced combustor performance and ceramic composite materials to help tackle current sustainability challenges facing commercial aviation. Interestingly, the development of advanced combustor performance and ceramic composite materials requires improved chemical kinetic models to be used in the computer-aided design process. And facilitating the advent of such chemical kinetic models is the focus of this thesis work.

Specifically, an experimental investigation of the gas-phase chemistry during thermal decomposition (pyrolysis) of 1) jet fuels and 2) methyltrichlorosilane (MTS - CH_3SiCl_3) was undertaken. A novel microflow tube reactor (MFTR) was used together with gas chromatography (GC) to track the evolution of the reactants and decomposed products at different experimental conditions. The species measurements helped infer important reaction pathways during the pyrolysis process that were important for validating, optimizing and simplifying chemical kinetic models. Optimized and simplified kinetic models are expected to facilitate the design of next-generation 1) jet engines and 2) chemical vapor infiltration (CVI) reactors for ceramics matrix composites (CMCs).

1.1 Motivation

1.1.1 Development of models to simulate soot formation

One of the major pollutants emitted from hydrocarbon-fuel combustion is soot particulates. Emission of soot poses harmful threats to human health [2] and the global climate [3–9]. Soot is cytotoxic and, thus, can cause adverse cardiovascular and pulmonary problems to human [10, 11]. In addition to negative effects on human health, the presence of soot particulates in the atmosphere can contribute to global warming. As a good light absorber, soot can strongly increase the absorption of sunlight by ambient air [12, 13]. On the other hand, soot particles may also serve as nuclei for cloud condensation, increasing the global cloud density [14]. Furthermore, soot deposited on polar ice can trigger ice melting by reducing surface albedo [9].

Given the harmful effects of soot particulates, minimization of soot formation is an important objective in the design of future efficient and clean-burning combustion engines. Indeed, significant research effort has focused on soot formation mechanism during combustion of hydrocarbon fuels [10, 15–19]. Soot formation mechanism can be simplistically described in three steps: 1) formation of soot precursors, 2) soot nucleation or inception, and 3) mass growth. In the early stage of soot formation, unburned hydrocarbon intermediates react and form polyaromatic hydrocarbons (PAHs). These PAHs have been shown to be precursors to soot formation [20–24]. The PAH precursors then combine to form PAH clusters. This process is known as soot nucleation or inception. The clusters further undergo coalescence to form incipient particles of a few nanometers in diameter. Subsequently, the incipient particles grow further through reactions of gas phase hydrocarbon species with the soot surface. The growing particles can collide and combine to form bigger soot aggregates.

The extensive research on soot formation mechanism has resulted in a number of models to simulate soot formation during hydrocarbon-fuel combustion. These models generally contain two parts: 1) a detailed chemical kinetic model of PAH formation and 2) a soot model of nucleation and mass growth steps. However, there exists significant uncertainty in these models due to the complexity of the reaction mechanism of PAH formation, particle nucleation and growth. In order to minimize the model uncertainty, the first step is to obtain an accurate detailed chemical model of PAH formation mechanism. Several detailed chemical models with thousands of species and reactions have been developed to simulate the formation of PAHs during combustion of hydrocarbon fuels [25–30]. Unfortunately, these detailed chemical models show inconsistent predictions of important intermediate species and PAH formation. As an example, Fig. 1.1 shows predictions of pyrolysis of ethylene into several important intermediate species by different models. The models on Fig. 1.1 not only show inconsistent predictions, but also omit important aromatic species (i.e., toluene - C_7H_8). Given the inconsistency in the predictability of the detailed chemical models, it is extremely important to have independent experimental data on PAH formation

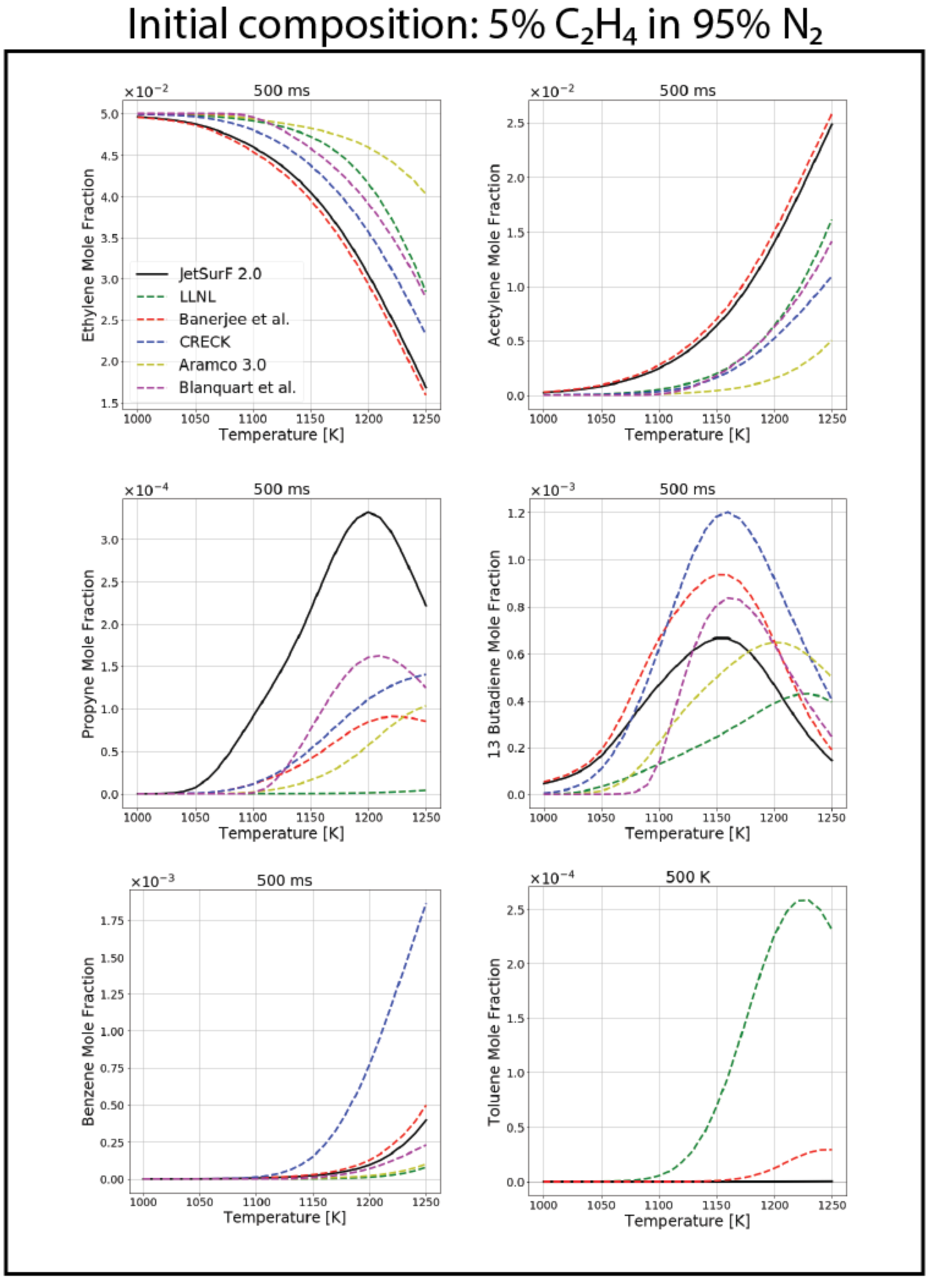

Figure 1.1: Predicted mole fractions of ethylene (C_2H_4), acetylene (C_2H_2), propyne (C_3H_4), 1,3 butadiene (C_4H_6), benzene (C_6H_6), and toluene (C_7H_8) by different models: JetSurF 2.0 [25], LLNL [26], Banerjee et al. [27], CRECK [28], Aramco 3.0 [29], and Blanquart et al. [30].

to validate these detailed chemical models. Thus, a validated detailed chemical model of PAH formation can then be used with a soot nucleation and growth model to better simulate soot formation during hydrocarbon-fuel combustion.

1.1.2 Effects of fuel chemical structure on PAH formation

Ethylene (C_2H_4) was used as the fuel in Fig. 1.1 to show a variation in the predictions of important intermediate species by different models. Ethylene was selected because it has been widely used as a reference fuel in experimental and theoretical studies of soot formation [31–34]. Ethylene has a simple structure and high propensity to produce soot. However, developing detailed chemical models for PAH formation primarily from ethylene combustion data may not completely capture the reaction pathways leading to PAHs. There exists evidence that the chemical structure of a fuel can enable or disable additional pathways for the formation of benzene, the first aromatic ring [30]. As an illustration, reaction pathway analyses of ethylene and n-dodecane pyrolysis were carried out with the JetSurF 2.0 model [25], and the results are shown in Fig. 1.2 for only major pathways. When ethylene is used as the fuel, acetylene (C_2H_2) is the only important intermediate species to the formation of benzene (C_6H_6), as seen on the left panel of Fig. 1.2. However, using n-dodecane as the fuel opens up additional reaction pathways for benzene formation through propargyl ($C_3H_3\bullet$) radicals (see the right panel on Fig. 1.2). Therefore, the fuel chemical structure needs to be considered in soot formation studies.

1.1.3 Soot formation studies with jet fuels

The effect of fuel chemical structure on PAH formation pathways was illustrated in Section 1.1.2 with ethylene and n-dodecane. However, these two hydrocarbon fuels are not accurate representations of jet fuels. n-Dodecane is often used as one of key fuel surrogates for kerosene-based jet fuels such as Jet A. This is because n-dodecane has

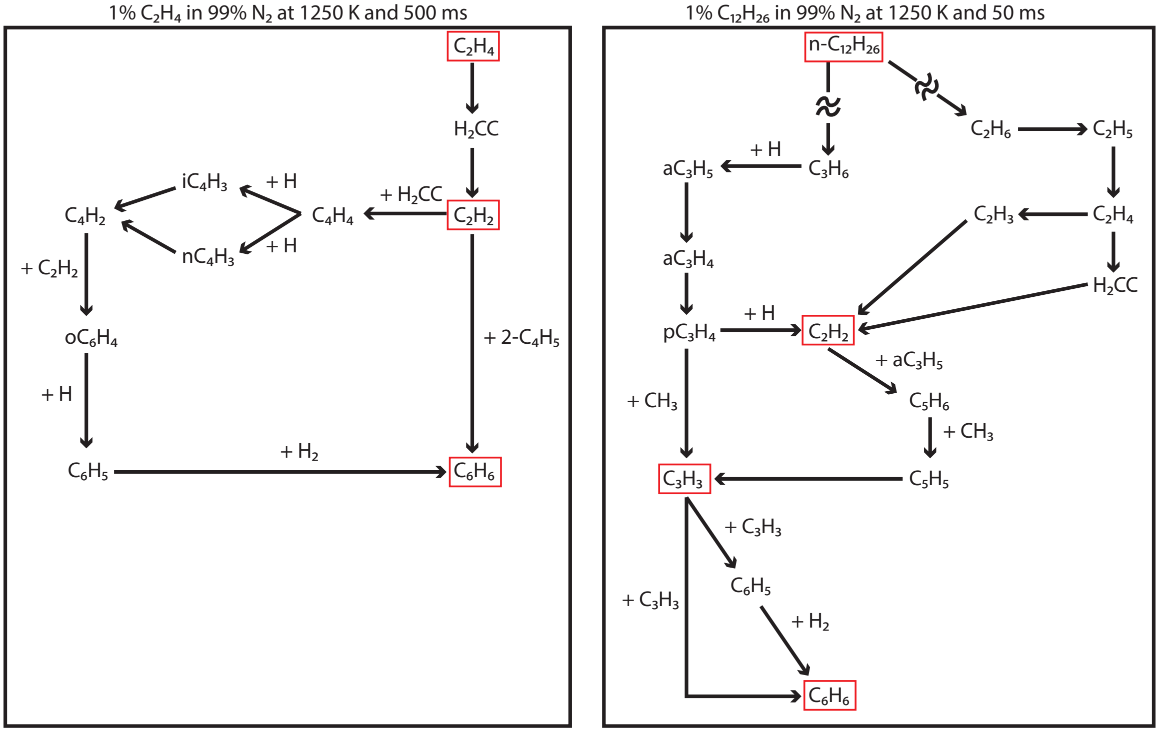

Figure 1.2: Simplified reaction pathways leading to benzene formation from two different fuels: ethylene (C_2H_4) and n-dodecane ($C_{12}H_{26}$)

the molecular mass and hydrocarbon to carbon ratio that better reflects the normal paraffin content in jet fuels. In reality, jet fuels, such as Jet A, consists of thousands of hydrocarbon compounds, including normal paraffins, iso-paraffins, cyclo-paraffins, alkenes and aromatics. Fig. 1.3 presents typical chemical compositions of three jet fuels: JP-8, Jet A, and JP-5. The complex chemical composition of jet fuels must influence PAH formation mechanism in ways that cannot be captured with ethylene or n-dodecane as a fuel. Thus, there exists a need to study PAH formation from the pyrolysis of jet fuels.

1.1.4 Silicon carbide fiber reinforced silicon carbide composites

In addition to minimizing pollutant production, increasing overall efficiency and lowering operational cost are important objectives in the design of future jet engines.

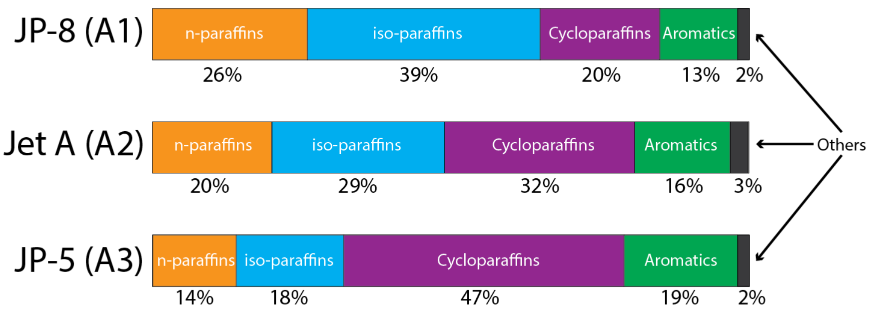

Figure 1.3: Chemical compositions of three jet fuels: JP-8, Jet A, and JP-5 (adapted from [35])

These objectives can be achieved with a new material: silicon carbide fiber reinforced silicon carbide (SiC_f/SiC_m) composites. SiC_f/SiC_m composites are one type of ceramics matrix composites (CMCs), consisting of SiC fibers embedded in a SiC matrix. SiC_f/SiC_m composites provide the same advantages of technical ceramics: low density, ultra-high temperature durability, excellent chemical and corrosion resistance, while overcoming major disadvantages of ceramics: brittle failure, low fracture toughness and limited thermal shock resistance. SiC_f/SiC_m composites have been used to make combustor liners, nozzles and high temperature turbine shroud on jet engines. The benefits of employing SiC_f/SiC_m composites are highlighted in Fig. 1.4, which compares the maximum service temperature of SiC_f/SiC_m composites to that of SiC ceramics, titanium (Ti) matrix composites, Ti alloys, and nickel-base alloys. It can be observed that SiC_f/SiC_m composites have higher service temperature, but weigh three times less than nickel-base alloys. Higher service temperature offered by SiC_f/SiC_m composites mean less air is diverted from thrust for cooling, allowing engines to run at higher thrust and more efficiently. Furthermore, the light weight of SiC_f/SiC_m composites translates to lower fuel consumption, decreasing operational cost for airliners.

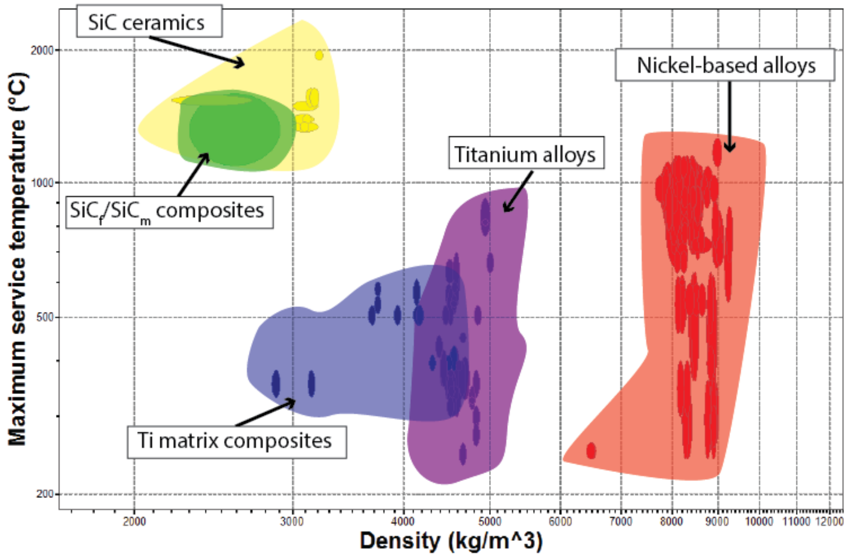

Figure 1.4: Max service temperature of SiC_f/SiC_m composites, technical ceramics, titanium (Ti) matrix composites, Ti alloys, and nickel-based alloys, as a function of density

1.1.5 SiC_f/SiC_m composite densification process: chemical vapor infiltration (CVI)

There are three main densification processes for SiC_f/SiC_m composites: 1) polymer infiltration and pyrolysis (PIP), 2) melt infiltration (MI), and 3) chemical vapor infiltration (CVI). While a combination of these process can be used, CVI has several advantages over the other methods [36]. CVI requires lower temperature and pressure, resulting in minimal mechanical damage to the fibers. Large complex shapes can be produced with CVI. In addition, CVI can produce very pure and uniform matrix material because the method utilizes high-purity gaseous reactants. The CVI process can be described with a simple schematics shown in Fig. 1.5. During CVI, one or several gaseous reactants, e.g., a mixture of methyltrichlorosilane (MTS - CH_3SiCl_3) and hydrogen (H_2), flow over a 3D fibrous structure called preform. The temperature of the preform is kept sufficiently high for the reactants to decompose into SiC precursors around it. Subsequently, the precursors diffuse into pores of the preform where they react and deposit SiC matrix, densifying the preform.

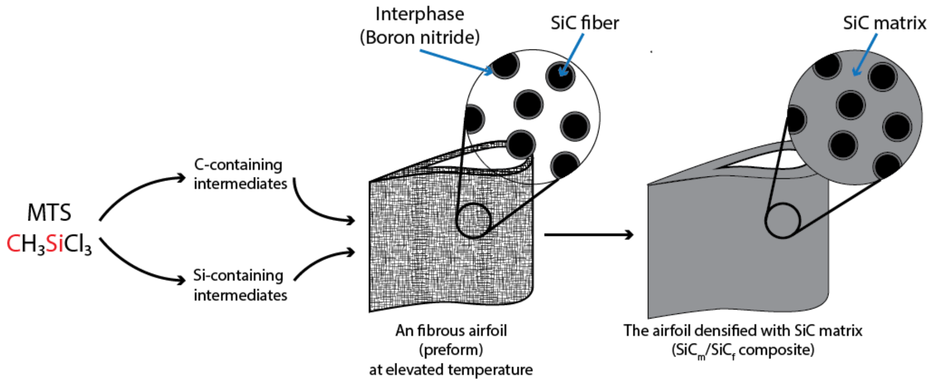

Figure 1.5: A schematic of the CVI process to densify a 3D fibrous structure called preform with SiC matrix produced by thermal decomposition of methyltrichlorosilane (MTS)

1.1.6 Premature pore entrance closure during a CVI process

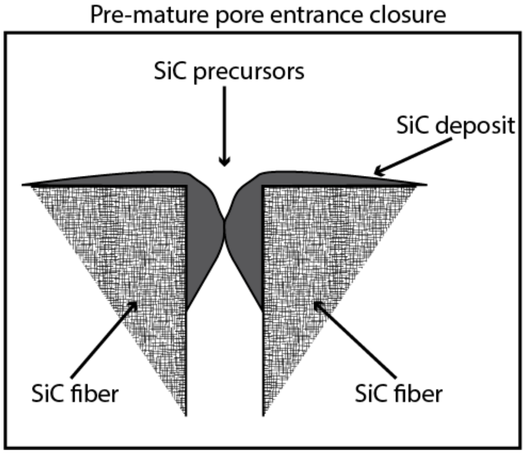

One of the major problems facing the CVI technique is the slow mass deposition rate. This can be associated with premature pore entrance closure. During a CVI process, the SiC precursors tend to react and deposit SiC at the pore entrance of a preform, blocking further SiC deposition deep down the pore network. Thus, the preform needs to be removed from the reactor and machined multiple times to unseal the pore entrance. This process is time consuming and can increase the production cost of $\mathrm{SiC}_f/\mathrm{SiC}_m$ in comparison to other materials (see Fig. 1.6).

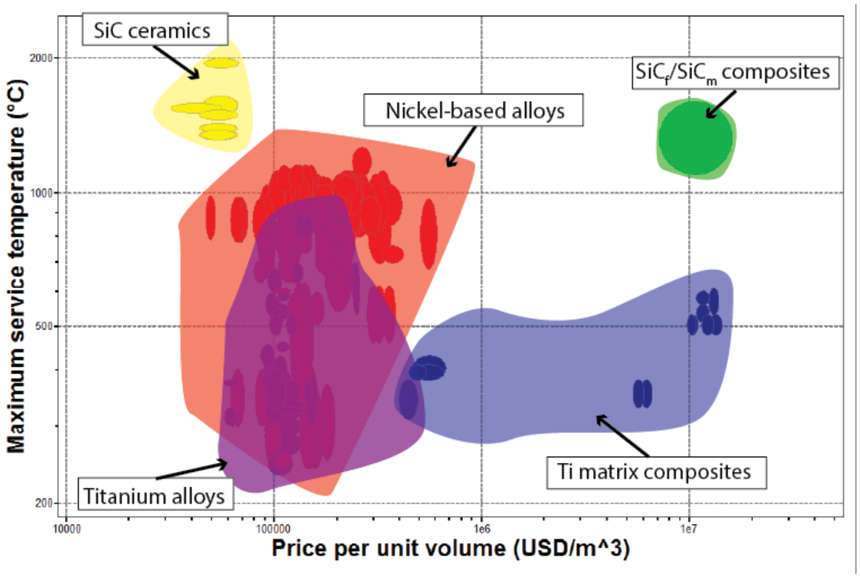

Figure 1.6: Production costs per unit volume of SiC$_f$/SiC$_m$ composites, technical ceramics, titanium (Ti) matrix composites, Ti alloys, and nickel-based alloys

1.1.7 A computer aided approach to minimize premature pore entrance closure

In order to minimize the premature pore entrance closure during a CVI process, numerous research studies have tried to obtain a thorough understanding of the CVI process [37–41]. The results of these studies show that the CVI process involves five steps:

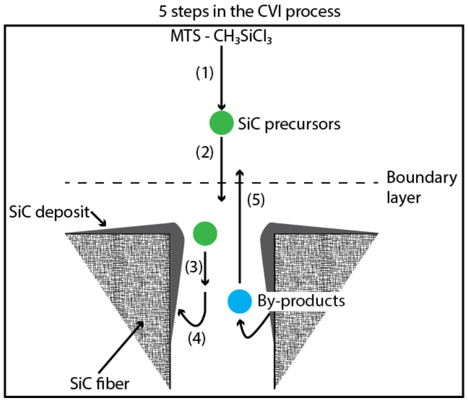

Step 1: decomposition of the reactants into SiC precursors

Step 2: diffusion of the precursors across the boundary layer

Step 3: diffusion of the precursors along the pore network

Step 4: reactions of the precursors on the pore surface, producing SiC matrix and gaseous by-products

Step 5: Diffusion of the by-products out of the pore network and out of the boundary layer

Based on this description, it is desirable that the rate of steps 2 and 3 (diffusion of the precursors) are much faster than the rate of steps 1 and 4 (reactions of the precursors) in order for the precursors to diffuse throughout the pore network, minimizing the premature pore entrance closure. The rates of these steps depend on process parameters such as: temperature, pressure, total flow rate of the reactants, and initial gas reactant composition. Thus, it can be stated that an optimal condition for minimal premature pore entrance closure can be found by systematically varying the process parameters. However, this approach is expensive and inefficient. Instead, a preferred method is to utilize a computer-aided reaction/reactor design (CARD) methodology to find the optimal condition [42]. The CARD methodology consists of three steps:

Step 1: construction of fundamental kinetic models for both gas phase and surface chemistry

Step 2: optimization and simplification of these models using experimental data

Step 3: implementation of CFD coupled with the models obtained in Step 2

Although a number of fundamental kinetic models is available, experimental data necessary for validating and optimizing these models is scare. Therefore, in order to successfully implement the CARD methodology, high quality experimental data on the gas phase chemistry during the CVI process is required.

1.2 Dissertation objectives

Given the need for experimental data to validate and optimize gas phase chemistry models for soot formation and silicon carbide (SiC) deposition, the research group at the Reacting Flow Laboratory (RFL) has developed a novel microflow tube reactor (MFTR) and verified its functionality to obtain the needed data. The purpose of this dissertation was to utilize the MFTR along with gas chromatography (GC) technique to experimentally capture the gas phase chemistry during soot formation and SiC deposition processes. An understanding of the gas phase chemistry of these two processes will help improve their respective chemical kinetic models, which may in turn be used for the design of future efficient and clean-burning jet engines.

This dissertation seeks to:

1. Obtain speciation data during ethylene (C_2H_4) pyrolysis to highlight the underlying causes of inconsistent predictions by available detailed kinetic models

2. Quantify stable species evolution during n-dodecane ($C_{12}H_{26}$) pyrolysis to highlight the effect of fuel chemical structure on formation of polyaromatic hydrocarbons (PAHs)

3. Validate different detailed kinetic models with experimental data of n-dodecane pyrolysis

4. Measure stable species concentration during pyrolysis of a commercial jet fuel, Jet A, and use the data to support a development of a fast pyrolysis-oxidation concept in modeling combustion of jet fuels

5. Investigate correlation of mass growth rate, morphology and preferred crystalline orientation of SiC deposits to variation of process parameters: temperature, pressure, total flow rate of reactants, and initial reactant composition

6. Measure stable gas phase species during pyrolysis of methyltrichlorosilane (CH_3SiCl_3) and use the data to validate, optimize and simplify a detailed chemical kinetic model for gas phase chemistry during SiC deposition

1.3 Dissertation organization

The above introduction has provided the motivation for the study contained here. It is very imperative to obtain accurate predictive models of: 1) soot formation during combustion of jet fuels and 2) SiC deposition during the chemical vapor infiltration (CVI) process, for the design of future efficient and clean-burning jet engines. Although the two processes are vastly different from one another, they share a commonality in that they both involve a similar formation mechanism: 1) gas phase reactions to produce the precursors, 2) transport of the precursors, and 3) surface reactions of these precursors. In order to construct accurate predictive models for these two processes, the first step is to obtain a thorough understanding of the gas phase chemistry because it controls the nature of the subsequent steps. The UVa MFTR is a robust device to provide high-quality information on the gas phase chemistry of these two systems.

Chapter 2 provides a brief description of the UVa MFTR. This chapter also describes two gas chromatography (GC) systems used in this work. The experimental conditions are also included.

Chapter 3 contains the experimental measurement of stable species concentrations during pyrolysis of 1) ethylene (C_2H_4) and 2) n-dodecane ($C_{12}H_{26}$). The chapter also shows comparisons between experimental data and predictions by different models. The objective of this chapter is to show how the influences of residence time, temperature and fuel chemical structure on the formation pathways of polycyclic aromatic hydrocarbons (PAHs).

Chapter 4 presents a similar measurement of stable species concentration during pyrolysis of a jet fuel, Jet A, at different experimental conditions. The experimental results are discussed and compared to prediction by a model that employs the fast pyrolysis-oxidation concept.

Chapter 5 is the beginning of the second part of this dissertation, which focuses on studying SiC deposition with the MFTR. The chapter presents experimental results of deposition rate, morphology, and preferred crystalline orientation of SiC deposits on quartz substrates at different experimental conditions. Throughout this chapter, two different regimes controlling SiC deposition are highlighted, as well as the effect of reactant depletion effect encountered in a hot-walled flow reactor similar to the MFTR.

Chapter 6 describes an experimental investigation of gas phase chemistry during pyrolysis of methyltrichlorosilane (MTS - CH_3SiCl_3). A comparison between the experimental data and prediction by a detailed chemical kinetics model is also included. Furthermore, this chapter includes a description of how to use the experimental data to optimize and simplify the model.

Finally, Chapter 7 serves to present key findings and summary of this work. It also addresses the major unanswered questions and proposes a set of future experiments to address those questions.

Chapter 2

Experimental and Modeling Approach

Accurate predictive models of 1) soot formation during jet fuel combustion and 2) silicon carbide (SiC) deposition during the chemical vapor infiltration (CVI) process are integral to the design of future efficient and clean-burning jet engines. The foundation of these models is a thorough knowledge of the formation of gaseous precursor species during the two processes. Hence, there exists a need for experimental kinetic studies on the formation of precursor species at different conditions. The obtained data can then be used to advance the development and optimization of predictive models for soot formation and SiC deposition processes.

Different reactor configurations, such as shock tubes, jet stirred reactors and flow reactors, are available to study the formation of precursor species during soot formation and SiC depostion processes. A brief description of each reactor configuration along with their limitations is provided. This description is intended to lay out the reasons why a microflow tube reactor developed at the University of Virginia (UVa) is a desirable tool and superior in certain aspects for this type of study. In addition, experimental conditions are summarized at the end of this chapter.

2.1 Different reactor configurations

An investigation of the gas phase chemistry during 1) jet fuel combustion and 2) chemical vapor infiltration (CVI) of SiC entails a number of requirements on a reactor configuration. Firstly, a reactor needs to be able to contain or introduce a stable non-reactive mixture of reactants at a homogeneous initial thermodynamic state: temperature, pressure and composition. Secondly, the reactor needs to support a uniform and instantaneous change in the mixture thermodynamic state to one where the mixture becomes reactive. Finally, the reactor has to provide access to one of the diagnostic methods: laser spectroscopy, gas chromatography (GC), mass spectrometry (MS), etc., for measuring the temporal evolution of species concentration, temperature and system enthalpy, which yield direct insight into the gas phase chemistry.

In practice, there exists a major challenge facing the design of reactors to investigate the gas phase chemistry: determining the true start time of the reaction of the reactants. On the one hand, if the reactants are uniformly premixed, then they must be heated to a target reacting temperature. The finite heating rate translates to a transient heating time, introducing uncertainty to true reaction start time. On the other hand, if the reactants are not premixed, a finite mixing rate similarly results in uncertainty in the reaction start time. However, numerous efforts has been dedicated to designing and building reactors that satisfy the aforementioned requirements: shock tubes, jet stirred reactors (JSRs), and flow reactors

2.1.1 Shock tubes

As illustrated in Fig. 2.1, a shock tube is a closed tube with two different sections: driver and driven, separated by a diaphragm. The driver section contains an inert driver gas at high pressure, while the driven section contains a driven gas: the reac-

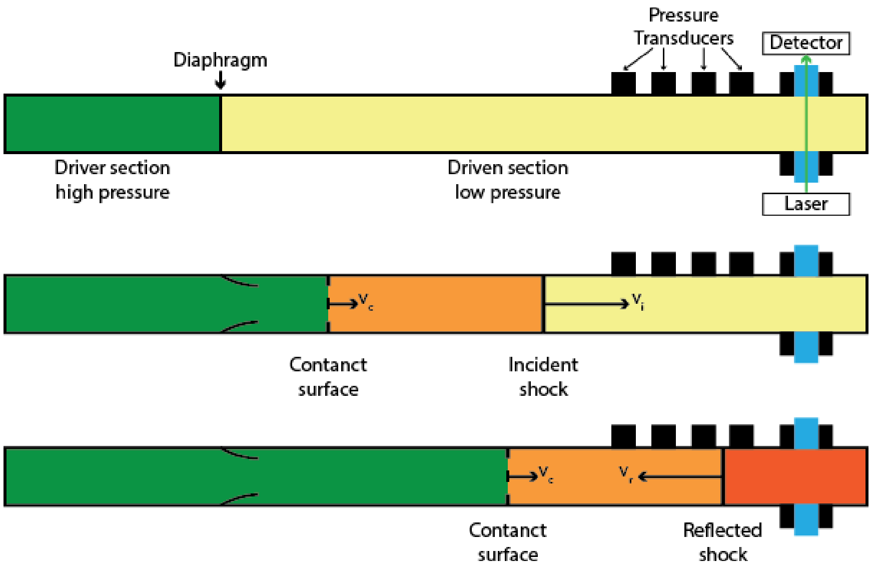

Figure 2.1: Schematics of a shock tube and its operation

tants usually diluted in an inert gas at much lower pressure. When the diaphragm bursts open under a specified condition, the sudden expansion of the driver gas at high pressure into a gas at low pressure produces a shock wave that propagates into the driven section. The shock wave rapidly increases the pressure and temperature of the reactive mixture. In most shock tube studies, a second rise in pressure and temperature is caused by reflected shock wave at the end of the tube [43–45]. The advantage of shock tubes is that they allow researchers to access high temperature and pressure conditions (up to 4000 K and 1000 atm). However, their usage to study the gas phase chemistry during soot formation and SiC deposition processes is limited by their short available test times (only up to 1 ms). The available test time in a shock tube study is determined by the time interval between the passage of the reflected shock wave at the diagnostic location and the interaction of the reflected shock wave with the contact surface [46, 47]. The contact surface is an interface that separates the driver and driven gases and it follows the incident shock wave at a slower speed. The interaction between the reflected shock wave and contact surface causes an acoustic discontinuity wave that passes through the reactive gas mixture at the diagnostic location and perturbs this gas in both pressure and temperature.

2.1.2 Jet stirred reactors

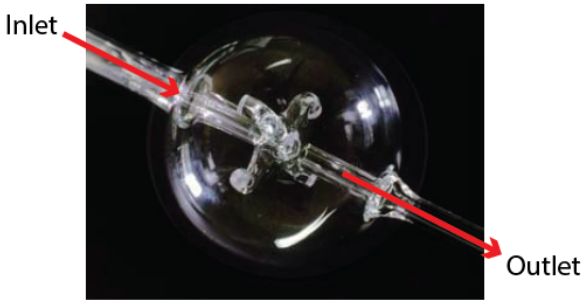

(a) A JSR used in Nancy, France

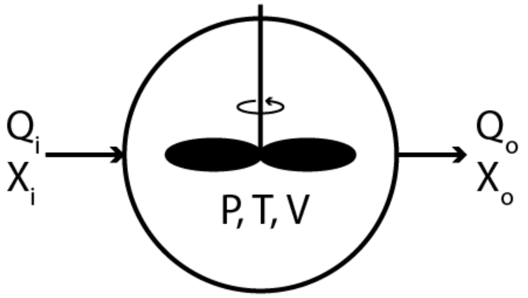

(b) Schematics of the JSR

Figure 2.2: (a) A jet stirred reactor (JSR) at Reactions and Process Engineering Laboratory in Nancy, France, and (b) the schematics of the JSR with volume V working at constant temperature T and pressure p conditions. X_i and X_o are mole fractions at the inlet and outlet, respectively. q_i and q_o are volume flow rates at the inlet and the outlet respectively. The figure is adapted from [48].

Jet stirred reactors (JSRs) consist of a spherical chamber with four or more internal nozzles from which a reactive mixture exits and gets continuously stirred to create a homogeneous mixture inside the reactor (see Fig. 2.2). JSRs are a useful tool to study the gas phase chemistry because the output composition is identical to the species composition inside the reactor, which is a function of residence time and temperature [49–51]. Thus, the output composition can be used to infer the chemistry of the reactants inside the reactor at different conditions. However, JSRs have two disadvantages. Firstly, there exists uncertainty associated with the residence time of the reactive mixture inside a JSR. Each JSR has a narrow residence time distribution, and the residence time of the gas is estimated by a mean residence time. In addition, one of requirements for the homogeneity of the gas phase composition in a JSR is that the speed of the gas exiting the four nozzles must be lower than the sonic speed at the temperature and pressure of the reaction [48]. This requirement sets a lower limit on accessible residence time around 80 ms. The second disadvantage of JSRs is the inhomogeneity of temperature. Because chemical reaction rates are a function of temperature, spatial temperature gradient can lead to variation of chemical activity throughout a JSR. To minimize spatial temperature gradient, preheating of cold fresh reactant gases before the reactor and diluting the reactants in an inert gas have been shown to be effective solutions.

2.1.3 Flow reactors

Because the accessible residence times from shock tubes (only up to 1 ms) and from JSRs (above 80 ms) are outside the range of interest to study formation of precursor species during 1) soot formation and 2) SiC depostion, flow reactors are a more sensible choice for this type of studies. The advantages of flow reactors can be illustrated with an isobaric plug flow reactor (PFR) as shown in Fig. 2.3. Under steady state conditions, the governing species and energy equations of the PFR are given by:

$$\rho U_{pl} \frac{\partial Y_i}{\partial z} = \dot{w}_i, \tag{2.1}$$

$$\rho U_{pl} c_p \frac{\partial T}{\partial z} = \dot{w} Q \tag{2.2}$$

with the well defined initial boundary conditions:

$$Y_i(z_0) = Y_{i,0}, \tag{2.3}$$

$$T(z_0) = T_0 \tag{2.4}$$

In equations 2.1-2.4, ρ is mass density, U_{pl} is plug flow velocity, Y_i is the mass fraction of species i, c_p is the mass-averaged specific heat capacity at constant pressure, T is temperature, z is the spatial coordinate in the axial direction, $\dot{w}_i$ is the rate of production or consumption of species i, and $\dot{w}Q$ is the overall heat release rate. The energy equation assumes idealized thermal conditions: either adiabatic or isothermal. In addition to the species and energy equations, the continuity equation of the PFR is satisfied by

$$u = U_{pl}(T(z), Y_i(z)), \tag{2.5}$$

where the cross-sectional area averaged plug flow velocity, U$_{pl}$, depends on local temperature and species mass fraction. The PFR also assumes negligible axial diffusion relative to axial convection and chemical reaction. Under these assumptions, a spatial-to-temporal coordinate conversion is possible with $t = \frac{z}{U_{pl}}$, yielding a new form of the species equation

$$\rho \frac{\partial Y_i}{\partial t} = \dot{w}_i \tag{2.6}$$

Thus, practical flow reactors that closely approximate the PFR can provide direct insight to the chemical source term $\dot{w}_i$ with the measured temporal profile of species mass fraction, $(Y_i(t))$. However, flow reactors are not without their own sets of uncertainty. The first set of uncertainty is associated with establishing initial conditions to the flow reactor, and the second set of uncertainty arises from the departure from the PFR in typical flow reactors due to non-idealities, such as radial and axial species gradients, species stratification due to Poiseuille flow, and heterogeneous effects from wall surface reactions.

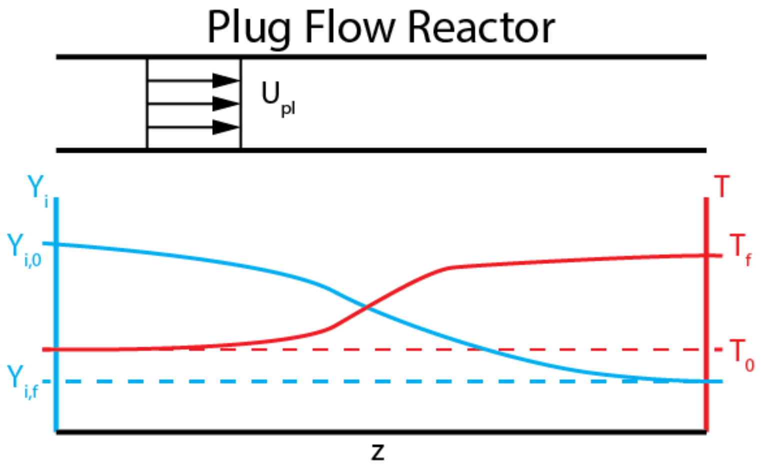

Figure 2.3: Schematics of a plug flow reactor (PFR) with velocity (U_{pl}), species mass fraction (Y_i), and temperature (T) profiles, adapted from [52].

Reactor inflow conditions

The PFR described above with its governing equations assume that the inflow/initial conditions $Y_{i,0}$ and T_0 (Eqs. 2.3-2.4) are readily available and well-characterized. However, in order to have such well-defined inlet conditions, the assumption requires a non-reactive gas mixture to undergo an instantaneous jump step in both mass fraction and temperature at time = 0. In practice, this perfect and instantaneous change in mass fraction and temperature is impossible. Therefore, experiments with flow reactors involve uncertainty in defining the true reaction start time. The uncertainty associated with reactor inflow/initial can be illustrated with two typical flow reactor configurations as shown in Fig. 2.4:

- **Type 1 flow reactor** involves individually pre-heating the reactants and diluents to the temperature T_0, and then rapidly mixing them to achieve the initial composition $Y_{i,0}$ at the entrance of the reactor. Reactors of this type tend to have large diameter (greater than 10 cm) and run at high Reynolds numbers to take advantage of turbulent effects to enhance radial mixing [53–55]. Because of the large diameter, species concentration can be probed at different axial locations inside the reactor. One notable example of such a reactor is the Princeton

Variable Pressure Flow Reactor (VPFR) [53].

- **Type 2 flow reactor** involves pre-mixing the reactants and diluents to the inflow/initial composition $Y_{i,0}$ at sufficiently low temperature to prevent reaction, and then rapidly heating the mixture to the temperature T_0 at the entrance of the reactor. Reactors of this type are small diameter (less than 10 mm) laminar flow reactors [56–60]. These small-scaled reactors are more affordable to run than type 1 flow reactors. Also, because of small diameter, species concentration is typically measured at the exit of the reactors, and thus, the variation in residence times can only be obtained by varying the mass flow rate.

In the type 1 flow reactor, the uncertainty associated with reactor initialization arises from the finite-rate mixing of reactants and diluents. If the mixing is too fast, the initial composition $\mathrm{Y}_{i,0}$ is obtained ahead of the mixing region exit, resulting in early start time. On the other hand, if the mixing rate is too slow, the initial composition is obtained after the mixing region exit, resulting in later start time.

In the type 2 flow reactor, the premixed reactants and diluents pass through a finite-rate heating region. The temperature ramping section blurs the starting line of the reaction region and thus the true start time.

Given the major uncertainty associated with reactor inflow/initial conditions, numerous studies have been performed to find solutions around this problem. One notable solution is to employ spatial or temporal coordinate shifting of the measured species or temperature profiles to match predicted results from chemical kinetic simulations with well-defined initial conditions. The coordinate shifting approach aligns the measured and predicted results by locating sensitive features such as 50% consumption point of a major reactant or the peak concentration of an important intermediate [52]. It will be shown later that the UVa microflow tube reactor (MFTR) overcomes the reactor initial condition problem without employing the coordinate-shifting approach.

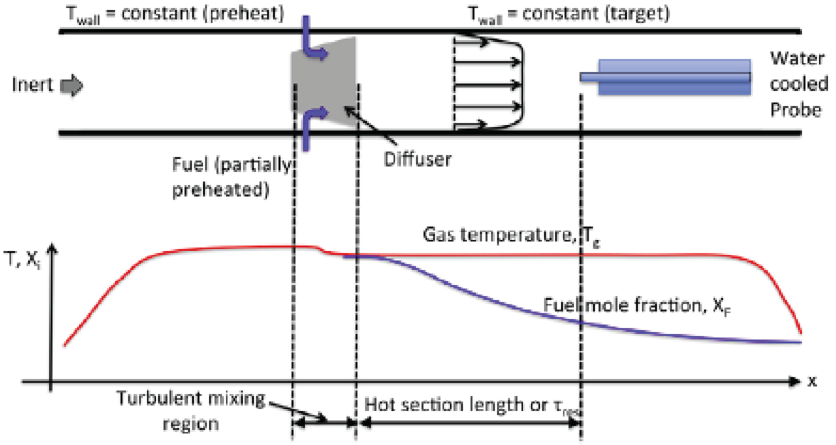

(a) Type 1 flow reactor

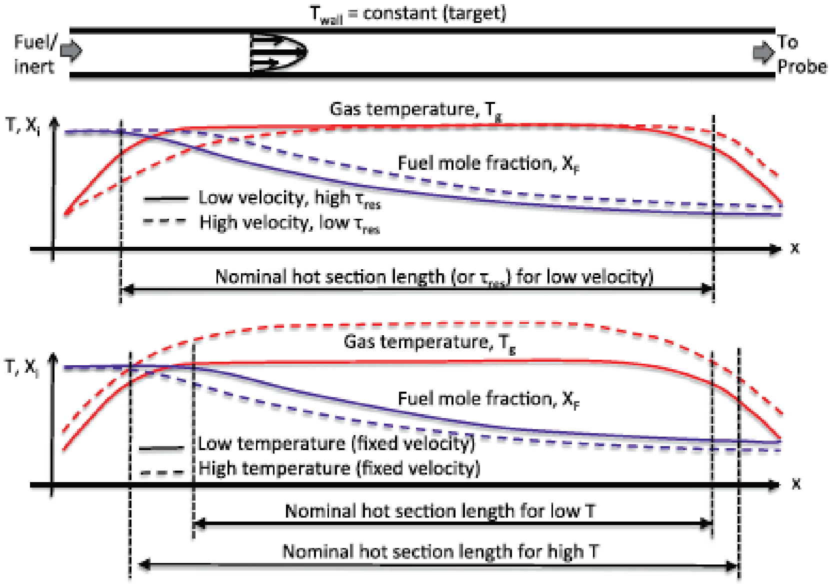

(b) Type 2 flow reactor

Figure 2.4: Illustrations of type 1 and type 2 flow reactors along with temperature (red line) and species concentration (blue line) profiles [61].

Departure from the plug flow reactor (PFR) idealization

In addition to challenges of well characterizing initial conditions, experimental studies with flow reactors can experience a number of non-idealities that cause the reactors to depart from the PFR idealization. These non-idealities include non-negligible radial and axial gradients of species concentration and temperature, species stratification due to Poiseuille flow and wall surface reactions. The extent of these effects can be highlighted with the non-dimensional 2D species governing equation for a flow reactor with circular cross section,

$$U(R)\frac{\partial Y_i}{\partial Z} - \frac{1}{\epsilon Pe_i}\left(\frac{1}{R}\frac{\partial}{\partial R}\left(R\frac{\partial Y_i}{\partial R}\right) + \epsilon^2\frac{\partial^2 Y_i}{\partial Z^2}\right) = Da_i\widehat{w}_i \tag{2.7}$$

The left hand side of Eq. 2.7 accounts for molecular transport, while the right hand side handles the consumption or production of species i with the non-dimensional chemical source term $\widehat{w}_i$. The molecular transport consists of axial convection $U(R)\frac{\partial Y_i}{\partial Z}$, and diffusion in the radial and axial directions: $\frac{1}{\varepsilon Pe_i}\left(\frac{1}{R}\frac{\partial}{\partial R}\left(R\frac{\partial Y_i}{\partial R}\right) + \varepsilon^2\frac{\partial^2 Y_i}{\partial Z^2}\right)$. Here R is the radial reactor coordinate normalized by the reactor diameter d; Z is the axial reactor coordinate scaled by the reactor length L; $U(R)$ is the axial velocity non-dimensionalized by the plug flow velocity U_{pl} and is a function of R; ϵ represents the ratio of the reactor diameter to its length $(\frac{d}{L})$ or the inverse of reactor aspect ratio; the parameter Pe_i is the mass transfer Peclet number and is defined as the ratio between convective and diffusive transport rates of species i, $Pe_i = \frac{U_{pl}d}{D_i}$; the Damkohler number $Da_i = \frac{L/U_{pl}}{\tau_{k,i}}$ is the ratio between convective and chemical time scales. It should be noted that Eq. 2.7 can also be used with the scalar temperature $(Y_i = T)$ to describe the energy distribution inside the reactor. When temperature is considered, the mass diffusivity D_i is replaced by the thermal diffusivity (a) and the mass transfer Peclet number becomes the heat transfer Peclet number Pe_{th}.

In order to used the PFR idealization in flow reactor studies, the flow reactors must be designed such that the governing equation Eq. 2.7 closely approximate those of a PFR (Eqs. 2.1-2.2). This means that the radial and axial terms in Eq. 2.7 must be small relative to axial convection and reaction terms. Negligible radial and axial diffusion can be achieved by selecting appropriate values for ϵ and the Peclet numbers. The ϵ value constrains the dimensions of the reactor whereas the Pe numbers specify the operational conditions: temperature, pressure, residence time and reactant/diluent composition. Small values of ϵ ($\epsilon \ll 1$) are preferable because the resultant flow reactors will be of small scale with low operational cost. With ϵ fixed, the ideal value for the Peclet numbers should be such that $Pe \sim O(1)$. Flow reactors with these characteristics ($\epsilon \ll 1$ and $Pe \sim O(1)$) are fast diffusivity fully developed laminar flow reactors [62–65]. Because of the small radius and high diffusivity, the radial diffusion term in Eq. 2.7 dominates all other terms and approximates to:

$$\frac{1}{R}\frac{\partial}{\partial R}\left(R\frac{\partial Y_i}{\partial R}\right) \simeq 0 \tag{2.8}$$

This equation admits the solution $Y_i(R) = const$, and indicates that radial thermal and species gradients are negligible. In other words, the radial mixing is fast in comparison to the convective and reaction rates under these flow reactor characteristics. However, because of small diameter and fast radial diffusion, wall reaction effects can be a potential issue in fast diffusivity fully developed laminar flow reactors.

Other values of Peclet numbers can introduce other non-idealities to the flow reactors. When Pe is propotional to ϵ or $Pe \ll 1$, attribution of axial diffusion term in Eq. 2.7 cannot be ignored. In this case, radial diffusion still dominates and uniform radial distribution of species concentration or temperature preserves ($Y_i(R) = const$), and Eq. 2.7 becomes

$$U(R)\frac{\partial Y_i}{\partial Z} - \frac{\epsilon}{Pe_i}\frac{\partial^2 Y_i}{\partial Z^2} = Da_i \widehat{w}_i \tag{2.9}$$

Under this condition, measured profile of Y_i can still yield direct information of the chemical source term $\widehat{w}_i$, but the spatial-to-temporal coordinate transformation using the plug flow velocity ($t = z/U_{pl}$) requires modification to account for the axial diffusion effect that tends to blur the ideal plug flow species and temperature gradients [66].

Another issue arises when Pe is proportional to $\frac{1}{\epsilon}$ or $Pe \gg 1$. Under this condition, only axial diffusion terms becomes negligible. The orders of radial diffusion, axial convection and chemical reaction are similar, so that Eq. 2.7 becomes

$$U(R)\frac{\partial Y_i}{\partial Z} - \frac{1}{\epsilon Pe_i}\left(\frac{1}{R}\frac{\partial}{\partial R}\left(R\frac{\partial Y_i}{\partial R}\right)\right) = Da_i\widehat{w}_i \tag{2.10}$$

It may be seen that the species concentration is not uniform in the radial reactor coordinate, considerably complicating experimental measurements of species concentration or temperature that only accounts for axial variation. Furthermore, modeling such reactors is more complex since it must now employ two-dimensional approach [66].

Once the governing equation of flow reactors closely approximates those of the PFR, i.e,

$$U(R)\frac{\partial Y_i}{\partial Z} = Da_i\widehat{w}_i, \tag{2.11}$$

it is important to note that the velocity term $U(R)$ is not a plug flow velocity but a function of the radial reactor coordinate R. Because of the non-uniform velocity in the R direction, species and temperature stratification arises (see Fig. 2.5). As a results, species at different radial locations experience different residence time and temperature conditions, leading to inhomogeneous reactions inside the flow reactors. Non-uniform velocity in the radial reactor coordinate thus requires both Damkohler and Peclet numbers to be considered during the design of flow reactors. When reaction rates are sufficiently fast, but radial diffusion is not fast enough to minimize the flow stratification effect, inhomogenous reactions can exacerbate the non-ideal effects of

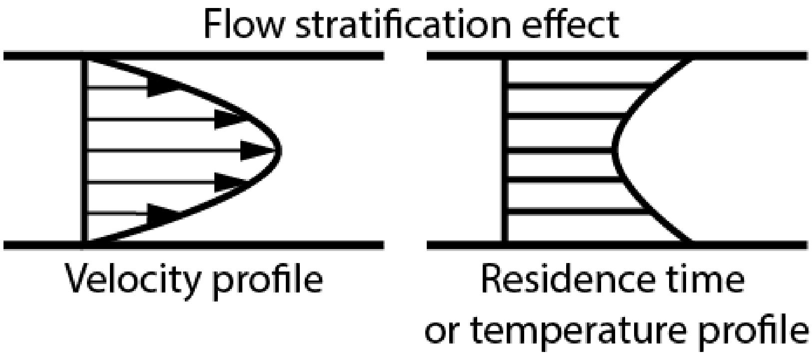

Figure 2.5: A typical velocity profile in a flow reactor that leads to as shown radial residence time or temperature profile.

species and temperature gradients in the radial and axial directions.

2.2 The UVa flow reactors

In this thesis work, two different flow reactor configurations were used to study the formation of precursor species in the gas phase during 1) soot formation and 2) SiC deposition (see Fig. 2.6). A microflow tube reactor (MFTR) with a complex design was employed to overcome the limitations that were described in Section 2.1.3. The MFTR was only used for soot formation study, while the SiC deposition study was conducted with a simpler premixed microflow tube reactor (PMFTR). Because SiC deposition studies produced SiC deposit on the inner reactor wall, a new reactor was needed for each experimental run at a new experimental condition. The MFTR cost more than $3000 to fabricate with quartz tubing; thus, it was not practical to use it for SiC deposition studies. Although the PMFTR (type 2 flow reactor in Fig. 2.4) involves a number of limitations that introduce considerable uncertainty to the measured data, thorough examination of the data along with vigorous simulation of the PMFTR with available chemical kinetic models can still yield insightful information on the gas phase chemistry during SiC deposition.

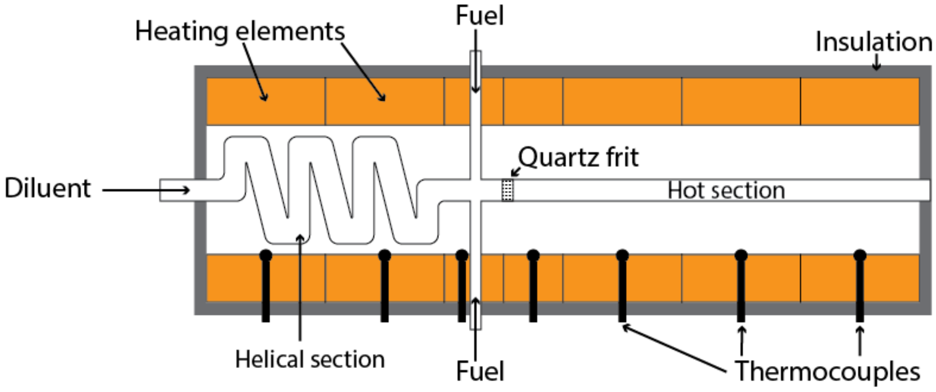

(a) UVA MFTR

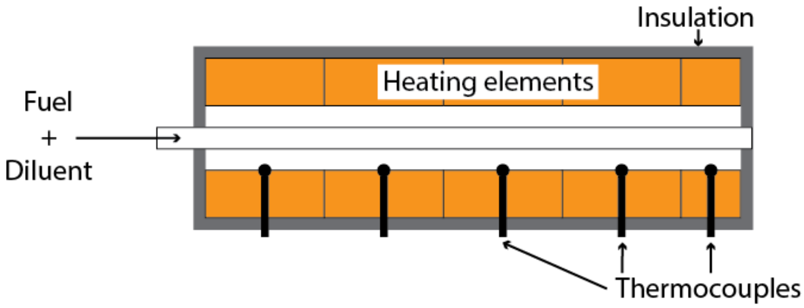

(b) UVA PMFTR

Figure 2.6: Schematics of UVA flow reactors: a) microflow tube reactor - MFTR and b) premixed microflow tube reactor - PMFTR

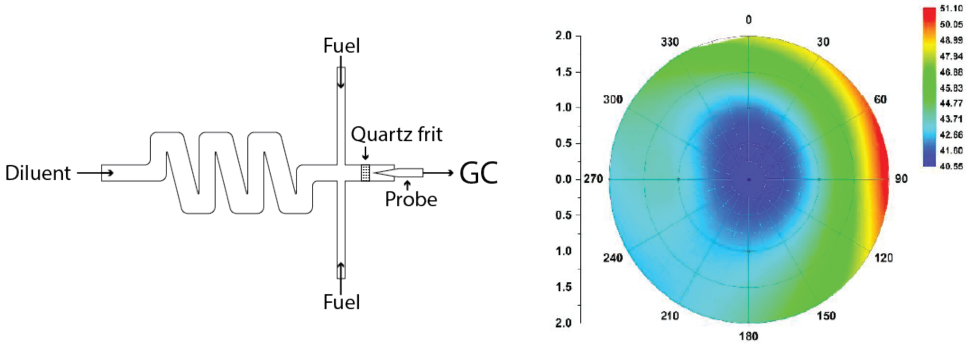

(a) Experimental schematics

(b) Radial fuel (C_2H_4) profile

Figure 2.7: (a) Schematics of a calibration experiment to determine the distribution of ethylene (C_2H_4) concentration in the radial coordinate. (b) A radial C_2H_4 concentration profile measured by gas chromatography (GC). In flow species concentration: $X_{C_2H_4} = 0.042$, $X_{N_2} = 0.757$ and $X_{O_2} = 0.201$. The figure is adapted from [67].

2.2.1 The UVa MFTR

Well characterized inlet conditions

A brief description of the MFTR is given here. A more detailed account of the reactor can be found in [61, 67, 68]. The reactor is designated as a microflow tube reactor because its volume flow rates are approximately five orders of magnitude (10^{-5}) less than those of the Princeton VPFR [53]. The MFTR is a quartz tube reactor with 4 mm ID as shown in Fig. 2.6(a). The reactor is placed inside a furnace that comprises seven modular heating elements from Thermcraft (Models RH211 and RH212) with a maximum temperature of 1573 K. The temperature inside the furnace and thus of the reactor is controlled and maintained by seven proportional integral dervative (PID) controllers connected via k-type thermocouples. The MFTR is a hybrid of the two types of flow reactors shown in Fig. 2.4. Because of the exponential dependence of reaction rate coefficients on temperature, the MFTR was designed without a temperature ramp-up section of type 1 flow reactor in order to avoid any uncertainty associated with finite-rate heating of the reactants. Instead, the main diluent flow is preheated to the target temperature in a 125 cm long helical section. The fuel under investigation is introduced via two side tubes of 1 mm ID immediately downstream of the helical section. A small mixing region of 0.2 cm^3 volume locates immediately after the junction between the helical section and the side tubes where rapid mixing of the fuel and main diluent is facilitated by a porous quartz frit. The homogeneity of the mixture exiting the mixing region has been verified with measurement of species mole fraction radially on a plane just downstream of the quartz frit (prior to fusing the hot section) (see Fig. 2.7) [67]. A key benefit of the small mixing volume is that, for the investigated fuels and flow conditions, it has eliminated a need for coordinate shifting.

The hot section (main reaction region) is 37 cm long and locates immediately after the quartz frit. The temperature of the hot section is controlled and maintained by the last four elements of the heater-PID system as shown in Fig. 2.6(a). In temperature calibration experiments, temperature inside and outside of the tube was measured under typical flow velocities with inert gas flow and showed a difference of less than 5 K. Typical temperature profiles obtained inside the reactor is shown in Fig. 2.8 at different volume flow rates (or residence times) or at different target temperatures. Because the reactor exit is open to the atmosphere, a temperature drop of about 100-150 K is observed near the exit. Numerical simulation with the observed temperature drop near the exit has revealed negligible effects (less than 4%) on the measured species data [61]. In addition, high dilution levels with inert nitrogen (N_2) gas (95-99.75%) are used to minimize temperature variation due to the endothermic nature of fuel pyrolysis process.

Design criteria for the PFR idealization

There exists a number of non-idealities: radial and axial gradients of species and temperature, flow stratification and wall surface reactions, that can cause flow reactors to depart from the plug flow reactor (PFR) idealization. In order to overcome these

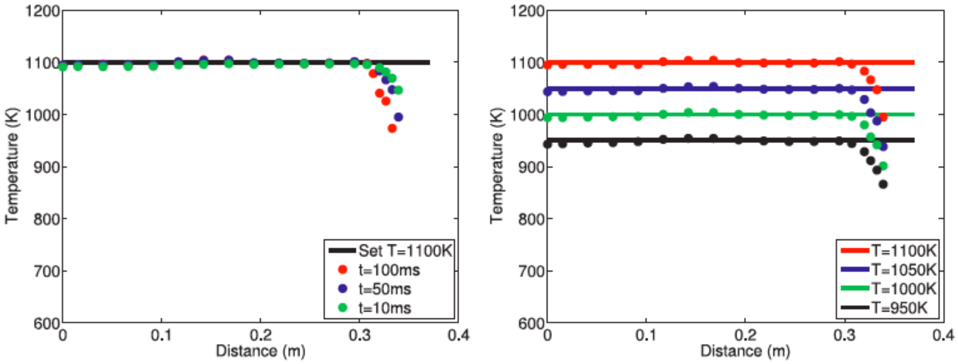

Figure 2.8: Measured temperature inside the hot section (a) for a target temperature of 1100 K with varying residence time values: 10-100 ms, and (b) for 10 ms residence time with varying temperature from 950-1100 K [61].

non-idealities, Cutler et al. [69] have critically evaluated the criteria for designing flow reactor studies on the basis of characteristic time scales associated with forced convection, axial and radial species diffusion, thermal diffusion, momentum transport and first-order chemistry. These criteria are shown in Table 2.1. Accordingly, all the experimental conditions: temperature, residence time and fuel-diluent composition, were selected such that the investigation of precursor species (PAHs) to soot formation with the MFTR would satisfy the listed criteria and the PFR idealization could be used to interpret the measured data. In addition, the selected experimental conditions were such that chemical and convective time scales ($\tau_k \simeq \tau_{c,L}$) were matched, indicating the measured data were in kinetically controlled regime.

2.2.2 The UVa PMFTR

For the investigation of gaseous precursor species that lead to SiC formation, a premixed microflow tube reactor (PMFTR) was used. The PMFTR is a type 2 flow reactor as shown in Fig. 2.4(b). In this reactor type, the fuel and diluent are premixed before they enter the reactor. As the mixture travels through the reactor, it gets heated to the target temperature, resulting in a temperature ramping length prior to an isothermal section. Because of this axial temperature profile, it is very

Table 2.1: Criteria of characteristic time scales for the validity of the PFR idealization reported by Cutler et al. [69]. Note: c - forced convection, R - radial reactor coordinate, sd - species diffusion, k - chemical kinetics, L - axial reactor coordinate, and td - thermal diffusivity. *The smaller of these two values should be employed.

For	Criteria	Criterion no.
Negligible axial diffusion	$\frac{\tau_{c,R}^2}{(\tau_{sd,R})(\tau_k)} \ll 0.1$	C1
	$\frac{\tau_{c,R}}{\tau_{sd,R}} < 0.02$	C2
	$\frac{\tau_{sd,R}}{48\tau_k} + \frac{\tau_{c,R}^2}{(\tau_k)(\tau_{sd,R})} \ll 1$	C3*
	$\frac{1}{(\tau_k)(\tau_{c,L})} \ll 2$	C4*
Negligible Poiseuille flow	$\frac{\tau_{sd,R}}{\tau_{c,R}} \ll 100$	C5
	$\frac{\tau_{sd,R}}{\tau_k} < 1$	C6
	$\frac{\tau_{c,R}}{\tau_k} < 0.05$	C7
Constant temperature	$\frac{\tau_{td}}{\tau_{c,L}} \ll 3.7$	C8

difficult to pinpoint the true start time of the reaction (reactant decomposition). An additional difficulty with this reactor type is that one cannot completely control temperature and residence time independently. If one wishes to study the effect of temperature variation at a fixed residence time, then changing temperature will induce a mixture density change which in turn changes the mixture velocity and thus the residence time. On the other hand, if the target temperature is kept constant while varying the residence time, then the experiment will change the mixture mass flow rate to change the residence time. However, a change in mass flow rate will lead to a change in the temperature profile because the heating length is dependent on the mass flow rate. Because of this interdependence between gas temperature profile and residence time, the measured data obtained with the PMFTR will be reported as a function of nominal residence time, which is defined as an amount of time for a reactant molecule to travel from the reactor inlet to the exit given a mass flow rate and a target temperature.

2.3 Experimental conditions

2.3.1 Soot precursor formation in the UVa MFTR

An investigation of the formation of gaseous precursor species responsible for soot during pyrolysis of fuels was conducted with the MFTR. The fuels, ethylene (C_2H_4), n-dodecane ($C_{12}H_{26}$), and Jet A (POSF10325), were selected to highlight the effect of the fuel chemical composition on the formation of soot precursors (polyaromatic hydrocarbons - PAHs). In addition, this thesis work also studied the effects of temperature and residence time variations. Here, the residence time was defined as $t_{res} = \tau_{c,L} = \frac{L}{U_{pl}}$, where L is the length of the hot section and U_{pl} is the cross sectional average flow velocity or plug flow velocity. The residence time was changed by changing the mass flow rate of the fuel and diluent into the reactor. However, the residence

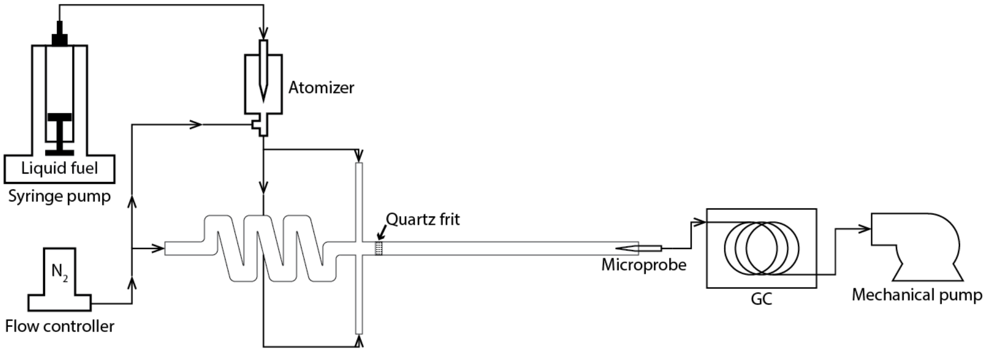

Figure 2.9: Schematic of the experimental apparatus used to study the gas phase chemistry during hydrocarbon fuel pyrolysis

time must not be lower than 27 ms for the considered temperature range (1000-1250 K) because the criterion for negligible flow stratification effect, $\tau_{sd,R}/\tau_{c,L} < 1$, would be violated when the flow residence time is smaller than 27 ms [61].

For the gaseous fuel (C_2H_4) and diluent (N_2) flows, a series of mass flow controllers (Sierra SmartTrak 100 with 1% accuracy at full scale) was used. A separate flow delivery system was used to introduce prevaporized liquid fuels ($C_{12}H_{26}$ and Jet A) to the reactor (see Fig. 2.9). The system consisted of two components: a 500 mL liquid syringe pump (Teledyne ISCO Model 500D) and an ultrasonic atomizer (Sono-Tek 120 kHz Ultrasonic Nozzle with microbore for low flow rates). The liquid syringe pump with flow and pressure capabilities of 0.001-204 mL/min and 10-3750 psi, respectively, was used for liquid fuel delivery to meet the requirement of small fuel flow rates (20-60 μL/min). The purpose of the ultrasonic atomizer was to generate a fine mist of 10-15 μm fuel droplets so that these small droplets would get completely vaporized when they mixed with a carrier flow of pre-heated diluent N_2 gas. A more detailed description of the ultrasonic atomizer can be found in [68].

All the experimental conditions of the fuel pyrolysis experiments are summarized in Tables 2.2-2.4. To ensure that the plug flow reactor (PFR) idealization could be used to interpret the measured data, all the criteria listed in Table 2.1 were evaluated at every experimental conditions. The calculation of the the criteria and the corresponding characteristic time scales closely followed the procedure described by Shrestha et al. [61]. A summary of all the equations of the characteristic time scales is provided here for completeness:

Name	Characteristic time	Formula
Radial convection	$\tau_{c,R}$	$\frac{r}{U_{pl}}$
Axial convection	$\tau_{c,L}$	$\frac{l}{U_{pl}}$
Radial species diffusion	$\tau_{sd,R}$	$\frac{r^2}{D_{ij}}$
Axial species diffusion	$\tau_{sd,L}$	$\frac{l^2}{G}$
Radial thermal diffusion	$\tau_{td,R}$	$\frac{r^2}{a}$
Chemical reaction	τ_k	$\frac{1}{k}$

where r is the reactor radius (2 mm), L is the length of the hot section (37 cm), U_{pl} is the cross sectional average velocity, D_{ij} is the binary species diffusion coefficient of the fuel in an environment of the diluent N_2 gas, G is the effective species diffusion coefficient with Taylor-Aris dispersion, a is the thermal diffusivity, and k is the first-order reaction rate coefficient. An expression for the effective species diffusion coefficient with Taylor-Aris dispersion was derived by Taylor [70] and Aris [71] for a parabolic velocity in a laminar flow regime:

$$G = D_{ij}\left(1 + \frac{Pe_i^2}{192}\right), \tag{2.12}$$

where Pe_i is the mass transfer Peclet number ($Pe_i = \frac{U_{pl}d}{D_{ij}}$). The characteristic chemical reaction time τ_k was estimated by assuming the fuel decomposition reaction was a first-order reaction. Thus, a value of fuel mole fraction at any time can be found by using the following expression:

$$X_{fuel,t} = X_{fuel,0}e^{-kt}, \tag{2.13}$$

where $X_{fuel,0}$ is the initial fuel mole fraction. The characteristic chemical reaction

Table 2.2: Experimental conditions of ethylene (C_2H_4) pyrolysis experiments

Ethylene pyrolysis experimental conditions				
$X_{fuel} = 5\%, X_{N_2} = 95\%$, and p = 1 atm				
T [K]	Time [ms]	ε	Da_{fuel}	Pe_{fuel}
1250	300	0.01	0.4139	21.86
	400		0.5518	16.3949
	500		0.6898	13.1159
	600		0.8277	10.9299
	700		0.9657	9.3685
1000	500	0.01	0.0015	19.0826
1050			0.0057	17.5765
1100			0.0206	16.2534
1150			0.0697	15.084
1200			0.2236	14.0445
1250			0.6898	13.1159

time τ_k was defined as the time at which only 1/e of the fuel mole fraction remained, i.e.,

$$\frac{X_{fuel,t}}{X_{fuel,0}} = e^{-1}, \tag{2.14}$$

or $\tau_k = 1/k$.

Ethylene pyrolysis experiments: the experimental conditions listed in Table 2.2 satisfy all the criteria for the validity of applying the PFR idealization to interpret the measured flow reactor data. In addition, the Damkohler numbers (Da) of the ethylene fuel are O(1), indicating the pyrolysis process was in the chemical kinetics controlled regime at all the experimental conditions.

Liquid fuel pyrolysis experiments: the criteria for the PFR idealization were only satisfied at low temperature conditions: 1000 and 1050 K when studying the pyrolysis of the liquid fuels: n-dodecane and Jet A. As temperature increased, the fuel decomposition became extremely fast, resulting in $Da_{fuel} \gg 1$. Fast fuel decomposition rate also contributed to the enhanced stratification effects due to Pouseuille flow (as shown in Table 2.5). In spite of the undesirable effects, the experiments needed to

Table 2.3: Experimental conditions of n-dodecane ($C_{12}H_{26}$) pyrolysis experiments

n-Dodecane pyrolysis experimental conditions

$X_{fuel} = 0.25\%, X_{N_2} = 99.75\%$, and p = 1 atm

T [K]	Time [ms]	ε	Da_{fuel}	Pe_{fuel}
1050	30	0.01	0.5556	1042.1593
	40		0.7407	781.6195
	50		0.9259	625.2956
	60		1.1111	521.0797
	70		1.2963	446.6397
1150	30	0.01	11.1111	891.6247
	40		14.8148	668.7185
	50		18.5185	534.9748
	60		22.2222	445.8124
	70		25.9259	382.1249
1000	50	0.01	0.1838	680.1085
1050			0.9259	625.2956
1100			4.3103	577.2892
1150			18.5185	534.9748
1200			71.4286	497.4606
1250			250	464.0252

be carried out at high temperature conditions (1100-1250 K) for production of important PAH species such as: benzene (C_6H_6), toluene (C_7H_8), and naphthalene (C_7H_8). The flow stratification effects was accounted for as the residence time uncertainty in the experimental data (see Appendix B).

2.3.2 SiC precursor formation in the UVa PMFTR

The UVa PMFTR (4.8 mm ID and 0.52 m length) made of non-porous alumina was used to study the gas phase chemistry during SiC deposition. Non-porous alumina replaced fused quartz as the reactor material to prevent crack formation on the reactor wall due to the difference in thermal expansion coefficients between fused quartz and deposited SiC. Similar to hydrocarbon fuel pyrolysis studies, flow residence time in the PMFTR was varied by changing the total mass flow rates of the reactant and diluent. However, as described in Section 2.2.2, changing mass flow rate would lead to

Table 2.4: Experimental conditions of Jet A (POSF10325) pyrolysis experiments

Jet A pyrolysis experimental conditions				
$X_{fuel} = 0.25\%, X_{N_2} = 99.75\%$, and p = 1 atm				
T [K]	Time [ms]	ε	Da$_{fuel}$	Pe$_{fuel}$
1050	30	0.01	0.7299	1281.5068
	40		0.9732	961.1301
	50		1.2165	768.9041
	60		1.4599	640.7534
	70		1.7032	549.2172
1150	30	0.01	20	1100.5105
	40		26.6667	825.3829
	50		33.3333	660.3063
	60		40	550.2553
	70		46.6667	471.6474
1000	50	0.01	0.1883	834.4553
1050			1.2165	768.9041
1100			6.8493	711.2761
1150			33.3333	660.3063
1200			166.6667	614.9765
1250			500	574.4592

Table 2.5: Evaluated criteria for negligible Pouseuille flow at conditions of n-dodecane pyrolysis experiment

Criteria for negligible Pouseuille flow			
n-Dodecane pyrolysis experiments			
Criteria no.	1000 K and 50 ms		1250 K and 50 ms
C4 ($\ll 100$)	340.05		232.0126
C5 (< 1)	0.3378		313.5306
C6 (< 0.05)	0.001		1.3513

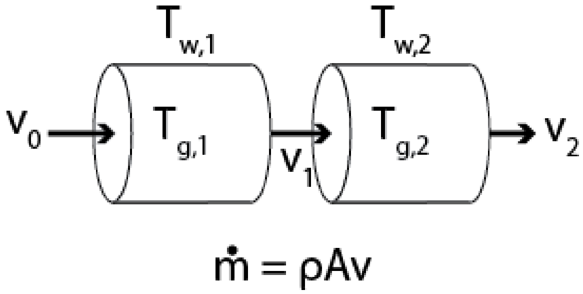

Figure 2.10: Schematics of the 1D PFR code, where v is gas velocity, T_g is gas temperature, T_w is reactor wall temperature, $\dot{m}$ is the total mass flow rate, ρ is gas density, and A is the cross sectional area of the reactor.

a change in the gas temperature profile and thus the time-temperature history inside the PMFTR. As a result, nominal residence time was used instead of true residence time. The nominal residence time was defined as the time a reactant molecule would take to travel from the reactor inlet to the exit given a mass flow rate and a target temperature. The nominal residence time was calculated with a 1D plug flow reactor (PFR) code with imposed reactor wall temperature. Simms [68] developed the heat transfer model used in the 1D code to obtain the gas temperature profile throughout the reactor based on its operating conditions. In the 1D code, the PMFTR was divided into small simulation unit cells. Given the total mass flow rate and axial gas temperature profile, gas velocity and thus residence time in one simulation cell was calculated as shown in Fig. 2.10. Then, the simulation advanced to the next cell with the exit conditions of the previous cell being the inlet conditions of the current cell. The simulation continued on to the last cell at the reactor exit to provide the total nominal residence time. It should be noted that the gas mass flow rate was calculated at a standard condition defined by the Sierra SmartTrak 100 mass flow controllers: 70 °F and 1 atm.

Methyltrichlorosilane (MTS - CH_3SiCl_3) and molecular hydrogen (H_2) were used as the reactants in this study. A mixture of MTS and H_2 was selected because of three reasons. Firstly, Papasouliotis and Sotirchos [72] have demonstrated that

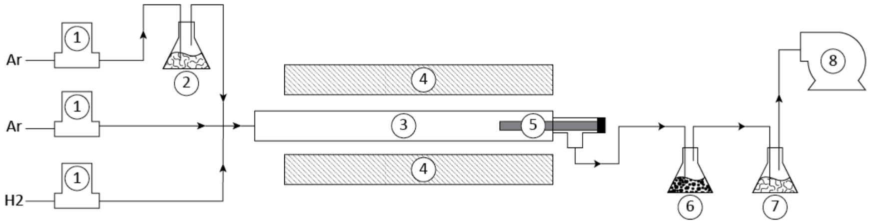

Figure 2.11: Schematics of experimental apparatus used to deposit SiC on quartz substrate: (1) mass flow controllers, (2) liquid MTS bath, (3) the UVA PMFTR, (4) heating furnace, (5) quartz substrate, (6) solid soda-lime trap, (7) water trap, and (8) mechanical pump.

MTS was ideal reactant for producing high quality SiC because MTS contained the same 1-to-1 Si-to-C ratio as the SiC material. Another motivation was that the gaseous by-product HCl might contribute to suppress the deposition of pure silicon (Si) crystal during the growth of SiC. Finally, the H_2 gas might favor the reduction of the Si-Cl bonds on the growing surface of SiC, thereby resulting in an increase in the deposition rate. The experiments were always run under high level of dilution in order to minimize SiC deposited on the reactor inner wall and temperature variation due to the endothermic nature of pyrolysis process. Argon (Ar) was used as the diluent gas whose concentration was kept at 95% of the total flow rate.

The gas delivery system used in these experiments slightly differed from that of the jet fuel pyrolysis (see Fig. 2.11). A series of Sierra SmartTrak 100 mass flow controllers was employed to control the flow rates of gaseous reactant (H_2) and diluent (Ar). A liquid bubbler was needed to deliver MTS vapor to the reactor. A secondary flow of Ar was allowed to bubble through a liquid bath of MTS to pick up MTS vapor and deliver them to the reactor. The liquid MTS bath was kept at 25 °C and 1 atm. The feed line after the liquid bath was always kept at 90 °C to prevent condensation of MTS vapor before they reached the reactor. The correlation between bubbling Ar flow rate and MTS mass flow rate can be found in Appendix A.

The effects of temperature, total flow rate (or nominal residence time) and initial H_2-to-MTS ratio ($\alpha = X_{H_2,0}/X_{MTS,0}$) on the formation of SiC precursor species

Table 2.6: Experimental conditions for SiC deposition on quartz substrates

Experimental conditions for SiC deposition on quartz substrates MTS and H_2 in 95% Ar				
T [K]	α	Q_{total} $[cm^3/s]$	Nominal residence time [ms]	
			0.5 atm	1 atm
1200	10	276	276	552
1250			267	534
1300			258	516
1350			250	500
1300	10	192	360	720
		276	258	516
		456	160	320
		709	106	212
1250	1	276	268	536
	5		267	534
	10		267	534
	15		267	534

were the primary focus of this study. However, the functionality of the PMFTR to study SiC deposition process must be tested before conducting the main experiments. This test was achieved with an investigation of SiC deposition on quartz substrates at different operating conditions (see Fig. 2.11). Specifically, variation of deposition rate, surface morphology and preferred crystal orientation of SiC deposits with varying temperature, total flow rate and α at two different pressures (0.5 and 1 atm) was examined. The experimental conditions of this investigation was summarized in Table 2.6.

After the functionality of the PMFTR was verified by producing results similar to those found in the literature, the main study of the effects of varying operating conditions on the formation of SiC precursors in the gas phase was carried out. Table 2.7 contains all the experimental conditions of this main study as well as the corresponding Damkohler ($Da_{MTS} = \frac{L/U_{pl}}{\tau_{k,MTS}}$) and Peclet ($Pe_{MTS} = \frac{U_{pl}d}{D_{MTS}}$ values of MTS. All the experiment conditions satisfied the criteria listed in Table 2.1 so that the PFR idealization could be used to interpret the experimental data. It should be

Table 2.7: Experimental conditions of MTS pyrolysis

Experimental conditions of MTS pyrolysis				
MTS and H_2 in 95% Ar				
T [K]	α	Nominal residence time [ms]	Da_{MTS}	Pe_{MTS}
1150	10	200	0.0997	165.7489
		300	0.1495	110.4993
		400	0.1994	82.8744
		500	0.2492	66.2996
		600	0.299	55.2496
		700	0.3489	47.3568
1250	10	200	1.1261	143.9528
		300	1.6892	95.9685
		400	2.2523	71.9764
		500	2.8153	57.5811
		600	3.3784	47.9843
		700	3.9414	41.1294
1100	10	500	0.0618	71.4886
1150			0.2492	66.2996
1200			0.8669	61.6925
1250			2.8151	57.5811
1300			8.7873	53.8947
1350			26.178	50.5751
1250	3	500	1.1773	62.0833
	5		1.0645	61.8778
	7		0.9684	61.7757
	10		0.8669	61.6925
	12		0.8193	61.6584
	14		0.7815	61.6335

noted that the calculation of the diffusion coefficient (D_{MTS}) was slightly different from that shown in Section 2.3.1. Because the reactant-diluent mixture used to study SiC deposition consisted of three components: MTS, H_2 and Ar, a multicomponent diffusion coefficient must be calculated for this mixture. Let MTS be species 1, H_2 species 2 and Ar species 3. Following the procedure described in [73], the multicomponent diffusion coefficient of MTS in a mixture of MTS, H_2 and Ar can be found by using,

$$D_{multi,1} = \left(\frac{X_2'}{D_{12}} + \frac{X_3'}{D_{13}} \right)^{-1}, \tag{2.15}$$

where D_{12}, D_{13} are binary diffusion coefficients of MTS in H_2 and in Ar, respectively; X_2', X_3' are the mole fractions of H_2 and Ar relative to the sum of H_2 and Ar mole fractions, i.e.,

$$X_2' = \frac{X_2}{X_2 + X_3} \tag{2.16}$$

and

$$X_3' = \frac{X_3}{X_2 + X_3} \tag{2.17}$$

The binary diffusion coefficient D_{12} (or similarly D_{13}) was calculated as follows,

$$D_{12} = 1.8583 \times 10^{-7} \frac{\sqrt{T^3 \left(\frac{1}{M_1} + \frac{1}{M_2} \right)}}{p \sigma_{12}^2 \Omega_D} \tag{2.18}$$

In Eq. 2.18, T is temperature [K], $M_{1,2}$ are the molecular weights of species 1 and 2 $[\frac{kg}{kmol}]$, p is the total pressure [atm], σ_{12} is the collision diameter between species 1 and 2 [Å], and Ω_D is the diffusion collision integral. The Lennard-Jones 12-6 potential was used to relate the intermolecular energy ψ between two molecules at a separation distance r [74],

$$\psi = 4\varepsilon \left[\left(\frac{\sigma}{r} \right)^{12} - \left(\frac{\sigma}{r} \right)^{6} \right], \tag{2.19}$$

where ε and σ are the characteristic Lennard-Jones energy and length, respectively.

Table 2.8: Physical properties of MTS, H_2 and Ar [73]

Quantity	Unit	MTS	H_2	Ar
Collision diameter, σ	Å	5.864	2.827	3.542
ε/k_b	K	390.48	59.7	93.3

Thus, the collision diameter σ_{12} could be found with the characteristic molecular diameters of species 1 and 2: σ_1 and σ_2,

$$\sigma_{12} = \frac{\sigma_1 + \sigma_2}{2} \tag{2.20}$$

Also, the collision integral Ω_D was obtained by using a polynomial of Neufield et al. [75],

$$\Omega_D = \frac{A}{(T^*)^B} + \frac{C}{exp(DT^*)} + \frac{E}{exp(FT^*)} + \frac{G}{exp(HT^*)}, \tag{2.21}$$

where $T^* = \frac{k_b T}{\varepsilon_{12}}$, A = 1.06036, B = 0.1561, C = 0.193, D = 0.47635, E = 1.03587, F = 1.52996, G = 1.76474, and H = 3.89411. A simple rule shown below was employed to find the value of $\frac{\varepsilon_{12}}{k_b}$:

$$\frac{\varepsilon_{12}}{k_b} = \left(\frac{\varepsilon_1}{k_b}\frac{\varepsilon_2}{k_b}\right)^{\frac{1}{2}} \tag{2.22}$$

The values σ and $\frac{\varepsilon}{k_b}$ for MTS, H_2 and Ar are provided in Table 2.8.

2.4 Species diagnostic system

The gaseous products of the pyrolysis of 1) hydrocarbon fuels and 2) MTS were continuously extracted using small diameter probes and analyzed via two Shimadzu gas chromatography (GC) systems (model 2014). For the fuel pyrolysis studies, a 75 μm ID quartz microprobe was selected in order to obtain equal pressure condition before and after the GC sampling loops. Larger probe diameters with higher species flow rates can result in a significant pressure differential across the GC sampling loops, and thus leading to species calibration uncertainty. On the other hand, for the

MTS pyrolysis studies, a 1 mm ID quartz tube was used as the probe. Because solid by-products from the pyrolysis of MTS deposited and built up at the tip of the probe, a 1 mm ID probe allowed higher run time before the probe must be replaced. The problem of pressure differential across the GC sampling loops caused by the 1 mm ID probe was resolved by precisely controlling the flow rate with a pair of Swagelok metering valves at the inlet and outlet of the sampling loops.

The two GCs were custom designed to detect and quantify a wide range of stable species: inert gases, hydrocarbons, silanes, and organochlorosilanes. The first GC (GC1) with a more complex column configuration and temperature program was used to analyze O_2, N_2, H_2, CO, CO_2 and light hydrocarbon C_1-C_4 species. GC1 consists of two sampling lines, and each line has its own valves, a sampling loop, and detectors. Line 1 is equipped with a 10-port and 6-port valves, a combination of 5 columns: Hayesep-N and -T, Molsieve-5A, Propak-N and QS-BOND, and two detectors: thermal conductivity detector (TCD) and methanizer/flame ionization dector (FID). The purpose of line 1 is to separate and quantify O_2, N_2, CO, CO_2, C_1-C_4 species. Line 2 with a 10-port valve and 2 columns: Hayesep-Q and Molsieve-5A, is used to quantify H_2 via a second TCD. The total analysis time with GC1 is about 20 minutes. A more detailed description of the GC1 can be found in [67]. However, with the current setup of GC1, not all C_4 species can be clearly separated. This C_4 species separation problem can be partially resolved with the second GC (GC2). The design of GC2 is much simpler than that of GC1. GC2 only contains one sampling line with a 10-port valve, one column and one FID. The reason behind the simple configuration of GC2 is to allow easy replacement of the column to quantify a wide range of chemical compounds. In this thesis work, two columns: Restek Rtx-1 and -200, were used for 1) fuel pyrolysis and 2) MTS pyrolysis studies, respectively. The Rtx-1 column allowed separation and quantification of large hydrocarbons (from C_4 and up), while the Rtx-200 column was used to separate and quantify: methane

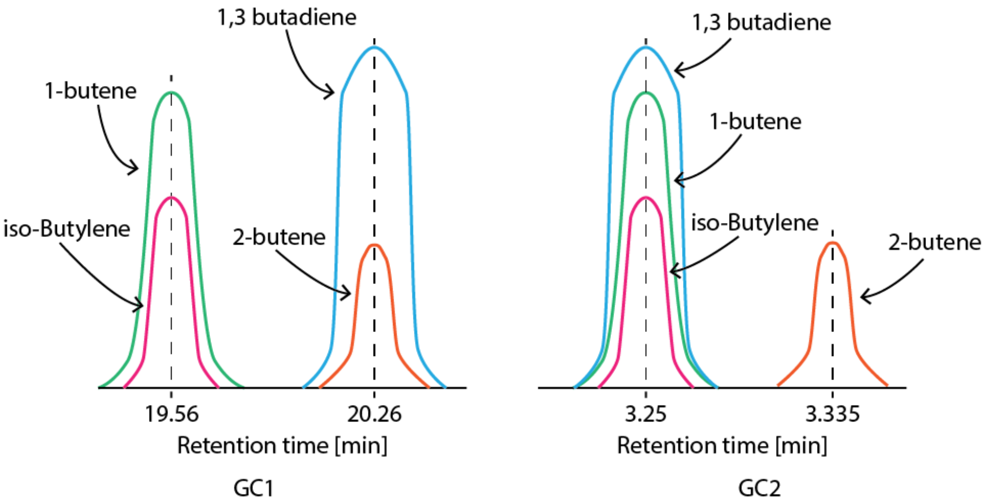

Figure 2.12: Detection of 1-butene (1-C_4H_6), iso-butylene (i-C_4H_8), 1,3 butadiene (C_4H_6), and 2-butene (2-C_4H_6) along with their corresponding retention times on GC1 and GC2

(CH_4), trichlorosilane ($SiHCl_3$), tetrachlorosilane ($SiCl_4$) and MTS.

As mentioned in the previous paragraph, GC1 is not able to clearly separate a number of hydrocarbon C_4 species. Specifically, as shown in Fig. 2.12, 1-butene (1-C_4H_6) and iso-butylene (i-C_4H_8) have the same retention time at 19.56 minutes, whereas both 1,3 butadiene (C_4H_6) and 2-butene (2-C_4H_6) are detected at 20.26 minutes. Although separately identifying 1-butene and iso-butylene is not possible, GC2 can be used to identify 1,3 butadiene and 2-butene. On GC2 with the Rtx-1 column, 1-butene, iso-butylene and 1,3 butadiene have the same retention time at 3.25 minutes. However, 2-butene comes out at a later time (3.335 minutes). Therefore, an absence or even a small peak of 2-butene detected by GC2 can help confirm that the majority of the peak at 20.26 minutes on GC1 is from 1,3-butadiene.

2.5 Summary

For the development and optimization of models for soot formation and SiC chemical vapor infiltration (CVI), a thorough understanding of the formation mechanism of precursor species in the gas phase plays an essential role. Among different reactor configurations, the UVa flow reactors have been shown to be well suited to the operating conditions of interest for the gas phase chemistry. The main non-idealities that may cause uncertainty in the measured data with the flow reactors have been extensively accounted for. As a result, Chapter 3 will begin to introduce the experimental results and how they can provide insight to the the gas phase chemistry of the two different processes, which will be beneficial for the development and optimization of detailed chemical kinetic models.

Chapter 3

Experimental Investigation of Ethylene and n-Dodecane Pyrolysis with a Microflow Tube Reactor

3.1 Introduction

As mentioned in Chapter 1, one of the pollutants generated during the combustion of hydrocarbon fuels is soot particulates. The production and emission of soot negatively impact the well-being of human and the global climate. As a result, minimization of soot formation during the combustion process has been a well-defined target for the design of next generation jet engines. Achieving this target demands a complete knowledge of the different processes leading from the original hydrocarbon fuel molecules to soot particles.

Numerous studies have focused on determining the formation mechanism of soot during combustion of hydrocarbon fuels [19, 21, 23, 24, 76]. Their effort has resulted in a good understanding of the general soot formation mechanism (see Fig. 3.1). The mechanism begins with the thermal decomposition or pyrolysis of the parent fuel into small intermediate species. In subsequent steps, the small intermediate species react and form polycyclic aromatic hydrocarbons (PAHs). The further growth and coagulation of these PAHs lead to the inception of small spherical soot particles. The incipient soot particles further gain mass either by surface reactions with gas phase species or by combining with other soot particles.

The above description of soot formation mechanism highlights the fact that the beginning of soot formation is largely determined by the gas phase chemistry leading up to the production and growth of PAHs. Thus, accurately predicting soot formation at different operational conditions requires a detailed information on the chemical road map from the pyrolysis of the parent fuel to the formation of PAHs. However, obtaining thorough knowledge of the PAH formation is rather challenging. The PAH formation mechanism consists of multiple stages and is highly kinetically controlled [23]. Thus, the ability to predict the evolution of the PAH compounds during combustion demands a complete understanding of the underlying mechanism and kinetics of every stage of the reaction sequence. Different reaction pathways control the formation and growth of PAHs. The inception of PAHs is marked by the formation of the first aromatic rings (e.g., benzene (C_6H_6) or phenyl radical ($C_6H_5\bullet$)). Two main reaction pathways have been proposed to account for the formation of the first aromatic rings: even carbon (C_2/C_4) and odd carbon (C_3) pathways. The C_2/C_4 pathway begins with a reaction between vinyl radical ($C_2H_3\bullet$) and acetylene (C_2H_2) [76, 77]. Different reactions follow this initial reaction depending on the temperature condition, as shown in Fig. 3.2. At high temperature, the reaction between the vinyl radical and acetylene results in vinylacetylene (C_4H_4), which subsequently reacts with hydrogen ($H\bullet$) atom to form n-$C_4H_3\bullet$. The addition of acetylene to n-$C_4H_3\bullet$ produces phenyl radical. On the other hand, at low temperature, the reaction between vinyl radical and acetylene produces n-$C_4H_5\bullet$, which, upon addition of acetylene, forms benzene. However, the C_2/C_4 pathway was dismissed by Melius et al. [78], who

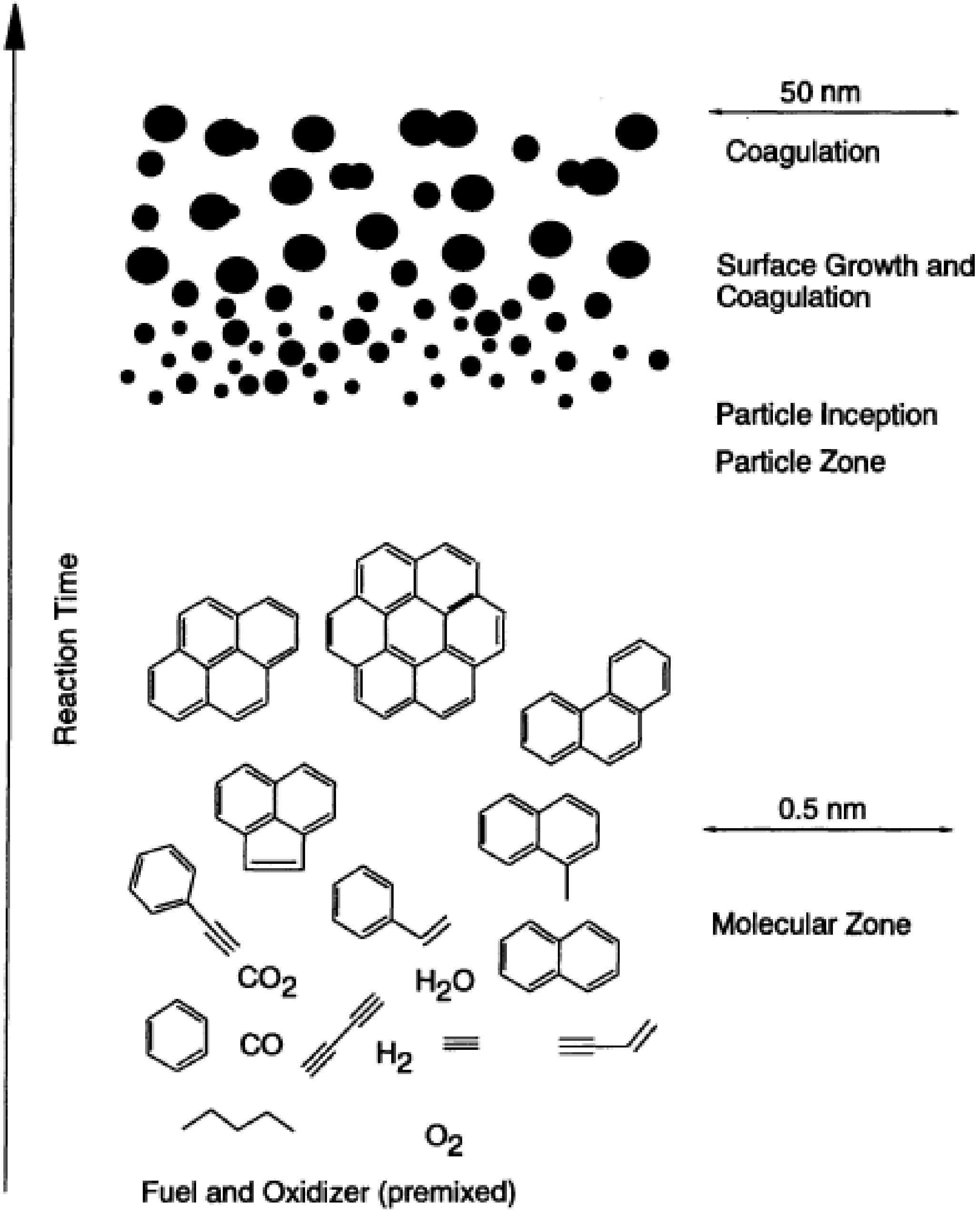

Figure 3.1: A simple description of soot formation mechansim in a pre-mixed flame [19].

argued that the n-C_4H_3• and n-C_4H_5• radicals vanish quickly via two isomerization reactions:

$$H + nC_4H_3 \leftrightarrow H + iC_4H_3 \tag{3.1}$$

and

$$H + nC_4H_5 \leftrightarrow H + iC_4H_5, \tag{3.2}$$

preventing the subsequent addition reaction with acetylene to form benzene or phenyl radical. Alternatively, Melius et al. [78] and others [79–82] proposed the C_3 pathway to represent the formation of the first aromatic ring. In the C_3 pathway, the propargyl (C_3H_3•) radical play a major role to the formation of benzene. The reaction pathways from propagyl radical to benzene can be summarized with two overall reactions:

$$C_3H_3 + C_3H_3 \rightarrow C_6H_6(linear) \xrightarrow{\text{cyclization}} benzene \tag{3.3}$$

and

$$C_3H_3 + aC_3H_4 \rightarrow benzene + H \tag{3.4}$$

In spite of the disagreement between the proponents of the two pathways, reported evidence suggest that the relevance of either or both pathways depend on the chemical composition of the original fuel and on the combustion conditions [30, 83].

Once the first aromatic rings form, they grow into polycyclic aromatic hydrocarbons (PAHs) through a well-known Hydrogen-Abstraction-Carbon-Addition (HACA) reaction sequence [76]. Since acetylene is usually the most abundant intermediate product, the carbon addition step is accomplished through acetylene. Although other species such as vinyl (C_2H_5•) and propargyl (C_3H_3•) radicals have been proposed as additional carbon suppliers [81, 84], their participation is negligible in comparison to acetylene. Fig. 3.3 shows a simplified depiction of the HACA reaction sequence. In the first step, the aromatic rings become radicals through the H-abstraction reaction

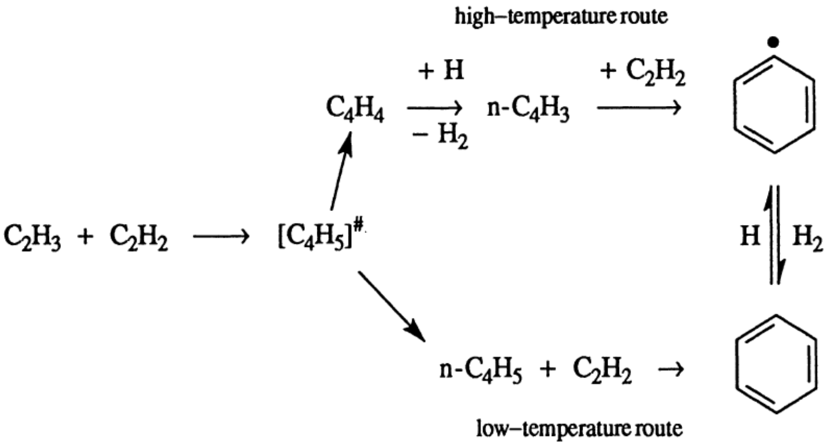

Figure 3.2: The C_2/C_4 reaction pathways leading to the formation of the first aromatic rings [76].

with H atoms. Then, the acetylene addition to the aromatic radicals helps the growth and eventual cyclization of PAHs. Other studies have also obtained evidence of the HACA reaction sequence, suggesting that the build-up of PAHs through HACA reaction sequence is valid over a wide range of combustion conditions [85–87]. However, the authors noted that the initiation of this sequence may be different for different fuels. For example, when benzene is used as the fuel, a combination of the intact aromatic rings becomes important during the initial stage of PAH growth [84].

Given the complex underlying mechanism of the formation and growth of PAHs in the gas phase, numerous research effort has been dedicated to constructing detailed chemical kinetic models that can accurately represent this mechanism. The result of the diligent work by the combustion community is a large number of detailed models [25–30,88,89]. These models consists of hundreds of species and thousands of reactions in order to account for all the possible reaction pathways from fuel decomposition to the formation of PAHs. However, there exists two main challenges that limit the implementation of these models in 3D CFD simulations of the actual combustion process. Firstly, detailed models developed by different research groups usually show inconsistent predictions of the chemical processes. The second challenge comes from

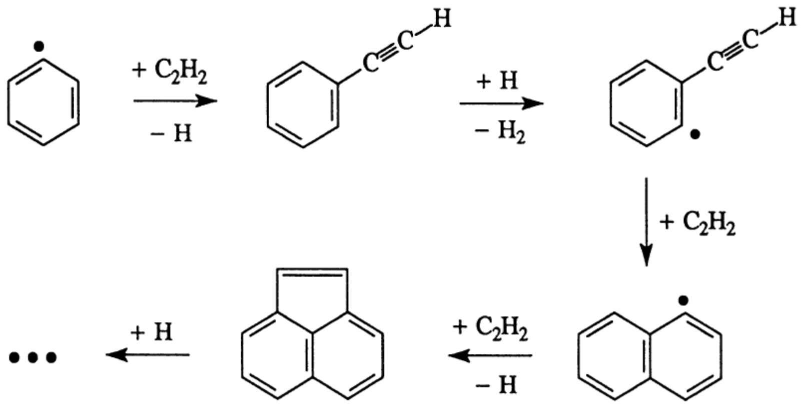

Figure 3.3: The Hydrogen-Abstraction-Carbon-Addition (HACA) reaction sequence of PAH growth [76].

the complexity and large scale of the detailed models. Despite rapid advancement in computing power, implementing detailed models with hundreds of species and thousands of reactions in CFD simulations of chemically reacting flows is prohibitively expensive. The computation cost has been shown to scale by the second power of the number of species, and, as a result, a 2D or 3D simulation of unsteady flow with large number of grid points or large number of time steps can easily overwhelm the capacity of any current supercomputer [90]. In addition, the wide range of time scales and non-linear coupling between species and reactions introduce stiffness when solving the balance equations [91]. Therefore, it is very important to simplify the detailed chemical models to appropriate size that can be practically implemented in CFD simulations. Different model reduction techniques have been proposed such as principal component analysis with sensitivities (PCAS) [92], direct relation graph error propagation (DRGEP) [93] and chemical lumping of species [94]. They have been successfully employed to obtain reduced models for a wide range of hydrocarbon fuels, for example, see [95–100]. Before these reduced models can be used in CFD simulations of practical combustion process, they need to be thoroughly examined by comparison with experimental data from fundamental combustion chemistry studies.

One of the objectives of this thesis work is an attempt to resolve the aforementioned challenges that are facing the modeling of PAH formation and growth in the gas phase. Specifically, this chapter will present experimental measurements of multiple species time histories during the pyrolysis of 1) ethylene (C_2H_4) and 2) n-dodecane (n-$C_{12}H_{26}$) at different experimental conditions. The measured data was used as an independent referee to validate different detailed and reduced chemical kinetic models. Two different fuels were selected in this investigation in order to accomplish three tasks. Firstly, the different in chemical composition of the two fuels would highlight the effect of fuel chemical composition on the PAH formation and growth process. Secondly, the data generated from ethylene pyrolysis could be used to test the core H_2/C_1-C_4 sub-models incorporated in the considered detailed and reduced models. In fact, reactions of H_2/C_1-C_4 species actually determine the combustion characteristics such as ignition delay and flame speed of practical fuels [88, 101, 102]. Finally, the n-dodecane pyrolysis data could be used to help the development and validation of future chemical kinetic models of fuel surrogates of jet fuels because n-dodecane not only contains a similar number of carbon but also represents the paraffin content in jet fuels [103–108].

3.2 Experimental and modeling procedure

Experimental investigation of the gas phase chemistry during fuel pyrolysis was conducted with the microflow tube reactor (MFTR) at the UVa. The detailed description of the MFTR was given in Chapter 2 and [61, 67, 68]. Two fuels: ethylene (C_2H_4) and n-dodecane ($C_{12}H_{26}$), were selected for this work. The effects of temperature and residence time on the evolution of the parent fuels and pyrolysis products were the focus of the investigation. All the experimental conditions are listed in Chapter 2.3.1.

One of the objectives of this thesis work is to use the experimental data to validate detailed and reduced chemical models of the PAH formation mechanism. The objective was accomplished by comparing the measured data to predictions by the models. Zero-dimensional (0D) simulations with the models were implemented at the experimental conditions in Cantera software [109], and the simulation results were used as model predictions. A total of six models was selected: Narayanaswamy et al. [95], Wang et al. [96], JetSurF 2.0 [25], Banerjee et al. [27], CRECK [28], and CNRS [89].

Narayanaswamy et al.: This model was developed by Narayanaswamy et al. [95] to describe low- and high-temperature combustion chemistry of a wide range of hydrocarbon fuels. The authors used a base model [30, 110] that was previously developed for aromatic species, and then added a skeletal version of a detailed model developed by Sarathy et al. [111] to account for n-dodecane chemistry. In addition, the authors also updated the reaction rates of a number of reactions based on newly available data. The model contains 180 species and 1204 reactions.

Wang et al.: this is a reduced model that was developed by Wang et al. [96]. The model is a combination of two reduced models. First of all, Wang et al. further reduced a reduced n-dodecane model that was developed by Ra and Reitz [99] for internal combustion engine simulations. Then, Wang et al. added a reduced PAH sub-model that was based on Slavinskaya et al. [112] detailed PAH model. The final model contains 100 species and 553 reactions.

JetSurF 2.0: this model is a latest version of the Jet Surrogate Fuel (JetSurF) model that describes the high temperature combustion of n-alkanes up to n-dodecane ($C_{12}H_{26}$) [25]. The base model of the JetSurF 2.0 model is the USC Mech 2 to which reactions describing high temperature combustion of n-alkanes, cyclohexane and mono-alkylated cyclohexane were appended. The model can be used to model low temperature combustion, but this function is still weak and needs further improvement. The model contains 348 species and 2163 reactions.

Banerjee et al.: this model is an optimized version of JetSurF 1.0 model. The model was developed by Banerjee et al. [27] using the Method of Uncertainty Minimization by Polynomial Chaos Expansion against a target set of n-dodecane combustion data. The model consists of 196 species and 1478 reactions.

CRECK: this model was developed by a group of researchers at the Chemical Reaction Engineering and Chemical Kinetics (CRECK) in Milan, Italy for the pyrolysis and oxidation of n-dodecane ($C_{12}H_{26}$) at high temperature condition [88]. The model construction employed a lumping or semi-detailed approach to simplify the descriptions of intermediate species and the reactions of these species. The model consists of 368 species and 14462 reactions.

CNRS: this model was developed by Mze-Ahmed et al. [89] at the French National Center for Scientific Research (CNRS) for the combustion of n-undecane ($C_{11}H_{24}$) and n-dodecane ($C_{12}H_{26}$) at both low- and high-temperature conditions. The model consists of 1377 species and 6014 reactions.

3.3 Results

In this section, measured speciation data are presented along with predictions by the models. The experimental data will highlight the effects of residence time and temperature on the pyrolysis of 1) ethylene (C_2H_4) and 2) n-dodecane ($C_{12}H_{26}$). Comparison between experimental data and model predictions helps evaluate the performance of the models. A model that most reasonably captures the experimental data trend can yield insight into the underlying chemistry that leads to the formation of stable products captured by the experimental data.

3.3.1 Ethylene pyrolysis

Over the considered experimental conditions, a number of fourteen species was quantified with the gas chromatography (GC) systems. These species are divided into

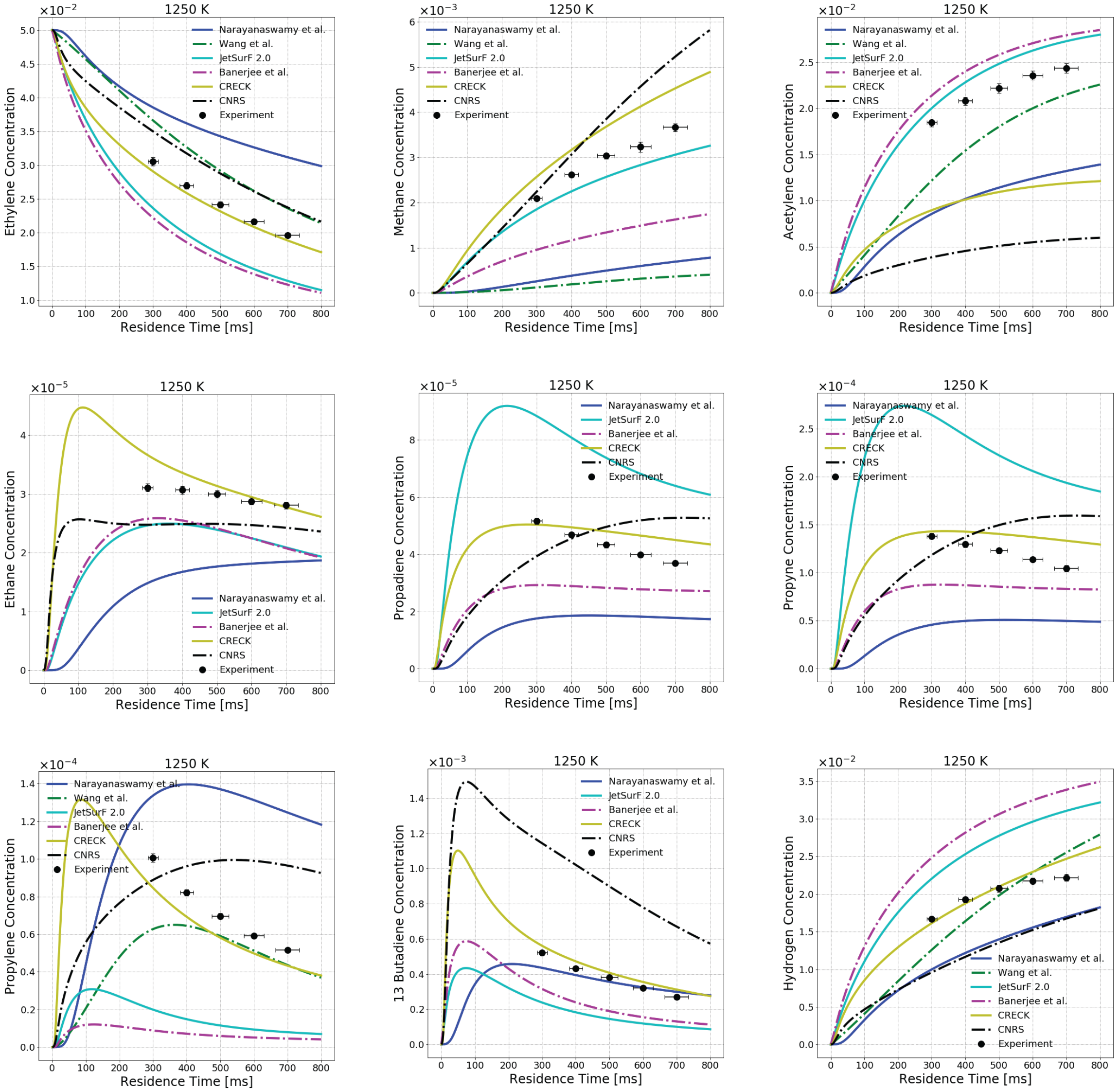

Figure 3.4: Measured and predicted mole fractions of C_1-C_4 hydrocarbon species and H_2 during ethylene pyrolysis as a function of residence time at T = 1250 K and p = 1atm. The ethylene (C_2H_4) mole fraction is shown in the first plot. Tested models: Narayanaswamy et al. [95], Wang et al. [96], JetSurF 2.0 [25], Banerjee et al. [27], CRECK [88], and CNRS [89].

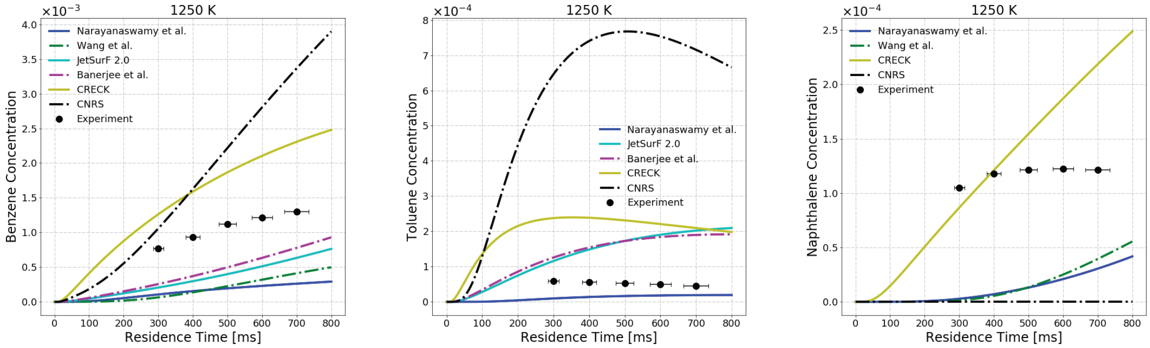

Figure 3.5: Measured and predicted mole fractions of benzene (C_6H_6), toluene (C_7H_8), and naphthalene ($C_{10}H_8$), during ethylene pyrolysis as a function of residence time at T = 1250 K and p = 1 atm. Tested models: Narayanaswamy et al. [95], Wang et al. [96], JetSurF 2.0 [25], Banerjee et al. [27], CRECK [88], and CNRS [89].

two groups. Group 1 contains C_1 to C_4 hydrocarbon species and molecular hydrogen (H_2), while group 2 includes hydrocarbon species with more than 4 carbon atoms. The effect of residence times on the evolution of these species at a fixed temperature of 1250 K is highlighted in Figs. 3.4 and 3.5, whereas Figs. 3.6 and 3.7 show the effect of temperature at a fixed residence time of 500 ms. The uncertainties of species measurement ($\leq$ 2.5 %) and residence time (5%) are also included with the data (a detailed account for experiment uncertainty can be found in Appendix B).

The first plots of Figs. 3.4 and 3.6 show the decomposition of the ethylene (C_2H_4) fuel with varying residence time and temperature, respectively. Both experimental data and predictions by the models agree that ethylene concentration decreased with increasing residence time and temperature. For the evolution of the stable pyrolysis products, predictions by the detailed models: JetSurF 2.0 [25], Banerjee et al. [27], CRECK [88], and CNRS [89] overall perform better than those by the reduced models: Narayanaswamy et al. [95] and Wang et al. [96]. Furthermore, the models show significant variation in their predictions. The experimental data lie within the variation of the model predictions, except for ethane (C_2H_6) and propylene (C_3H_6) evolution with changing temperature (see Fig. 3.6). If the variation of the model predictions is assumed to represent the uncertainty of the kinetic parameters used in the

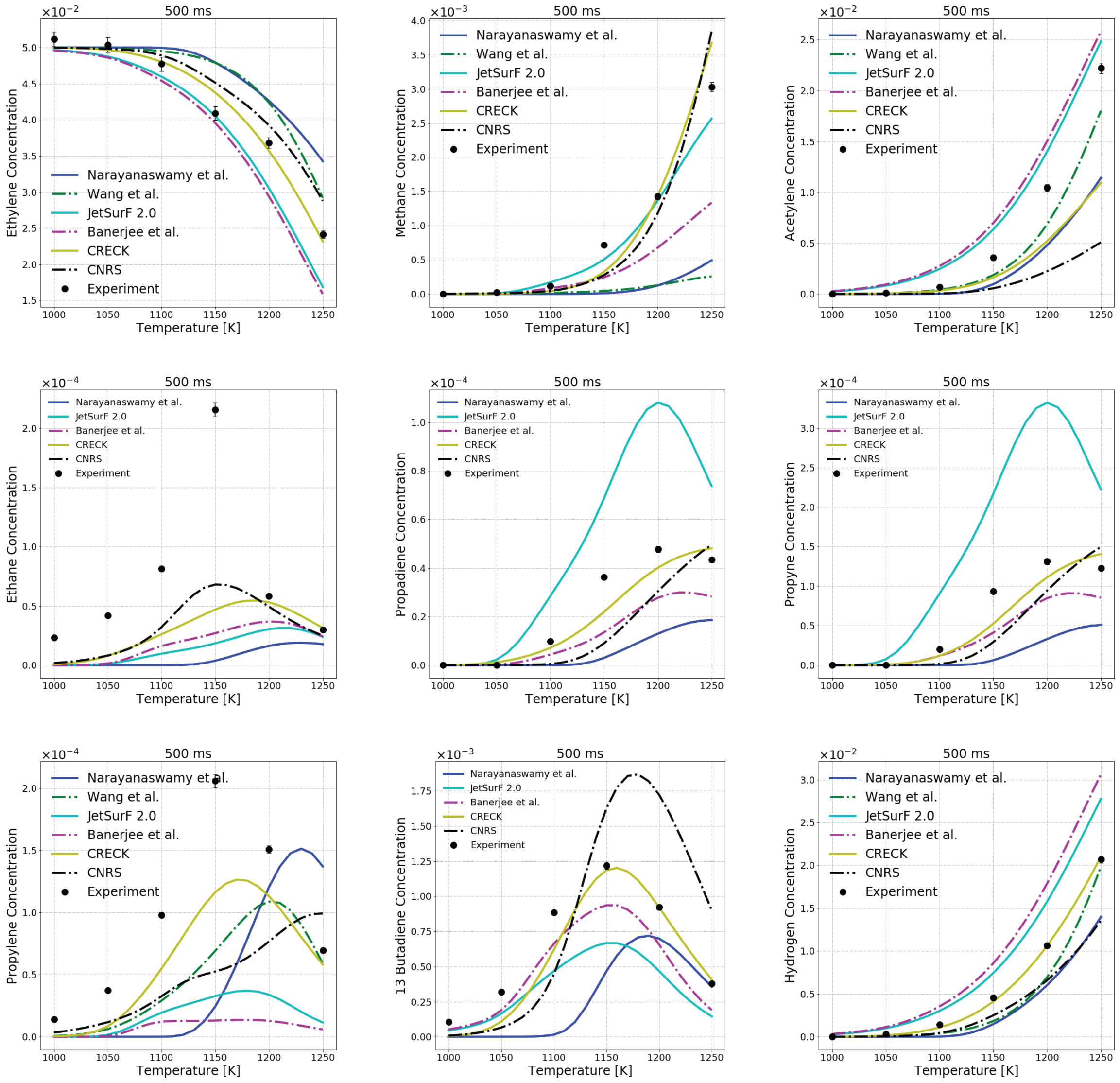

Figure 3.6: Measured and predicted mole fractions of C_1-C_4 hydrocarbon species and H_2 during ethylene pyrolysis as a function of temperature at t = 500 ms and p = 1 atm. The ethylene (C_2H_4) fuel mole fraction is shown in the first plot. Tested models: Narayanaswamy et al. [95], Wang et al. [96], JetSurF 2.0 [25], Banerjee et al. [27], CRECK [88], and CNRS [89].

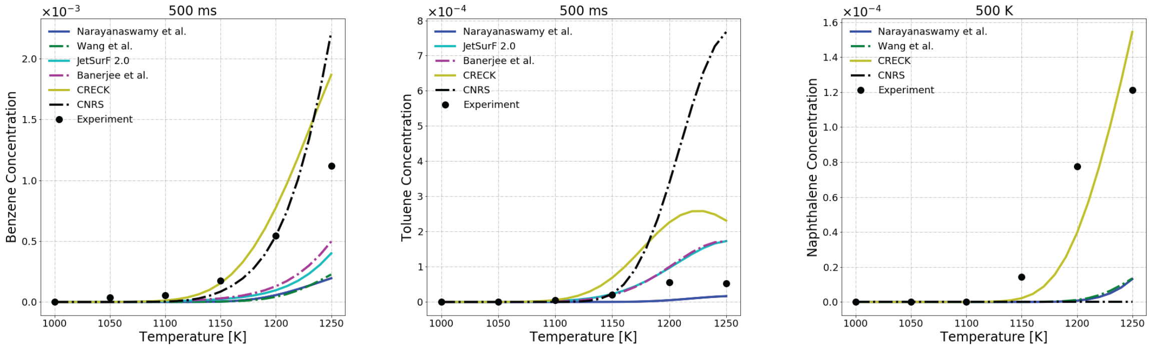

Figure 3.7: Measured and predicted mole fractions of benzene (C_6H_6), toluene (C_7H_8), and naphthalene ($C_{10}H_8$), during ethylene pyrolysis as a function of temperature at $t = 500$ ms and $p = 1$ atm. Tested models: Narayanaswamy et al. [95], Wang et al. [96], JetSurF 2.0 [25], Banerjee et al. [27], CRECK [88], and CNRS [89].

models, then the fact that the measured data lies within the the model uncertainty area indicates that the experimental data can be used to minimize the uncertainty of the model kinetic parameters.

In addition, only three products containing more than four carbon atoms were detected from the pyrolysis of ethylene. They are benzene (C_6H_6), toluene (C_7H_8), and napthalene ($C_{10}H_8$). These species are aromatic hydrocarbons, ranging from one to two aromatic rings. The evolution of these species with varying residence time and temperature can be used to describe the initial steps of PAH formation and growth process. It should be noted that not all six models contain the combustion chemistry of the three aromatic species. While all the models show predictions of benzene mole fraction, only five and four models contain the combustion chemistry of toluene and naphthalene, respectively. This fact will be considered when selecting the most representative model to help interpret the experimental data.

The carbon (C) balance and hydrogen-to-carbon ratio at all the experiment conditions were calculated and summarized in Fig. 3.8 as a function of residence time and temperature. The values of these two quantities are used to determine whether or not all the products from ethylene pyrolysis were accounted for. As shown in Fig. 3.8, the C balance values range from 95 to 105%, and the H-to-C ratio remains constant

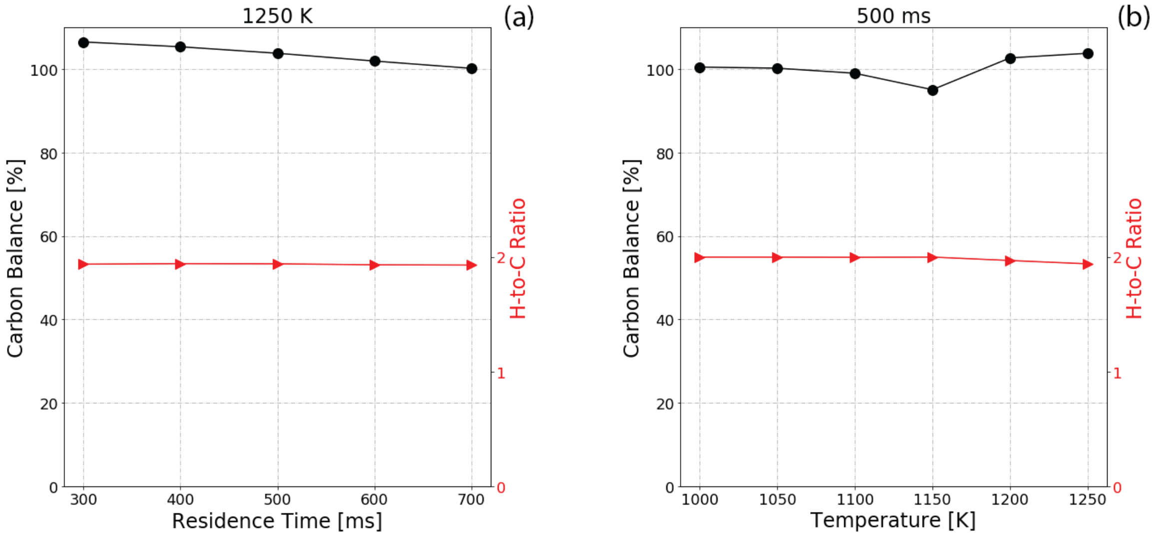

Figure 3.8: Measured carbon (C) balance (●) and recovered hydrogen-to-carbon (H-to-C) ratio (▶) from the pyrolysis of ethylene as a function of (a) residence time and (b) temperature.

at 1.95 over the considered experimental conditions. The measured H-to-C values are very close to the ethylene H-to-C ratio of 2. As a result, the species that were quantified in this study represent almost all the products from ethylene pyrolysis. It should also be noted that more than 100% of C balance values were obtained because of the experimental uncertainty.

3.3.2 n-Dodecane pyrolysis

Comparison to model predictions

In comparison to ethylene pyrolysis experiments, a higher number of species was detected during the pyrolyis of n-dodecane ($C_{12}H_{26}$). The number of species was sixteen, ranging from C_1 to C_{12} hydrocarbon species as well as H_2. The new species that were not detected during ethylene pyrolysis were 1-pentene (C_5H_{10}), 1-hexene (C_6H_{12}), and 1-heptene (C_7H_{14}). These species are alkene molecules, which are unsaturated hydrocarbons that contain a carbon-carbon double bond (similar to ethylene). These species will be shown later to be the intermediate products from the pyrolysis of n-dodecane leading to ethylene, and thus they were not detected during the ethylene pyrolysis experiments. It should be pointed out that naphthalene (two-ring PAH molecule) was not detected among the aromatic products during the n-dodecane pyrolysis.

Figs. 3.9 and 3.10 show the effect of residence time at a fixed temperature of 1050 K, while Figs. 3.11 and 3.12 show the effect of temperature at a fixed residence time of 50 ms. Similar to the ethylene pyrolysis results, the decomposition of the n-dodecane ($C_{12}H_{26}$) fuel was presented in the first plots of Figs. 3.9 and 3.11. The decomposition rate of n-dodecane increased with increasing residence time and temperature. The model predictions capture the evolution of the parent fuel and the products with varying residence time and temperature reasonably well, except for those by the Wang et al. model [96]. Furthermore, there still exists a variation in the model predictions.

At 1050 K, detected species containing more than four carbon atoms were all n-alkene species (see Fig. 3.10). The detection of two aromatic species: benzene and toluene, began at 1100 and 1150 K, respectively. Both the data and model predictions show that benzene and toluene concentration increased with increasing temperature. In addition to the measured data and model predictions, the species measurement uncertainty is also presented for each experimental condition. The uncertainty of measurement ranges from 2 to 15%. The higher uncertainty in n-dodecane pyrolysis experiments mainly stemmed from higher experimental repeatability uncertainty that was caused by a notable fluctuation in n-dodecane volume flow rate from the atomizer.

The calculated values of carbon (C) balance and hydrogen-to-carbon (H-to-C) ratio as a function of residence time and temperature are shown in Fig. 3.13. The C balance values range from 82 to 95% with varying residence time at a fixed temperature of 1050 K, while they range from 83 to 115% with varying temperature at a fixed residence time of 50 ms. On the other hand, the H-to-C ratio remains constant

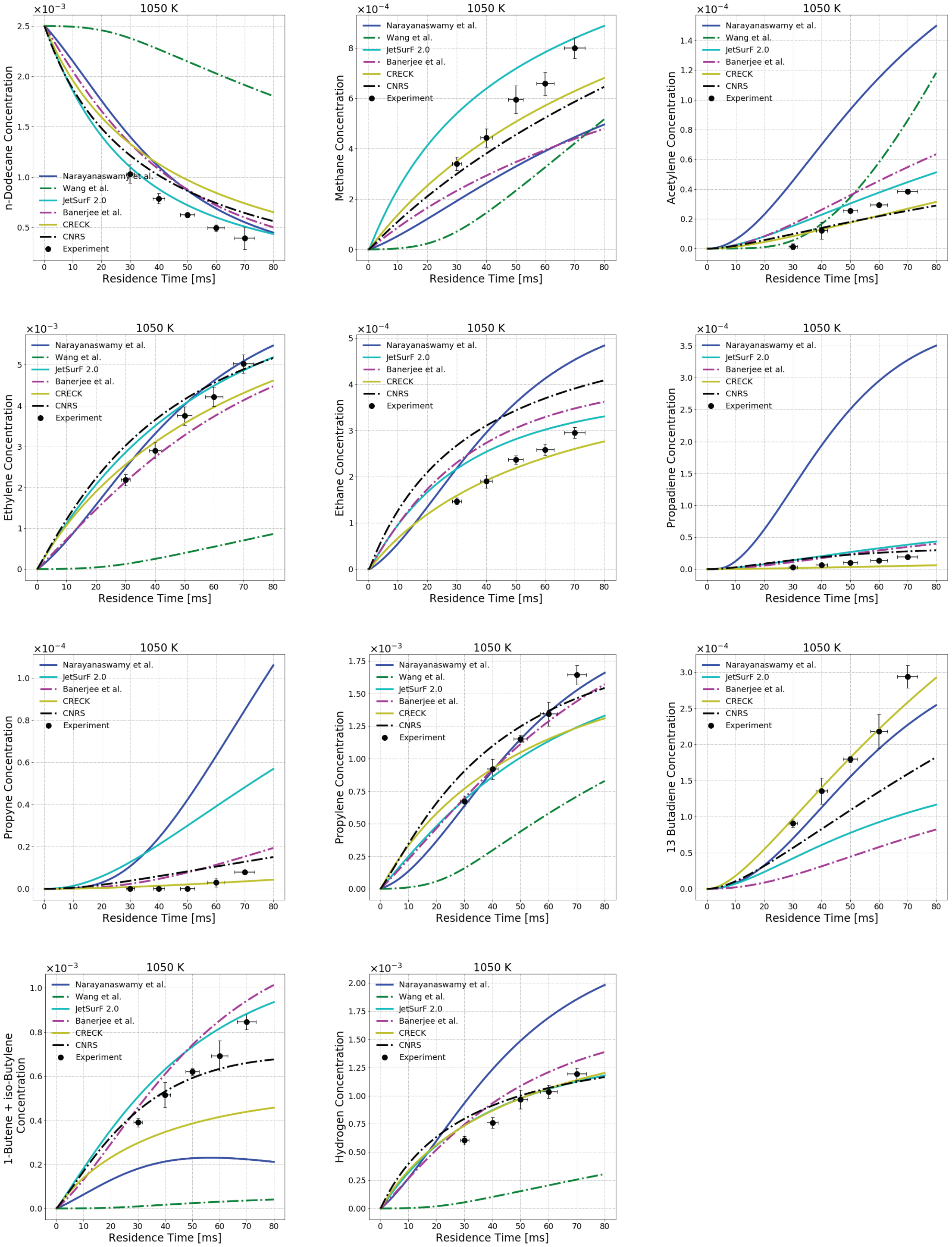

Figure 3.9: Measured and predicted mole fractions of C_1-C_4 hydrocarbon species and H_2 during n-dodecane pyrolysis as a function of residence time at T = 1050 K and p = 1 atm. The n-dodecane ($C_{12}H_{26}$) fuel mole fraction is shown in the first plot. Tested models: Narayanaswamy et al. [95], Wang et al. [96], JetSurF 2.0 [25], Banerjee et al. [27], CRECK [88], and CNRS [89].

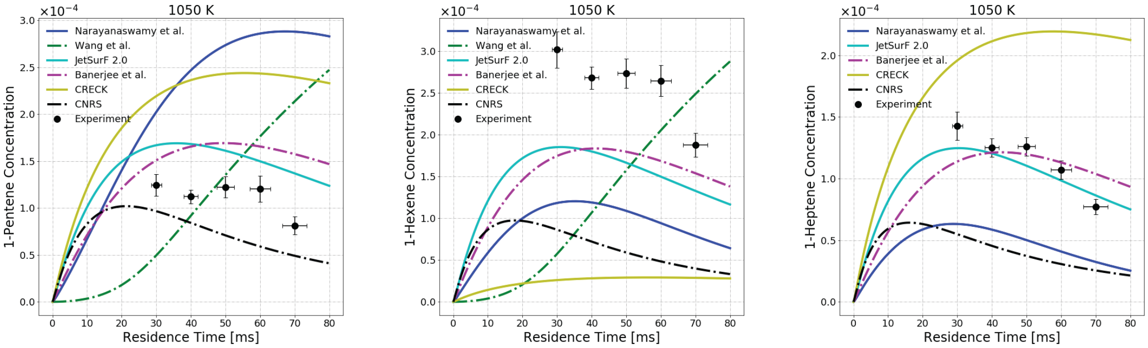

Figure 3.10: Measured and predicted mole fractions of 1-pentene (C_5H_{10}), 1-hexene (C_6H_{12}), and 1-heptene (C_7H_{14}), during n-dodecane pyrolysis as a function of residence time at T = 1050 K and p = 1 atm. Tested models: Narayanaswamy et al. [95], Wang et al. [96], JetSurF 2.0 [25], Banerjee et al. [27], CRECK [88], and CNRS [89].

at 2.15, which is very close to the n-dodecane H-to-C ratio of 2.17. Although the C balance values notably vary due to the experimental uncertainty, both C balance and H-to-C ratio values indicate that more than 80% of the products from n-dodecane pyrolysis were accounted for in this study.

Compare to available n-dodecane pyorlyis data

Before the performance of the models can be assessed with the experimental data, the data need to be compared to available data on n-dodecane pyrolysis to ensure its reliability. n-Dodecane pyrolysis and oxidation have been extensively studied because n-dodecane represents one important chemical component of jet fuels: normal paraffin or n-alkane [103–108,113,114]. As a result, data on its combustion chemistry can be readily found in the literature. Two studies that employed different reactor configurations from a flow reactor were selected. Malewicki and Brezinsky [113] performed experiments on n-dodecane pyrolysis with a high-pressure single pulse shock tube (HPST) at the Univeristy of Illinois in Chicago (UIC). The other n-dodecane pyrolysis study was conducted by Herbinet et al. [114] with a quartz jet stirred reactor (JSR) in Nancy, France. The experimental conditions of the two studies are

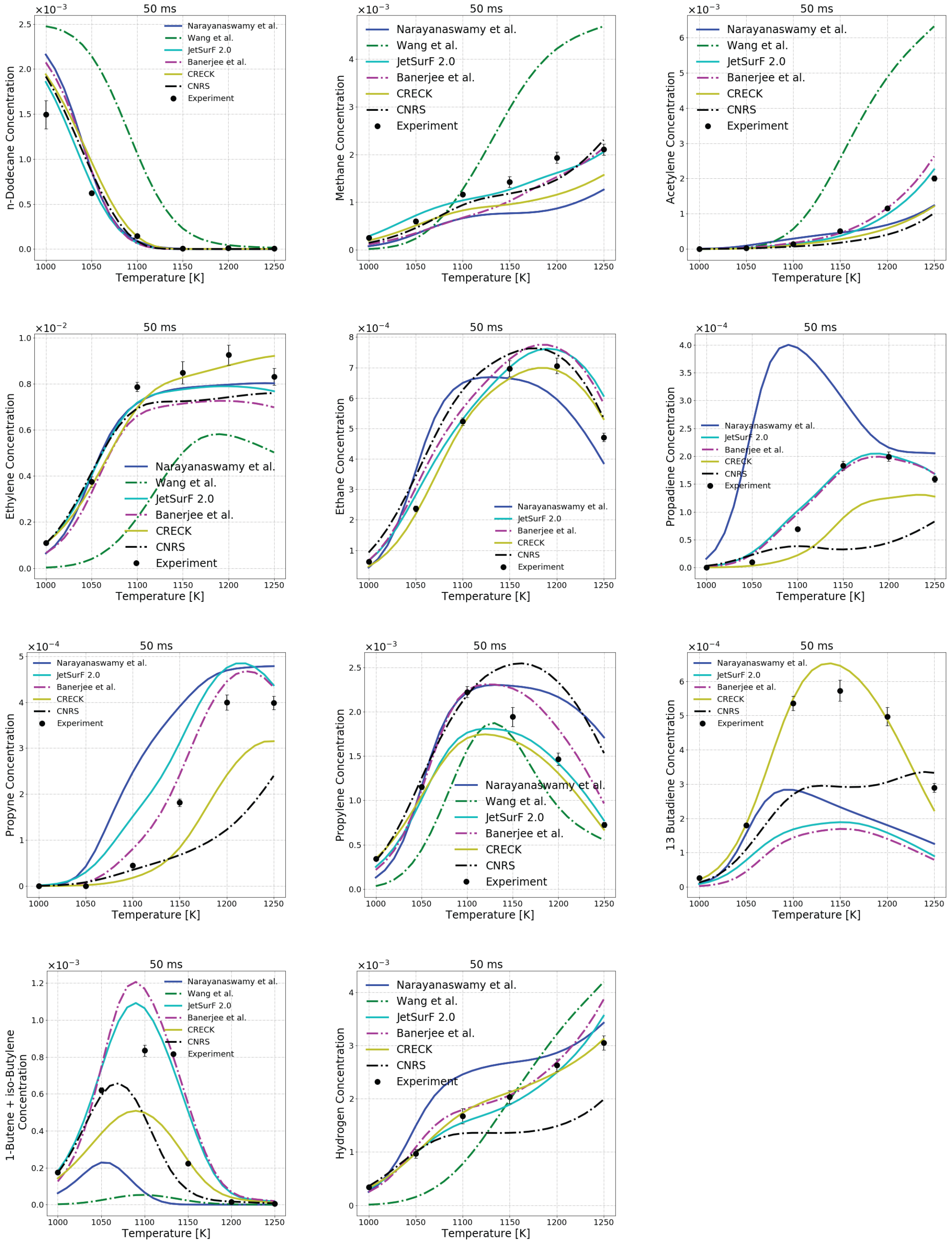

Figure 3.11: Measured and predicted mole fractions of C_1-C_4 hydrocarbon species and H_2 during n-dodecane pyrolysis as a function of temperature at t = 50 ms and p = 1 atm. The n-dodecane ($C_{12}H_{26}$) fuel mole fraction is shown in the first plot. Tested models: Narayanaswamy et al. [95], Wang et al. [96], JetSurF 2.0 [25], Banerjee et al. [27], CRECK [88], and CNRS [89].

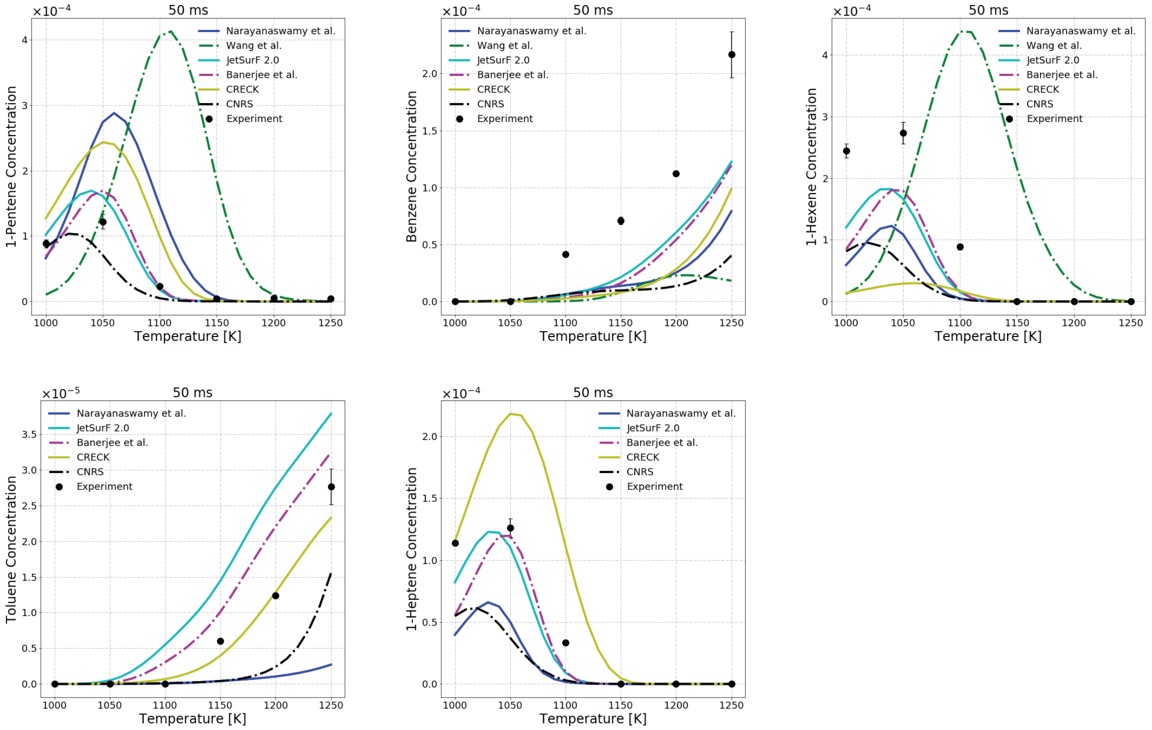

Figure 3.12: Measured and predicted mole fractions of 1-pentene (C_5H_{10}), benzene (C_6H_6, 1-hexene (C_6H_{12}, toluene (C_7H_8) and 1-heptene (C_7H_{14}), during n-dodecane pyrolysis as a function of temperature at t = 50 ms and p = 1 atm. Tested models: Narayanaswamy et al. [95], Wang et al. [96], JetSurF 2.0 [25], Banerjee et al. [27], CRECK [88], and CNRS [89].

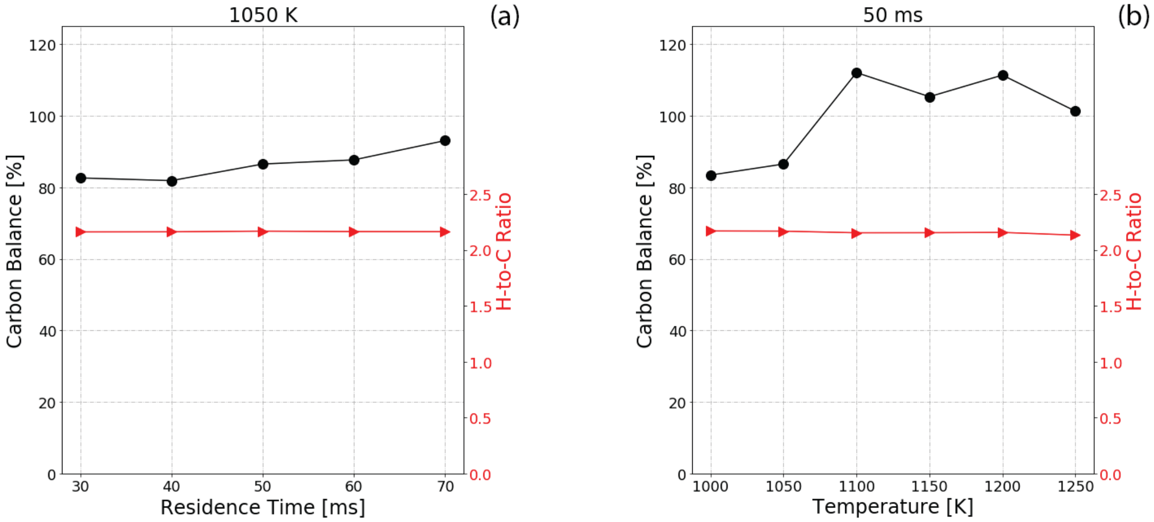

Figure 3.13: Measured carbon (C) balance (●) and recovered hydrogen-to-carbon (H-to-C) ratio (▶) from the pyrolysis of n-dodecane as a function of (a) residence time and (b) temperature.

Table 3.1: n-Dodecane pyrolysis conditions of this work (UVa MFTR), Malewicki and Brezinsky (shock tube) [113], and Herbinet et al. (JSR) [114]

Data set	$X_{fuel,0}$ [ppm]	p [atm]	T [K]	Time [ms]
UVa MFTR	2500	1	1000-1250	50
			1050	30-70
			1150	30-70
Shock tube [113]	73.6	19-26.6	867-1739	1.27-32.8
	79.2	41-55.2	926-1683	1.22-2.37
JSR [114]	20000	1	823-1073	1000
			873	970-5280
			973	980-4740

summarized in Table 3.1.

As shown in Table 3.1, n-dodecane pyrolysis was conducted at different conditions at the three facilities. Thus, comparison of the three data sets could only be done with iso-conversion plots where the mole fraction of species i was normalized by the initial n-dodecane mole fraction and plotted as a function of n-dodecane fuel conversion. Fig. 3.14 shows eight iso-conversion plots of ethane, acetylene, ethylene, ethane, propyne, propylene, benzene and hydrogen. Symbols are the experimental data: UVa MFTR (●), shock tube (►, ★) [113], and JSR (■) [114]. Colors were used to highlight data measured with varying residence times but at fixed temperature: 873 K, 973 K, 1050 K, and 1150 K. The temperatures 973 K and 1050 K were assigned the same color because the two temperature values are close to each other and the data taken at these two temperature with the UVa MFTR and JSR [114] are similar in values. The black color was reserved for data taken with varying temperature but at fixed residence time. These data filled the gaps between the color-coded data. The shock tube data are represented by two symbols: ► and ★ for two different average pressure conditions: 22.84 and 49.42 atm, respectively. In addition, predictions by the CRECK model [88] are included in Fig. 3.14. The predictions are plot as lines whose colors represent the same temperature conditions to the experimental data.

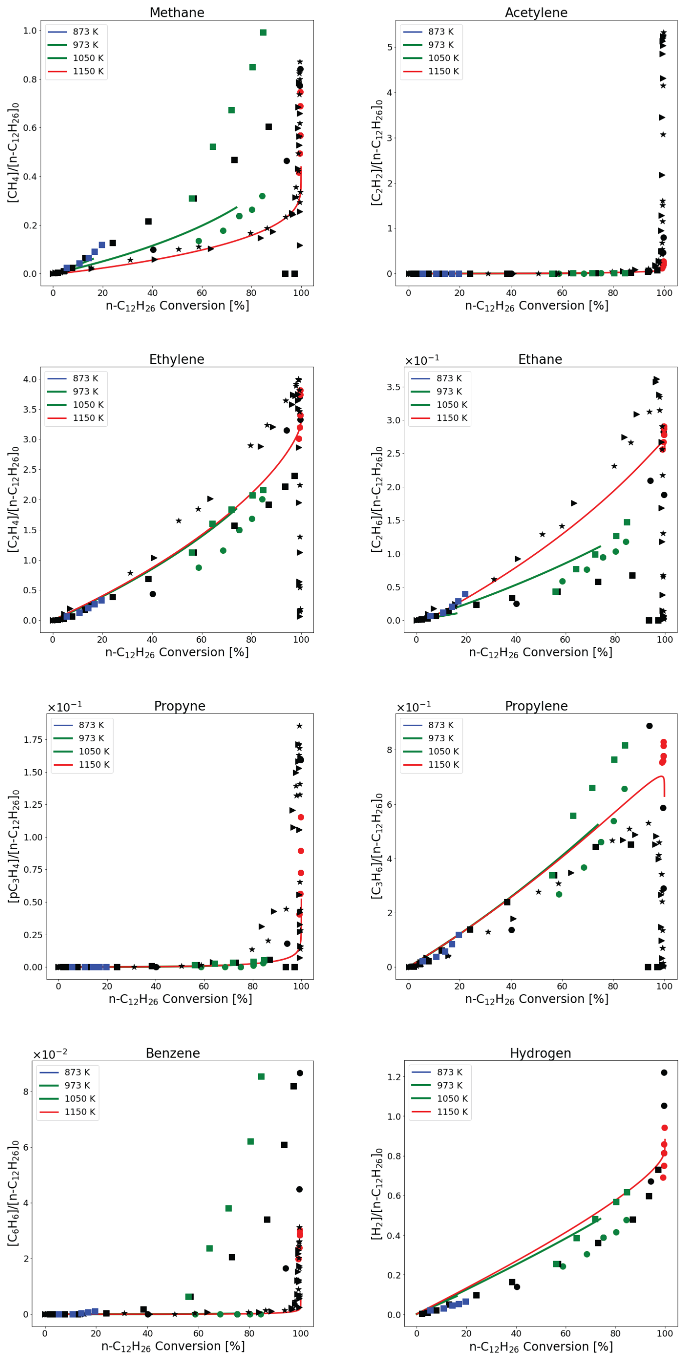

Methane

Acetylene

Ethylene

Ethane

Propyne

Propylene

Benzene

Hydrogen

Figure 3.14: Iso-conversion comparison of species mole fractions normalized by initial n-dodecane mole fractions. Symbols are experimental data: UVa MFTR (●), shock tube (▶, ★) [113], and JSR (■) [114]. Lines are predictions by the CRECK model [88]. The set temperature conditions at which the effect of residence time was investigated are represented by 3 colors: 873 K, 973 K, 1050 K, and 1150 K. Data taken with varying temperature and fixed residence time are presented in black. The shock tube data are presented with two symbols: ▶ and ★ , for two different average total pressure conditions: 22.84 and 49.42 atm, respectively.

The data for C_1-C_4 hydrocarbon species from three data sets reasonably agree with each other. It is interesting to note that the production of acetylene, ethylene, propyne, and propylene is not affected by temperature or pressure. On the other hand, production of n-alkane species such as methane and ethane is influenced by temperature. Specifically, with increasing temperature, methane production decreases while ethane production increases. In addition, although molecular hydrogen was not detected by Malewicki and Brezinsky [113] in their shock tube study, the UVa MFTR and JSR data reasonably agree with each other in regards to hydrogen production.

In contrast to the data of C_1-C_4 species, the JSR data shows a different benzene production trend from the UVa MFTR and shock tube data. Benzene production from the JSR data appears to be influenced by experiment conditions, whereas the UVa MFTR, shock tube data and predictions by the CRECK model shows an independence of benzene production from the experiment conditions. This disagreement between the data sets recommends further investigation of the effect of experiment facility on benzene production from n-dodecane pyrolysis. Nevertheless, there exists a general agreement between the UVa MFTR data and the data from shock tube [113] and JSR [114] facilities. The UVa MFTR data can therefore be used to validate the detailed chemical kinetic models.

3.4 Discussion

3.4.1 Variation in model predictions

The comparison between experimental data and model predictions in Section 3.3 showed a significant variation in the model predictions. The model predictions depend on the accuracy of parameters, such as the collision frequency (A) and activation energy (E_a), that are incorporated in the models ($k_{reaction} = Aexp(-E_a/RT)$). Therefore, an evaluation of the reaction rate coefficients used by the models can provide insight to the cause of the variation in model predictions. One of the important methods to understand how the reaction rate coefficients influence the performance of the models is sensitivity analysis. In sensitivity analysis, the contribution of a reaction k (or its reaction rate coefficient) to the evolution of a species i is quantified through a sensitivity coefficient $S_{i,k}$, which is defined as follows

$$S_{i,k} = \frac{p_k}{X_i}\frac{\partial X_i}{\partial p_k}$$

where p_k is a parameter on the rate coefficient of reaction k, and X_i denotes the mole fraction of species i. As an example, Fig. 3.15 shows the result of a sensitivity analysis of collision frequency (A) for the species ethylene ($\mathrm{C_2H_4}$) obtained with the Banerjee et al. model [27]. Fig. 3.15 contains the sensitivity coefficients of ten most sensitive reactions to the evolution of ethylene at 1200 K and 500 ms. The reactions with negative sensitivity coefficients facilitate the decomposition of ethylene, while the reactions with positive sensitivity coefficients retard ethylene decomposition.

Sensitivity analysis of the two fuels: ethylene and n-dodecane, was conducted with the six models in order to find the most sensitive reactions to the evolution of these species. Subsequently, the reaction rate coefficients of the selected reactions were calculated over a temperature range between 1000 and 1250 K. Starting with the ethylene fuel, the six models all agree that ethylene decomposes mainly via two reaction pathways, which are highlighted in Fig. 3.15. The first reaction pathway is where ethylene breaks down into acetylene and molecular hydrogen

$$C_2H_4(+M) \leftrightarrow C_2H_2 + H_2(+M)$$

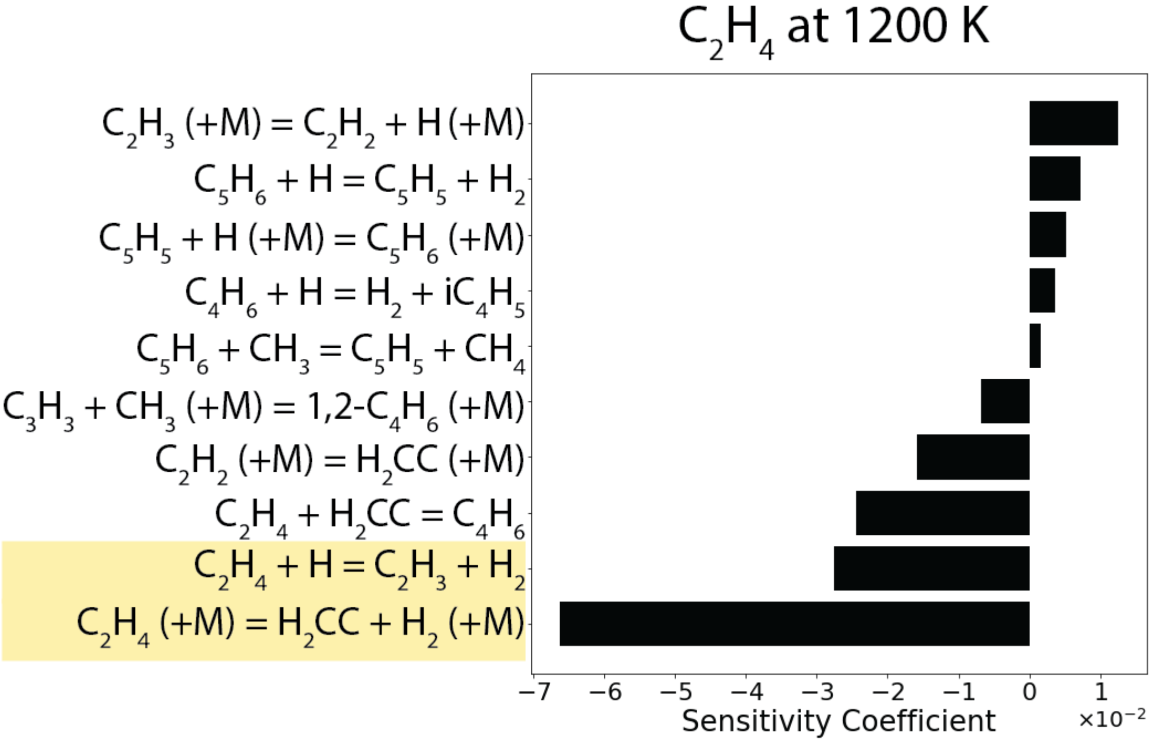

Figure 3.15: Sensitivity coefficients of the most sensitive reactions to the evolution of ethylene (C_2H_4). The sensitivity analysis was conducted with the Banerjee et al. model [27] at 1200 K and 500 ms.

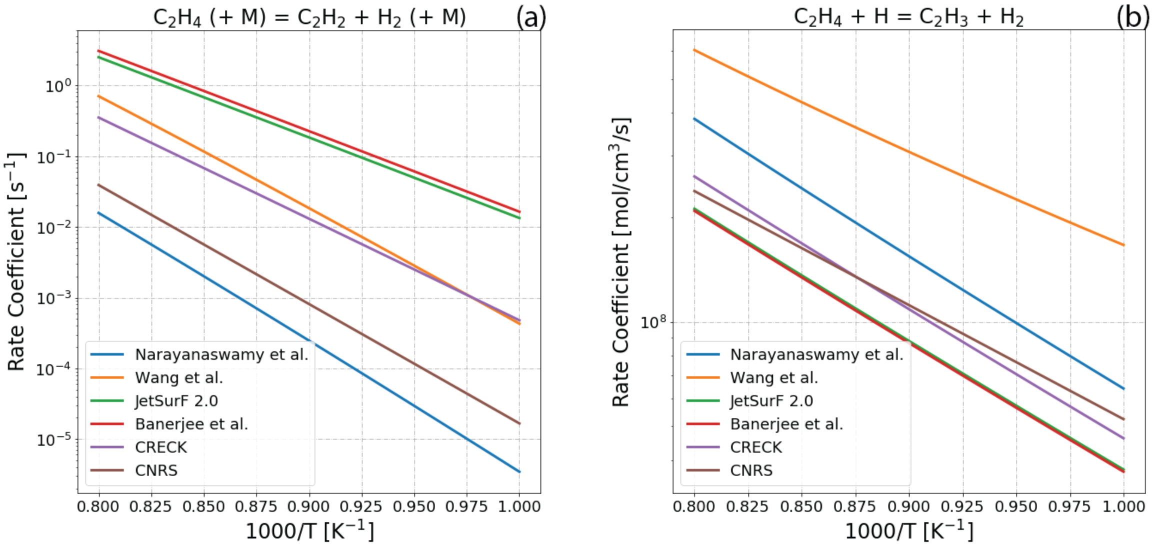

Figure 3.16: Reaction rate coefficients of (a) ethylene decomposition reaction and (b) H-abstraction reaction by H, plotted against inverse temperature

The second pathway is the H-abstraction of ethylene by an H atom

$$C_2H_4 + H \leftrightarrow C_2H_3 + H_2$$

The reaction rate coefficients of these two reaction pathways as a function of temperature are presented in Fig. 3.16(a) and (b), respectively. According to Fig. 3.16, there exists a significant variation in the reaction rate coefficients used by the models to predict ethylene decomposition. As a result, varying predictions of ethylene mole fraction by the models shown in Figs. 3.4 and 3.6 can be attributed to the difference in model reaction rate coefficients.

Similar to ethylene, n-dodecane decomposition also undergoes two main reaction pathways: 1) C-C fission and 2) H-abstraction by either H or CH_3 radical. Thus, the calculation of reaction rate coefficients were conducted with the models. Fig. 3.17(a) and (b) shows the reaction rate coefficients of the H-abstraction reactions of n-dodecane by H and CH_3 radicals, respectively. Again, a significant variation is observed in the reaction rate coefficients used by the models. In addition, the models

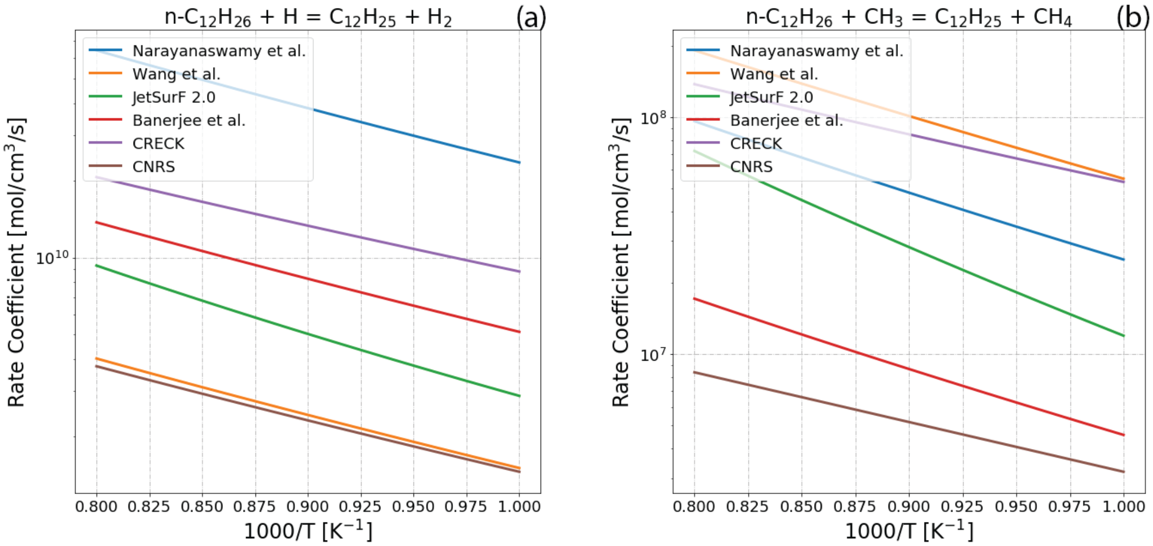

Figure 3.17: Reaction rate coefficients of H-abstraction reactions of n-dodecane by (a) H and (b) CH_3 radicals, plotted against inverse temperature

express the C-C fission reaction pathways of n-dodecane decomposition differently from each other. The five models: Narayanaswamy et al. [95], Wang et al. [96], JetSurF 2.0 [25], Banerjee et al. [27], and CNRS [89], describe the C-C fission reaction of n-dodecane in a number of parallel reactions, for example

$$nC_{12}H_{26} \leftrightarrow C_9H_{19} + C_3H_7$$

$$nC_{12}H_{26} \leftrightarrow C_6H_{13} + C_6H_{13}$$

On the other hand, the CRECK model [88] employs a lumping approach where isomers of n-dodecane decomposition products are lumped together, which leads to reactions with non-integer stoichiometric coefficients as shown below

$$nC_{12}H_{26} \rightarrow 0.5C_2H_5 + 0.5nC_3H_7 + 0.5nC_7H_{15} + 0.5nC_{12}H_{25}$$

$$nC_{12}H_{26} \rightarrow 0.5pC_4H_9 + 0.5nC_5H_{11} + 0.9nC_7H_{15} + 0.1nC_{12}H_{25}$$

The reaction rate coefficients of these two reactions are different from the net reaction rate coefficients of all the C-C fission reactions used by Narayanaswamy et al. [95], Wang et al. [96], JetSurF 2.0 [25], Banerjee et al. [27], and CNRS [89] models. Variation in the reaction rate coefficients was similarly found for all the important reactions to the experimentally detected species. In summary, two main conclusions can be drawn from the analysis of reaction rate coefficients used in the models. First of all, the inconsistency in model predictions is the result of the uncertainty in the reaction rate coefficients employed by the models. Secondly, the core H_2/C_1-C_4 sub-models incorporated in the models need further improvement to better represent the combustion chemistry of practical fuels.

3.4.2 Effects of temperature, residence time and fuel chemical composition

After comparing the experimental data to predictions by the models, the CRECK model [88] was selected to help interpret the experimental data. The CRECK model was selected because of two reasons. Firstly, it contains the combustion chemistry n-alkanes up to n-dodecane ($C_{12}H_{26}$) and all the aromatic species: benzene (C_6H_6), toluene (C_7H_8), and naphthalene ($C_{10}H_8$), that were detected experimentally. Secondly, predictions by the CRECK model agree with the data more reasonably than the predictions by the other models. The effects of temperature, residence time and fuel chemical composition on the formation and growth of PAHs can then be investigated with reaction pathway analysis with the CRECK model.

Starting with ethylene (C_2H_4) as the fuel, Fig. 3.18 shows the reaction pathways from ethylene decomposition to the formation of benzene, toluene, and naphthalene at 1250 K and 500 ms. Ethylene pyrolysis began at 1050 K via three main reaction pathways. The most dominant reaction way was the H-abstraction reaction by hydrogen (H) atoms,

$$C_2H_4 + H \leftrightarrow C_2H_3 + H_2,$$

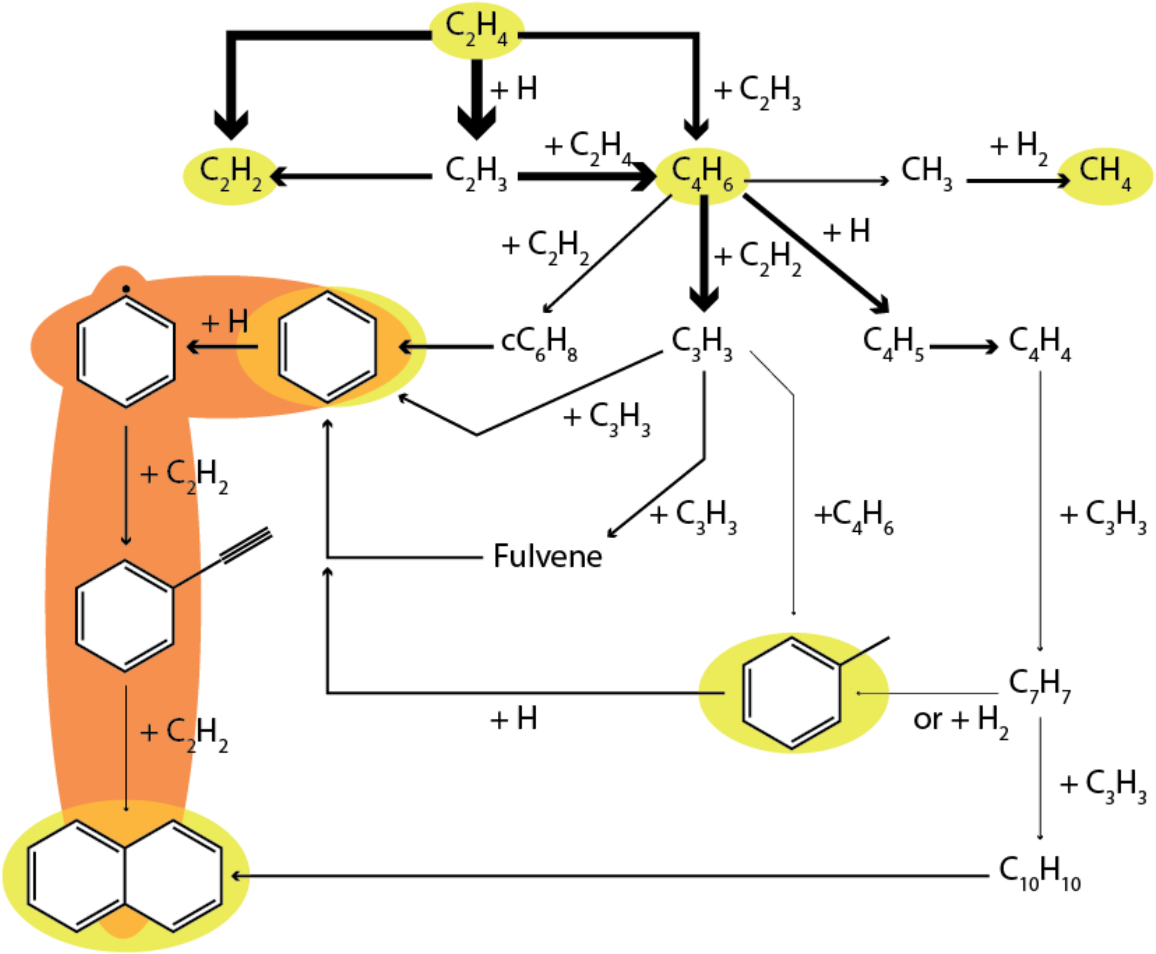

Figure 3.18: Reaction pathways from ethylene pyrolysis to the formation of aromatic species, obtained with the CRECK model [88] at 1250 K and 500 ms. The experimentally detected species are highlighted in yellow, while the Hydrogen-Abstraction-Carbon-Addition (HACA) reaction sequence is highlighted in orange. The thickness of an arrow represents the relative flux (importance) of a reaction pathway.

which was followed by the thermal decomposition reaction to form acetylene (C_2H_2),

$$C_2H_4 \leftrightarrow C_2H_2 + H_2$$

The third main reaction pathway was a reaction between ethylene and ethylenyl ($C_2H_3\bullet$) radicals to form 1,3 butadiene (C_4H_6) and H atoms,

$$C_2H_4 + C_2H_3 \leftrightarrow C_4H_6 + H$$

From 1,3 butadiene, methane (CH_4) was formed by a sequence of two reactions:

$$C_4H_6 \rightarrow CH_3 + C_3H_3$$

and

$$CH_3 + H_2 \leftrightarrow CH_4 + H$$

In addition to helping methane form, 1,3 butadiene was responsible for the formation of benzene, toluene and naphthalene. As temperature increased, a series of reactions between 1,3 butadiene and acetylene became possible. Firstly, 1,3 butadiene reacted with acetylene to produce 1,4 cyclohexadiene (cC_6H_8), which subsequently underwent an isomerization reaction to form benzene. This reaction sequence is the C_2/C_4 reaction pathway that was described by [76, 77]. The second reaction between 1,3 butadiene and acetylene produced propargyl ($C_3H_3\bullet$) radicals. The propargyl radicals then reacted with themselves to produce benzene via two different pathways, which are the C_3 reaction pathway described by [78–82]:

$$C_3H_3 + C_3H_3 \leftrightarrow C_6H_6$$

and

$$C_3H_3 + C_3H_3 \leftrightarrow fulvene \rightarrow C_6H_6$$

Thus, both the C_3 and C_4 reaction pathways contributed to benzene formation when ethylene was used as the fuel. In addition, toluene and naphthalene began to appear around 1150 K. The formation of toluene can be traced back to the reaction between cyclobutadiene (C_4H_4) and the propargyl radicals,

$$C_4H_4 + C_3H_3 \leftrightarrow C_7H_7,$$

which produced benzyl ($C_7H_7\bullet$) radicals. Subsequently, the benzyl radicals reacted either with H_2 or H• to form toluene. However, toluene later reacted with H• atoms to produce benzene, resulting in small amount of toluene remained in the gas phase. The benzyl radicals also participated in the production of naphthalene via a sequence of reactions,

$$C_7H_7 + C_3H_3 \leftrightarrow C_{10}H_{10} \leftrightarrow C_{10}H_8$$

However, this reaction sequence was less important to naphthalene production than the Hydrogen-Abstraction-Carbon-Addition (HACA) reaction sequence, which is highlighted in Fig. 3.18. The growth of benzene began with the H-abstraction reaction of benzene by H• atoms, which produced phenyl ($C_6H_5\bullet$) radicals. The phenyl radicals gained more carbon atoms with acetylene addition. Further addition of acetylene and subsequent polymerization resulted in naphthalene.

A similar reaction pathway analysis was conducted for n-dodecane pyrolysis using the CRECK model. The analysis results are concisely presented in Figs. 3.19 and 3.20. n-Dodecane already decomposed significantly at 1000 K. According to Fig. 3.19, n-dodecane pyrolysis underwent two main reaction pathways: C-C fission and H-abstraction by either H• or $CH_3\bullet$ radicals. In subsequent reactions, the initial pyrolysis products, e.g., heptyl ($nC_7H_{15}\bullet$) and dodecyl ($nC_{12}H_{25}\bullet$) radicals, decomposed

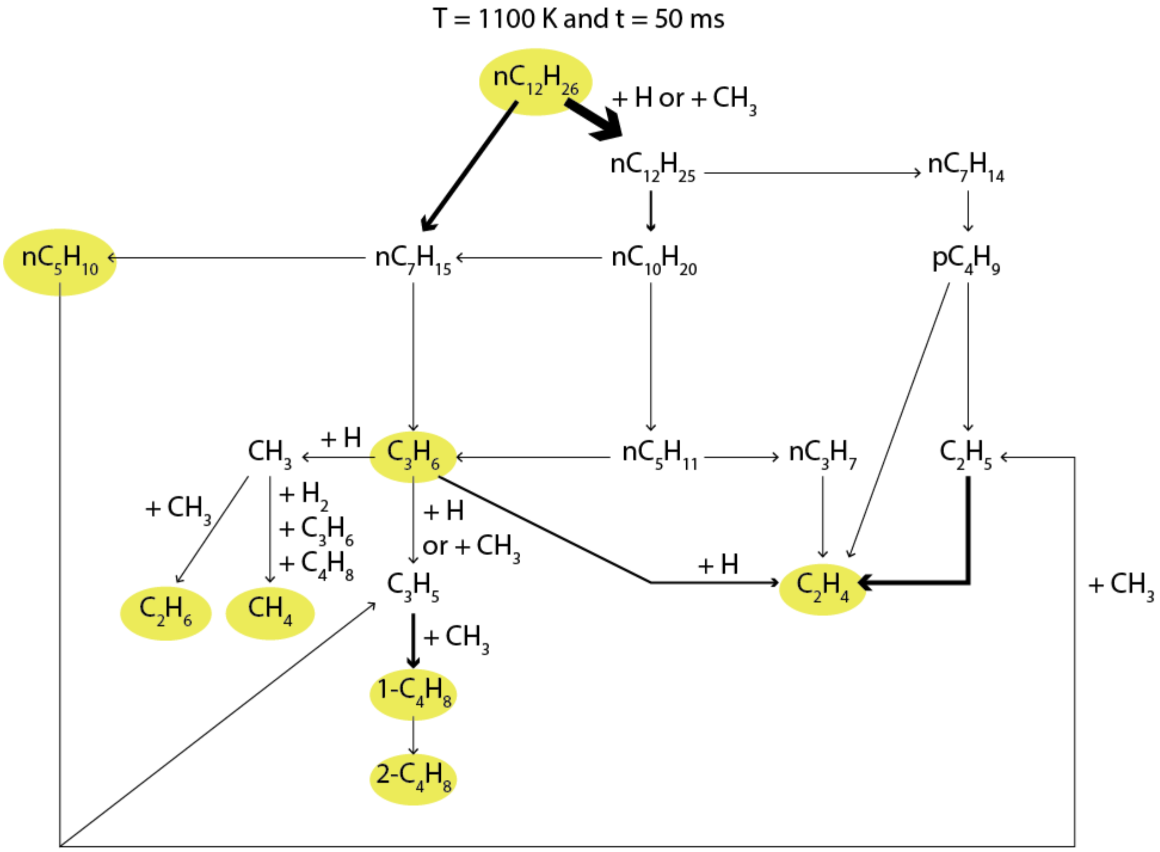

Figure 3.19: Reaction pathways from n-dodecane pyrolysis to the formation of C_4 species, obtained with the CRECK model [88] at 1100 K and 50 ms. The experimentally detected species are highlighted. The thickness of an arrow represents the relative flux (importance) of a reaction pathway.

into smaller alkene species such as: 1-pentene (1-C_5H_{10}) and 1-heptene (1-C_7H_{14}) that were detected experimentally. The majority of these alkene species continued to break down into the smallest alkene species, ethylene. In addition, a small proportion of the heptyl radicals thermally decomposed into propylene (C_3H_6). From propylene, other experimentally detected products such as methane (CH_4), ethane (C_2H_6), 1- and 2-butene (1- and 2-C_4H_8) were formed as shown in Fig. 3.19. As temperature increased, these species started to undergo different reaction pathways that led to other products as shown in Fig. 3.20. Ethane became ethylene via a sequence of two reactions: 1) H-abstraction either by $CH_3\bullet$ or $H\bullet$ radicals,

$$C_2H_6 + CH_3 \leftrightarrow C_2H_5 + CH_4,$$

and 2) thermal decomposition of C_2H_5 radicals to ethylene,

$$C_2H_5 \leftrightarrow C_2H_4 + H$$

Ethylene also underwent a similar two-reaction sequence to produce acetylene, and the extent of this reaction sequence increased with increasing temperature. The formation of aromatic species such as benzene and toluene became possible above 1100 K. At high temperature, the decomposition of 1-butene provided necessary ingredients for benzene and toluene formation. A majority of 1-butene reacted with $H\bullet$ atoms to produce propylene, which dominantly got converted to ethylene. However, a small proportion of propylene went on to produce propadiene or allene (aC_3H_4). Part of propadiene subsequently produced the propargyl radicals, which underwent the C_3 reaction pathway [78–82] that led to benzene. The observed benzene formation pathways with n-dodecane as the fuel are different from those with ethylene as the fuel (see Fig. 3.18). During the pyrolysis of ethylene, 1,3 butadiene acted as the important intermediate species that enabled both the C_3 and C_2/C_4 reaction

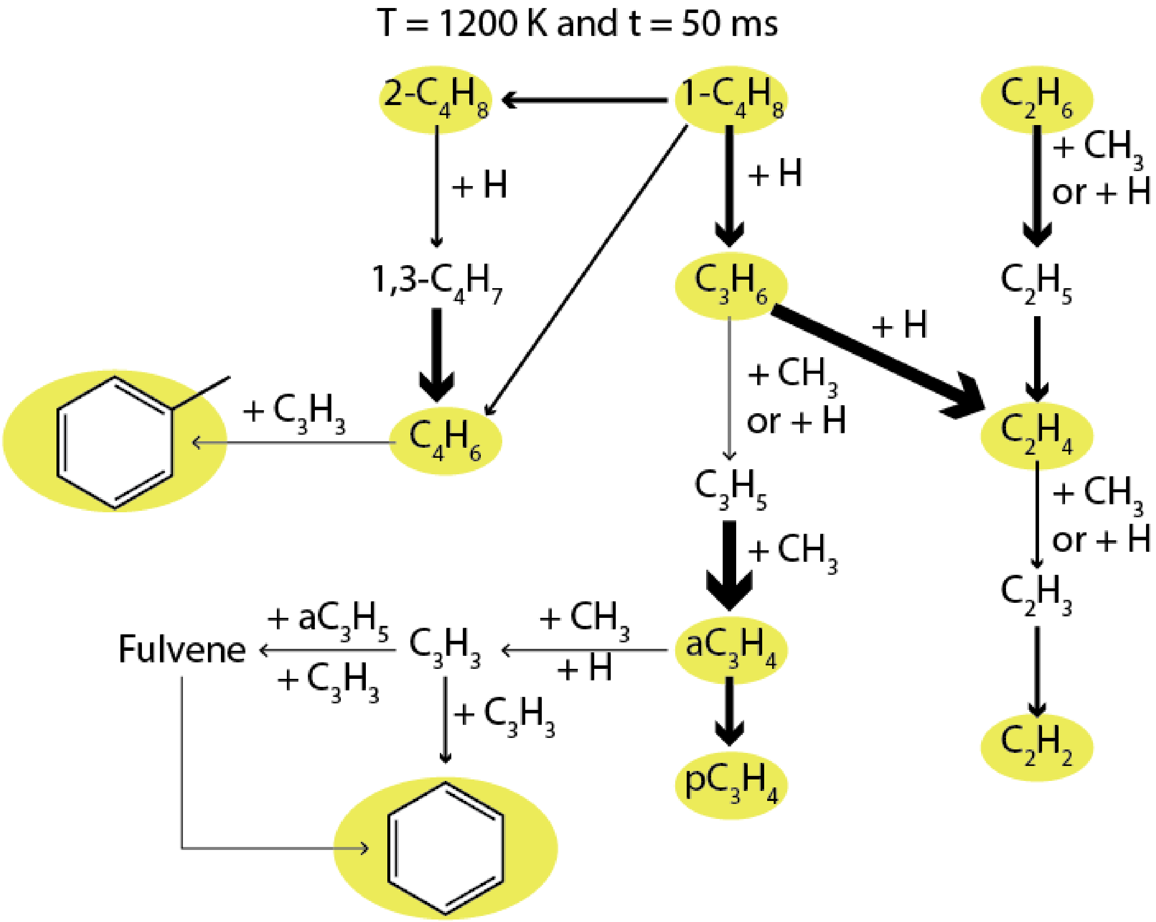

Figure 3.20: Reaction pathways from intermediate C_2-C_4 species to the formation of aromatic species, obtained from n-dodecane pyrolysis with the CRECK model [88] at 1200 K and 50 ms. The experimentally detected species are highlighted. The thickness of an arrow represents the relative flux (importance) of a reaction pathway.

pathways for benzene formation. On the other hand, during n-dodecane pyrolysis, 1-butene became the important intermediate species, but it only enabled the C_3 reaction pathway. This difference shown by the two fuels highlights the effect of fuel chemical composition on benzene formation mechanism.

The remaining amount of 1-butene get converted to 1,3 butadiene, which subsequently reacted with the propargyl radicals to form toluene as shown in Fig. 3.20. Naphthalene was not detected during n-dodecane pyrolysis over the considered experimental conditions. Reaction pathway analysis with the CRECK model [88] showed that notable naphthalene production became possible when residence time increased to 500 ms at 1250 K or temperature needed to be higher than 1250 K for the experimentally considered residence time range.

3.5 Summary

This chapter describes an experimental investigation of aromatic species formation and their growth into PAHs during pyrolysis of ethylene and n-dodecane. The collected data were intended to highlight the effects of temperature, residence time and fuel chemical composition on the PAH formation process. The second application of the experiment results was to evaluate the performance of detailed and reduced chemical kinetics models in predicting the evolution of the pyrolysis process under different conditions. The evaluation showed that, although the model predictions were inconsistent with each other, the detailed models still performed better than the reduced models. The validity of the experimental data for these two tasks was confirmed by a good agreement between the results of this investigation and those from shock tube and jet stirred reactor (JSR) studies. Finally, a detailed model that most reasonably captured the experimental data was selected to provide a concise map of reaction pathways from the fuel decomposition to the formation of PAHs. The acquired reaction pathways underlined the important effect of the fuel chemical composition. When ethylene was used as the fuel, benzene was the product of both the C_2/C_4 and C_3 reaction pathways. However, when n-dodecane was used as the fuel, only the C_3 reaction pathways led to benzene formation.

Chapter 4

Experimental Investigation of Jet A Pyrolysis with a Microflow Tube Reactor

4.1 Introduction

The experimental and modeling results that are described in Chapter 3 show the effect of fuel chemical composition on the formation of benzene during pyrolysis of two pure hydrocarbon fuels: ethylene (C_2H_4) and n-dodecane ($C_{12}H_{26}$). The effect of fuel chemical composition becomes even more important when real jet fuels or aviation fuels are considered. Real jet fuels are complex mixtures of various classes of hydrocarbons [115, 116]. Therefore, it is impossible to identify all the individual molecules present in real jet fuels and to account for their contribution to the formation of benzene and polycylic aromatic hydrocarbons (PAHs). Furthermore, the complex chemical composition of real jet fuels does not allow for tractability and repeatability of experimental and modeling investigations. Two approaches have been proposed in order to overcome the difficulty of characterizing jet fuel chemical compositions in experiments and computation. The objective of this chapter is to describe these two approaches and use experimental data from pyrolysis of a jet fuel to validate them.

There are three jet fuels that have been commonly used in aviation: Jet A, Jet A-1, and JP-8. Jet A and Jet A-1 are commercial jet fuels. The main difference between these two fuels are their freezing points. Jet A-1 has a lower freezing point at -47 °C, whereas the freezing point of Jet A is -40 °C [117]. In addition, Jet A is used mainly in the United States, while Jet A-1 is used in the rest of the world. On the other hand, JP-8 is the military equivalent of Jet A and Jet A-1, but with trace amounts of additives such as corrosion inhibitors and anti-icing and static-dissipation compounds [117]. Despite the various chemical compositions of these jet fuels, their constituents can be categorized into three main classes: linear and branched alkanes (35-50%), cycloalkanes (30-35%), and aromatics (20-25%) [101]. Number of researchers have taken advantage of this fact and proposed using fuel surrogates to emulate real jet fuels. Fuel surrogates are mixtures of a small number of reference hydrocarbons that represent the main chemical classes found in real jet fuels. Fuel surrogates can be formulated to mimic the physical properties (physical surrogates), chemical properties (chemical surrogates), or both physical and chemical properties of a jet fuel (comprehensive surrogates). Using fuel surrogates to simulate the combustion performance of jet fuels has a number of advantages. Firstly, fuel surrogates allow fuel composition to be accurately controlled and monitored during experiments and simulations. Secondly, with well-defined chemical composition, studies with fuel surrogates can be reproducible by different research groups. Given these advantages, numerous research efforts have been dedicated to formulating fuel surrogates of jet fuels. A brief literature review of the formulation progress of fuel surrogates for Jet A is included in this section because Jet A is one of the target fuels of this thesis work. More comprehensive reviews on fuel surrogates of Jet A as well as Jet A-1 and JP-8 can be found in a number of excellent review articles [46, 118, 119].

As one of the pioneers of fuel surrogates, Gueret et al. [120] formulated a three-component fuel surrogate and compared its combustion performance to that of the kerosene fuel in a jet stirred reactor (JSR). The authors also constructed a semi-global chemical kinetic model of the fuel surrogate. Zabanick [121] modeled the autoxidation of the jet fuels with a one-component fuel surrogate around 200 °C and captured the importance of alkyl hydroperoxides to the autoxidation process. Maurice et al. [122] experimentally investigated the gas phase chemistry of CO and NO_x emission during combustion of pure hydrocarbons and Jet-A. The authors used the experimental data to construct a detailed chemical kinetic model to predict the CO and NO_x emission with Jet A being represented by a two-component fuel surrogate. Lindstedt and Maurice [123] evaluated different aromatic compounds in a search of an appropriate candidate to be used in future fuel surrogates of Jet A. The authors found that benzene was not a good candidate to capture the PAH formation. Instead, the authors recommended alkyl-substituted aromatics. Humer et al. [124] formulated three fuel surrogates from five reference hydrocarbons: n-decane ($nC_{10}H_{22}$), n-dodecane ($nC_{12}H_{26}$), methylcyclohexane ($CH_3C_6H_{11}$), toluene (C_7H_8) and o-xylene (C_8H_{10}). The authors evaluated the performance of these three fuel surrogates in emulating the combustion properties of Jet A and JP-8. With the experimental data, the authors also constructed a semi-detailed chemical kinetic model for the fuel surrogates. Dean et al. [125] formulated three fuel surrogates and compared their ignition delay times to those of Jet A in a heated shock tube. Although the ignition delay times of these three fuel surrogates correlate well with those of Jet A, the authors found that fuel surrogates demonstrated stronger autoignition than Jet A. Dooley et al. [126,127] formulated two fuel surrogates (1^{st} and 2^{nd} generation surrogates) based on chemical group theory to match both physical and chemical properties of Jet A. The two fuel surrogates were validated by a wide range of experimental testing such as oxidation in a flow reactor and shock tube, autoignition in a rapid compression machine, laminar burning velocities in a counterflow and premixed flame, and the propensity to form soot in a diffusion flame. Malewicki et al. [128] futher validated the 2^{nd} generation fuel surrogate that was formulated by Dooley et al. [127]. The authors confirmed that the fuel surrogate emulated the combustion properties of Jet A very well. As a result, the authors developed a detailed chemical model to simulate the combustion of the fuel surrogate under different conditions. Kim et al. [129] formulated two fuel surrogates (UMI and UMII) to emulate the fuel properties that affected the spray development and gas phase ignition of Jet A. The authors showed that the two fuel surrogates were capable of emulating various physical and chemical properties of Jet A. Narayanaswamy et al. [130] developed a component library framework from which models of reference hydrocarbon components of a fuel surrogate could be chosen and combined to form a detailed model of the fuel surrogate. As an example, the authors formulated a three-component fuel surrogate and constructed a detailed model for it. Kang et al. [131] validated the two fuel surrogates developed by Kim et al. [129] by comparing the derived cetane number (DCN) and ignition behaviors of these two surrogates to those of Jet A. The authors found that one of the two fuel surrogates (UMII) better represented the physical and chemical properties of Jet A. Kim and Violi [132] used a surrogate model optimizer to evaluate a number of hydrocarbon compounds for future formulation of fuel surrogates of Jet A and alternative jet fuels. The authors found that a mixture of n-tetradecane and n-dodecane were suitable normal alkane representatives for conventional jet fuels, while the use of three C_9 alkyl-benzene was better than mixtures of toluene and C_{10} alkyl-benzene at reproducing aromatic contents and distillation curves of Jet A.

A large number of fuel surrogates has been formulated to model Jet A. Although these fuel surrogates reasonably emulated the combustion properties of Jet A, there still exists a wide variation in the composition of the fuel surrogates. In addition, a similar amount of detailed chemical kinetic models has been developed for these fuel surrogates. The fuel surrogate models were built by merging the models of reference hydrocarbon constituents. However, as shown in Chapter 3, the reaction rate coefficients employed in these reference hydrocarbon models still contain significant uncertainty. Since the production of reduced chemical kinetic models to be used in CFD simulations is based upon the detailed models, the validity of the reduced models is as good as that of the detailed models. Therefore, the detailed models of fuel surrogates need to be thoroughly validated by the results of independent fundamental combustion studies of Jet A before they can be used to produce reduced models for CFD simulations of practical combustion process.

Recently, an alternative concept has been proposed to substitute the fuel surrogate approach in modeling the combustion of real jet fuels [133–136]. In addition to the aforementioned limitations of fuel surrogates, four additional disadvantages have motivated a collaborative effort to develop a new approach in modeling real jet fuels [133–136]. The first limitation is that formulating a fuel surrogate to mimic a real fuel is empirical. Successful fuel surrogates must be confirmed by experimentally comparing their combustion properties to those of real jet fuels at conditions relevant to practical combustion processes. However, experimental measurements must be extensive and time consuming because the range of conditions in practical combustors is usually large. Secondly, detailed chemical kinetic models of fuel surrogates may not account for the interaction between the fragments of the reference constituents. Detailed models of fuel surrogates are constructed by merging the individual models of their constituents, and thus, additional testing is required for the interaction between the components of the fuel surrogates under practical combustion conditions. Thirdly, the numbers of species and reactions in detailed models for fuel surrogates are immense. As a result, it is impossible to verify the accuracy of chemical reaction rate parameters by first principles or experiments. Finally, using fuel surrogates of four or five neat hydrocarbon components may not capture the breakup and evaporation

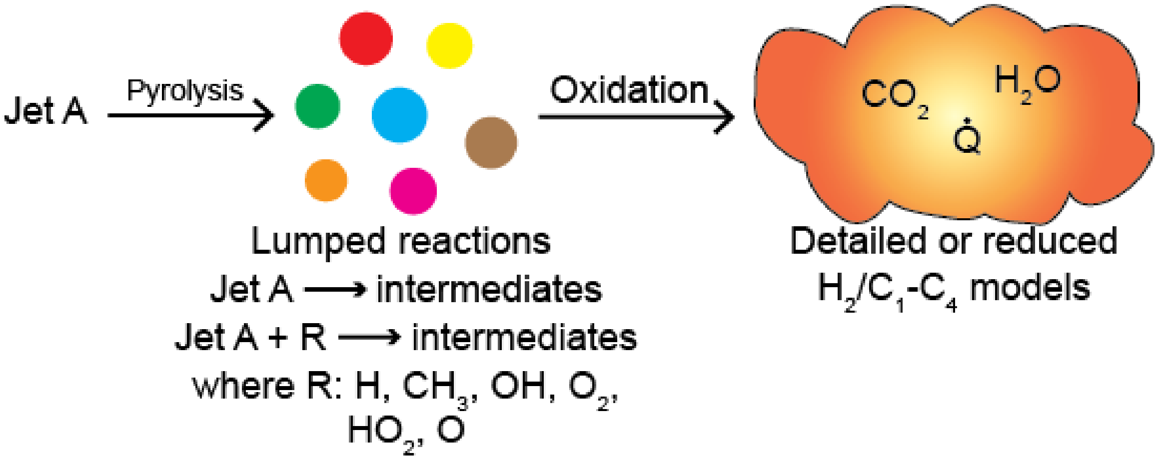

Figure 4.1: Representation of the fuel combustion process as a two-step process at high temperature condition. The fuel initially undergoes thermal and oxidative decomposition into eight primary products. The subsequent step is the oxidation of these eight pyrolysis products to form combustion products. The figure is adapted from [134].

processes during injection of real fuels into an engine as a spray.

The new approach to substitute fuel surrogate models is called Hybrid Chemistry (HyChem), which employs ”a physics-based understanding of the primary reaction pathways in fuel combustion” [133]. At high temperature conditions of practical combustors, the fuel combustion process resembles a two step process: pyrolysis of the fuel into a small number of low molecular weight fragments and subsequent oxidation of these pyrolysis fragments to produce final combustion products, as shown in Fig. 4.1. At these conditions, the fuel pyrolysis step is fast and can be treated as instantaneous. On the other hand, the oxidation of the pyrolysis fragments is rate limiting. As a result, the fuel pyrolysis process is modeled by a set of seven experimentally constrained, lumped reactions steps, while the oxidation process is modeled by a detailed foundational chemical kinetic model. It has been observed that the composition of the pyrolysis fragments determines the combustion behaviors (e.g., ignition delay time and laminar flame speed) of the real fuels. This observation indicates that the ability of HyChem models to accurately describe the combustion properties of real fuels depends on two factors. The first factor is the uncertainties in the experimental formulation of the seven reactions that describe the fuel pyrolysis step. The second factor is the predictability of the detailed foundational model that is used to represent the combustion of the pyrolysis products. Given the benefits of the HyChem approach (simple representation of real jet fuel chemical composition and manageable numbers of species and reactions), additional research effort is needed to minimize the uncertainties of the above two factors in order to support the development of the approach to be used in simulative CFD of practical combustion processes.

Both fuel surrogate and HyChem models need to be further validated by independent fundamental studies, especially fuel pyrolysis studies, in order to minimize the uncertainties of reaction rate parameters used by the models. Recognizing this need, this thesis work intended to provide experimental speciation data from pyrolysis of Jet A in the UVA microflow tube reactor (MFTR). The effects of temperature and residence time on the evolution of the pyrolysis products were investigated at normal atmospheric pressure. The experimental results will be described in the Chapter as well as comparison between the data and predictions by fuel surrogate and HyChem models.

4.2 Experimental and modeling procedure

Experimental investigation of the gas phase chemistry during fuel pyrolysis of was conducted with the microflow tube reactor (MFTR) at the University of Virginia. The detailed description of the MFTR was given in Chapter 2 and [61, 67, 68]. The target jet fuel of this investigation was Jet A (POSF 10325). The measured data was used to highlight the effects of temperature and residence time on the evolution of pyrolysis products. The experimental conditions of Jet A pyrolysis are listed in Chapter 2.3.

One of the objectives of this thesis work is to use the experimental data to validate fuel surrogate and HyChem models. The objective was accomplished by comparing the measured data to predictions by the models. Zero-dimensional (0D) simulations with the models were implemented at the experimental conditions in Cantera software [109], and the simulation results were used as model predictions. The tested models included three fuel surrogate models: Malewicki et al. [128], Narayanaswamy et al. [130], and CRECK [88], as well as the HyChem model for Jet A [133].

Malewicki et al.: Malewicki et al. [128] developed a detailed chemical kinetic model for a fuel surrogate to emulate the combustion properties of Jet A (POSF 4658). The fuel surrogate was referred as the 2^{nd} generation fuel surrogate that was developed by Dooley et al. [127]. The fuel surrogate consisted of four components: 40.4 mol% n-dodecane ($nC_{12}H_{26}$), 28.8 mol% iso-octane (iC_8H_{18}), 23.4 mol% n-propylbenzene (nC_9H_{12}), and 7.4 mol% 1,3,5-trimethylbenzene (1,3,5-C_9H_{12}). The chemical kinetic model contains 2080 species and 12373 reactions.

Narayanaswamy et al.: Narayanaswamy et al. [130] developed a flexible and evolutive component library framework for future developers of fuel surrogates to mix and match individual models of surrogate components to obtain concise chemical models with only the necessary kinetics for the desired fuel surrogates. In order to test the framework, the authors formulated a fuel surrogate of Jet A (POSF 4658). The fuel surrgate consisted of three components: 30.3 mol% n-dodecane ($nC_{12}H_{26}$), 48.5 mol% methylcyclohexane ($CH_3C_6H_{11}$), and 21.2 mol% m-xylene (mC_8H_{10}). The model consisted of 362 species and 1861 reactions.

CRECK: The same CRECK model [88] that was used in Chapter 3 is employed here with a fuel surrogate to simulate the pyrolysis of Jet A in the MFTR. The fuel surrogate was referred as UMII that was developed by Kang et al. [131] at the University of Michigan to model Jet A (POSF 4658). The fuel surrogate consisted of four components: 28.97 mol% n-dodecane ($nC_{12}H_{26}$), 14.24 mol% iso-cetane ($iC_{16}H_{34}$), 31.88 mol% decalin ($C_{10}H_{18}$), and toluene (C_7H_8). The CRECK model contains 368 species and 14324 reactions.

HyChem: This model [133] is one of a number of models that were constructed using the HyChem approach. This model is specifically for the combustion of Jet A (POSF 10325). Although the chemistry of the negative temperature coefficient (NTC) region was available, only the high temperature chemistry of Jet A combustion was considered in this thesis work. The model contains 119 species and 841 reactions.

It should be noted that two different batches of Jet A fuel were considered in this investigation. The experiments and HyChem model employed Jet A POSF 10325, while the three fuel surrogate models [88, 128, 130] were developed to represent Jet A POSF 4658. The POSF numbers are the identification numbers that are used by the Air Force Research Laboratory (AFRL) to identify different batches of fuels. Jet A POSF 10325 was procured from the Shell Mobile refinery in June 2013 [116]. On the other hand, Jet A POSF 4658 is a composite of a number of different Jet A batches, and thus, its properties are representative of a nominal Jet A [129].

4.3 Results

This section presents measured concentrations of stable products from pyrolysis of Jet A (POSF 10325) with varying residence and temperature at normal atmospheric pressure. A total of sixteen (16) species were quantified by the two GC systems: hydrogen (H_2), methane (CH_4), acetylene (C_2H_2), ethylene (C_2H_4), ethane (C_2H_6), propadiene (aC_3H_4), propyene (pC_3H_4), propylene (C_3H_6), 1,3-butadiene (C_4H_6), 1-butene (C_4H_8), iso-butylene (iC_4H_8), 1-pentene ($1\text{-}C_5H_{10}$), 1-hexene ($1\text{-}C_6H_{12}$), 1-heptene ($1\text{-}C_7H_{14}$), benzene (C_6H_6), and toluene (C_7H_8). It should be noted that the GC systems could not separate 1-butene and iso-butylene, and thus, the sum of these two species concentrations is presented. In addition, comparison to predictions by the four models: Malewicki et al. [128], Narayanaswamy et al. [130], CRECK [88], and HyChem [133], is included to evaluate the performance of the models and the associated fuel surrogates.

4.3.1 Effect of residence time at 1050 K

The effect of residence time on species production during pyrolysis of Jet A at a temperature of 1050 K is presented first. Fig. 4.2 shows the measured concentrations of H_2 and C_1-C_4 hydrocarbon species, while Fig. 4.3 shows the measured concentrations of hydrocarbon species that contain more than four C atoms. The measured data indicate that, at 1050 K, concentrations of H_2 and C_1-C_4 species increased with increasing residence time (see Fig. 4.2). The predictions by the four models also show a similar trend. However, the prediction values of the three fuel surrogate models were inconsistent with each other. The predictions by the HyChem model [133] reasonably agreed with the measured data, although there existed a disagreement between the model prediction and the date for ethane and 1,3-butadiene.

For species with more than four C atoms, Fig. 4.3 shows that concentrations of alkene species (1-pentene, 1-hexene, and 1-heptene) decreased with increasing residence time, while the concentrations of aromatic species (benzene and toluene) gradually increased with increasing residence time. Only the fuel surrogate models included the alkene species in their models. However, their predictions significantly differed from each other. Among the three models, only Malewicki et al. model [128] with the 2^{nd} generation surrogate [127] consistently captured measured concentrations of the alkene species. In contrast to the alkene species, all four models contains the two aromatic species and they predicted an increase in production of the species with increasing residence time at 1050 K. The HyChem model [133] predicted much higher production of benzene and toluene than the experimental data and the predictions by the fuel surrogate models. It should be noted that the CRECK model [88] with the UMII fuel surrogate [131] showed a significant amount of toluene at zero time

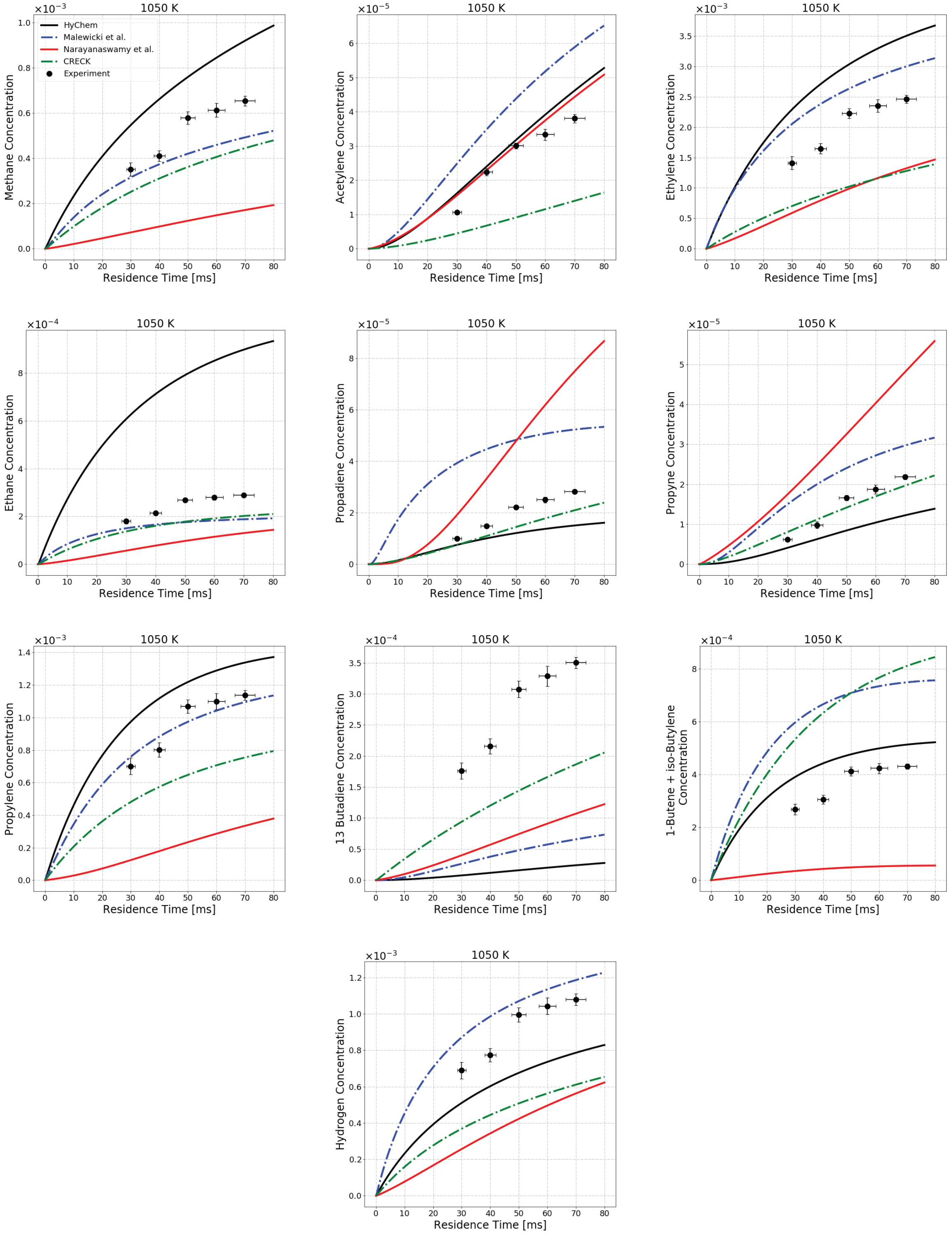

Figure 4.2: Measured and predicted mole fractions of H_2 and C_1-C_4 hydrocarbon products from pyrolysis of Jet A as a function of residence time at 1050 K and 1 atm. Tested models are Malewicki et al. [128], Narayanaswamy et al. [130], CRECK [88], and HyChem [133].

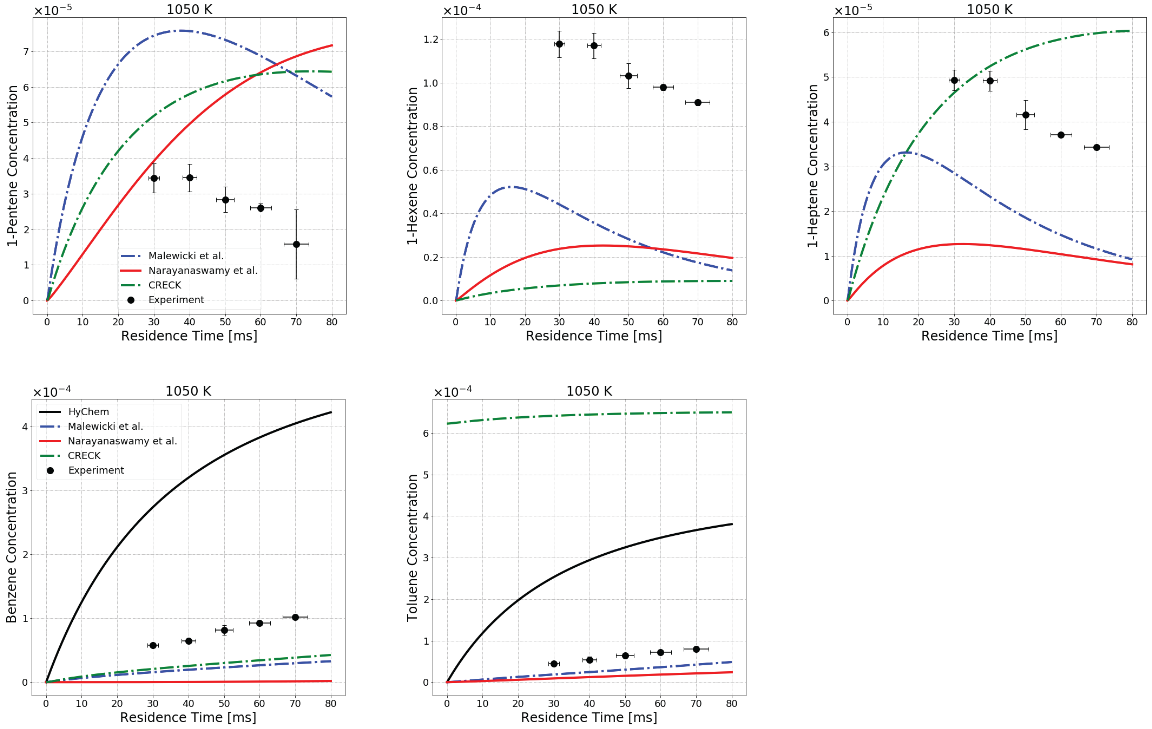

Figure 4.3: Measured and predicted mole fractions of hydrocarbon products with more than 4 C atoms from pyrolysis of Jet A as a function of residence time at 1050 K and 1 atm. Tested models are Malewicki et al. [128], Narayanaswamy et al. [130], CRECK [88], and HyChem [133].

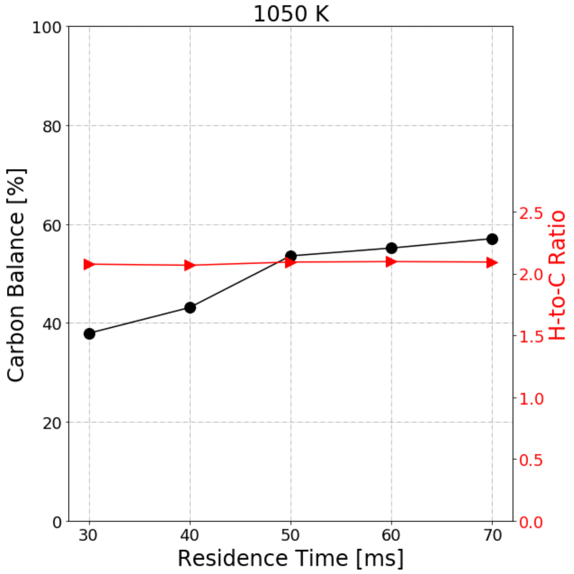

Figure 4.4: Measured carbon (C) balance (●) and recovered hydrogen-to-carbon (H-to-C) ratio (▶) from the pyrolysis of Jet A (POSF10325) as a function of residence time at 1050 K.

because toluene was one of the constituents in the UMII surrogate, but, similar to the experimental data, production of additional toluene with time was gradual as shown in Fig. 4.3.

The carbon (C) balance and hydrogen-to-carbon (H-to-C) ratio as a function of residence time at 1050 K were calculated and summarized in Fig. 4.4. The values of these two quantities are used to determine whether or not all the products from ethylene pyrolysis were accounted for. Similar to the HyChem model [133], this study assumed that Jet A had a chemical formula of $C_{11.4}H_{21.7}$. The carbon balance result showed that less than 60% of the original carbon number in the fuel were accounted for at 1050 K, although improved carbon number was recovered with increasing residence time. On the other hand, the calculated H-to-C ratio from the measured data remained constant at around 2.1 at this experimental condition. This H-to-C value is higher than that of Jet A (1.9).

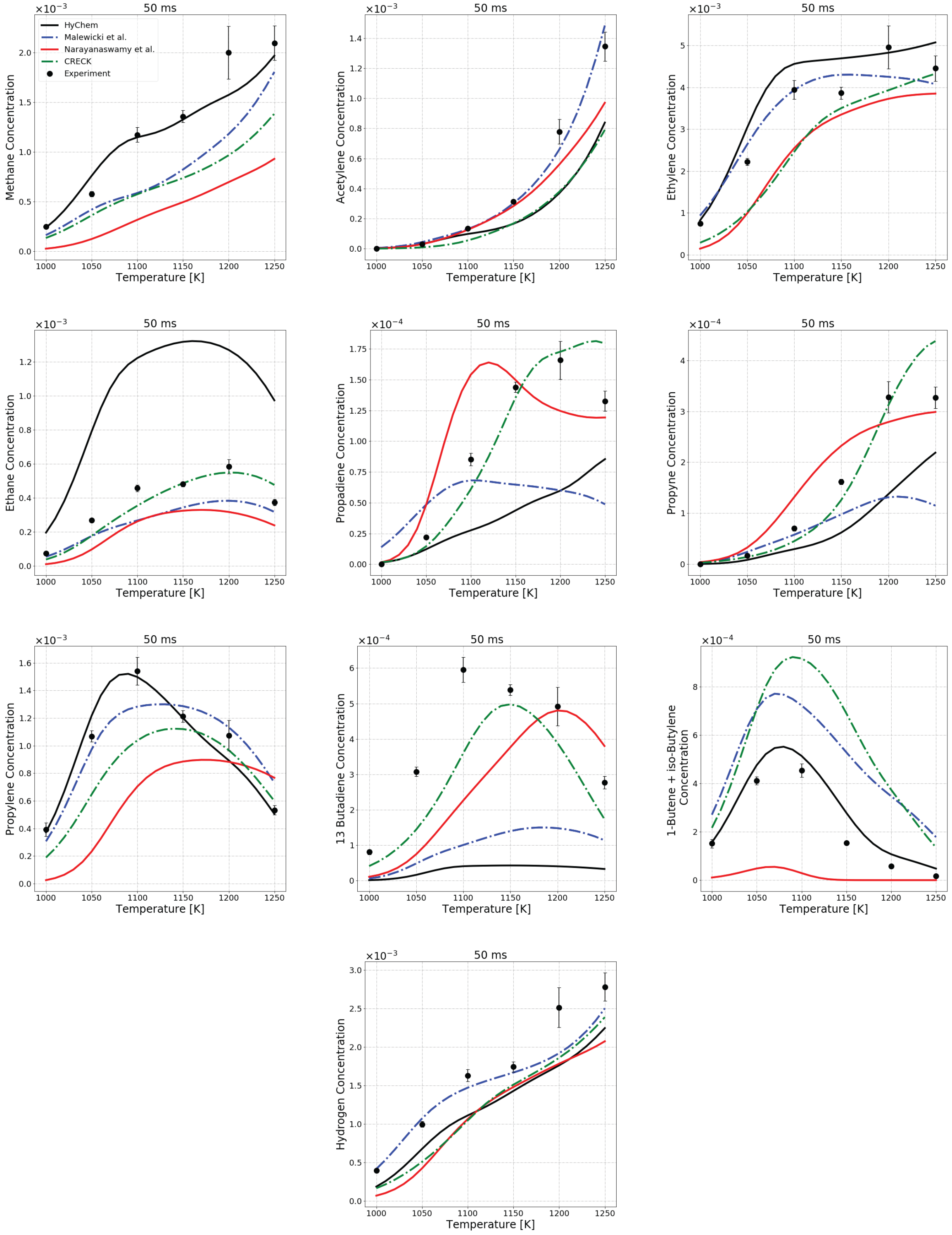

Figure 4.5: Measured and predicted mole fractions of H_2 and C_1-C_4 hydrocarbon products from pyrolysis of Jet A as a function of temperature at 50 ms and 1 atm. Tested models are Malewicki et al. [128], Narayanaswamy et al. [130], CRECK [88], and HyChem [133].

4.3.2 Effect of temperature at 50 ms

In addition the effect of residence time, the effect of temperature on the evolution of the products from pyrolysis of Jet A was also investigated at a fixed residence time of 50 ms. Fig. 4.5 contains plots of measured concentrations for H_2 and C_1-C_4 hydrocarbon species as a function of temperature, while Fig. 4.6 shows the measured concentrations of hydrocarbon species that contain more than four C atoms. According to Fig. 4.5, production of H_2, methane, and acetylene during experiments increased with increasing temperature, whereas the other C_2-C_4 species experienced a transition from production to consumption as temperature increased. Comparisons between the experimental data and predictions by the models show that the HyChem model [133] performed reasonably well in capturing the experimental data, although notable disagreement between the model predictions and the data existed for ethane, propadiene, propyne and 1,3-butadiene. On the other hand, predictions by the three fuel surrogate models for H_2 and C_1-C_4 species varied significantly and failed to capture the experimental data.

Fig. 4.6 shows the evolution of pyrolysis products with more than four C atoms as a function of temperature. Only the three fuel surrogate models contain the experimentally quantified alkene species: 1-pentene, 1-hexene, and 1-heptene. Both the experimental data and predictions by these three models agreed that the production of the alkene species was considerable over a temperature range from 900 to 1050 K. After 1050 K, these alkene species started to be consumed to produce smaller alkene species (e.g., ethylene). The concentrations of these alkene species completely disappeared after 1100 K. The experimentally captured evolution of these alkene species with varying temperature further justified the omission of these species in the HyChem model [133] when considering the combustion of Jet A at high temperature conditions of practical combustors.

In addition, two aromatic species: benzene and toluene, were quantified during the

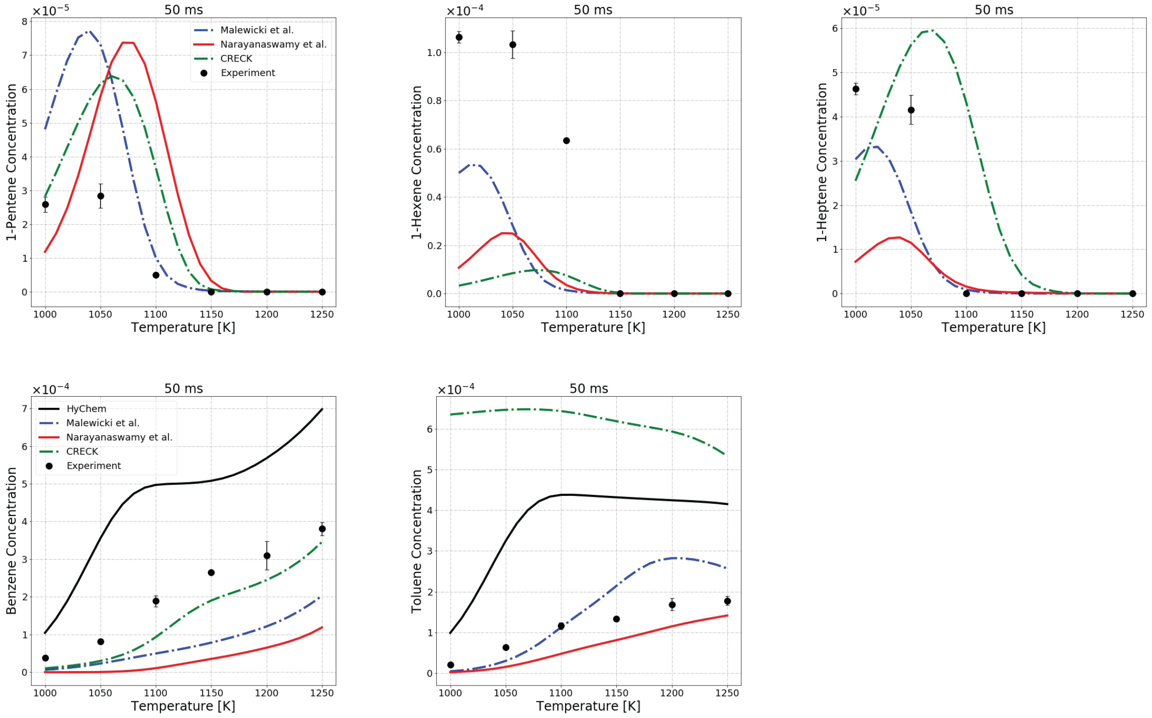

Figure 4.6: Measured and predicted mole fractions of hydrocarbon products with more than 4 C atoms from pyrolysis of Jet A as a function of temperature at 50 ms and 1 atm. Tested models are Malewicki et al. [128], Narayanaswamy et al. [130], CRECK [88], and HyChem [133].

experiments. Both the experimental data and predictions by the four models agreed that production of benzene increased with increasing temperature. However, only prediction by the CRECK model [88] with the UMII surrogate [131] closely captured the measured benzene concentration. Similar to the cases of varying residence time (Fig. 4.3), the HyChem model [133] predicted higher production of benzene than the experiments. On the other hand, unanimous agreement regarding the evolution of toluene could not be reached between the experiment and the model predictions. The measured data and the prediction by the Narayanaswamy et al. model [130] indicate that toluene concentration increased with increasing temperature, whereas predictions by the other three models showed an initial production of toluene followed by its consumption as temperature increases.

The carbon (C) balance and hydrogen-to-carbon (H-to-C) ratio as a function of temperature at 50 ms were calculated and summarized in Fig. 4.7. Again, a chemical formula of $C_{11.4}H_{21.7}$ was used to represent Jet A (POSF10325). The calculated carbon balance showed only a small amount of carbon number from the original fuel was recovered at 1000 K, but the carbon number improved as temperature increased. From 1100 to 1250 K, more than 80% of the carbon number was recovered, indicating that a majority of pyrolysis products was accounted for over this temperature range. Similar to the result in Fig. 4.4, the H-to-C ratio remained constant at around 2.1, which is higher than that of the Jet A fuel (1.9).

4.4 Discussion

This section contains an attempt to explain the differences between the experimental data and predictions by the models. The main focus is on six species: ethane (C_2H_6), propadiene (aC_3H_4), propyne (pC_3H_4), 1,3-butadiene (C_4H_6), benzene (C_6H_6), and toluene (C_7H_8). Reaction pathway and sensitivity analyses were utilized to determine

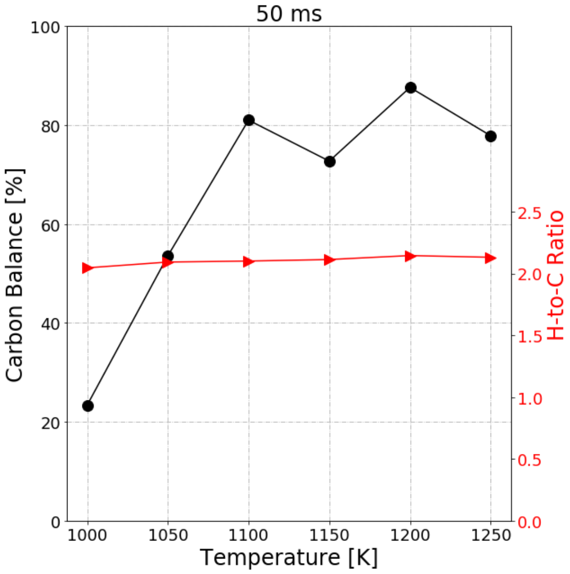

Figure 4.7: Measured carbon (C) balance (●) and recovered hydrogen-to-carbon (H-to-C) ratio (▶) from the pyrolysis of Jet A (POSF10325) as a function of temperature at 50 ms.

the primary reactions responsible for the formation and consumption of these six species and their reaction rate coefficients.

4.4.1 Ethane

The comparison between measured ethane concentration and predictions by the four models showed that HyChem model [133] predicted much higher ethane concentration, while the measurement and predictions by the other models were in a reasonable agreement over the considered temperature and residence time conditions (see Figs. 4.2 and 4.5). The search for the cause of this difference began with locating the most important reactions to the evolution of ethane. And sensitivity analysis was a excellent tool for this purpose. As described in Chapter 3, the sensitivity analysis quantifies the contribution of a reaction k (or its reaction rate coefficient) to the evolution of a species i through a sensitivity coefficient $S_{i,k}$, which is defined as follows

$$S_{i,k} = \frac{p_k}{X_i}\frac{\partial X_i}{\partial p_k} \tag{4.1}$$

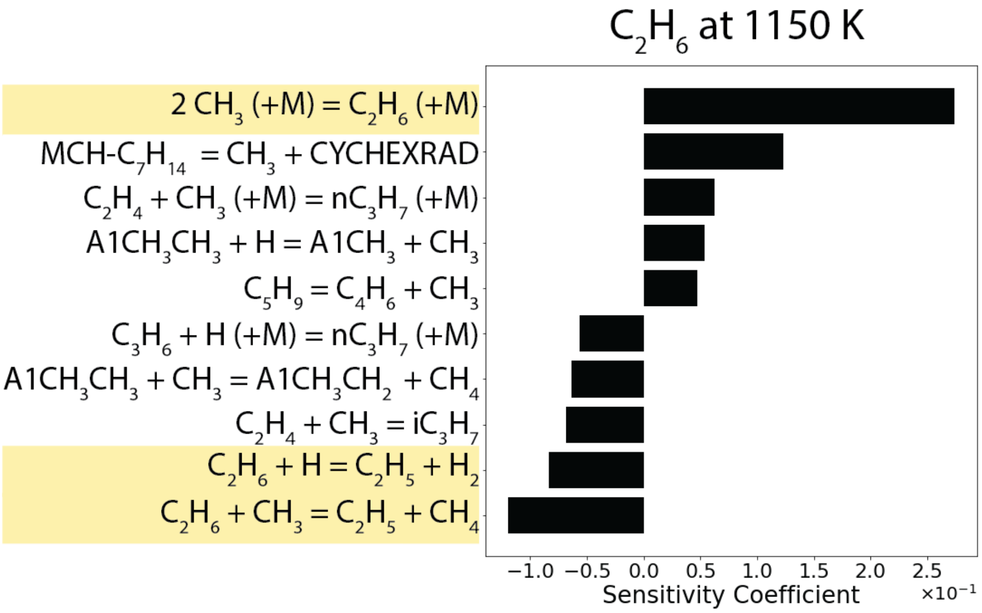

Figure 4.8: The result of a sensitivity analysis of ethane (C_2H_6) conducted with the Narayanaswamy et al. model [130] at 1150 K and 50 ms.

where p_k is a parameter on the rate coefficient of reaction k, and X_i denotes the mole fraction of species i. Fig. 4.8 shows an example of the result of a sensitivity analysis with ethane using the Narayanaswamy et al. model [130] at 1150 K and 50 ms. In Fig. 4.8, there are ten reactions that are most sensitive to the evolution of ethane. The reactions with positive sensitivity coefficients facilitate the production of ethane, while the reactions with negative sensitivity coefficients retard ethane production or promote the consumption of ethane. Among these ten reactions, the most important reaction to the formation of ethane was the recombination of two methyl radicals ($CH_3\bullet$) that led to ethane,

$$CH_3 + CH_3(+M) \leftrightarrow C_2H_6(+M) \tag{4.2}$$

while ethane consumption occurred through the H-abstraction of ethane by either H● or $CH_3\bullet$ radicals as follows

$$C_2H_6 + H \leftrightarrow C_2H_5 + H_2, \tag{4.3}$$

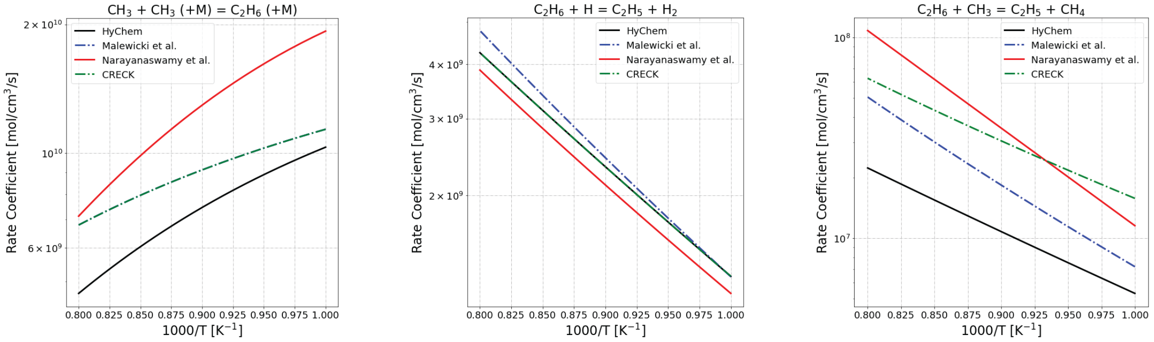

Figure 4.9: Reaction rate coefficients of the three important reactions to the evolution of ethane (C_2H_6) as a function of inverse temperature.

$$C_2H_6 + CH_3 \leftrightarrow C_2H_5 + CH_4 \tag{4.4}$$

All four models agreed that these three reactions were primarily responsible for the evolution of ethane concentration over the considered conditions. Thus, the next step was to compare the reaction rate coefficients of these three reactions. Fig. 4.9 shows the reaction rate coefficients of the three reactions plotted as a function of inverse temperature. A number of observations can be drawn from Fig. 4.9. First of all, there exists a variation in the reaction rate coefficients used by the models, but this variation is small (about a factor of five). Secondly, the rate coefficients of ethane producing reaction 4.2 decrease with increasing temperature, while those of ethane consuming reactions 4.3 and 4.4 increase with increasing temperature. This opposing relation between the rate coefficients and temperature explains the transition from production to consumption of ethane as temperature increased (see Fig. 4.5). Finally, the rate coefficients employed by the HyChem model [133] are smaller than those in the other models. This fact fails to account for the higher ethane concentration that was predicted by the HyChem model [133].

Sensitivity analysis and reaction rate coefficient calculation were only able to explain the ethane evolution with changing temperature during Jet A pyrolysis. However, they could not explain why the HyChem model [133] predicted higher ethane concentration than the measurement and predictions by the other models. The next available tool to analyze the model predictions was reaction pathway analysis. As shown by Fig. 4.8, the methyl radicals ($CH_3\bullet$) were the main source of ethane formation. Thus, the determination of different reaction pathways that led to the formation of $CH_3\bullet$ from Jet A pyrolysis could highlight the underlying cause of inconsistent ethane predictions by the models. Figs. 4.10 and 4.11 show simplified reaction pathways from the pyrolysis of Jet A and its fuel surrogate to the formation of $CH_3\bullet$ at 1000 K and 50 ms. The HyChem model [133] employed a lumped reaction to describe the pyrolysis of Jet A into eight different products,

$$\begin{aligned} POSF10325 \rightarrow {} & 1.7427C_2H_4 + 0.8191C_3H_6 + 0.2114(1C_4H_8) \\ & + 0.1633C_6H_5CH_3 + 0.17C_6H_6 + 1.5CH_3 + 0.5H + 0.08713(iC_4H_8) \end{aligned} \quad (4.5)$$

whose stoichiometric coefficients were determined by Jet A pyrolysis and oxidation experiments in a flow reactor and shock tube [133]. Whereas the fuel surrogate models used a sequence of reactions to portray $CH_3\bullet$ formation from the pyrolysis of each fuel surrogate component. It is possible that reaction equation 4.5 in the HyChem model [133] over-estimated the production of $CH_3\bullet$, resulting in higher ethane concentration predicted by the model. Indeed, HyChem model [133] predicted higher $CH_3\bullet$ concentration than the fuel surrogate models over the considered temperature and residence time conditions (see Fig. 4.12). The lumped pyrolysis reactions in the HyChem model must be re-evaluated in order to address the higher prediction of $CH_3\bullet$ production.

4.4.2 Propadiene and propyne

The predictions of propadiene (aC_3H_4) and propyne (pC_3H_4) by the HyChem model [133] also disagreed with the experimental data, while the predictions by two fuel surrogate models: Narayanaswamy et al. [130] and CRECK [88], reasonably captured

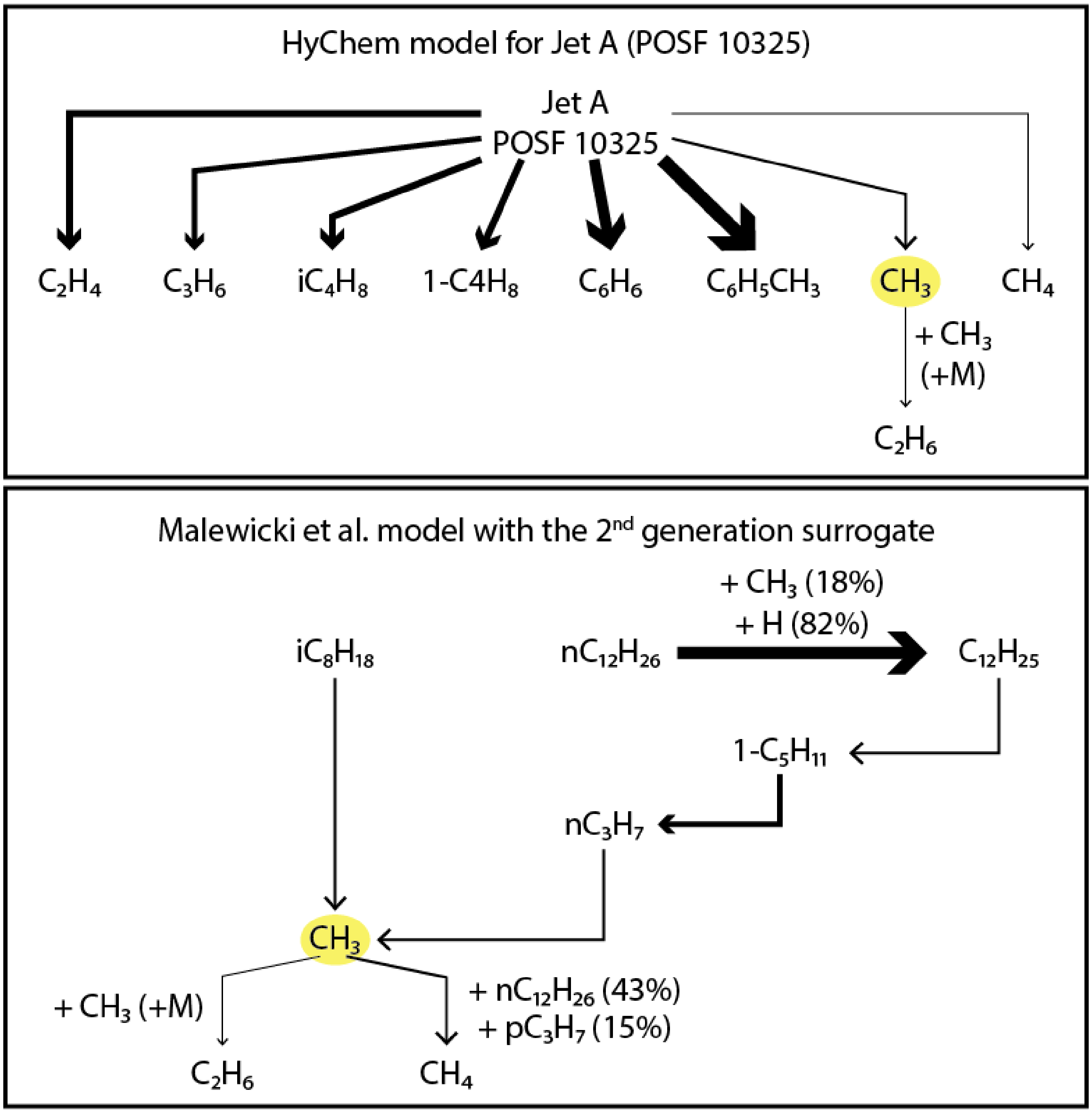

Figure 4.10: Simplified reaction pathways from pyrolysis of Jet A and its fuel surrogate to formation of methyl radical ($CH_3\bullet$). The results were obtained with the HyChem [133] and Malewicki et al. [128] models at 1000 K and 50 ms.

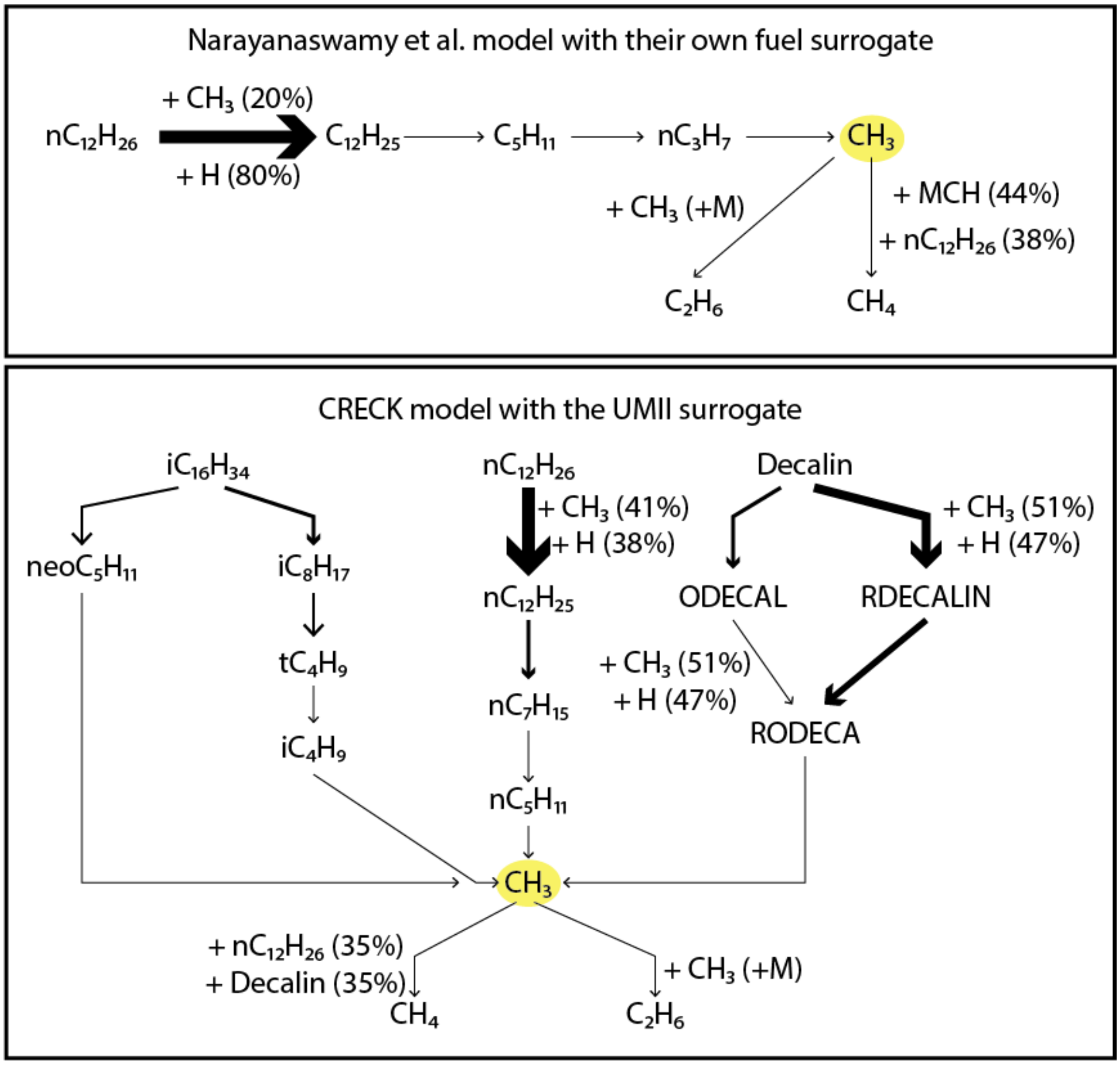

Figure 4.11: Simplified reaction pathways from pyrolysis of Jet A fuel surrogates to formation of methyl radical ($CH_3\bullet$). The results were obtained with the Narayanaswamy et al. [130] and CRECK [88] models at 1000 K and 50 ms.

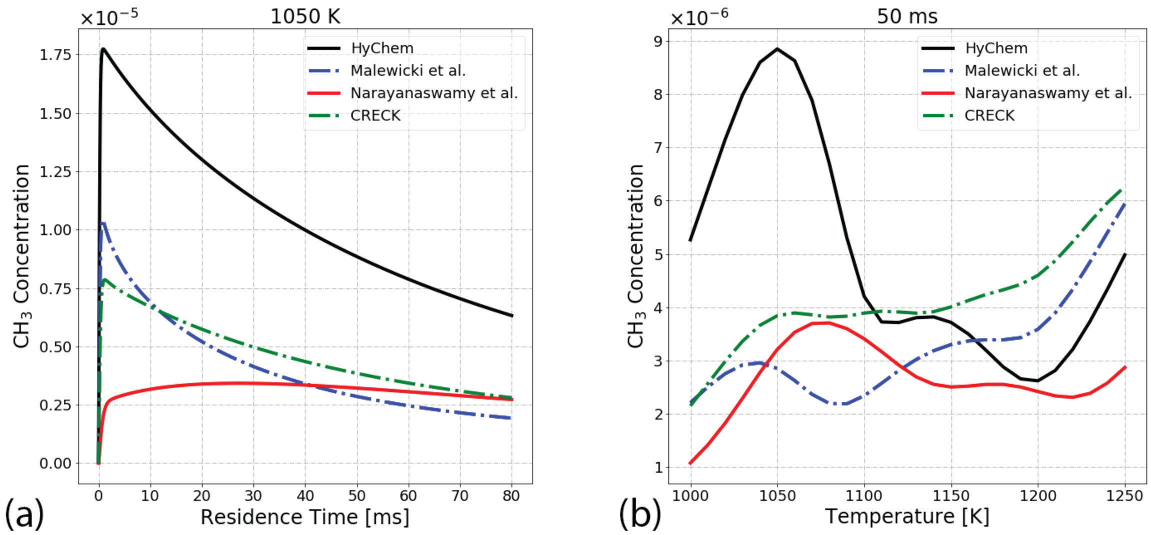

Figure 4.12: Predicted $CH_3\bullet$ concentrations by the HyChem [133], Malewicki et al. [128], Narayanaswamy et al. [130], and CRECK [88] models as a function of (a) residence time at 1050 K and (b) temperature at 50 ms.

the data. Thus, a comparison between these three models was carried out to find the possible cause of the difference between the HyChem model and the experimental data. Reaction pathway and sensitivity analyses were conducted for propadiene and propyne over the considered experimental conditions. First of all, the results of the analyses showed that all three models agreed that propylene (C_3H_6), 1-butene (1-C_4H_8) and iso-butylene (iC_4H_8) were the primary sources of propadiene. Around a temperature of 1100 K, propylene and 1-butene initially produced allyl radicals ($aC_3H_5\bullet$) via

$$C_3H_6 + CH_3 \leftrightarrow aC_3H_5 + CH_4,$$

and

$$1 - C_4H_8(+M) \leftrightarrow aC_3H_5 + CH_3(+M)$$

Then, the $aC_3H_5\bullet$ radicals decomposed into propadiene as follows

$$aC_3H_5 \leftrightarrow aC_3H_4 + H$$

A portion of propadiene underwent an isomerization reaction to produce propyne,

$$aC_3H_4 \leftrightarrow pC_3H_4$$

As temperature increased to around 1150 K, iso-butylene started to contribute to the production of propadiene by undergoing H-abstraction reactions by either H• or CH_3• radicals to produce iC_4H_7• radicals as follows

$$iC_4H_8 + H \leftrightarrow iC_4H_7 + H_2$$

The iC_4H_7• radicals subsequently decomposed to form propadiene as shown by the following reaction,

$$iC_4H_7 \leftrightarrow aC_3H_4 + CH_3$$

However, in addition to the reaction pathways shown above, the two fuel surrogate models, Narayanaswamy et al. [130] and CRECK [88], showed contribution from cyclo-paraffins that was not captured by the HyChem model [133]. The Narayanaswamy et al. model [130] showed that methylcyclohexane (MCH - C_7H_{14}) could produce propadiene through two different pathways. The first pathway was through the aC_3H_5• as follows

$$MCH \rightarrow C_6H_{11} \rightarrow aC_3H_5 \rightarrow aC_3H_4$$

The second pathway was where MCH produced an isomer of the aC_3H_5• radical, which subsequently decomposed into propadiene as shown by,

$$MCH \rightarrow tC_3H_5 \rightarrow aC_3H_4$$

On the other hand, the CRECK model [88] highlighted contribution from another cyclo-paraffin species, decalin (C_8H_{18}). Around 1100 K, decalin decomposed to form the $aC_3H_5\bullet$ radicals, which then decomposed to form propadiene. Through the contribution of cyclo-paraffins shown by the two fuel surrogate models, the lower propadiene and propyne concentrations predicted by the HyChem model [133] might stem from an under-estimation of cyclo-paraffin contribution by the HyChem model.

4.4.3 1,3 Butadiene

There also existed a disagreement between predictions by the HyChem model [133] and the measured data on 1,3 butadiene. However, the predictions by two fuel surrogate models (Narayanaswamy et al. [130] and CRECK [88]) reasonably captured the measured concentration of 1,3 butadiene over the considered experimental conditions. Comparing the chemistry of 1,3 butadiene in the HyChem model [133] and these two fuel surrogate models could highlight an area in the HyChem model [133] that possibly needed further improvement. Reaction pathway analysis was again employed to investigate the chemistry from pyrolysis of the parent fuel to the formation of 1,3 butadiene.

Over the considered experimental conditions, the HyChem model [133] predicted that 1,3 butadiene production began at 1050 K. The primary reaction pathways were as follows

$$POSF10325 \rightarrow 1 - C_4H_8$$

and

$$1 - C_4H_8 + H \rightarrow C_4H_7 + H_2$$

and

$$C_4H_7 \rightarrow C_4H_6 + H$$

At 1100 K, additional reaction pathways producing 1,3 butadiene involved ethylene (C_2H_4) and methyl radical ($CH_3\bullet$), which were the products of Jet A pyrolysis. As temperature increased to 1150 K, 1,3 butadiene started to get consumed to form cyclobutadiene (C_4H_4). An additional reaction pathway that produced 1,3 butadiene opened up when temperature reached 1200 K,

$$C_3H_3 + CH_3(+M) \rightarrow 1,2C_4H_6 \rightarrow C_4H_6$$

However, the extent of this reaction was small. The consumption of 1,3 butadiene also became significant. In addition to producing cyclobutadiene, 1,3 butadiene also helped form acetylene (C_2H_2) and toluene (C_7H_8).

Reaction pathway analysis with two fuel surrogate models: Narayanaswamy et al. [130] and CRECK [88], showed that these two models predicted the onset of 1,3 butadiene production at lower temperature than the HyChem model [133] (1000 vs. 1050 K). Simulation with the Narayanaswamy et al. model [130] was conducted with a three-component fuel surrogate: n-dodecane ($C_{12}H_{26}$), methylcyclohexane (C_7H_{14} or MCH), and m-xylene (mC_8H_{10}). At 1000 K, 1,3 butadiene was produced by the pyrolysis of MCH. MCH produced cyclopental radical ($C_5H_9\bullet$), which subsequently decomposed to form 1,3 butadiene as follows

$$C_5H_9 \rightarrow C_4H_6 + CH_3$$

As temperature continued to increase, two additional reaction pathways producing 1,3 butadiene became activated. Firstly, from n-dodecane pyrolysis, 1,3 butadiene was formed by

$$nC_{12}H_{26} \rightarrow C_{12}H_{25} \rightarrow C_7H_{14} \rightarrow C_4H_7 \rightarrow C_4H_6$$

Secondly, pyrolysis of MCH contributed another intermediate species (cylohexene or

cC_6H_{10}) that subsequently produced 1,3 butadiene,

$$MCH \rightarrow cC_6H_{10} \rightarrow C_4H_6$$

However, when temperature reached 1150 K, 1,3 butadiene started to get converted cyclopentadiene. 1,3 Butadiene further got consumed to produce acetylene (C_2H_2), ethylene (C_2H_4) and propargyl radicals ($C_3H_3\bullet$) with increasing temperature.

On the other hand, simulation with the CRECK model [88] was conducted with a four-component fuel surrogate: n-dodecane, iso-cetane ($iC_{16}H_{34}$), decalin ($C_{10}H_{18}$), and toluene (C_7H_8). 1,3 Butadiene production was noted at 1000 K. The fuel surrogate component that was responsible for 1,3 butadiene formation was decalin. At this temperature, decalin produced cyclohexyl radical ($cC_6H_{11}\bullet$), which then decomposed to form 1,3 butadiene. When temperature increased to 1100 K, contribution of n-dodecane to 1,3 butadiene formation became active through reaction pathways that were similar to those shown by the Narayanaswamy et al. model [130]. As temperature continued to go up to 1150 K, 1,3 butadiene production from pyrolysis of methylcyclohexane or MCH became possible through the formation of 1-heptene ($1\text{-}C_7H_{14}$), 1-butene ($1\text{-}C_4H_8$), and 2-butene ($2\text{-}C_4H_8$). However, 1,3 butadiene also started to get consumed at 1150 K to produce propargyl radical and toluene. The consumption of 1,3 butadiene became more significant with increasing temperature.

Comparing the results of reaction pathway analysis between the HyChem model [133] and the two fuel surrogate models highlights a number of important similarities and differences that may help explain the contradicting predictions of 1,3 butadiene concentration. First of all, the 1,3 butadiene producing reaction pathways demonstrated by the HyChem model are very similar to those involving only n-dodecane by the two fuel surrogate models. It is possible that the HyChem model [133] failed to sufficiently accounts for the contribution of cyclo-paraffin species such as methylcyclohexane and decalin to the formation of 1,3 butadiene. As a result, the HyChem model [133] predicted a much lower 1,3 butadiene concentration than these two fuel surrogate models and the experiments. Nevertheless, all three models agreed on the reaction pathways that consumed 1,3 butadiene at high temperature conditions. This agreement explains how the three models were able to capture the trend of measured 1,3 butadiene concentration as a function of temperature.

4.4.4 Benzene and toluene

In Figs. 4.3 and 4.6, the HyChem model [133] predicted much higher benzene (C_6H_6) and toluene (C_7H_8) concentrations than the measurements and predictions by the three fuel surrogate models. Sensitivity and reaction pathway analyses with the four models were again employed to determine the cause of this difference in model predictions. The results of the analyses showed that, at low temperature (1000 - 1150 K), the three fuel surrogate models did not predict any notable production of benzene and toluene. However, the HyChem model [133] predicted considerable benzene and toluene production via three lumped pyrolysis reactions,

$$\begin{aligned}POSF10325 &\rightarrow 1.7427C_2H_4 + 0.8191C_3H_6 + 0.2114(1C_4H_8)\\ &+ 0.1633C_6H_5CH_3 + 0.17C_6H_6 + 1.5CH_3 + 0.5H + 0.08713(iC_4H_8),\end{aligned}$$

$$\begin{aligned}POSF10325 + H &\rightarrow H_2 + 0.45CH_4 + 1.5946C_2H_4 + 0.7495C_3H_6 + 0.0797(iC4H8)\\ &+ 0.2392(1C_4H_8) + 0.2465C_6H_6 + 0.2368C_6H_5CH_3 + 0.3H + 0.7CH_3,\end{aligned}$$

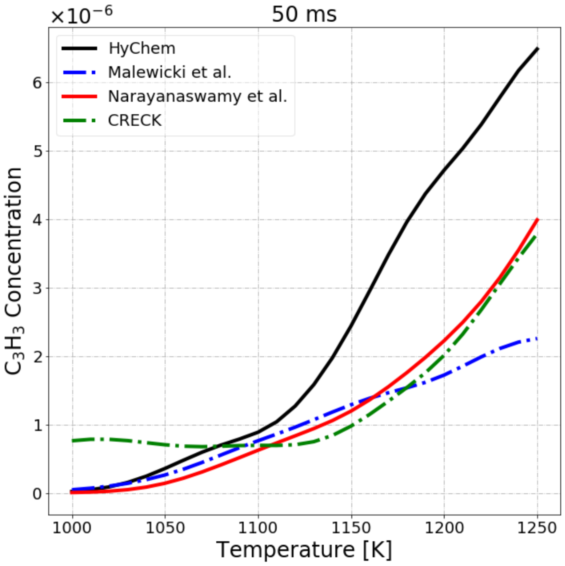

Figure 4.13: Predicted concentrations of the propargyl (C_3H_3●) radical as a function of temperature at 50 ms. Tested models are Malewicki et al. [128], Narayanaswamy et al. [130], CRECK [88], and HyChem [133].

and

$$POSF10325 + CH3 \rightarrow 1.45CH_4 + 1.5946C_2H_4 + 0.7495C_3H_6 + 0.0797(iC_4H_8) \\ + 0.2392(1C_4H_8) + 0.2465C_6H_6 + 0.2368C_6H_5CH_3 + 0.3H + 0.7CH_3$$

In addition, as temperature increased beyond 1150 K, an additional reaction pathways that produced benzene became active. Specifically, all the models agreed that reactions involving propargyl radicals (C_3H_3●) were the primary source of benzene production,

$$C_3H_3 + C_3H_3 \leftrightarrow C_6H_6,$$

$$C_3H_3 + C_3H_3 \leftrightarrow C_6H_5 + H,$$

and

$$C_6H_5 + H_2 \leftrightarrow C_6H_6 + H$$

However, when comparing the C_3H_3● concentrations predicted by the models, the

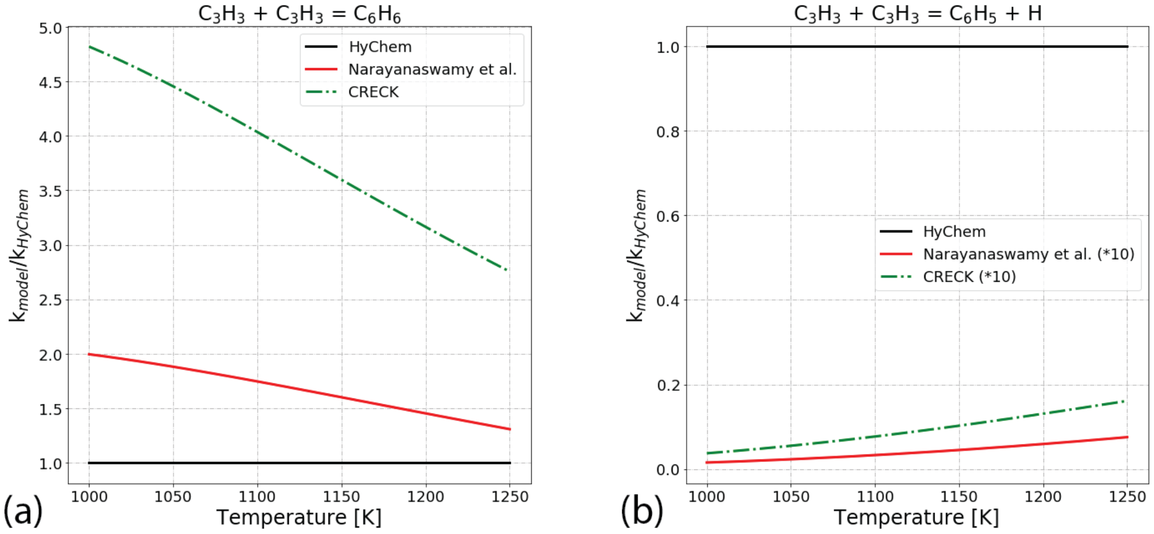

Figure 4.14: Rate coefficients of two reactions responsible for benzene formation above 1150 K. The values were extracted from three models: HyChem [133], Narayanaswamy et al. [130], and CRECK [88].

HyChem model [133] showed a notably higher $C_3H_3\bullet$ concentration than the other models (see Fig. 4.13). In addition to the higher $C_3H_3\bullet$ concentration prediction, the HyChem model also employed a significantly higher rate coefficient for the $C_3H_3 + C_3H_3 \leftrightarrow C_6H_5 + H$ than those in the fuel surrogate models. Fig. 4.14 shows a comparison of rate coefficients of the two reactions involving $C_3H_3\bullet$ used by the HyChem [133], Narayanaswamy et al. [130], and CRECK [88] models. The rate coefficients of $C_3H_3 + C_3H_3 \leftrightarrow C_6H_6$ reaction only slightly differed from one another (about a factor of 5 at 1000 K). On the other hand, the rate coefficient of $C_3H_3 + C_3H_3 \leftrightarrow C_6H_5 + H$ used by the HyChem model [133] was more 200 times higher than those in the Narayanaswamy et al. [130] and CRECK [88] models. Higher $C_3H_3\bullet$ concentration coupled with its higher reaction rate coefficients might be the cause of higher benzene concentration predicted by the HyChem model [133] at temperature higher than 1150 K. Through the comparison of the aromatic chemistry in the models, it appears that both the lumped pyrolysis reactions and benzene chemistry in the HyChem model needs to be re-evaluated in order to better capture the evolution of benzene and toluene during the pyrolysis of Jet A.

4.5 Summary

Experimental investigation of Jet A (POSF 10325) pyrolysis was conducted with the MFTR in order to study the effects of temperature and residence time on the evolution of pyrolysis products. The measured data was also used to validate four chemical kinetic models of Jet A combustion. Three of the models employ the fuel surrogate concept to emulate the combustion properties of Jet A, while the other one (HyChem) uses the Hybrid Chemistry approach, which describes jet fuel combustion as a two step process. The first step is the thermal and oxidative decomposition of the jet fuel into a small number of low molecular weight products. Then, these pyrolysis products will undergo an oxidation process in the second step. The HyChem consists of seven lumped reactions whose rate and species stoichiometric coefficients were determined experimentally to describe the pyrolysis process, and of a detailed foundational chemical kinetic model to describe the oxidation of the pyrolysis products. Comparison between the experimental data and model predictions showed that the HyChem model [133] overall performed better than the fuel surrogate models at capturing the experimental data. However, further improvement can still be made to the lumped pyrolysis reactions to enhance their predictability for species such as ethane, propadiene, propyne, 1,3 butadiene, benzene and toluene.

Chapter 5

Experimental Investigation of Species Transport and Chemical Kinetics on Silicon Carbide Deposition in a Premixed Microflow Tube Reactor

5.1 Introduction

Silicon carbide (β-SiC) is a ceramic material with excellent refractory properties [137, 138]. SiC has been widely used in a variety of applications, such as electronic circuit elements and ceramic matrix composites (SiC_m/SiC_f CMCs), and containment vessels for nuclear fuel particles [139, 140]. All of these applications require high quality and fast growth rate of SiC that is free of defects to prevent crack induction, propagation, and ultimately failure of the component. Common techniques for depositing SiC are chemical vapor deposition (CVD) on flat surfaces and chemical vapor infiltration (CVI) on porous structures (preforms). During these two processes, it has been shown that the micro-structure and morphology of the deposits depend on the reactor operating conditions: temperature, total pressure, flow rate (or characteristic residence time), and initial ratio of the reactant gas mixture.

Chemical vapor deposition and chemical vapor infiltration of silicon carbide are controlled by one of two rate-limiting steps: chemical kinetics and mass transport [37]. Depending on whether chemical kinetics or transport control is dominating, the deposited SiC layer can have either desirable or undesirable surface roughness or morphology. Literature suggests that chemical kinetics control is readily achieved at low pressure conditions [38,141–143], although the species mass flux rate is independent of pressure, and is given by $J_i = \rho D_i \nabla X_i$, where ρ is the density, D_i diffusion coefficient of species i, X_i the mole fraction of species i. With the considered deposition conditions, these authors have identified distinct SiC deposits that were characteristics to the two different rate-limiting regimes. In addition, variation in input gas ratios, total flow rates, and substrate location in low-pressure hot wall reactors were also observed to influence the micro-structure and morphology of SiC deposits [144–146].

However, growth of SiC at sub-atmospheric pressure, especially in iso-thermal CVI (I-CVI) is extremely slow. Several approaches have been used to reduce the long fabrication time of the deposition process at sub-atmospheric pressure. Application of temperature and/or pressure gradients, or forced flow in a CVI reactor has shown the potential to significantly reduce the fabrication time. But these approaches introduce additional cost and complexity to the fabrication process. An alternative approach is to optimize the iso-thermal CVI by determining the ideal reactor operating conditions. A number of studies, both theoretical and experimental, have been reported to demonstrate the potential of reducing fabrication time and improving quality of the deposits in I-CVI at atmospheric pressure [39–41, 72].

Given the need to better understand the pressure effects on I-CVI reactor oper-

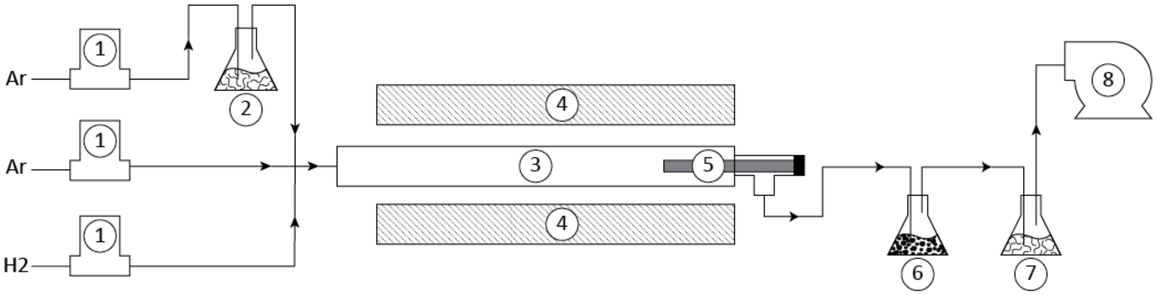

Figure 5.1: A schematic of the experimental setup: 1) flow controllers, 2) a MTS bath, 3) the alumina tube reactor, 4) modular furnace, 5) 1 mm substrate inserted near the exit, 6) solid trap, 7) water trap, and 8) exhaust pump

ation, one of the objectives of this thesis work was to compare the deposition rate and morphology of SiC deposits at atmospheric and sub-atmospheric pressures with well controlled flow reactor temperature-residence time profiles. The deposition of SiC was conducted on thin quartz substrate rods (1 mm OD) in a small-diameter laminar tubular flow reactor (4.8 mm ID and 0.52 m length) with minimal radial temperature gradients [61]. Methyltrichlorosilane (CH_3SiCl_3 or MTS) and hydrogen (H_2) were used as the reactant gases, which was diluted in argon (Ar). The effects of deposition temperature, total volume flow rates (or residence time), and H_2-to-MTS partial pressure ratios (α) were investigated at two different total pressures. The present experimental results may facilitate future investigators in selecting optimal operation conditions for SiC deposition at atmospheric pressure.

5.2 Experimental procedures

The experimental apparatus used in this study consisted of a tubular, laminar flow reactor (4.8 mm ID non-porous alumina of 0.52 m length), in which a quartz substrate (1 mm in diameter) was inserted into the reactor such that it was aligned with the reactor axis and its tip was 50 mm from the the reactor exit. Fig. 5.1 shows the schematic of the experimental setup. Methyltrichlorosilane (MTS) (99% from Sigma Aldrich) was used as the precursor gas, together with hydrogen (H_2) (ultra-high purity

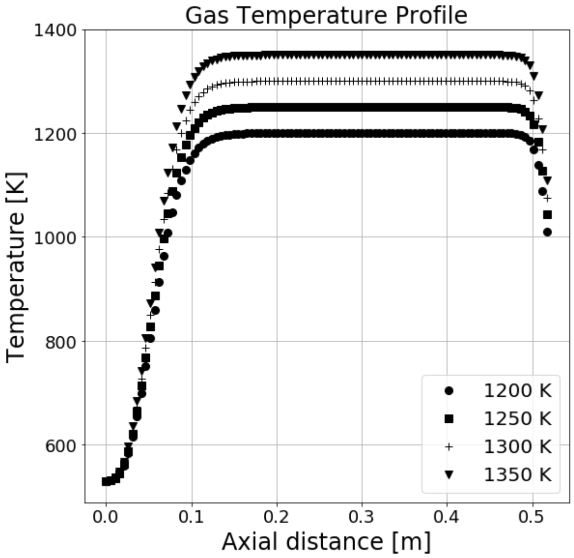

Figure 5.2: Typical gas temperature profiles along the reactor axis at four different set-point temperatures: 1200, 1250, 1300, and 1350 K, with Ar volume flow rate of 500 sccm and p = 1 atm

from Praxair) and argon (Ar) (ultra-high purity from Praxair) as the carrier gas. The tubular reactor was heated with five modular heating elements, whose temperature was controlled by K-type thermocouples connected to PID controllers. Measurements of the temperature profiles inside the reactor has been characterized with inert gas flow, showing three separate regions: temperature ramp-up at the entrance (100 cm), isothermal hot-section (370 cm), and temperature ramp-down at the exit (50 cm). Fig. 5.2 shows the typical temperature profiles for four different set-point temperatures (1200-1350 K) at atmosphere pressure with Ar gas flow of 500 SCCM (corresponding cross-sectional area averaged velocity of 1.9-2.1 m/s). In experiments with MTS, the total Ar flow rate was always kept at 95% mole fraction of the total mixture. All the deposition experiments were run for 1 hr at atmospheric pressure, whereas at sub-atmospheric pressure (0.5 atm) the experimental run times were extended for 2 hrs to obtain similar thickness of deposits for analysis. The effluent stream exiting the reactor was successively passed through a solid trap containing soda lime and a water trap before exhausting through a mechanical pump.

5.3 Results and discussion

5.3.1 Effect of deposition temperature

A number of studies have shown that, under typical CVD conditions, the decomposition process of MTS is in the fall-off pressure regime, implying that the collisional energy transfer and chemical reactions play a role in the kinetics of the decomposition [147–149]. Furthermore, Ganz et al. [150] has reported that the MTS reaction rate is directly proportional to the partial pressure of MTS. Here, the effects of temperature and pressure on the deposition rate of SiC during the CVD process was investigated.

SiC mass growth rate

Fig. 5.3 shows the natural log of mass growth rate of SiC as a function of inverse temperature at a pressure of 1 atm (●) and 0.5 atm (■). The results show that mass growth rates at the two pressures differ significantly from each other, almost an order of magnitude difference at 1300 K. Since MTS mass flux rate is independent of pressure (see Section 5.1), the lower mass growth rate at 0.5 atm can be attributed to the lower decomposition rate of MTS. This implies that in the MTS decomposition rate expression, $\omega = [MTS]^n A \exp(-E/RT)$, the overall reaction order (n) is greater than unity (note: A is the overall collision frequency and E the overall activation energy). The observed lower deposition rate of SiC from MTS at lower total pressure is consistent with the literature [149, 150]. However, extracting the exact reaction order with respect to MTS concentration requires further investigations, including better understanding of contributions from homogeneous vs heterogeneous kinetics.

At 1 atm, Fig. 5.3 shows that the mass growth rate has two distinct regions - an increasing growth rate from 1200 to 1300 K, followed by a nearly constant growth rate from 1300 to 1350 K. The 1200 to 1300 K region with strong temperature dependence can be associated with an underlying SiC deposition rate controlled by chemical ki-

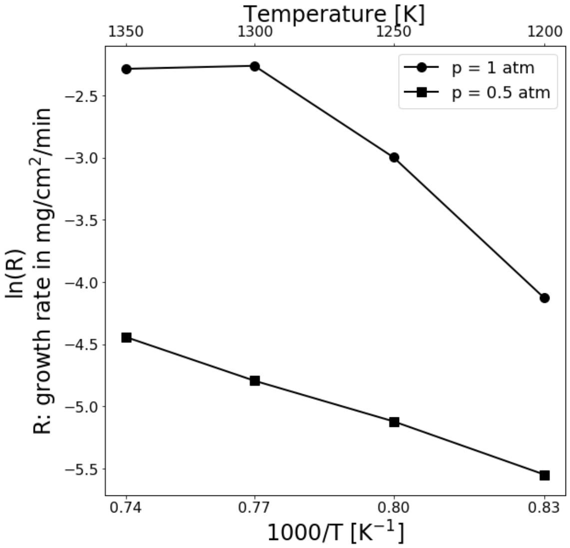

Figure 5.3: Growth rate variations as a function of reciprocal temperature for $\alpha = 10$ and $Q_{total} = 276$ SCCM at two total pressures (1 atm and 0.5 atm).

netics. Whereas for the 1300 to 1350 K region with weak temperature dependence, the growth rate can be associated with mass transfer controlled processes. In contrast, at 0.5 atm, over the entire temperature range considered, the SiC deposition rate increases with increasing temperature. The near linear rate on a semi-log plot indicates a constant activation energy of 23.48 kcal/mole for the global kinetic rate. The absence of transition to a transport control regime at 0.5 atm implies that the even at the highest temperature of 1350 K considered, the chemical kinetics remains too slow due to [MTS]^n term with low MTS concentration and $n > 1$.

Morphology of SiC deposits

The effect of temperature on the morphology of SiC deposits was also studied at two pressures of 1 and 0.5 atm. Fig. 5.4 shows images of the surface of SiC deposits on quartz substrates at different temperature conditions: (a) 1200, (b) 1250, (c) 1300, and (d) 1350 K, with left column showing images at 1 atm and right column at 0.5 atm, respectively. Overall, relatively smooth images seen at 0.5 atm supports the hypothesis that the SiC growth is kinetically controlled as shown in Fig. 5.3.

Furthermore, changing morphology at 1 atm is also consistent with Fig. 5.3 indicating a transition from kinetic controlled to transport control occurring at around 1300 K.

High-resolution SEM images at 1 atm and 1200-1250 K (chemical kinetic controlled regime) show that SiC deposits consist of hemispherical structures. Closer examination reveals that each hemispherical structure of the 1200 K sample consists of much smaller *spherical* particle-like structures with an average diameters of 50 nm. On the other hand, the 1250 K sample shows very smooth hemispherical structure with an average diameter of 1 μm. Moreover, the 1250 K sample also shows a coalescence of a portion of these hemispherical structures. In contrast, SiC deposits at higher temperatures of 1300 and 1350 K (transport controlled regime) exhibit notably flatter, smoother surface. There is still a small number of hemispherical structures present, but these features are different from those observed at lower temperatures. Specifically, the hemispherical structures at 1300 and 1350 K samples consist of particles with *angular* surfaces with an average size of 100 nm and appears to be made up of a network of nano-structures.

Following the work by Lespiaux et al. [151] and Xu et al. [152], the observed variation of SiC morphology with temperature seen in this study can be explained on the basis of the supersaturation and nucleation mechanism. At 1 atm and lower temperature range explored, i.e. 1200 to 1250 K, SiC deposition is controlled by reaction kinetics, specifically by surface reaction kinetics. At this temperature range, with fast homogeneous MTS decomposition leading to the formation of intermediate species, results in a bottle-neck of reaction pathway due to to the slower heterogeneous reaction rate. Thus, the supersaturation of these intermediate species results in formation of nucleation sites at the surface. Due to rapid transport of intermediate species, these nucleation sites grow in size and eventually coalesce to form hemispherical SiC aggregates observed. With increasing temperature, faster surface reaction rates can reverse the supersaturation phenomena leading to a smoother surface morphology as seen at

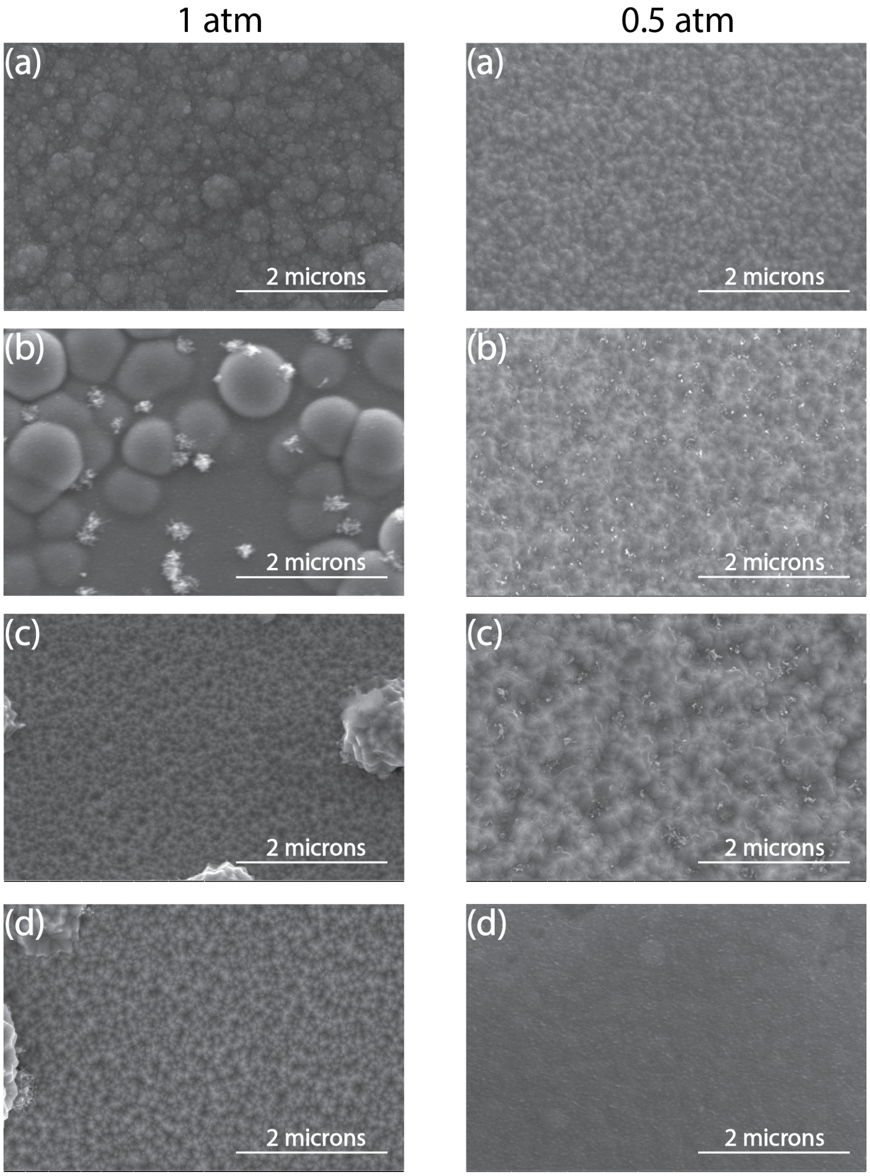

Figure 5.4: SEM images of SiC films grown on quartz substrates at two different pressures: p = 1 and 0.5 atm, and at four different temperatures: a) 1200 K, b) 1250 K, c) 1300 K, and d) 1350 K, with $\alpha = 10$ and $Q_{total} = 276$ SCCM.

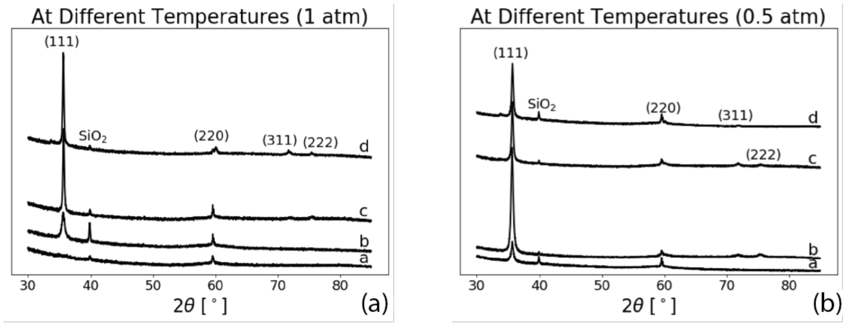

Figure 5.5: XRD of SiC films grown at four different temperatures: a) 1200 K, b) 1250 K, c) 1300 K, and d) 1350 K, with $\alpha = 10$ and at two different pressure: p = 1 and 0.5 atm.

1300-1350 K. In contrast, the relatively smooth morphology observed at 0,5 atm and at 1200 and 1250 K can be attributed to the lower homogeneous decomposition rate of MTS owning to its lower partial pressure and never attaining the supersaturation conditions.

Preferred orientation of SiC deposits

X-ray diffraction (XRD) analysis was performed to determine the variation of crystalline phase and preferred orientation of SiC deposits with varying temperature at two different pressures: 1 and 0.5 atm. Fig. 5.5 shows the 2θ peak values obtained from SiC deposits at four different temperatures: 1200, 1250, 1300, and 1350 K, and at the two pressures. The obtained 2θ peaks correspond to the (111), (220), (311) and (222) planes, which are identical to SiC with face centered cubic (FCC) structure. Therefore, the deposits at these conditions are polycrystalline β-SiC. However, there is an additional 2θ peak at 39.89°. This peak comes from the quartz substrate. Because of a difference in the thermal expansion coefficients between SiC and quartz, cracking has occured to the deposits, and, as a result, small portion of the SiC coating is chipped away from the substrate, leaving some area of the quartz uncovered.

Preferred orientation of each SiC sample can be compared on the basis of the estimated by texture coefficient (TC$_{hkl}$) using the Harris method [153],

$$TC_{hkl} = \frac{I_{hkl}/I_{O,hkl}}{\frac{1}{N}\sum I_{hkl}/I_{O,hkl}}, \tag{5.1}$$

where I_{hkl} is the intensity of the (hkl) peak (measured from XRD data in Fig. 5.5), $I_{O,hkl}$ represent standard intensity taken from International Center for Diffraction Data (ICCD), and N is the number of diffraction planes. The texture coefficients (TC) of (111) and (220) planes as a function of temperature is shown in Fig. 5.6 for two different total pressures. For SiC samples deposited at 1 atm (Fig. 5.6(a)), the value of (220) TC is higher than that of (111) TC at low temperature (1200 and 1250 K), whereas the (111) TC becomes much larger at high temperature (1300 and 1350 K). This change in preferred orientation of the SiC deposits with increasing temperature at 1 atm appears to accompany the change in morphology of the samples seen in Fig. 5.4 (at 1 atm). At low temperatures of 1200 and 1250 K, with the morphology of the SiC deposits mainly consisting of hemispherical structures formed by nucleation of saturated vapor with subsequent crystallized SiC may explain the preferred (220) orientation at low temperature [152]. At high temperatures of 1300 and 1350 K, the preferred orientation of the SiC deposits is (111), which indicates a significant improvement in the crystallinity state of the deposits because (111) plane is the most densely packed atomic plane [154] when compared to the 220 orientation.

The texture coefficients (TC) of (111) and (220) planes for SiC samples deposited at 0.5 atm pressure show a slightly different trend (see Fig. 5.6-0.5 atm). The (220) plane is the preferred orientation only at 1200 K, whereas the preferred orientation changes to the (111) plane at 1250 to 1350 K. The XRD data shows that the low pressure condition improves the crystallinity of the SiC samples even at low temperature (1200 and 1250 K). At 1200 K, comparing the values of (111) and (220) TCs at the two pressure conditions shows that the (220) TC remains relatively constant,

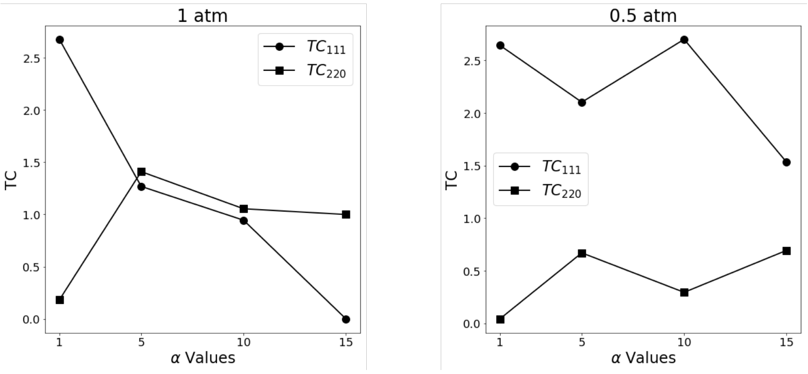

Figure 5.6: Texture coefficients as a function of temperatures, with $\alpha = 10$ and $Q_{total} = 276$ SCCM.

but the value of (111) TC increases with decreasing pressure. This improvement of crystallinity at lower pressure may be attributed to the lower MTS decomposition rate at this condition. As stated before, the lower MTS decomposition rate results in a smaller species gradient across the boundary layer at the substrate location, leading to a smaller species flux towards the substrate surface. The smaller species flux prevents supersaturation of gaseous species from occurring, and thus allowing more active sites to become available on the substrate surface for the deposition of SiC crystals from surface reactions of small gaseous precursors. The XRD data and morphology of SiC samples at 0.5 atm are consistent with those seen at 1 atm, where the improved crystallinity is accompanied by a change in morphology from having a rugged surface with hemispherical structures to having a relatively flat surface with angular structures.

5.3.2 Effects of H_2-to-MTS ratio, α

SiC mass growth rate

The influence of initial input gas composition or initial gas ratio (α) on the CVD of SiC was investigated at two different total pressures. The initial input gas ratio (α) was varied from 1 to 15 at a fixed temperature of 1250 K and a fixed total flow rate

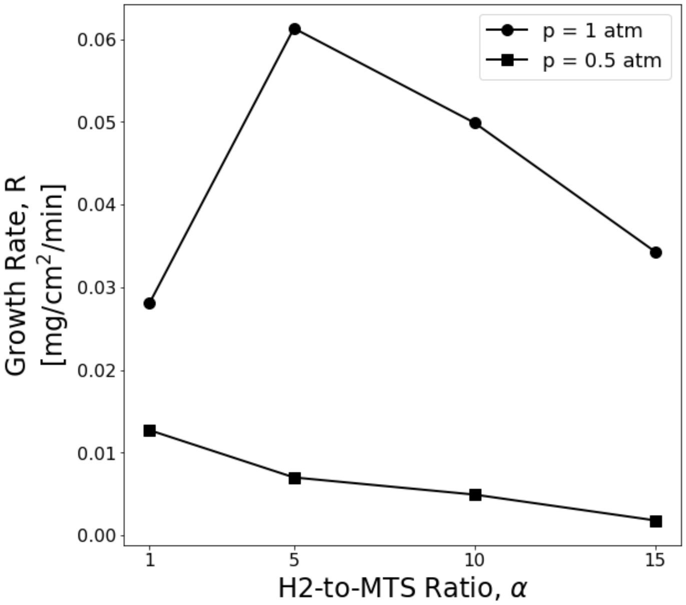

Figure 5.7: Growth rate variations with H_2-to-MTS ratios (α): 1, 5, 10, and 15, at 1250 K and $Q_{total} = 276$ SCCM for two different pressures (1 atm and 0.5 atm).

of 276 sccm. Fig. 5.7 shows the variation of the mass growth rate as a function of initial input gas ratio for the two total pressures. Similar to the results in Section 5.3.1, the lower SiC mass growth observed at 0.5 atm is attributed to lower MTS decomposition rate at this pressure condition. In addition, the influence of α on SiC mass growth rate differs at the two pressure conditions. At 1 atm, the mass growth rate initially increases to a maximum value at $\alpha = 5$, upon which the growth rate starts to decrease. On the other hand, the mass growth rate at 0.5 atm only increases with decreasing initial gas input ratio.

At 1 atm, the mass growth rate is divided into two regions. In the high α region ($\alpha = 5$-15), the mass growth decreases with increasing α. Here, SiC deposition is controlled by reaction kinetics. The mass growth rate decreases with increasing α because increasing in α reduces the initial MTS concentration, which translates a lower MTS decomposition rate according to the rate expression, $\omega = [MTS]^n A \exp(-E/RT)$. On the other hand, in the low α region ($\alpha = 1$-5), the mass growth rate decreases with decreasing α. The abrupt change in SiC mass growth rate as α decreases can

Table 5.1: The multi-component coefficient of the MTS reactant in an mixture of MTS, H_2, and Ar gas environment

α	$X_{MTS,0}$	$D_{multi,MTS}$ [m^2/s]
1	0.025	9.62×10^{-5}
5	0.0083	9.74×10^{-5}
10	0.0045	9.77×10^{-5}
15	0.0031	9.78×10^{-5}

be attributed to the transition from reaction controlled to mass transfer controlled regime. The multi-component diffusion coefficients of MTS in a mixture of MTS, H_2, and Ar were calculated at all the α values (see Chapter 2.3). The calculation results are summarized in Table 5.1. It can be seen that reducing α or increasing initial MTS concentration lowers the diffusion coefficients of MTS and gaseous SiC precursors, resulting in the deposition being controlled by mass transfer at the lower α values. Oh et al. also reported a similar behavior of SiC mass growth rate as a function of initial input gas ratio [145]. However, the authors postulated that decreasing the initial input gas ratio makes the boundary layer around the substrate thicker, hindering the diffusion of SiC precursors to the substrate surface and lowering the deposition rate of SiC. Therefore, it is possible that decreasing α values at 1 atm pressure condition reduces the diffusivity of the SiC precursors as well as increases the boundary layer thickness, rendering mass transport the rate-limiting step in SiC deposition.

However, at 0.5 atm, the mass growth rate only increases with decreasing α. The SiC deposition at lower total pressure is only controlled by chemical reaction kinetics. Although the diffusivity of SiC precursors decreases with decreasing α value, this decrease is offset by the enhanced diffusivity of the SiC precursors at lower total pressure because the diffusion coefficient is inversely proportional to the total pressure ($D \sim \frac{1}{p}$). And a decrease in α leads to higher initial concentration of MTS, which enhances the MTS decomposition rate at 0.5 atm total pressure

Morphology of SiC deposits

Fig. 5.8 shows the effect of initial input gas ratio (α) on the morphology of SiC deposits at two different total pressures: 1 and 0.5 atm. As seen in Fig. 5.8, the variation of α has different effects on the morphology of SiC deposits at the two total pressures. At 1 atm (Fig. 5.8 - 1 atm), the changing morphology as α decreases (from (d) to (a)) corresponds to the transition from reaction kinetics to mass transfer regime. In the reaction kinetics regime (α = 5 - 15), SiC deposits show a morphology with smooth hemispherical structures. The size of these structures appears to increase with decreasing α or increasing mass growth rate (see Fig. 5.7). However, as α continues to decrease, SiC deposition transitions to the mass transfer regime, where the morphology of the SiC deposits drastically changes (Fig. 5.8 - 1 atm (a) and (b)). The morphology still consists of hemispherical structures, but they are much larger and no longer smooth. The structures appear to be made up of angular or star-shaped nanostructures. These angular or star-shaped structures have been reported to be characteristics to the mass transfer regime [154, 155].

In contrast, the morphology of the SiC samples at 0.5 atm appears relatively flat. The morphology of the samples at low pressure condition is consistent with the results shown in Section 5.3.1. At low pressure condition, the lower MTS decomposition rate and the resultant smaller species flux favor the deposition of SiC crystals on the substrate surface. As a result, SiC samples at 0.5 atm have a relatively flat morphology. Moreover, the size of the nanostructures on the SiC samples increases with decreasing α values (from Fig. 5.8-0.5 atm (d) to (a)). This increase in size of the nanostructure is due to an increase in an increase in MTS decomposition rate with decreasing α or increasing initial MTS concentration. Moreover, a closer examination of Fig. 5.8(a) at both pressure conditions highlights the different morphologies of SiC deposits that are characteristic to the reaction kinetics and mass transfer controlled regime. Specifically, the observed angular or star-shaped nanostructures on the sample at 1 atm is

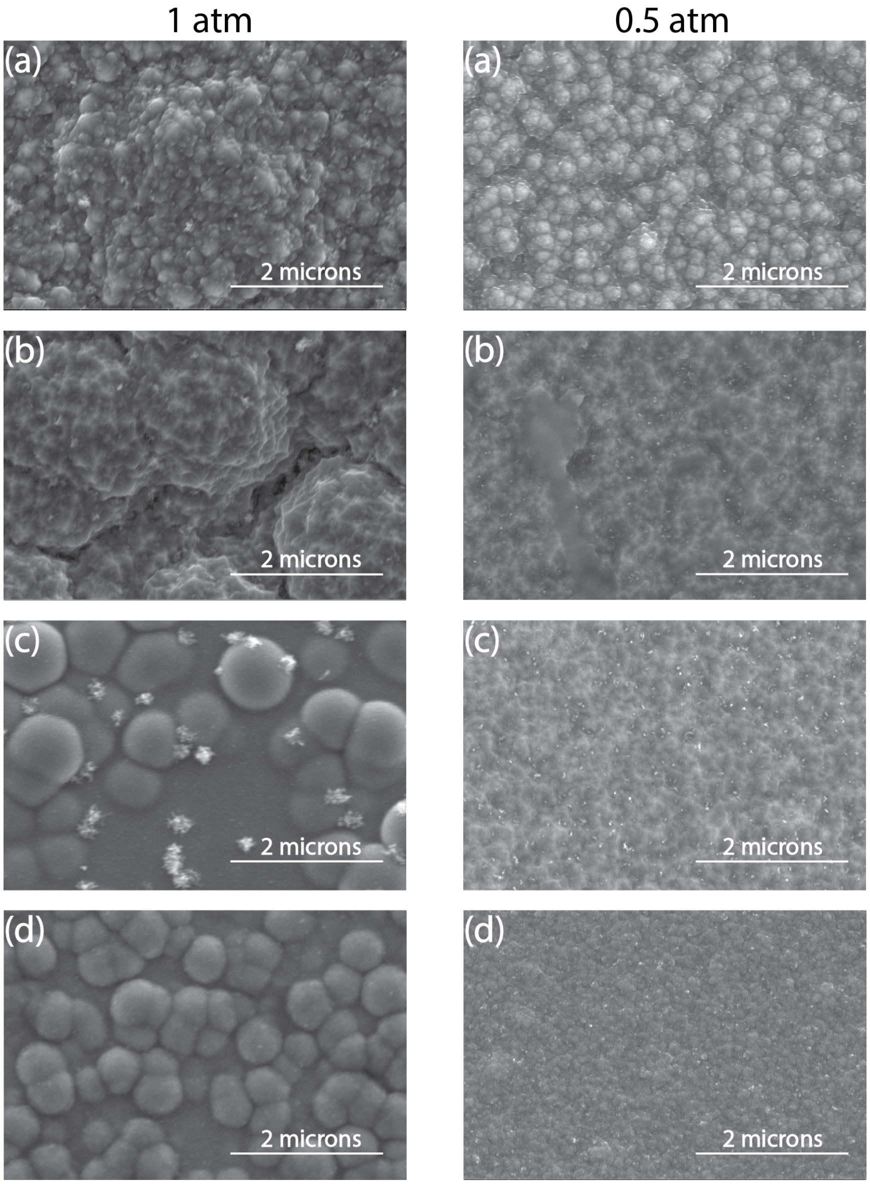

Figure 5.8: SEM images of SiC films grown on quartz substrates at 1250 K for two different pressures: p = 1 and 0.5 atm, and with four different H_2-to-MTS ratios: a) $\alpha = 1$, b) $\alpha = 5$, c) $\alpha = 10$, and d) $\alpha = 15$, and $Q_{total} = 276$ SCCM.

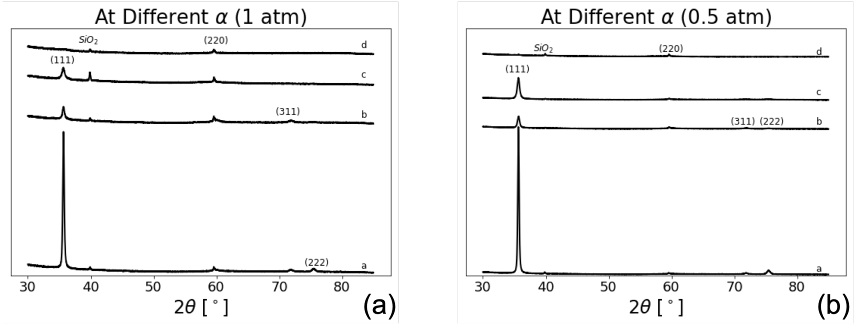

Figure 5.9: XRD of SiC films grown at 1250 K, residence time = 500 ms, and two different pressures: p = 1 and 0.5 atm, with four different α values: a) 1, b) 5, c) 10, and d) 15.

unique to the mass transfer controlled regime, whereas the particle-like structures on the sample at 0.5 atm is characteristic to the reaction kinetics controlled regime.

Preferred orientation of SiC deposits

XRD analysis was performed to determine the crystalline phase and preferred orientation of the SiC films as a function of α. As seen in Fig. 5.9, the diffraction planes of β-SiC, i.e., (111), (220), (311) and (222) planes, were obtained in the films deposited at the two total pressures: 1 and 0.5 atm. Again, a 2θ peak at 39.89° was detected from the contribution of the quartz substrate. Preferred orientation was estimated by texture coefficient (TC_{hkl}) using the Harris method (see Eq. 5.1). The variation of the texture coefficient of (111) and (220) planes with α is shown in Fig. 5.10 for the two total pressures: 1 and 0.5 atm. At 1 atm, the (220) plane is the preferred orientation of the SiC deposits at α values (α = 5-15), whereas the preferred orientation is (111) plane at the lowest value of α ($\alpha = 1$). The change in the preferred orientation from (220) to (111) plane as α value decreases coincides with a change in the morphology of the samples shown in Figure 5.8-1 atm (d) to (a). The appearance of angular nanostructures signifies an improvement in crystallinity of the SiC deposits. This relationship between the morphology and the preferred orientation is also observed in Section 5.3.1.

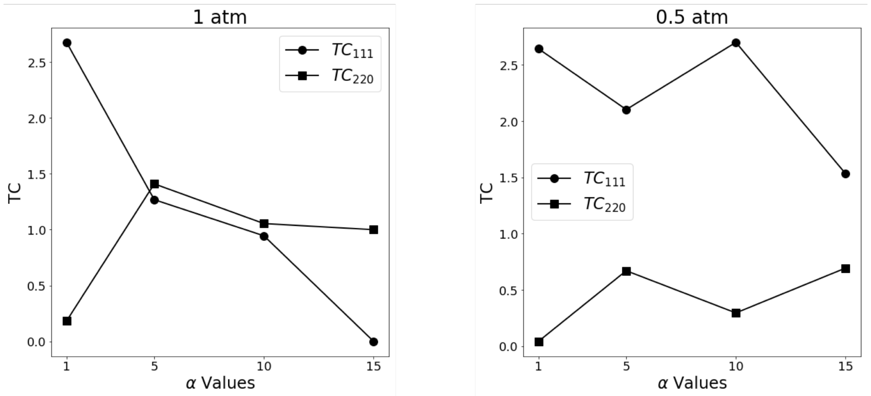

Figure 5.10: Texture coefficients as a function of α values, at 1250 K and $Q_{total} =$ 276 SCCM.

On the other hand, at 0.5 atm, the preferred orientation of all the samples is (111) plane. This result is consistent with that shown in Section 5.3.1. At low pressure condition, SiC crystals deposit on the substrate surface from surface reactions of small gaseous precursors, resulting in a high level of crystallinity of the SiC deposits.

5.3.3 Effects of total flow rates

SiC mass growth rate

The influence of total flow rates was studied at a fixed temperature and at two different total pressures. Fig. 5.11 shows the mass growth rate of SiC at four different total flow rates: 192, 276, 456 and 709 sccm. The operation conditions were set at temperature of 1300 K, initial gas composition (α) of 10, and at two different total pressures: 1 (●) and 0.5 atm (■). Similar to the results in Sections 5.3.1 and 5.3.2, higher SiC mass growth rate at 1 atm is attributed to the higher MTS decomposition rate at this pressure condition than at 0.5 atm. Moreover, variation in total flow rate influences the SiC mass growth rate different at the two pressure conditions. At 1 atm, the mass growth rate increases as the total flow rate increases from 192 to 276 sccm, but it starts to decrease beyond 276 SCCM. In contrast, the mass growth rate of SiC at 0.5 atm increases with increasing total flow rate. This difference in mass growth rate as a

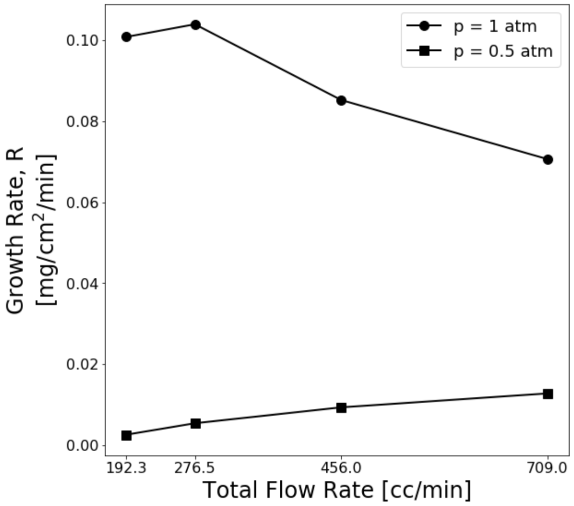

Figure 5.11: Growth rate variations with total gas flow rates: 192, 276, 456, and 709 SCCM, at 1300 K and $\alpha = 10$ for two total pressures (1 atm and 0.5 atm).

function of total flow rate can be explained by a balance between reactant depletion effect and residence time, and between diffusion time and residence time.

A number of studies has reported a depletion of reactant in the direction of gas flow in horizontal hot-walled reactors [144, 154]. Horizontal hot-walled reactors like the PMFTR in this study consist of a short temperature ramp-up near the entrance followed by a relatively long isothermal region. Thus, as the source gas (MTS) enters the reactor, it starts to decompose near the reactor entrance and form SiC precursors. A portion of these precursors will react on the inner wall surface of the reactor to form SiC. Less and less precursors, as a result, are available further downstream of the reactor. The depletion effect tends to increase with increasing temperature and total pressure [156]. However, the depletion effect has been reported to decrease with decreasing residence time (or increasing gas velocity/total flow rate) [157]. At 1 atm, the SiC mass growth rate increases as the total flow rate increases from 192 to 276 sccm. This increase in mass growth rate can indeed be attributed to the mitigation of the depletion effect by increasing the total flow rate (or reducing the residence time). However, as the total flow rate continues to increase, the SiC mass growth rate at 1 atm starts to decrease. This decrease in mass growth rate can be explained by the balance between residence time and diffusion time of the SiC precursors. At this operation condition: T = 1300 K, $\alpha = 10$ and p = 1 atm, the SiC deposition is controlled by mass transfer or diffusion of SiC precursors across the boundary layer to the substrate surface (see Fig. 5.3). As the total flow rate increases, the residence time of the SiC precursors over the substrate becomes shorter. Therefore, it is suspected that the decrease in mass growth rate with increasing total flow rate is because the SiC precursors do not have enough time to reach the substrate surface to react and form SiC before being blown away by the upcoming gas.

On the other hand, the SiC mass growth rate increases with increasing total flow rate at the total pressure of 0.5 atm. At this condition: T = 1300 K, $\alpha = 10$ and p = 0.5 atm, SiC deposition is controlled by reaction kinetics, especially surface reaction kinetics. In addition, the depletion effect at lower pressure (0.5 atm) is much less than at high pressure (1 atm) [156], which allows for higher concentration of SiC precursors present at the location of the substrate location. Therefore, even though increasing total flow rates reduces the residence time of SiC precursors over the substrate, these precursors still have enough time to reach the substrate surface because greater concentration gradient facilitate their diffusion across the boundary layer.

Morphology of SiC deposits

The effect of total flow rate on the morphology of SiC deposit was investigated at two different pressures. Fig. 5.12 shows the morphology of SiC deposited at four different total flow rates: 192, 276, 456 and 709 sccm, and at two different total pressures: 1 (left column) and 0.5 atm (right column). As stated earlier, the operation conditions here were set at a temperature of 1300 K and an initial gas composition (α) of 10. Thus, the morphology of these SiC samples resemble that of the SiC samples deposited at 1300 K shown in Fig. 5.4 (c). At 1 atm (left column of Fig. 5.12), the SiC samples show a morphology consisting of angular nanostructures with an occasional presence of hemispherical clusters of these nanostructures. The effect of total flow rate on the SiC morphology can be observed with the variation of size of the nanostructures with changing total flow rate. On the left column of Fig. 5.12 (1 atm), the size of the nanostructures remains relatively constant at 192 and 276 sccm total flow rates, but it starts to decrease beyond 276 sccm. This variation in size the of nanostructures is consistent with the mass growth rate data at 1 atm shown in Fig. 5.11.

The morphology of SiC samples deposited at 0.5 atm shows a correspondence to mass growth data shown in Fig. 5.11. The nanostructures on the samples increase in size with increasing total flow rate because of higher SiC precursor concentration generated by the mitigated reactant depletion effect with increasing flow residence time and lowering total pressure condition.

Preferred orientation of SiC deposits

At a deposition temperature of 1300 K, the results of X-ray diffraction (XRD) analysis as a function of total flow rate are shown in Fig. 5.13 for two different total pressures: 1 and 0.5 atm. All the XRD peaks are of (111), (220), (311) and (222) planes, which are identical to SiC with face centered cubic structure. Thus, SiC deposits at these conditions are polycrystalline β-SiC. In addition, there is one peak at 39.9°, originating from the quartz substrate. The degree of preferred orientation of a certain (hkl) plane can be estimated by the texture coefficient (TC_{hkl}) using the Harris method (see Eq. 5.1). The results of texture coefficient (TC) of (111) and (220) planes as a function of total flow rate are summarized in Fig. 5.14 for the two different pressures. At both total pressures, the preferred orientation of SiC deposit is (111) plane for all the total flow rates. The XRD results are consistent with those observed in Section 5.3.1. As stated in Section 5.3.1, SiC crystals deposit on the substrate surface from surface reactions of small gaseous precursors at these conditions, resulting in a high

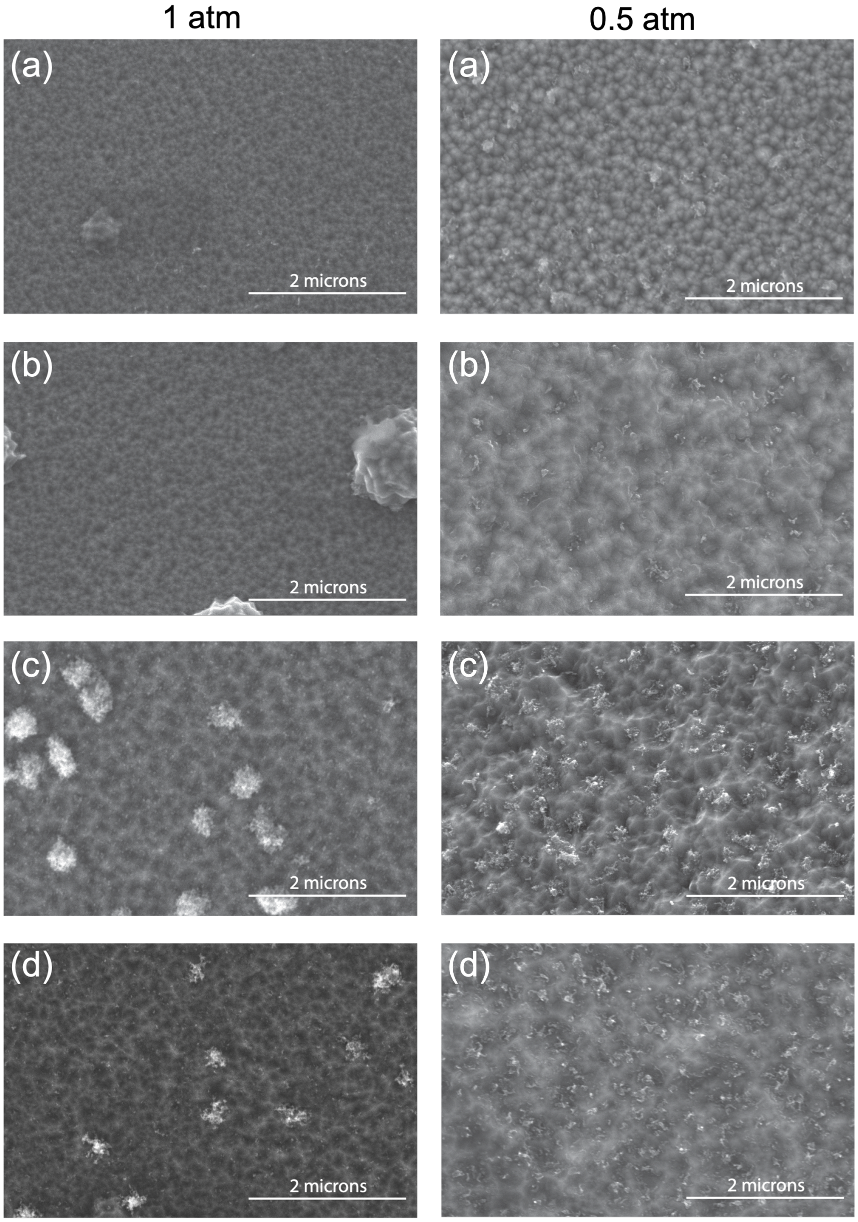

Figure 5.12: SEM images of SiC films grown on quartz substrates at 1300 K and $\alpha = 10$ for two different pressures: p = 1 and 0.5 atm, and with four different total flow rates: a) 192, b) 276, c) 456, and d) 709 SCCM.

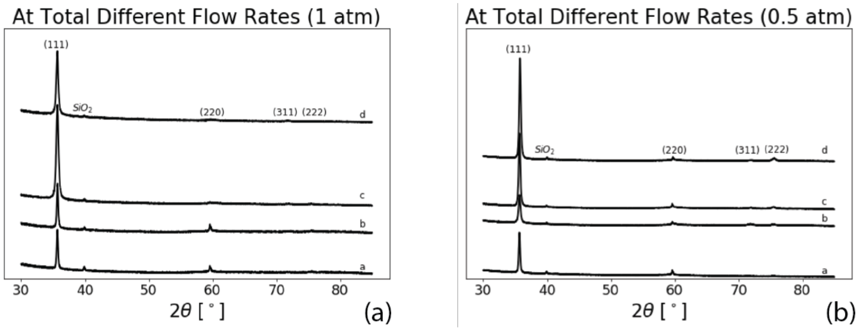

Figure 5.13: XRD of SiC films grown at 1300 K, $\alpha = 10$, and two different pressures: p = 1 and 0.5 atm, with four different total flow rates: a) 192, b) 276, c) 456, and d) 709 SCCM.

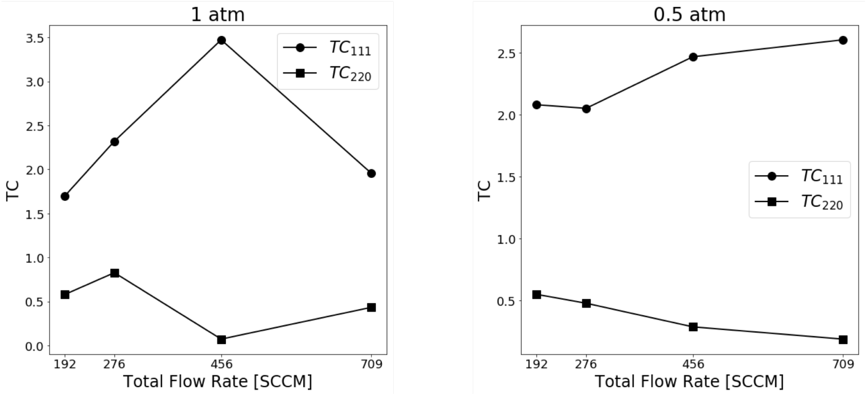

Figure 5.14: Texture coefficients as a function of total flow rates, at 1300 K and $\alpha = 10$.

level of crystallinity portrayed by the dominant value of (111) TC seen in Fig. 5.14.

5.4 Summary

In this study, the effects of process parameters: deposition temperature, total flow rate, and initial input gas ratio, on SiC deposition was investigated at two different total pressures. SiC deposition from MTS and H_2 was carried out in a horizontal hot-walled reactor. All the process parameters differently influence SiC deposition: mass growth rate, morphology, and preferred orientation, depending on the total pressure. At 1 atm total pressure, changing deposition temperature or initial gas ratio can transition the deposition from being controlled by reaction kinetics to being controlled by mass transfer. However, the SiC depostion process is only controlled by reaction kinetics at lower pressure. Furthermore, the effect of reactant depletion is also observed with a variation of total flow rate. The results show that reactant depletion affects SiC deposition at 1 atm total pressure more than it does at 0.5 atm total pressure. Finally, difference in morphology and preferred orientation of SiC deposits is also noted for the two total pressures.

Chapter 6

Experimental Investigation of Species Evolution During Pyrolysis of Methyltrichlorosilane/Hydrogen Mixtures in a Premixed Microflow Tube Reactor

6.1 Introduction

Silicon carbide (SiC) ceramics reinforced with SiC fibers (SiC_m/SiC_f composites) have become popular material because of their excellent high temperature properties, including high strength, modulus of elasticity, corrosion resistance, and chemical stability [137, 138]. SiC_m/SiC_f composites have found applications in gas turbines and structural components in aerospace industry, nuclear reactors and heat engines. Chemical vapor infiltration (CVI) is often used to produce SiC_m/SiC_f composites. CVI is a process in which a porous structure (preform) is surrounded by a reactive gas mixture that decomposes under thermal activation and fills the preform with solid deposits. The advantage of CVI is its ability to manufacture complex net- or near-net-shape components at relatively low temperature, thus avoiding potential damage to the preform structure. Typical gas mixtures used in CVI are: 1) silanes and hydrocarbons (e.g., $SiH_4 + C_3H_8$) and 2) methyltrichlorosilane (MTS: CH_3SiCl_3) in hydrogen (H_2) carrier gas. Of the two mixtures, the MTS/H_2 mixture is a better system for two reasons: 1) MTS has the same Si to C ratio as SiC, and 2) the byproduct HCl has been shown to suppress deposition of pure Si in favor of SiC [158].

In order for CVI to be used on a mass scale, it is necessary to improve deposition rate without compromising the uniformity of film formation. CVI of SiC using the MTS/H_2 system involves two steps: 1) the unimolecular decomposition of MTS in the gas phase, which produces C- and Si-containing precursors, and 2) heterogeneous reactions of the precursors on the surface of the substrate to form SiC [159]. In the second step, adsorption of gaseous species on the surface can either limit deposition by blocking the available free sites, or contribute to deposition. Therefore, the composition of the gas phase must be known to predict the actual deposition rate.

Furthermore, deeper understanding of the gas phase chemistry will help optimize the process conditions at reasonable cost with Computer Aided Reaction/Reactor Design (CARD) methodology. The CARD approach consists of three steps: 1) construction of fundamental kinetics models for both the gas phase and surface chemistry, 2) optimization and simplification of these models via comparison with experimental results and sensitivity analysis, and 3) implementation of CFD coupled with the constructed chemical models to determine the optimal process conditions for SiC deposition [42]. Over the past few years, considerable progress has been made in understanding the chemical mechanism of SiC deposition from MTS, and several kinetic models have been proposed. Loumagne et al. [160] and Lu et al. [161] correlated the deposition rate of SiC matrix to the overall decomposition of MTS in H_2 carrier gas. However, the authors found that the reaction order of SiC deposition with respect to MTS concentration varied with temperature and pressure. Furthermore, they reported contradictory results on the dependence of SiC deposition rate on the initial H_2 concentration. This disagreement between kinetic data suggests that MTS is not the primary precursor for SiC deposition, but the reaction mechanism involves several immediate steps. Based on this observation, a number of research groups have proposed detailed chemical models for SiC deposition from MTS. Papasouliotis and Sotirchos [162], Jong and Mayyappan [163], and Ge et al. [164] have all constructed models involving several tens of chemical species and reactions. Their common approach to the construction of these models is to 1) search for important species according to the evaluation of thermodynamic equilibrium of the Si-C-Cl-H system, 2) select reasonable reactions among those reported in the literature, and 3) derive reaction rate constants for the selected reactions through experiments and/or theoretical calculation. However, before these models can be used with the CARD approach, their validity must be confirmed experimentally.

Experimental investigation of the gas-phase composition during pyrolysis of MTS is necessary to validate existing detailed models of SiC deposition from MTS. Several studies [150, 165–169] have looked at the effect of either temperature, total pressure, total flow rate (residence time), initial MTS-H_2 composition, or the aspect ratios of the reactor on deposition rate. A wide range of diagnostic techniques was used, including gas chromatography (GC), Fourier transform infrared spectroscopy (FTIR), and coherent anti-Stokes Raman spectroscopy (CARS). However, most experimental papers often failed to provide complete information regarding the reactor dimensions, process parameters and other details needed to validate available chemical models with their experimental data.

In order to supplement the missing data, an MTS pyrolysis investigation was conducted in the premixed microflow tube reactor (PMFTR) at typical conditions of

SiC deposition. Specifically, the effects of temperature, residence time, and initial MTS-H_2 composition at normal atmospheric pressure are described. Gas chromatography (GC) is used to measure concentrations of the reactant MTS and a number of carbon- and silicon-containing intermediate species. Experimental uncertainty in concentration measurements is also presented along with the data. The objective of this study is to provide experimental speciation data for the validation of available detailed kinetics models. Therefore, a comparison between experimental data and predictions by the model of Ge et al. is presented as an example [164].

6.2 Experimental procedure

All experiments were performed in a hot-walled flow reactor made of alumina (4.8 mm inner diameter and 0.52 m length). A schematics of the flow reactor, chemical reagent delivery system and diagnostic tool is shown in Fig. 6.1. The gas mixture consisted of MTS (99%, from Sigma Aldrich), H_2 (99.999%, from Praxair), and argon (Ar) (99.999%, from Praxair). The concentration of Ar diluent gas was always kept at 95% by volume. MTS vapor was delivered to the reactor by bubbling a secondary Ar flow (3-17 SCCM) through a liquid MTS bath. The temperature and pressure of the MTS bath were kept at 25 °C and 1 atm, respectively. The gas delivery line before the reactor was heated to 90 °C to prevent condensation of MTS vapor. The MTS decomposition products were fed to the GC from the reactor exit for quantification. The feed line was also kept at 90 °C to prevent condensation of the products. The GC (Shimadzu 2014) was equipped with a capillary RTX-200 column (Restek) and a flame ionization detector (FID).

The experimental conditions were selected to illustrate the effects of temperature, residence time, and initial H_2-MTS composition ($\alpha = [H_2]/[MTS]$) on the gas phase chemistry during pyrolysis of MTS. The temperature was varied from 1100 to 1350

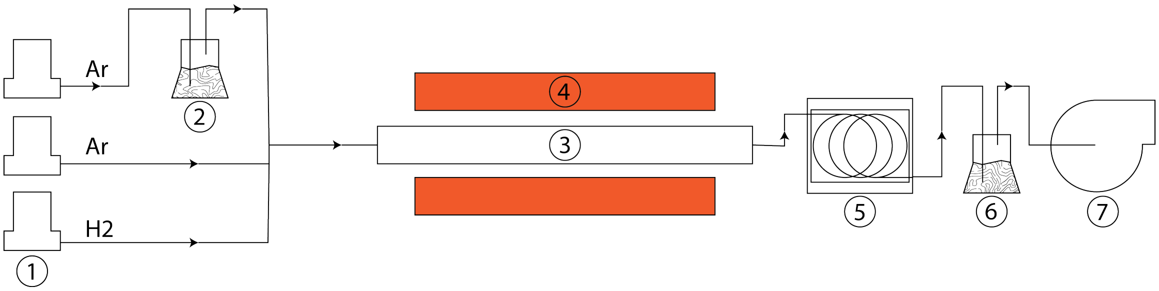

Figure 6.1: A schematics of the experimental apparatus: 1) flow controllers, 2) an MTS bath, 3) the alumina reactor, 4) modular furnace, 5) GC, 6) water trap, and 7) mechanical pump

K with a 50 K increment, while nominal residence time and α were kept at 500 ms and 10, respectively. Subsequently, total flow rate was varied so that the nominal residence time varied from 200 to 700 ms at a temperature of 1250 K, with constant α value of 10. Finally, α was varied such that α ranged from 3 to 14 at constant temperature of 1200 K and nominal residence time of 500 ms. Four stable species were detected and quantify, including the reactant MTS and three decomposition products: methane (CH_4), trichlorosilane ($SiHCl_3$), and silicon tetrachloride ($SiCl_4$).

Experimental uncertainty of speciation data was also analyzed. There were two main sources of the uncertainty: 1) calibration of GC species concentration, and 2) random variation of measured concentration during experimental runs. Experimental data was compared to predictions by the kinetics model of Ge et al. [164]. The model predictions were obtained by implementing a plug flow reactor (PFR) code with the model in Cantera software [109]. The reactor dimensions and measured wall temperature were imported to the PFR code in order to obtain an accurate simulation of the system. The measured wall temperature as a function of reactor length is illustrated in Fig. 6.2 for different set temperatures.

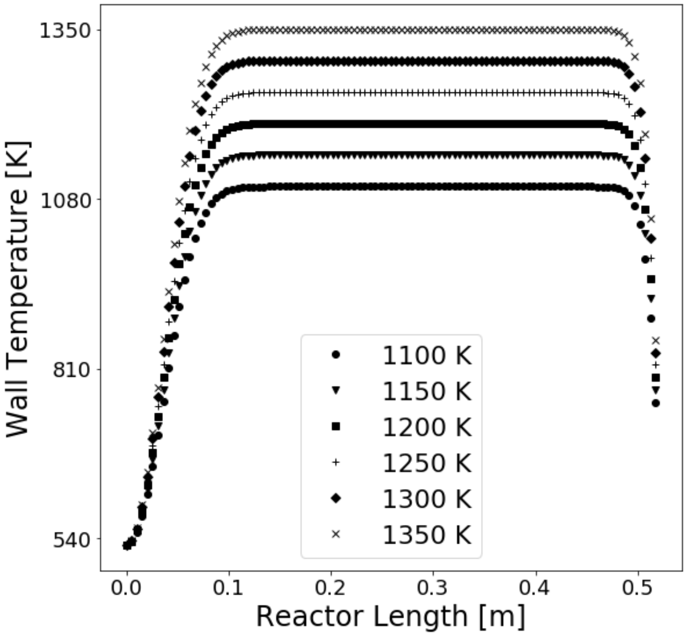

Figure 6.2: Measured reactor wall temperature profiles as a function of reactor length at different set temperatures: 1100, 1150, 1200, 1250, 1300, and 1350 K.

6.3 Results

This section presents species concentrations of MTS, methane (CH_4), trichlorosilane ($SiHCl_3$), and silicon tetrachloride ($SiCl_4$) at three sets of experimental condition. The importance of this type of experimental data can be illustrated with a plot of primary reaction pathways during MTS decomposition. Fig. 6.3 shows reaction pathways of C- and Si-containing intermediate species formed from MTS decomposition at T = 1250, norminal residence time = 500 ms, and initial H_2-to-MTS ratio (α) = 10. The reaction pathways were extracted from the model of Ge et al. [164]. The four species detected in this study are highlighted in Fig. 6.3. The detection of these species can either confirm the existing reaction pathways in chemical kinetics models, or suggest that additional reaction pathways are needed for an accurate description of gas phase chemistry during MTS decomposition.

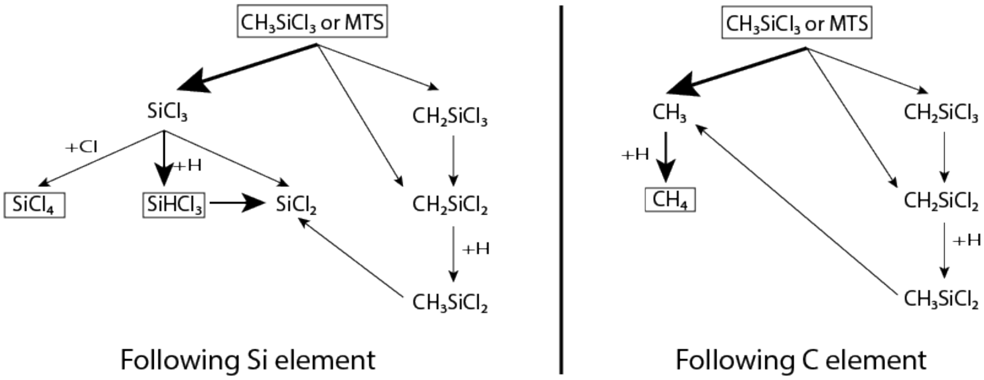

Figure 6.3: Reaction pathways of C- and Si-containing intermediate species during MTS decomposition at T = 1250K, t = 50 ms, and $\alpha = 10$.

Table 6.1: Experimentally measured species concentrations of MTS, CH_4, $SiHCl_3$, and $SiCl_4$ at six temperatures. Initial gas composition: $X_{MTS} = 0.00455$, $X_{H2} = 0.04545$, and $X_{Ar} = 0.95$.

T [K]	MTS	CH_4	$SiCl_4$	$SiHCl_3$
1100	0.0045	0.00008	0	0
1150	0.0039	0.00056	0	0
1200	0.0022	0.0019	0	0.00098
1250	0.00059	0.0030	0.00082	0.0017
1300	0.00026	0.0033	0.0012	0.0028
1350	0.00025	0.0031	0.00021	0.0035

6.3.1 The effect of temperature

The effect of temperature on concentrations of the four detected species is shown in Table 6.1. The measured data are also plotted against predictions by the Ge et al. model [164] as a function of temperature in Fig. 6.4.

MTS: According to experimental results, MTS started to decompose at 1150 K. The decomposition rate of MTS increased with increasing temperature such that only 5% of the initial concentration remained at 1350 K. In contrast, the predictions by the Ge et al. model [164] showed that MTS started to decompose at a higher temperature (around 1200 K). The model also predicted an increase in MTS decomposition with increasing temperature, causing nearly all MTS to decompose around 1450 K.

CH_4: Methane (CH_4) was the only carbon containing decomposition product

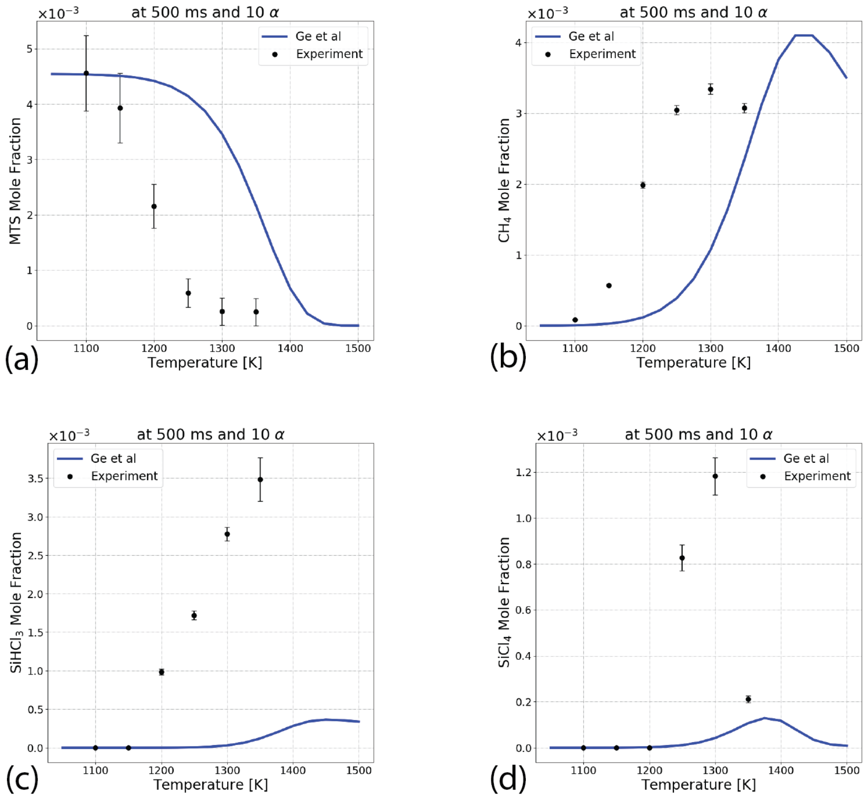

Figure 6.4: Measured and predicted concentrations of four species: MTS, CH_4, $SiHCl_3$, and $SiCl_4$ vs. temperature, at nominal residence time of 500 ms and α of 10.

detected. The experimental results show that the production of CH_4 started at 1100 K. Its concentration continued to increase as temperature rose, and peaked at 1300 K. After 1300 K, CH_4 concentration started to decrease. On the other hand, the predictions by the Ge et al. model [164] showed the onset of CH_4 production around 1250 K. However, the predicted values followed a similar trend to that of experimental data.

$SiHCl_3$: One of the two Si-containing decomposition products is trichlorosilane ($SiHCl_3$). Experimentally, production of $SiHCl_3$ began at 1200 K and increased with temperature. On the other hand, the predictions by the Ge et al. model [164] showed the appearance of $SiHCl_3$ at a higher temperature (around 1275 K). The model predicted much lower $SiHCl_3$ concentration than the experimental data. In addition, the model showed that $SiHCl_3$ concentration began to plateau around 1450 K, while the measured $SiHCl_3$ concentration kept increasing with increasing temperature.

$SiCl_4$: The second Si-containing product detected is silicon tetrachloride ($SiCl_4$). The experimental data shows production of $SiCl_4$ began around 1250 K and peaked at 1300 K. Although the predictions by the model also showed the beginning of $SiCl_4$ production around 1250 K, its peak value was at a higher temperature (around 1475 K). Moreover, the model predicted a much lower concentration of $SiCl_4$ than the measured data.

6.3.2 The effect of residence time

Table 6.2 contains the measured concentrations of the four species at different nominal residence times at 1250 K and $\alpha = 10$. The measured data are also plotted against predictions by the Ge et al. model [164] as a function of nominal residence time in Fig. 6.5.

MTS: The experimental results show that more than 50% of MTS already decomposed at 200 ms. Measured MTS concentration decreased as nominal residence

Table 6.2: Experimentally measured species concentrations of MTS, CH_4, $SiHCl_3$, and $SiCl_4$ as a function of nominal residence time at 1250 K and $\alpha = 10$. Initial gas composition: $X_{MTS} = 0.00455$, $X_{H2} = 0.04545$, and $X_{Ar} = 0.95$.

Time [ms]	MTS	CH_4	$SiCl_4$	$SiHCl_3$
200	0.0020	0.00216	0	0.001
300	0.0012	0.00270	0.00032	0.0015
400	0.00083	0.00297	0.00049	0.0019
500	0.00059	0.00305	0.00082	0.0017
600	0.00047	0.00300	0.00087	0.0016
700	0.00039	0.00298	0.00080	0.0015

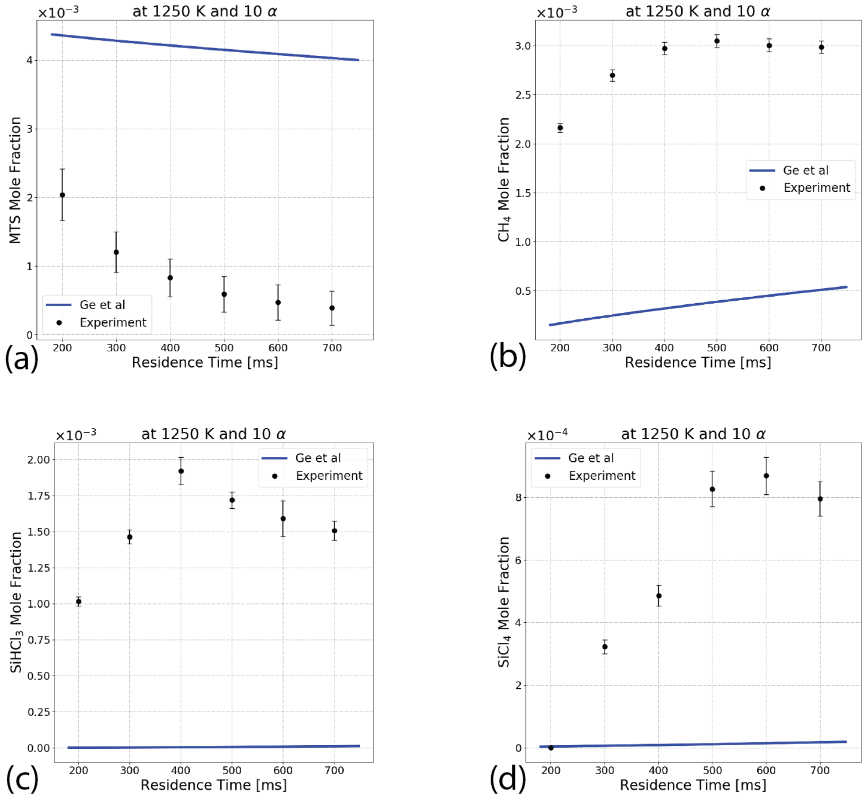

Figure 6.5: Measured and predicted concentrations of four species: MTS, CH_4, $SiHCl_3$, and $SiCl_4$ at different nominal residence times: 200, 300, 400, 500, 600, and 700 ms, at 1250 K and $\alpha = 10$.

time increases. In contrast, the predictions by the Ge et al. model [164] showed only minimal decomposition of MTS at 1250 K over the considered nominal residence times.

CH_4: At 200 ms, the experimental data shows significant CH_4 production. Its concentration grew to its maximum value at 500 ms and gradually reduced afterwards. However, the predictions by the model showed negligible production of CH_4, which is consistent with the minimal consumption of MTS predicted by the model.

$SiHCl_3$: The measured $SiHCl_3$ concentration starts at 200 ms and increases to its highest value at 400 ms and then decreases. On the other hand, the model shows zero production of $SiHCl_3$ over the considered nominal residence time at 1250 K.

$SiCl_4$: Experimental results show positive production of $SiCl_4$, whereas the model predicts zero production of $SiCl_4$. The measured data shows that $SiCl_4$ starts to appear at 300 ms. Its concentration increases with increasing nominal residence time, and reaches its peak at 600 ms and then decreases afterwards.

6.3.3 The effect of H_2-to-MTS ratio (α)

The effect of varying α on the species evolution was investigated at a fixed temperature of 1200 K and a fixed nominal residence time of 500 ms. Three species: MTS, CH_4, and $SiHCl_3$, are detected. $SiCl_4$ was not produced at this temperature. Table 6.3 contains the measured concentrations of the species at different α values.

The measured and predicted mole fractions of three species: MTS, CH_4, and $SiHCl_3$, are presented as a function of α in Fig. 6.6. Both the experimental data and predictions by the model showed decreasing MTS concentrations with increasing α (or decreasing input MTS concentration, $X_{MTS.0}$), although the predicted values were lower than the experimental data. Similarly, measured CH_4 and $SiHCl_3$ concentrations also decreased with increasing α. However, the CH_4 predictions by the model showed a similar trend to the experimental data only at small α values (α = 3-6),

Table 6.3: Experimentally measured species concentrations of MTS, CH_4, and $SiHCl_3$ as a function of α at a temperature of 1200 K and a nominal residence time of 500 ms. Concentration of Ar is kept constant at 95% by volume.

α	MTS	CH_4	$SiHCl_3$	$SiCl_4$
3	0.0073	0.0061	0.0031	0
5	0.0049	0.0042	0.0023	0
7	0.0036	0.0032	0.0017	0
10	0.0023	0.0019	0.0010	0
12	0.0019	0.0015	0.0006	0
14	0.0016	0.0012	0.0004	0

but zero CH_4 production at higher α values (α = 6-15). On the other hand, while a significant amount of $SiHCl_3$ was produced experimentally, the model predicted zero $SiHCl_3$ production over the considered α values.

6.4 Model optimization

Experimental data and predictions by the Ge et al. model [164] showed vastly different trends in the evolution of MTS, CH_4, $SiHCl_3$, and $SiCl_4$ at different experimental conditions. The model not only required higher temperature for MTS pyrolysis to start, but also predicted lower production of the intermediate species. This disagreement with the experimental data indicated that the reaction rates used in the model were slower than those shown by the experiment. Thus, the experimental data was used as a benchmark to optimize the model reaction rates. The optimization process involved two steps: 1) selecting important reactions through sensitivity and reaction pathway analyses at all experimental conditions, and 2) optimizing the reaction rates of the selected reactions in order to minimize the difference between measured and predicted species concentrations.

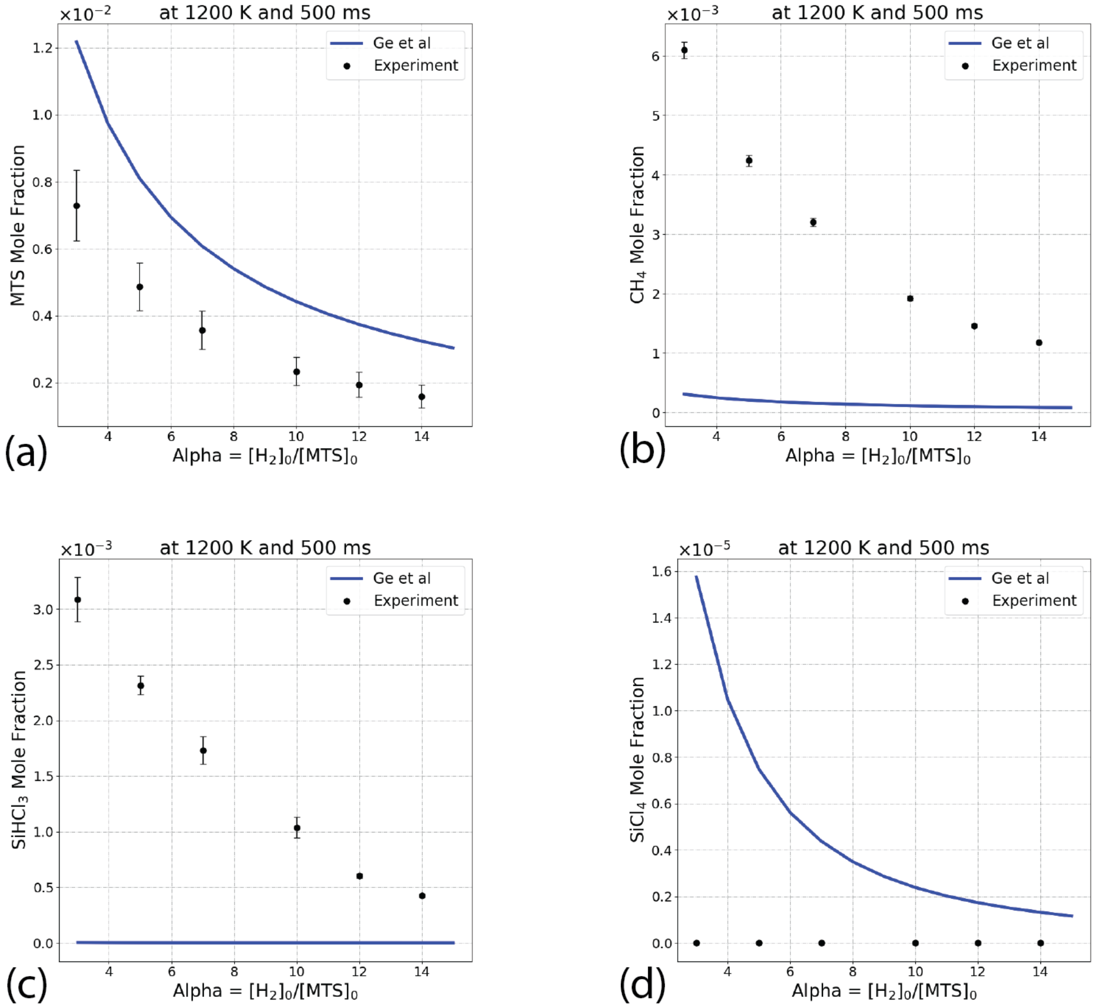

Figure 6.6: Measured and predicted concentrations of four species: MTS, CH_4, and $SiHCl_3$ at different α values: 3, 5, 7, 10, 12, 14, at a temperature of 1200 K and a nominal residence time of 500 ms.

Table 6.4: A list of the most sensitive reactions to the evolution of four species: MTS, CH_4, $SiHCl_3$, and $SiCl_4$, as well as their original values for pre-exponential factor (A) and activation energy (E_a) at all experimental conditions. Note: the unit of pre-exponential factor (A) is s^{-1} or m^3 $kmol^{-1}$ s^{-1} for uni- or bi-molecular reactions, respectively.

Index	Reaction	A	E_a [J/kmol]
R1	$CH_3 + H_2 \leftrightarrow CH_4 + H$	5.55e3	4.70e7
R2	$H_2 + SiCl_3 \leftrightarrow H + SiHCl_3$	1.35e2	5.95e7
R3	$HCl + SiCl_3 \leftrightarrow H + SiCl_4$	1.36e-1	5.78e7
R4	$SiHCl_3 \leftrightarrow HCl + SiCl_2$	7.30e12	2.83e8
R5	$CH_4 + SiCl_3 \leftrightarrow CH_3 + SiHCl_3$	1.65e-2	7.05e7
R6	$CH_3SiCl_3 + SiCl_3 \leftrightarrow CH_3SiCl_2 + SiCl_4$	1.18e1	7.42e7
R7	$CH_3SiCl_2 \leftrightarrow CH_3 + SiCl_2$	1.87e14	1.90e8
R8	$CH_3SiCl_3 \leftrightarrow CH_3 + SiCl_3$	2.63e15	3.86e8

6.4.1 Selection of the most important reactions

The first step in the optimization process was to select important reactions to the evolution of the four species: MTS, CH_4, $SiHCl_3$, and $SiCl_4$. This step was done by implementing sensitivity analysis of the species with respect to all the reactions in the Ge et al. model [164] (see Fig.6.12), as well as reaction pathway analysis (see Fig. 6.3). Table 6.4 contains all the selected reactions in order of their appearance in the model.

6.4.2 Reaction rate optimization

The reaction rates of eight important reactions in Table 6.4, i.e., pre-exponential factors (A) and activation energies (E_a), were varied to minimize the difference between model predictions and experimental data. The difference between model predictions and experimental data was expressed as the sum of squared errors as follows

$$Error = \sum_{i=1}^{4}\sum_{j=1}^{4}(X_{exp} - X_{model}(k))_{ij}^2$$

where i and j are number of experimental conditions and detected species, respectively, X_{exp} and X_{model} are measured and predicted species mole fractions, and k are reaction rate coefficients of the eight reactions in Table 6.4. The result of this optimization step is summarized in Table 6.5.

Table 6.5: A list of factors by which the rate coefficients (i.e., A and E_a) of the eight reactions are modified in order to minimize the difference between the experimental data and predictions by the Ge et al. model [164].

Index	Reaction	% A	% E_a
R1	$CH_3 + H_2 \leftrightarrow CH_4 + H$	14.4	-9.3
R2	$H_2 + SiCl_3 \leftrightarrow H + SiHCl_3$	-3.8	-15.4
R3	$HCl + SiCl_3 \leftrightarrow H + SiCl_4$	17	6.5
R4	$SiHCl_3 \leftrightarrow HCl + SiCl_2$	20.2	-40.1
R5	$CH_4 + SiCl_3 \leftrightarrow CH_3 + SiHCl_3$	7.9	-21.2
R6	$CH_3SiCl_3 + SiCl_3 \leftrightarrow CH_3SiCl_2 + SiCl_4$	28.1	10
R7	$CH_3SiCl_2 \leftrightarrow CH_3 + SiCl_2$	-1.7	-16.6
R8	$CH_3SiCl_3 \leftrightarrow CH_3 + SiCl_3$	4.8	-14.9

6.4.3 Predictions by the optimized model

Comparison between experimental data and predictions by the optimized Ge et al. model is presented here for each species at different operating conditions: 1) varying temperature, 2) varying residence time at two temperatures: 1150 K and 1250 K, and 3) varying initial H_2-MTS composition (α). In addition, a brief discussion of the contribution of eight reactions in Table 6.4 to the evolution of the four species is also included.

MTS: A comparison between experimental data and the predictions for MTS is shown in Fig. 6.7. Relative to the original Ge et al. model [164], the optimized model showed much higher MTS decomposition rate, which reasonably matched the experimental data. Among the eight modified reactions, reactions R6 and R8 in Table

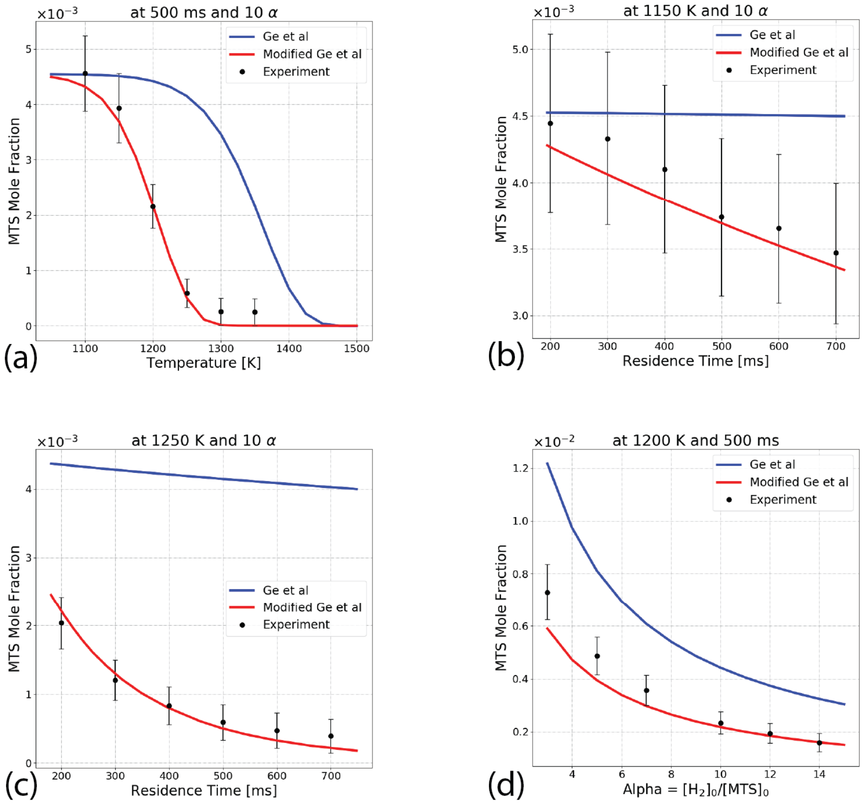

Figure 6.7: Comparison between experimental data and predictions by models for MTS concentration at four different operation conditions: 1) varying temperature, 2) varying residence time at 1150 K, 3) varying residence time at 1250 K, and 4) varying α at 1200 K.

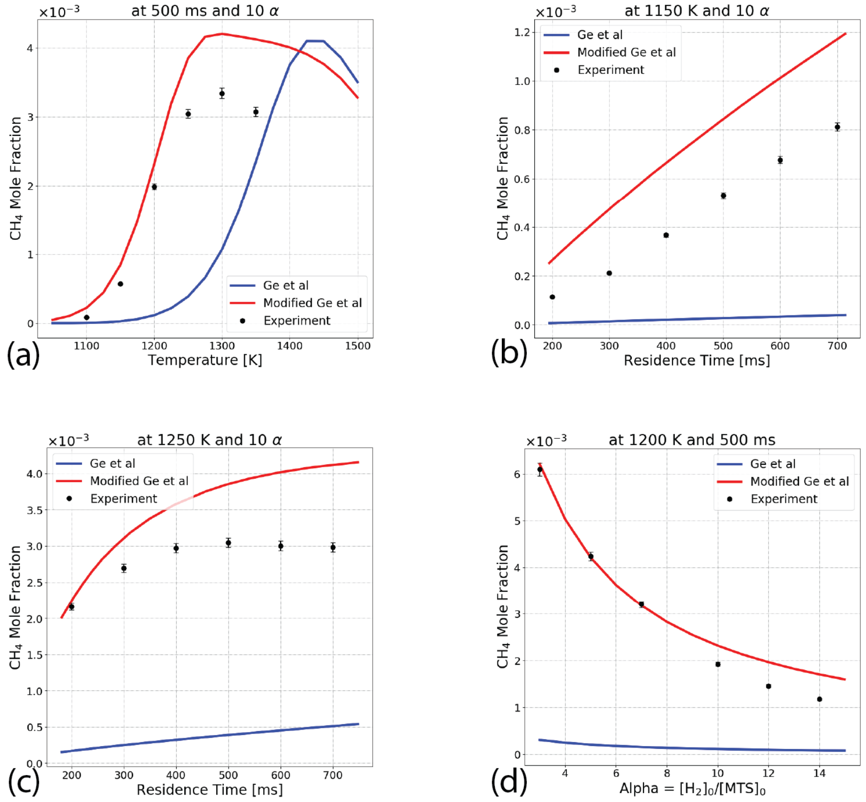

Figure 6.8: Comparison between experimental data and predictions by models for CH_4 concentration at four different operation conditions: 1) varying temperature, 2) varying residence time at 1150 K, 3) varying residence time at 1250 K, and 4) varying α at 1200 K.

6.4 directly contributed the consumption of MTS:

$$CH_3SiCl_3 + SiCl_3 \leftrightarrow CH_3SiCl_2 + SiCl_4$$

and

$$CH_3SiCl_3 \leftrightarrow CH_3 + SiCl_3$$

Thus, it is possible that these two reactions played a more important role in the MTS consumption than expected by the original Ge et al. model [164]. It should be noted that the reaction rates of the reactions involving $CH_3SiCl_2\bullet$, $CH_3\bullet$, and $SiCl_3\bullet$ (reactions R1, R2, R3, R5, and R7) were also improved, further contributing to the consumption of MTS by preventing the re-combination of these species back to MTS.

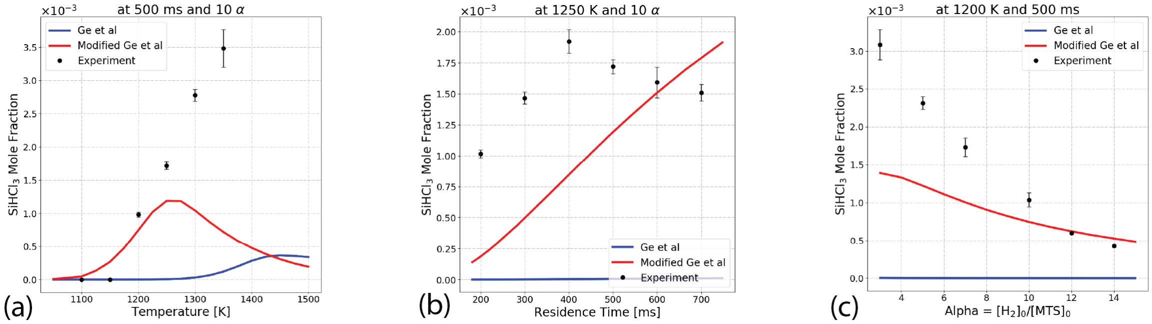

Figure 6.9: Comparison between experimental data and predictions by models for $SiHCl_3$ concentration at three different operation conditions: 1) varying temperature, 2) varying residence time at 1250 K, 3) varying α at 1200 K.

CH_4: Prediction of CH_4 production by the optimized Ge et al. model is compared to the experimental data in Fig. 6.8. The predicted CH_4 concentration reasonably approximates experimental data at all the experimental conditions. At these conditions, the formation of CH_4 was directly related to the decomposition of MTS. Specifically, decomposition of MTS via the Si-C bond cleavage pathway (reaction R8) created methyl radicals ($CH_3\bullet$) that subsequently reacted with H_2 to form CH_4 (reaction R1) as follows

$$CH_3 + H_2 \leftrightarrow CH_4 + H$$

Furthermore, the $SiCl_3\bullet$ radical produced in reaction R8 consumed CH_4 to create $SiHCl_3$ (reaction R5) as follows

$$CH_4 + SiCl_3 \leftrightarrow CH_3 + SiHCl_3$$

Reaction pathway analysis showed that this reaction became more important as temperature increased. Therefore, it is possible that the decrease in CH_4 concentration at high temperature might be attributed to reaction R5.

$SiHCl_3$: The comparison between experimental results and predicted values for $SiHCl_3$ is shown in Fig. 6.9. Only three sets of experimental conditions are shown because $SiHCl_3$ was not detected at the temperature of 1150 K.

With varying temperature, the optimized model predicted an increase in $SiHCl_3$ production from 1100 to 1275K, after which $SiHCl_3$ started to be consumed. This change in $SiHCl_3$ concentration with temperature can be attributed to a competition between reactions R2, R5

$$H_2 + SiCl_3 \leftrightarrow H + SiHCl_3$$

$$CH_4 + SiCl_3 \leftrightarrow CH_3 + SiHCl_3$$

and reaction R4

$$SiHCl_3 \leftrightarrow HCl + SiCl_2$$

Reactions R2 and R5 contributed to $SiHCl_3$ production, whereas reaction R4 consumed $SiHCl_3$. Reaction pathway analysis showed that reaction R4 became more relevant with increasing temperature, which might explain a reduction in $SiHCl_3$ concentration at high temperature. However, the measured data showed that $SiHCl_3$ production continued at least up to 1350 K. This difference between the measured data and model predictions indicates that additional reactions may need to be added to the optimization process in order to enhance $SiHCl_3$ production with increasing temperature. Thus, future experiments should be conducted at higher temperature than 1350 K and at different conditions to provide additional data to better optimize the Ge et al. model [164].

On the other hand, when the effect of varying residence time at 1250 K was considered, the predictions by the optimized model showed increased $SiHCl_3$ concentration with increasing residence time, while the experimental data showed that $SiHCl_3$ concentration only increased from 200 to 400 ms and then decreased afterward. According to the optimized model, at 1250 K, reaction R8 and the reverse of reaction R5 were responsible for $SiHCl_3$ production, while reaction R6 prevented $SiHCl_3$ from forming by taking away the necessary $SiCl_3\bullet$ radical. However, the extent of reaction R6 was

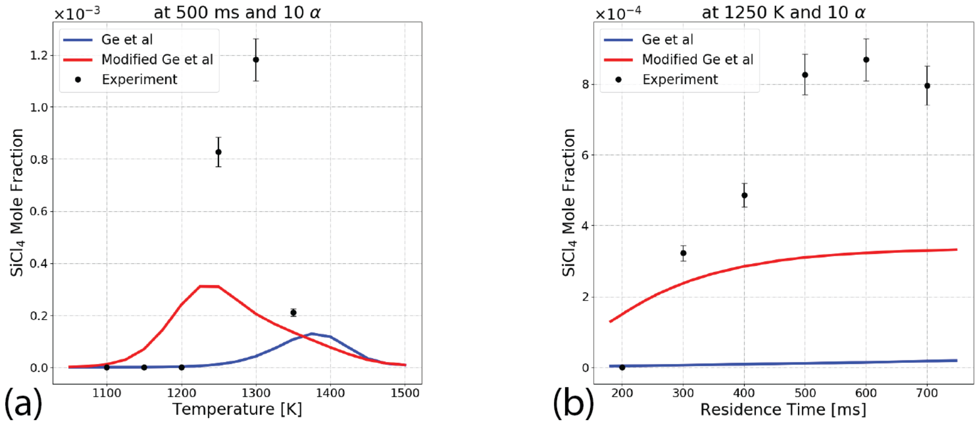

Figure 6.10: Comparison between experimental data and predictions by models for $SiHCl_3$ concentration at two different operating conditions: 1) varying temperature, and 2) varying residence time at 1250 K.

much smaller than the other two reactions even with increasing residence time. As a result, the optimized model only predicted an increase in $SiHCl_3$ concentration as residence time increased at 1250 K. Nevertheless, the change in $SiHCl_3$ concentration with residence time that was captured by the experiments might be attributed to the reactant depletion effect typically encountered in hot-walled reactors such as the one in this study.

The next set of experimental conditions was variation of α at a fixed temperature and residence time. Here, the predictions by the optimized model showed that $SiHCl_3$ concentration decreased with increasing α, which was similar to the experimental results. However, the predicted concentration was still lower than the experimental data, especially at low α values ($\alpha =$ 3-10). The decrease in $SiHCl_3$ concentration with increasing α was due to the fact that less MTS was sent into the reactor, resulting in a smaller production of $SiCl_3\bullet$ necessary for $SiHCl_3$ formation.

$SiCl_4$: A comparison of model prediction to measured $SiCl_4$ concentration is shown in Fig. 6.10 at two set of conditions: 1) varying temperature with fixed nominal residence time of 500 ms and α of 10, and 2) varying residence time with fixed temperature of 1250 K and α of 10. The effect of alpha on this species formation is not included because $SiCl_4$ was not detected below 1250 K. Although Fig. 6.10 indicates that the optimized model still needs further improvement, the optimized model was able to reasonably capture the experimental trend of $SiCl_4$ concentration.

When the effect of temperature was considered, both the experimental data and predictions by the optimized model showed a shift from production to consumption of $SiCl_4$ with increasing temperature. However, the model predicted the peak of $SiCl_4$ concentration at a lower temperature than experiment (1250 K vs. 1300 K). When the effect of residence time was investigated, both the measured data and predictions by the optimized model showed $SiCl_4$ concentration initially increased with residence time up to 500 ms, after which the concentration began to plateau. However, the predicted concentration was much lower than the measured data.

The evolution of $SiCl_4$ shown in Fig. 6.10 could be attributed to the behavior of two reactions (R3 and R6) with changing temperature or changing residence time

$$HCl + SiCl_3 \leftrightarrow H + SiCl_4$$

$$CH_3SiCl_3 + SiCl_3 \leftrightarrow CH_3SiCl_2 + SiCl_4$$

At low temperature or residence time, these two reactions produced $SiCl_4$, i.e, the reactions go from left to right. In addition, reaction R6 always produced $SiCl_4$. That is to say the reverse of this reaction remained negligible even at high temperature or high residence time. However, the reverse of reaction R3 became more dominant at high temperature or residence time, consuming $SiCl_4$ to produce $SiCl_3\bullet$ and HCl. Because the reverse of reaction R3 became so dominant at high temperature and residence time, more $SiCl_4$ was consumed than produced.

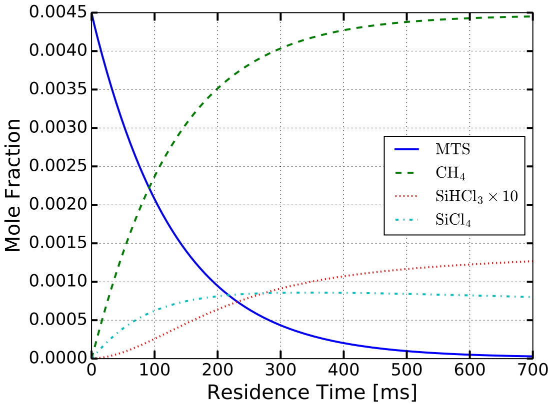

Figure 6.11: Species profiles from the constant temperature Senkin simulation using the optimized Ge model.

6.5 Model Reduction

Principal component analysis (PCA) is an important tool in the reduction of chemical kinetic models [170]. A generalized routine to perform model reduction based on sensitivities from a range of targets was developed by Esposito and Chelliah [92]. This routine was applied to the optimized Ge model to produce comprehensive skeletal chemical kinetic models for MTS pyrolysis. A sensitivity matrix of all the measured species (MTS, CH_4, $SiHCl_3$ and $SiCl_4$) with respect to the irreversible reaction rates was the basis for the PCA. These were obtained by a brute force method from constant temperature, time-dependent, zero-dimensional pyrolysis simulations with Senkin [171]. The sensitivities are defined as

$$s_{i,k} = \frac{\partial X_i}{\partial r_k} \tag{6.1}$$

where $s_{i,k}$ indicates the sensitivity of species i to reaction k, X_i is the mole fraction of species i and r_k is the k-th reaction-rate constant.

Sensitivities were calculated at a constant temperature of 1250 K and a residence time of 200 ms as all measured species showed significant gradients under these conditions as seen in Figs 6.7-6.9. Note that the sensitivity simulations did not account

Table 6.6: Details of the conditions at which the sensitivity analysis was performed for constant temperature pyrolysis where τ is the residence time and composition is given in mole fractions.

τ [ms]	p [atm]	T [K]	MTS	H_2	Ar
200.0	1.0	1250	0.0045	0.045	0.9505

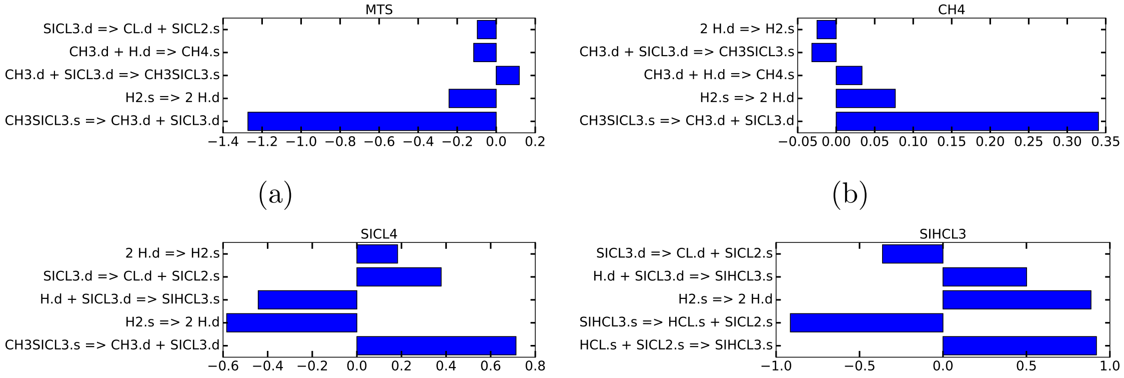

(c) (d)

Figure 6.12: Top five sensitive reactions for the target species from a sensitivity analysis with the modifed Ge et al. chemical kinetic model [164].

for the temperature ramp up time in the experiment. The 200 ms residence time for a constant temperature simulation thus approximately corresponded to a 300 ms residence time in the experiment. A summary of the conditions as well as species composition for the Senkin simulations are given in Table 6.6 and the most sensitive reactions for each target species are shown in Fig 6.12.

6.5.1 Performance of a skeletal model

The performance of two skeletal models is evaluated against the detailed optimized Ge et al. model. A comparison of mole fractions of four species: MTS, CH_4, $SiHCl_3$, and $SiCl_4$, predicted by the detailed and skeletal Ge et al. models is presented in Fig. 6.13 as a function of temperature. The results of this comparison show that, with only 23 species, the skeletal model was able to preserve the performance of the detailed optimized model of 47 species, while further reducing the number of species introduced errors to the predictions of the three intermediate species by the skeletal model. However, with 13 species, the skeletal model still shows species predictions that are reasonably close to those of the detailed optimized model, except for CH_4 prediction at temperature above 1300 K.

An additional advantage of progressively reducing the number of species in the skeletal model and comparing its predictions to those by the detailed optimized model is that new information on the gas phase chemistry during MTS pyrolysis can be obtained. Reducing from 23 to 22 species caused the skeletal model to predict higher methane (CH_4) concentration, especially above 1300 K. Comparing skeletal models with 23 and 22 species showed that the removed species was ethylene (C_2H_4). Along with C_2H_4, one reaction channel that consumed ethyl ($C_2H_5\bullet$) radicals was removed

$$C_2H_5 \rightarrow C_2H_4 + H$$

Because of this, the other channel that consumed $C_2H_5\bullet$ became enhanced,

$$C_2H_5 + H \rightarrow CH_3 + CH_3$$

The increased production of CH_3 resulted in higher formation of CH_4 via two reaction pathways

$$CH_3 + H_2 \rightarrow CH_4 + H$$

$$CH_3 + HCl \rightarrow CH_4 + Cl$$

Furthermore, the skeletal model predicted that CH_4 concentration plateaued out after 1300 K in contrast to the experimental data and prediction by the detailed optimized model. This difference in CH_4 evolution at high temperature was due to the removal of the reaction $C_2H_5 \rightarrow C_2H_4+H$, depleting the $H\bullet$ radicals needed for the consumption of CH_4 at high temperature condition.

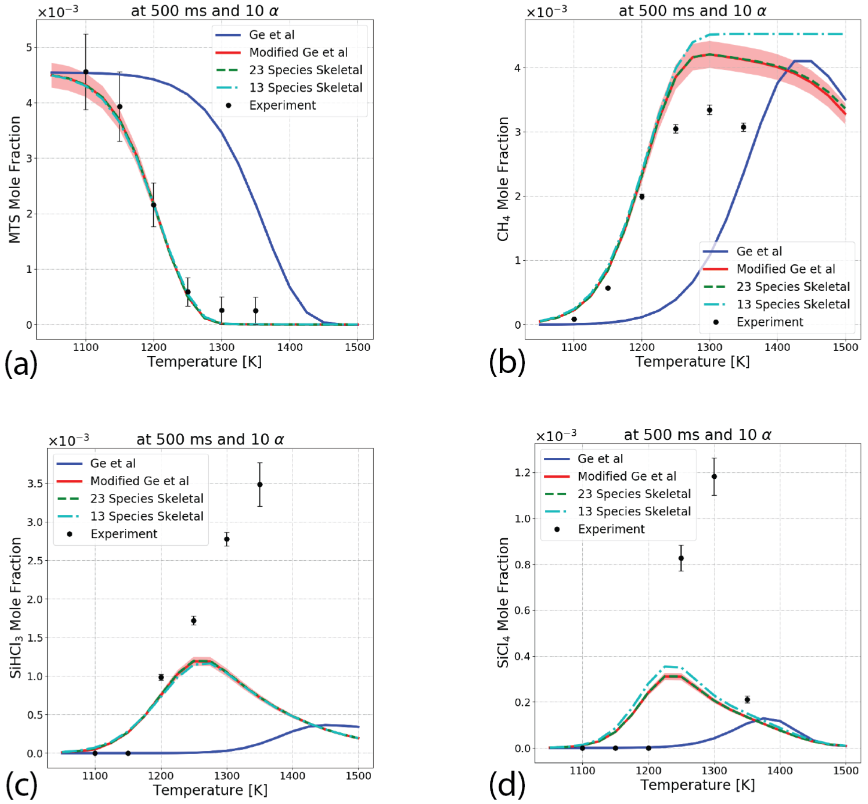

Figure 6.13: Measured and predicted mole fractions of MTS, CH_4, $SiHCl_3$, and $SiCl_4$ as a function of temperature at fixed residence time of 500 ms and α of 10. The red shaded area shows a 5% error region in which the performance of a skeletal is deemed acceptable.

Errors in $SiCl_4$ predictions arose when the number of species in the skeletal model was reduced from 17 to 16. With this number of species, the skeletal model predicted slightly higher $SiCl_4$ production over the considered temperature range. The removed species in this case was $CH_2SiCl_3\bullet$ radical. The removal of this species also eliminated a reaction that consumed $SiCl_3\bullet$ radicals,

$$CH_3SiCl_3 + SiCl_3 \rightarrow CH_2SiCl_3 + SiHCl_3$$

As a result, slightly higher $SiCl_3\bullet$ concentration became available to produce $SiCl_4$ by participating in reaction R6 in Table 6.4.

Removing one more species from the skeletal model to have 15 species resulted in a slightly lower $SiHCl_3$ concentration predicted over a temperature range from 1200 to 1300 K. The cause of this small reduction in $SiHCl_3$ concentration was the removal of $SiHCl_2\bullet$ radical and its associated reactions such as

$$H_2 + SiCl_3 \rightarrow HCl + SiHCl_2$$

$$SiHCl_2 \rightarrow H + SiCl_2$$

and

$$HCl + SiHCl_2 \rightarrow H + SiHCl_3$$

The first two reactions contributed the necessary HCl and $SiCl_2\bullet$ to production of $SiHCl_3$ as shown by the reverse of reaction R4 in Table 6.4. Nevertheless, the contribution of these three reactions to $SiHCl_3$ production was small, and thus their removal only resulted in a slight reduction in $SiHCl_3$ concentration.

6.6 Summary

The importance of understanding gas phase chemistry of SiC deposition from a MTS/H_2 system has been recognized by many researchers. Numerous chemical kinetics models have been proposed to describe both gas phase and surface chemistry of SiC deposition. However, in order for the models to be used to find optimum conditions for SiC deposition, they need to be validated against experimental data. Recognizing this need, this study collected information of gas phase composition during the pyrolysis of MTS at typical conditions for SiC deposition. A hot-walled reactor with relatively long isothermal length is used. Stable species including the reactant MTS and three decomposition products (CH_4, $SiHCl_3$, and $SiCl_4$) were detected and quantified with a GC. The experimental data is used to compare with predictions by the Ge et al. model. The model shows a much slower reactivity than the experiment at all conditions. As a result, the data is used as a benchmark to optimize a number of reaction rates incorporated in the model. The optimized model is able to reasonably capture the experimental data at most experimental conditions. However, further study is still needed to improve additional reaction pathways in the model to fully capture the experimental data. In addition to model optimization, this study also attempted model reduction. The result of the model reduction process was a skeletal model with nearly half the number of species and reactions but with matching performance to the optimized detailed model.

Chapter 7

Summary and Recommendations for Future Studies

The design of future jet engines has to meet the requirements of lower pollutant emission and higher efficiency. One of the main pollutants is soot particulates, whose emission not only affects the global climate and human well-being, but also indicates an inefficient combustion process. As a result, minimizing soot formation in jet engines can reduce both the economic and social costs of transportation. In addition to minimizing soot formation, the overall efficiency of jet engines can be improved by replacing the current metal super-alloy materials with ceramic matrix composites (CMCs), particularly silicon carbide matrix/silicon carbide fiber ($\mathrm{SiC}_m/\mathrm{SiC}_f$) composites. $\mathrm{SiC}_m/\mathrm{SiC}_f$ composites offer similar, if not better, maximum service temperature to the metal alloys, but only at one-third of the weight. Employing the composites will increase 1) the combustion efficiency with higher allowable flame temperature, 2) the engine thrust with smaller air flow diverted for cooling, and 3) the fuel mileage with lighter engines.

However, there exists a number of challenges that hinder the achievement of minimal soot formation and cost-effective production of $\mathrm{SiC}_m/\mathrm{SiC}_f$ composites. The processes of soot formation and $\mathrm{SiC}_m/\mathrm{SiC}_f$ composite fabrication have one step in common: the production of important gas phase precursors from decomposition of the parent fuel or reactants. Numerous research efforts have been dedicated to studying the gas phase chemistry during these two processes, which have been reviewed throughout this thesis work. Such efforts have resulted in a large number of detailed chemical kinetic models whose purpose is to predict the soot formation and $\mathrm{SiC}_m/\mathrm{SiC}_f$ composite fabrication processes in CFD simulations. Unfortunately, the models are still facing two major limitations: 1) significant uncertainties in reaction rate coefficients incorporated in the models and 2) huge numbers of species and reactions that render the models impractical for complex CFD simulations. In order to overcome these two limitations, there exits a need for fundamental experimental data that be used to 1) validate and optimize the models to minimize the reaction rate coefficient uncertainties, and 2) reduce the model size while preserving their performance for practical CFD simulations of soot formation and $\mathrm{SiC}_m/\mathrm{SiC}_f$ composite fabrication processes.

Recognizing this need for experimental data, the Reacting Flow Laboratory (RFL) at the University of Virginia (UVa) has constructed and verified an excellent analytical system for chemical kinetic studies. The main component of the the analytical system is a microflow tube reactor (MFTR) whose design was demonstrated to be able to eliminate the problems associated with defining the initial conditions and minimize typical non-idealities encountered by flow reactors [61, 67, 68]. An additional advantage of the MFTR is that it can be paired with different diagnostic tools, such as: gas chromatography (GC), gas chromatography/mass spectrometry (GM/MS), molecular beam mass spectrometry (MBMS), and scanning mobility particle sizer (SMPS), to quantify stable and radical gaseous species, and solid products during thermal and oxidative decomposition of hydrocarbon fuels or other chemicals of interest.

This thesis work is a continued effort of previous studies [61, 67, 68] to provide independent fundamental experimental data on precursor formation in the gas phase during thermal decomposition (pyrolysis) of various hydrocarbon fuels. The objectives were to identify and quantify additional stable species (i.e., hydrocarbons with more than four C atoms), and to use the measured data to validate a number of chemical kinetic models over a wide range of experimental conditions and with different fuels of increasingly complex chemical composition. Moreover, this thesis work is the first of its kind at the RFL to expand the ability of the analytical system to investigate the gas phase chemistry during SiC formation from methyltrichlorosilane/hydrogen (MTS/H_2) mixtures. The experimental data were used not only to validate and optimize a detailed chemical kinetic model, but also to reduce its size for a potential implementation in complex CFD simulations.

7.1 Summary

The first part of this thesis work focused on the effects of temperature and residence time on the evolution of products during pyrolysis of three different hydrocarbon fuels: ethylene (C_2H_4), n-dodecane ($nC_{12}H_{26}$), and Jet A (POSF 10325). Ethylene is the smallest alkene species (straight chain hydrocarbons with one C-C double bond). n-Dodecane is a normal alkane species (straight chain hydrocarbons with only C-C single bond). And Jet A is a commercial aviation fuel that contains thousands of hydrocarbon species. The three fuels were selected with progressively complex chemical composition in order to highlight the role of fuel chemical composition on the formation pathways of important precursors to soot particles, such as benzene (C_6H_6), toluene (C_7H_8) and naphthalene ($C_{10}H_8$). In addition, the three fuels also provided a comprehensive evaluation of detailed chemical kinetics models. The detailed models were constructed in a hierarchical manner. Starting with a base model of small hydrocarbon species (C_1-C_4), larger species with their own sets of reactions were appended to the base model to form a final detailed model. Thus, the data from ethylene and n-dodecane pyrolysis were used to examine different sub-models in six comprehensive models. The results showed significant uncertainty existed with the reaction rate coefficients used by the models. Among the six models, the CRECK model [88] predicted species concentration values that most reasonably agreed with the experimental data. As a result, the CRECK model was used to interpret the experimental data, and the model show different chemical pathways for benzene formation were activated depending on the fuel used. With ethylene, both the C_2/C_4 and C_3 chemical pathways were responsible for benzene formation, while only the C_3 chemical pathways were relevant when n-dodecane was the fuel of interest. However, the Hydrogen-Abstraction-Carbon-Addition (HACA) sequence was the main route for the growth from benzene to polycyclic aromatic hydrocarbons (PAHs) regardless of the parent fuel.

The experimental data from Jet A pyrolysis delivered an ultimate test of the detailed chemical kinetic models. Because of the chemical complexity of Jet A, it is impossible to account for all of its components in a model. Two approaches have been utilized to overcome this problem. The first approach is formulating fuel surrogates. Fuel surrogates are mixtures of four to five pure hydrcarbon components that tries to emulate the combustion properties of Jet A. The fuel surrogates have been experimentally tested against Jet A, and detailed chemical kinetic models have been developed for them. However, a major problem might arise for these models because of their hierarchical construction method. Each module of the detailed models was tested for the species that it was supposed to model. These detailed model might have omitted the possibility of interaction between different components of Jet A. To avoid this problem, an alternative approach was proposed to model the combustion of Jet A and other jet fuels. The approach is known as the Hybrid Chemistry or HyChem approach [133]. The HyChem approach considers the fuel combustion as a two-step process. The fuel initially undergoes thermal or oxidative decomposition to produce about ten products, which then get oxidized to form the final combustion products such as CO_2 and H_2O. At high temperature condition of practical engines, the pyrolysis step is sufficiently fast to be assumed instantaneous, whereas the oxidation step is the rate-limiting step. Thus, the combustion of Jet A can be viewed as the oxidation of its pyrolysis products. The HyChem approach models the pyrolysis process with seven reactions, whose rate coefficients and species stoichiometric coefficients were determined experimentally, whereas the oxidation step is modeled by a detailed foundational chemical kinetic model. Given the importance of the pyrolysis step in representing the chemical composition of a jet fuel, it needs to be thoroughly examined in order to ensure that the HyChem approach can accurately model the combustion of Jet A. Therefore, this thesis work set out to investigate the pyrolysis of Jet A over a wide range of temperature and residence time conditions with the MFTR in order to provide a benchmark for evaluating a number of fuel surrogate and the HyChem model. The results showed that the HyChem model overall predicted the species concentration values better than the fuel surrogate models. However, both the seven pyrolysis reactions and the detailed foundational model in the HyChem model still needs to be further improved in order to accurately predict the evolution of ethane (C_2H_6), propadiene (aC_3H_4), propyne (pC_3H_4), 1,3-butadiene (C_4H_6), benzene (C_6H_6), and toluene (C_7H_8).

In addition to pyrolysis of hydrocarbon fuels, this thesis work also employed the analytical system to investigate species transport and chemical kinetics during silicon carbide (SiC) deposition from pyrolysis of methyltrichlorosilane/hydrogen (MTS/H_2) mixtures. First of all, the effects of experimental conditions such as temperature, total flow rate and pressure on the deposition rate, morphology and preferred crystal orientation of SiC on quartz substrates were investigated in a hot-walled flow reactor (the PMFTR in Chapter 2). The analysis showed that the SiC deposition was controlled by either chemical kinetics or species transport depending on the experimental conditions. At normal atmospheric pressure (1 atm), increasing either temperature or initial MTS concentration transitioned SiC deposition from being controlled by chemical kinetics to being controlled by species transport. On the other hand, reduced pressure condition (0.5 atm) extended the transition conditions to higher values, i.e., higher temperature or higher initial MTS concentration. The morphology and preferred crystal orientation of the SiC deposits also changed in accordance with the deposition controlling regime. Furthermore, the experimental results were able to capture the reactant depletion effect that have been typically encountered in hot-walled flow reactors similar to the PMFTR. Either increasing total flow rate or decreasing total pressure helped mitigate the reactant depletion effect.

Besides SiC deposition on quartz substrates, the formation of SiC precursors in the gas phase during pyrolysis of MTS/H_2 mixtures was also investigated over a wide range of temperature and nominal residence time at normal atmospheric pressure (1 atm). Four species: MTS, methane (CH_4), trichlorosilane (CH_3SiCl_3), and silicon tetrachloride ($SiCl_4$), were quantified by GC. The measured data were compared to predictions by the Ge et al. model [164]. The results of the comparison showed that the reactivity of the MTS/H_2 mixture predicted by Ge et al. model was much slower that that shown by the experimental data. Therefore, modification of the model was attempted with the data serving as the benchmark. Sensitivity and reaction pathway analyses were conducted to determine the most important reactions to the evolution of the four detected species. Then, the rate coefficients (pre-exponential factors and activation energies) were modified until minimum error between model prediction and data was reached. The modified model was able to reasonably capture the experimental data with varying temperature and nominal residence time, but the model failed to do so when the effect of initial gas composition ($\alpha = [H_2]_0/[MTS]_0$) was considered. Nevertheless, an attempt to reduced the size of the modified Ge et al. model was carried out with the procedure developed by Esposito and Chelliah [92]. The result was a skeletal model that preserved the performance of the detailed optimized model but with half the size (26 vs. 47 species and 66 vs. 112 reactions).

7.2 Recommendations for future studies

This thesis work has demonstrated the excellent ability of the PMFTR and MFTR at the RFL to study two different chemical kinetic systems, and has delivered some encouraging results that showed the fidelity of the measured data for chemical kinetic model validation and optimization. Nevertheless, the work to achieve minimum soot formation and cost-effective fabrication of $\mathrm{SiC}_m/\mathrm{SiC}_f$ composites has not yet been completed. Thus, the following strategies are recommended for future works to achieve these goals:

1. Only the effects of temperature and residence time on the formation of soot precursors were investigated at normal atmospheric pressure (1 atm). However, there exists a great need for similar speciation data to be measured at elevated pressure conditions. A converging nozzle can be added to the exit of the MFTR to create choke flow and increase the total pressure inside the reactor.

2. In addition to data at elevated pressure, detection and quantification of radical species during pyrolysis of hydrocarbon fuels are also necessary for model validation and optimization. A molecular beam mass spectrometry (MBMS) is available at the RFL for this purpose. The device has been demonstrated by Simms to be able to detect methyl and cylcopentadienyl radicals during pyrolysis of JP-10 [68]. Thus, the MBMS can also be used to measure radical species during pyrlysis of the fuels studied in this work.

3. As described in Chapters 1, 2, and 3, soot formation process involves three steps: 1) formation of soot precursors in the gas phase, 2) soot inception, and 3) soot

mass growth. The MFTR can also be used to study step 3 of the soot formation process. An available scanning mobility particle sizer (SMPS) can be placed at the exit of the reactor to collect the information on soot particle size distribution at different experimental conditions. The functionality of the SMPS has been demonstrated with ethylene pyrolysis at both normal and elevated pressure conditions [172, 173]. Future efforts should focus on utilizing this device with liquid fuels such as n-dodecane and Jet A.

4. Up until this point, fuel pyrolysis has been the target process for the MFTR. Another aspect of combustion of hydrocarbon fuels can be probed with the MFTR. Oxidation of liquid hydrocarbon fuels has displayed two distinct regions: negative temperature coefficient (NTC) and high temperature. The NTC region is very important to understanding engine knocking encountered in spark ignition engines. Because temperature increase due to the heat release from the oxidation process at this condition can be minimized with high level of dilution, the MTFR can be used to investigate NTC oxidation of liquid hydrocarbon fuels, and the data can be used to validate and develop chemical kinetic models of the NTC region.

5. High-temperature oxidation of liquid hydrocarbon fuels can also be investigated in a counter-flow burner at the RFL. The burner provides an access for laser diagnostic tools such as: LII, PLIF, and CARS, to measure flame temperature, extinction strain rate, and soot volume fraction at different different fuel-to-oxidizer ratios. These types of data can be used to further test the performance of chemical kinetic models in predicting the global properties of a combustion process.

6. For the investigation of SiC deposition on quartz substrates, the temperature of the substrates was equal to that of the gas temperature. Thus, the effects of gas

and surface temperature on the SiC deposition rate could not be distinguished. To address this issue, a tube reactor with bigger inner diameter can be used to accommodate larger substrates that come with their own heating system. One potential challenge with using a reactor with bigger cross section is longer temperature ramp-up section at the inlet and more intense temperature ramp-down section at the exit. This challenge will limit the temperature and total flow rate conditions accessible by the new reactor. Replacing argon (Ar) by helium (He) as the diluent gas can mitigate the extent of these two temperature ramp-up and ramp-down regions because He has higher heat transfer coefficient than Ar.

7. For the investigation of the gas phase chemistry during pyrolysis of MTS/H_2 mixtures, only four species were quantified. Additional species are required to better study this chemical kinetic system. In addition to GC, the GC/MS available at the RFL will need to be used. However, extreme caution should be exercised in order to be able to quantify additional species and to protect the GC/MS. The inner surface of most of the gas delivery lines on the GC/MS should be deactivated to prevent surface adsorption of the pyrolysis products.

8. The measured speciation data from pyrolysis of MTS/H_2 mixtures were used to validate and optimize the Ge et al. model [164]. Specifically, reaction rate coefficients (pre-exponent factors and activation energies) of a number of important reactions were modified. However, predictions of the optimized model for $SiHCl_3$ and $SiCl_4$ failed to satisfactorily capture the experimental data. Further studies need to be conducted at temperature higher than 1350 K and at different conditions to provide additional data to better optimize the Ge et al. model.

9. After obtaining a better optimized model, the model reduction procedure should

be done again to produce an improved skeletal model. The skeletal model can be further simplified with a combination of chemical lumping, graphical reaction flow analysis, and elimination methods [174].

Appendices

Appendix A

Liquid Species Calibration with Gas Chromatography (GC)

This appendix describes the calibration procedure of liquid species with gas chromatography (GC). The appendix consists of two main sections: 1) calibration of chlorosilanes and organochlorosilanes, and 2) calibration of hydrocarbons

A.1 Chlorosilanes and organochlorosilanes

The calibrated chlorosilanes and organochlorosilanes are trichlorosilane ($SiHCl_3$), silicon tetrachloride ($SiCl_4$) and methyltrichlorosilane (MTS - CH_3SiCl_3). These species were delivered to the GC by bubbling ultra high purity argon (Ar) gas (Praxair) through a liquid bath of each species. Thus, the first step was to determine the mass flow rate ($\dot{m}$) of these liquid species given a volume flow rate of Ar.

A.1.1 Measurement of mass flow rates

The delivery system consists of a Pyrex storage bottle with a screw cap. Three holes were drilled on the cap: two of them are for gas inlet and outlet tubing, and the other for a K-type thermocouple to monitor the liquid temperature. Silcosteel coated stainless steel tubing (Restek) was used in order to prevent surface adsorption of the liquid species. A pressure gauge was installed on the gas inlet line to monitor the pressure of the liquid bath. Fig. A.1 shows the schematics of the delivery system. All measurements were conducted at room temperature (25 °C) and normal atmospheric pressure (1 atm).

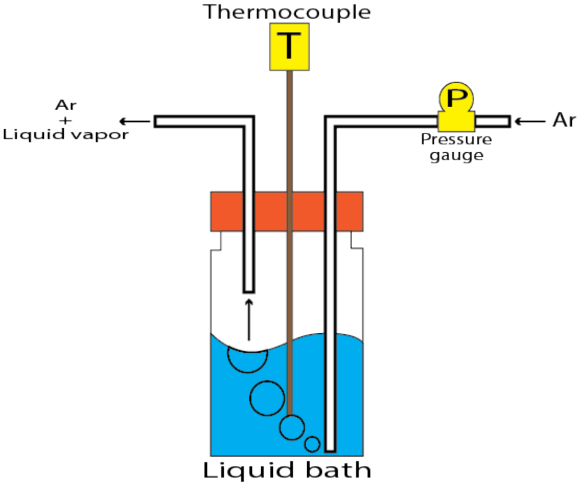

Figure A.1: A schematics of the liquid species delivery system that was used for species calibration with GC

Mass flow rate of the liquid species at a given Ar volume flow rate was determined in the following steps. First of all, the weight of the liquid bath was measured. Then, a known Ar volume flow rate was sent to the liquid bath. After 2 hours, the Ar flow was turned off and the weight of the liquid bath was measured again. The mass flow rate of the liquid species was the difference in weight of the liquid bath divided by 2 hours. At least three different Ar flow rates were selected to determine the correlation between Ar flow rate and liquid species mass flow rate. Fig. A.2 shows the mass flow rates of the three liquid species plotted against Ar volume flow rates, as well as linear fits of the data. The linear fits were used to calculate the mass flow rate of the liquid species, given a known Ar volume flow rate for later calibration with the GC.

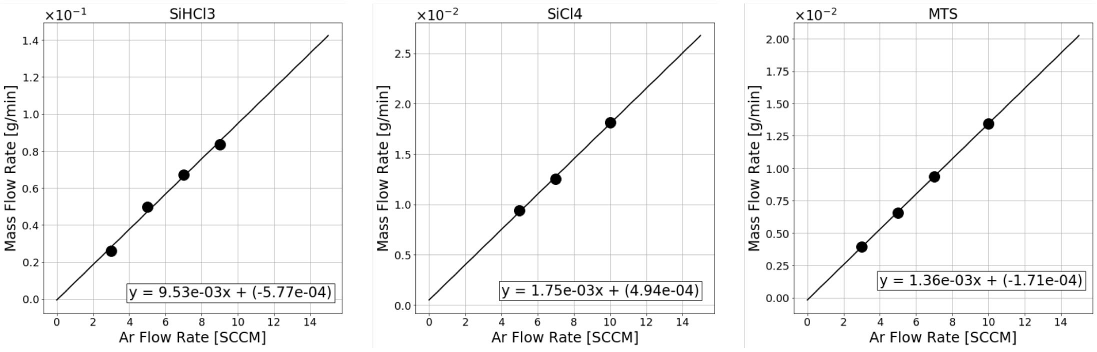

Figure A.2: Mass flow rates of $SiHCl_3$, $SiCl_4$, and MTS at different Ar volume flow rates

A.1.2 Calibration of the liquid species with GC

The calibration of the three liquid species with the GC proceeded in the following steps. The liquid delivery system shown in Fig. A.1 was connected to a straight alumina tube reactor with 0.5 mm ID and 0.5 m length. Fig. A.3 shows the entire experimental apparatus for the calibration process. Two different Ar flows were sent to the reactor. One of them was bubbling through the liquid species bath to deliver vapor of the liquid species to the reactor. The reactor temperature was kept at 100 °C to prevent liquid condensation. A vapor mixture of the liquid species and Ar was delivered to the GC through a feed line connecting the reactor exit and the GC. The temperature of the feed line was also kept at 100 °C to prevent liquid condensation.

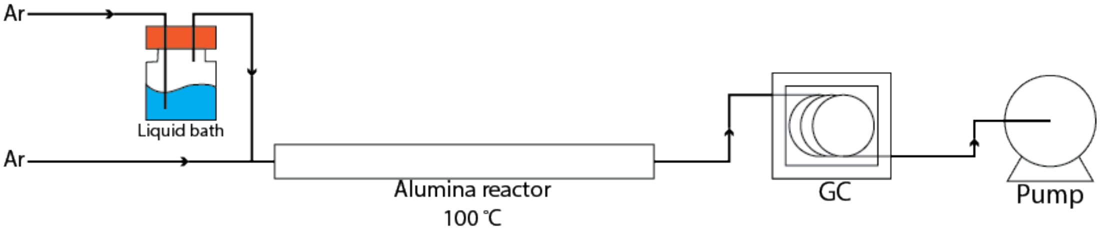

Figure A.3: A schematics of an alumina straight tube reactor that was used to calibrate liquid species with the GC

This paragraph describes the steps taken in calculating the concentration or mole fraction of the liquid species. The concentration of the liquid species was calculated by

$$X_{liquid} = \frac{\dot{n}_{liquid}}{\dot{n}_{total}} = \frac{\dot{n}_{liquid}}{\dot{n}_{liquid} + \dot{n}_{Ar}} \tag{A.1}$$

where X_{liquid} is concentration of the liquid species, $\dot{n}_{liquid}$ is mole flow rate of the liquid species, and $\dot{n}_{Ar}$ is mole flow rate of Ar. The mole flow rate of the liquid species was obtained by

$$\dot{n}_{liquid} = \frac{\dot{m}_{liquid}}{M_{liquid}} \tag{A.2}$$

where $\dot{m}_{liquid}$ is mass flow rate of the liquid species, and M_{liquid} is the molar mass of the liquid species. Then, the calculation of Ar mole flow rate ($\dot{n}_{Ar}$) involved a conversion from Ar volume flow rate to mass flow rate. This step was done by

$$\dot{m}_{Ar} = q_{Ar}\rho_{Ar} \tag{A.3}$$

where $\dot{m}_{Ar}$ is mass flow rate of Ar, q$_{Ar}$ is volume flow rate of Ar, and ρ_{Ar} is density of Ar. The density of Ar was obtained with the equation of state for an ideal gas

$$\rho_{Ar} = \frac{p}{R_{Ar}T} \tag{A.4}$$

where p is pressure (1 atm), R_{Ar} is Ar gas constant, and T is temperature (25 °C. With Ar mass flow rate found, Ar mole flow rate was obtained by

$$\dot{n}_{Ar} = \frac{\dot{m}_{Ar}}{M_{Ar}} \tag{A.5}$$

where M_{Ar} is molar mass of Ar. Finally, the concentration of the liquid species was calculated using Eq. A.1.

A.2 Hydrocarbons

The calibrated hydrocarbon species are: n-hexane (C_6H_{14}), n-heptane (C_7H_{16}), n-dodecane ($C_{12}H_{26}$), 1-pentene (C_5H_{10}), 1-hexene (C_6H_{12}), 1-heptene (C_7H_{14}), cyclopentene (C_5H_8), cyclohexene (C_6H_{10}), methylcyclohexane (C_7H_{14}), benzene (C_6H_6), and toluene (C_7H_8). The calibration procedure of these species is similar to that of chlorosilanes and organochlorosilanes described in Section A.1. The only difference is that Ar was replaced by nitrogen (N_2) gas. Fig. A.4 shows the mass flow rates of the hydrocarbon species plotted against N_2 volume flow rate, as well as linear fits of the data. Thus, the concentration of hydrocarbon species could be calculated using Eqs. A.1-A.5, but with N_2 substituting Ar.

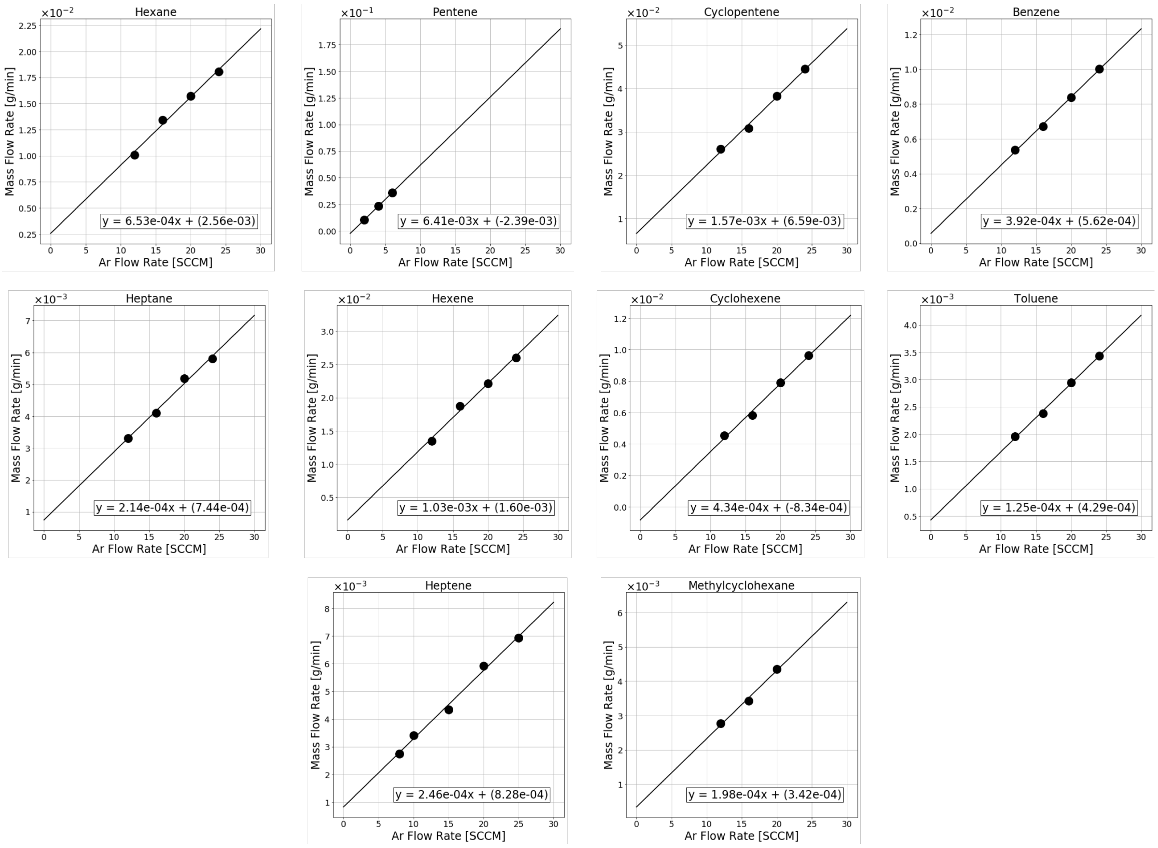

Figure A.4: Mass flow rates of the hydrocarbon species at different N_2 volume flow rates

Note: a different procedure was used to calibrate n-dodecane ($C_{12}H_{26}$) with the

GC because of small vapor pressure of n-dodecane at 25 °C (0.135 mm Hg vs. 46 mm Hg of n-heptane). A known volume flow rate of n-dodecane ($Q_{dodecane}$) was sent to the same reactor shown in Fig. A.3 by a syringe pump (Teledyne 500D). Thus, the concentration of n-dodecane ($\mathrm{X}_{dodecane}$) was calculated by

$$X_{dodecane} = \frac{\dot{n}_{dodecane}}{\dot{n}_{total}} = \frac{\dot{n}_{dodecane}}{\dot{n}_{dodecane} + \dot{n}_{N_2}} \tag{A.6}$$

where $\dot{n}_{dodecane}$ and $\dot{n}_{N_2}$ are mole flow rates of n-dodecane and the diluent N_2 gas, respectively. The mole flow rate of n-dodecane ($\dot{n}_{dodecane}$)is found by

$$\dot{n}_{dodecane} = \frac{\dot{m}_{dodecane}}{M_{dodecane}} = \frac{Q_{dodecane}\rho_{dodecane}}{M_{dodecane}} \tag{A.7}$$

where $\rho_{dodecane}$ and $M_{dodecane}$ are density and molar mass of dodecane, respectively. Then, the mole flow rate of N_2 ($\dot{n}_2$) is found in similar steps to Eqs. A.3-A.5, but with N_2 substituting Ar.

Appendix B

Experimental uncertainty of measured liquid species concentrations

This appendix describes the uncertainty analysis of experimentally measured concentrations of liquid species: methyltrichlorosilane, silicon tetrachloride, trichlorosilane, 1-pentene, 1-hexene, 1-heptene, hexane, heptane, cyclopentene, cyclohexene, methylcyclohexane, benzene, toluene and n-dodecane. The total experimental uncertainty (u_{total}) stems from uncertainty of the calibration process (u_{cal}) and from uncertainty of the experiment runs (u_{exp})

$$u_{total} = \sqrt{u_{cal}^2 + u_{exp}^2} \tag{B.1}$$

In addition, a description of the uncertainty analysis of residence time values reported in this thesis work is presented here. The uncertainty analysis takes into account the fact that the flow velocity profile in the UVA microflow tube reactor (MFTR) and pre-mixed microtube reactor (PMFTR) has a parabolic shape, which creates residence time stratification in the radial reactor direction. However, the majority of the experimental conditions were selected to minimize this stratification effect. Only liquid fuel pyrolysis cases at high temperature conditions (1150-1250 K) were notably affected by the flow stratification effect because the chemical reaction rate was faster than the radial species diffusion rate at these conditions.

B.1 Uncertainty of the species calibration process, $\mathbf{u}_{cal}$

During the calibration process of liquid species with gas chromatography (GC), the concentration of a species (X_s) was calculated as

$$X_s = \frac{\dot{n}_s}{\dot{n}_{total}} = \frac{\dot{n}_s}{\dot{n}_s + \dot{n}_d} \tag{B.2}$$

where $\dot{n}_s$ and $\dot{n}_d$ are mole flow rates of the species and a diluent (Ar or N_2), respectively. Thus, the uncertainty of X_s is due to uncertainties of $\dot{n}_s$ ($\sigma_{\dot{n}_s}$) and of $\dot{n}_d$ ($\sigma_{\dot{n}_d}$). The uncertainty of X_s can be expressed as

$$\sigma_{X_s} = \sqrt{(\frac{\partial X_s}{\partial \dot{n}_s})^2(\sigma_{\dot{n}_s})^2 + (\frac{\partial X_s}{\partial \dot{n}_d})^2(\sigma_{\dot{n}_d})^2} \tag{B.3}$$

Expanding the two partial derivatives in Eq. B.3 yields

$$\sigma_{X_s} = \frac{\sqrt{(\sigma_{\dot{n}_s}\dot{n}_d)^2 + (\sigma_{\dot{n}_d}\dot{n}_s)^2)}}{(\dot{n}_s + \dot{n}_d)^2} \tag{B.4}$$

In order to evaluate σ_{X_s} in Eq. B.4, $\sigma_{\dot{n}_s}$ and $\sigma_{\dot{n}_d}$ are needed. The determination of $\sigma_{\dot{n}_s}$ is presented first. The mole flow rate of a calibrated species ($\dot{n}_s$) was obtained by

$$\dot{n}_s = \frac{\dot{m}_s}{M_s} \tag{B.5}$$

where $\dot{m}_s$ is the measured mass flow rate of the calibrated species (see Appendix 1), and M_s is the molar mass of the species. Thus, $\sigma_{\dot{n}_s}$ can be found as

$$\sigma_{\dot{n}_s} = \frac{1}{M_s}\sigma_{\dot{m}_s} \tag{B.6}$$

where $\sigma_{\dot{m}_s}$ is the uncertainty of measured mass flow rate of the calibrated species. This quantity ($\sigma_{\dot{m}_s}$) can be found as

$$\sigma_{\dot{m}_s} = \frac{1}{\Delta t}\sqrt{(\sigma_{m_1})^2 + (\sigma_{m_2})^2} \tag{B.7}$$

where Δt is the time duration of the measurement of liquid species mass flow rate (see Appendix 1) and σ_{m_1} and σ_{m_2} are the uncertainties of the weight of the liquid species reservoir before and after Δt. σ_{m_1} and σ_{m_2} have the same value of ±0.0001 g, which is the error of the mass balance used during the measurement.

Then, the evaluation of the uncertainty of the diluent mole flow rate ($\sigma_{\dot{n}_d}$) can be obtained by looking at the calculation of the diulent mole flow rate, i.e.

$$\dot{n}_d = \frac{\rho_d}{M_d}q_d \tag{B.8}$$

where ρ_d and M_d are the density and molar mass of the diluent (Ar or N_2), respectively; and q_d is the diluent volume flow rate. Thus, the uncertainty of the diluent mole flow rate ($\sigma_{\dot{n}_d}$) can be calculated by

$$\sigma_{\dot{n}_d} = \frac{\rho_d}{M_d}\sigma_{q_d} \tag{B.9}$$

where σ_{q_d} is the uncertainty of the diluent volume flow rate. σ_{q_d} is the uncertainty of the mass flow controllers, which is 2% of full scale as specified in the Sierra Smart-Trak 100 Flow Controller manual. With $\sigma_{\dot{n}_d}$ found, the uncertainty of species concentration during calibration (σ_{X_s}) can be found in Eq. B.4.

Note: the analysis of uncertainty during the calibration process for n-dodecane is slightly different from that for the other species because of a different calibration procedure (see Appendix 1). The uncertainty of n-dodecane concentration during the calibration process can still be found with Eq. B.4. However, the calculation of the uncertainty of the mole flow rate of n-dodecane ($\sigma_{\dot{n}_s}$) is different from Eq. B.6. Specifically, this quantity is calculated by

$$\sigma_{\dot{n}_s} = \frac{\rho_s}{M_s}\sigma_{q_{dodecane}} \tag{B.10}$$

where ρ_s and M_s are density and molar mass of n-dodecane, respectively; and $\sigma_{q_{dodecane}}$ is the uncertainty of n-dodecane volume flow rate. $\sigma_{q_{dodecane}}$ is the flow rate accuracy listed for Teledyne 500D syringe pump, which has a value of ±0.5% of the set flow rate.

B.2 Uncertainty of experimental runs, $\mathbf{u}_{exp}$

The reported experimentally measured concentration of a species is an averaged value of four different measurements, as illustrated in Table B.1.

Table B.1: An example of how the reported concentration of a species is calculated

Run	Concentration
1	x_1
2	x_2
3	x_3
4	x_4
Average	x_{avg}

Thus, the uncertainty of experimental runs (u_{exp}) is the standard deviation of these four values (s_{exp})

$$u_{exp} = s_{exp} \tag{B.11}$$

With the uncertainties of the calibration process (u_{cal}) and experimental runs (u_{exp}) accounted for, the total experimental uncertainty (u_{total}) can be found in Eq. B.1.

B.3 Uncertainty of species residence time

In a laminar flow reactor similar to the MFTR and PMFTR, the velocity profile is parabolic:

$$U(r) = U_{max}\left[1 - \left(\frac{r}{R}\right)^2\right] \tag{B.12}$$

where U_{max} is the velocity at the centerline of the reactor, r is the radial reactor coordinate, and R is the reactor radius. U_{max} is related to the total volume flow rate q_0 as follows

$$U_{max} = \frac{2q_0}{\pi R^2} \tag{B.13}$$

Thus, Eq. B.12 can be written in terms of the total volume flow rate

$$U(r) = \frac{2q_0}{\pi R^2}\left[1 - \left(\frac{r}{R}\right)^2\right] \tag{B.14}$$

And the residence time of a fluid element at a radius r is

$$t(r) = \frac{L}{U(r)} = \frac{\pi R^2 L}{q_0}\frac{1}{2[1 - (\frac{r}{R})^2]} \tag{B.15}$$

Since the space time or average residence time is defined as

$$\tau = \frac{V}{q_0} = \frac{\pi R^2 L}{q_0} \tag{B.16}$$

where V is the reactor volume, and thus, Eq. B.15 becomes

$$t(r) = \frac{\tau}{2[1 - (\frac{r}{R})^2]} \tag{B.17}$$

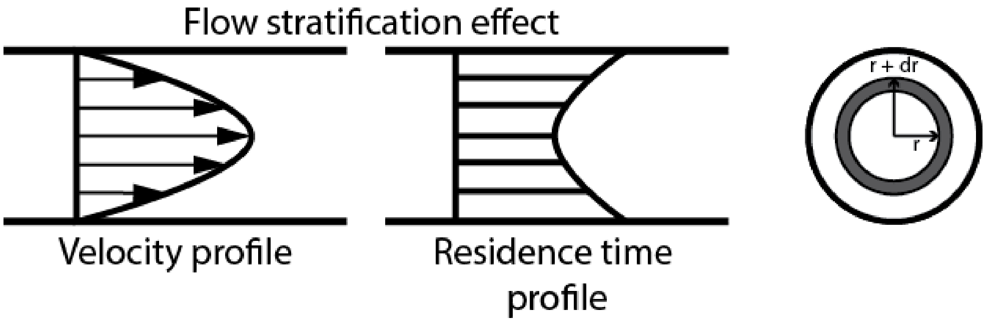

Figure B.1: Stratification of species residence time due to parabolic velocity profile.

Given this residence time profile, the calculation of uncertainty associated with species residence time requires a knowledge of the residence time distribution (RTD) in a laminar flow reactor. The calculation of the RTD described here closely follows the procedure listed in [ref]. The RTD, E(t) is a function that quantitatively describes the amount of time different fluid elements have spent in the reactor. Thus, the quantity E(t)dt is the fraction of fluid exiting the reactor that has spent between time t and t + dt inside the reactor. With E(t), the mean residence time (t_m) and the variance (σ^2) can be found by using

$$t_m = \int_0^\infty tE(t)dt \tag{B.18}$$

and

$$\sigma^2 = \int_0^\infty (t - t_m)E(t)dt \tag{B.19}$$

The standard deviation (σ), which is the square root of the variance, can be used to quantify the residence time uncertainty.

The RTD function E(t) can be found by considering the volume flow rate of fluid out of the reactor between r and r + dr (as shown in Fig. B.1)

$$dq = U(r)2\pi rdr \tag{B.20}$$

Then, the fraction of total fluid passing out between r and r + dr is

$$\frac{dq}{q_0} = \frac{U(r)2\pi r dr}{q_0} \tag{B.21}$$

The fraction of fluid between r and r + dr has a flow rate between q and q + dq and spends a time between t and t + dt in the reactor. Thus, this fraction of fluid can be related to the RTD function E(t) as

$$E(t)dt = \frac{dq}{dq_0} \tag{B.22}$$

An expression for dt can be found by differentiating Eq. B.17, yielding

$$dt = \frac{4t^2}{\tau R^2} r dr \tag{B.23}$$

Combing Eqs. B.17, B.22, and B.23 produces an expression for E(t)

$$E(t) = \frac{\tau^2}{2t^3} \tag{B.24}$$

With the E(t) expression, the minimum time the fluid may spend in the reactor can be found

$$t_{min} = \frac{L}{U_{max}} = \frac{V}{2q_0} = \frac{\tau}{2} \tag{B.25}$$

As a result, the complete RTD function for a laminar-flow reactor is

$$E(t) = \begin{cases} 0 & t < \dfrac{\tau}{2} \\ \dfrac{\tau^2}{2t^3} & t \geq \dfrac{\tau}{2} \end{cases} \tag{B.26}$$

In addition, the mean residence time can be found by using Eq. B.18, which shows that $t_m = \tau$, or the mean residence time equals the space time when the total volume flow rate is constant.

However, when E(t) is used to find the variance (σ^2) with Eq. B.19, the variance is infinite. As a result, the residence time uncertainty is estimated with the fraction of fluid elements that has resided for an amount of time τ (the mean residence time) before exiting the reactor:

$$X_\tau = \int_0^\tau E(t)dt = \int_{\frac{\tau}{2}}^{\tau} \frac{\tau^2}{2t^3} dt = \frac{3}{4} \tag{B.27}$$

The result of Eq. B.27 shows that 75% of fluid elements have spent the mean residence time inside the reactor before exiting, and these fluid elements located around the center of the reactor axis (see Fig. B.1). In other words, 25% of fluid elements have different residence time, and these fluid elements concentrated near the reactor wall. In addition, a microprobe with really small inner diameter (75 μm) was placed at the exit of the reactor to extract stable species for measurement in the GC systems. This small microprobe was carefully aligned with the reactor axis to avoid sampling species near the reactor wall. As a result, a value of 10 % was assumed to be the residence time uncertainty for the liquid fuel pyrolysis cases at high temperature condition (1150 - 1250 K) to account for the flow stratification effect due to fast chemical kinetics. However, at the other conditions, where all the criteria for the plug flow reactor (PFR) idealization were satisfied, only 5% is assumed to be the residence time uncertainty.

Appendix C

Additional Experimental Data

Only a subset of experimental data on species concentrations was presented in Chapters 3, 4, and 6. The rest of the data is presented in this Appendix.

C.1 n-Dodecane pyrolysis

Figs. C.1 and C.2 show the measured concentrations of the n-dodecane fuel and its pyrolysis products as a function of residence time at 1150 K.

C.2 Jet A pyrolysis

Similarly, Figs. C.3 and C.4 show the measured concentrations of the products from pyrolysis of Jet A (POSF 10325) as a function of residence time at 1150 K.

C.3 MTS pyrolysis

Finally, Fig. C.5 shows the measured concentrations of MTS and methane (CH_4) as a function of nominal residence time at 1150 K and $\alpha = 10$.

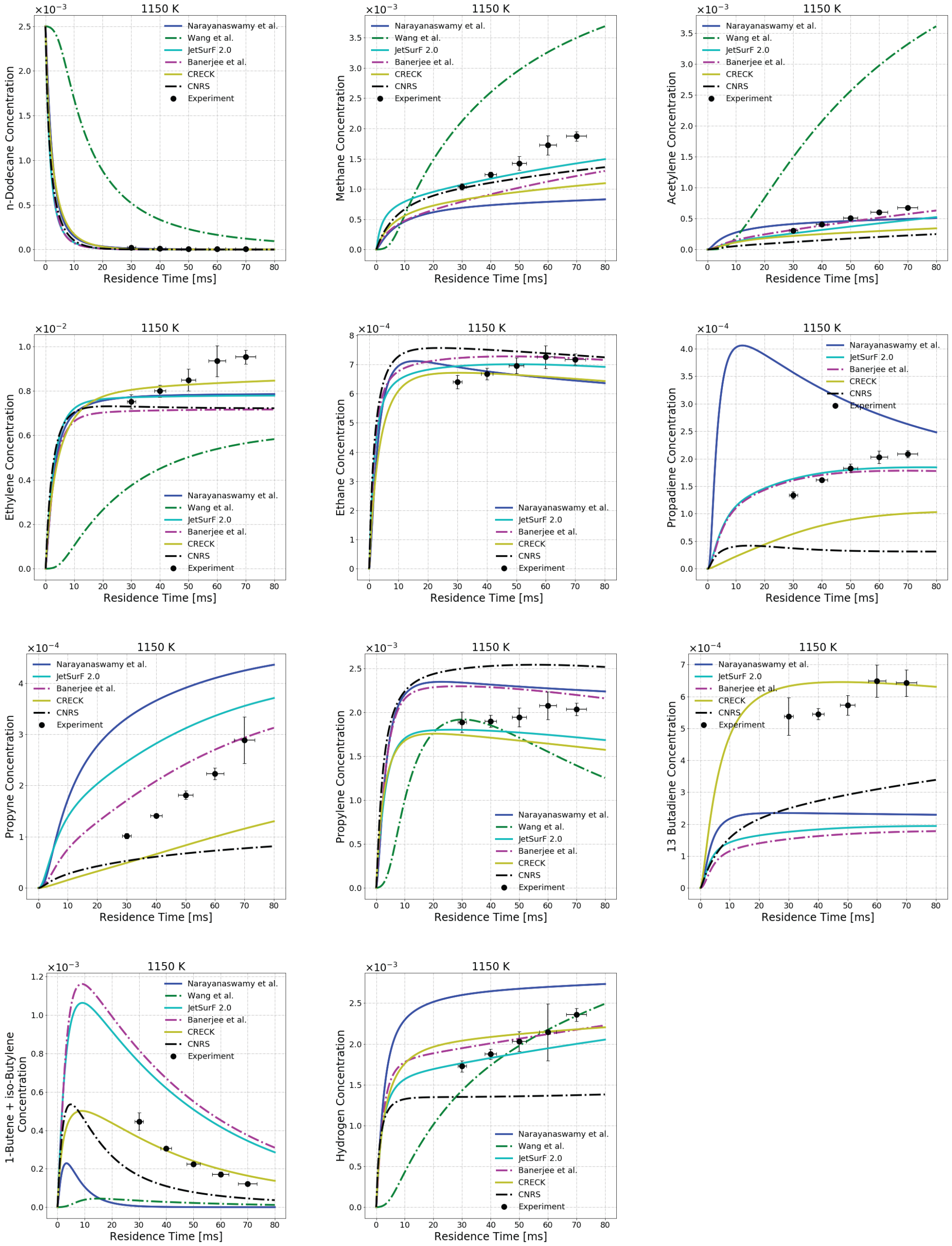

Figure C.1: Measured and predicted mole fractions of C_1-C_4 hydrocarbon species and H_2 during n-dodecane pyrolysis as a function of residence time at T = 1150 K and p = 1 atm. The n-dodecane ($C_{12}H_{26}$) fuel mole fraction is shown in the first plot. Tested models: Narayanaswamy et al. [95], Wang et al. [96], JetSurF 2.0 [25], Banerjee et al. [27], CRECK [88], and CNRS [89].

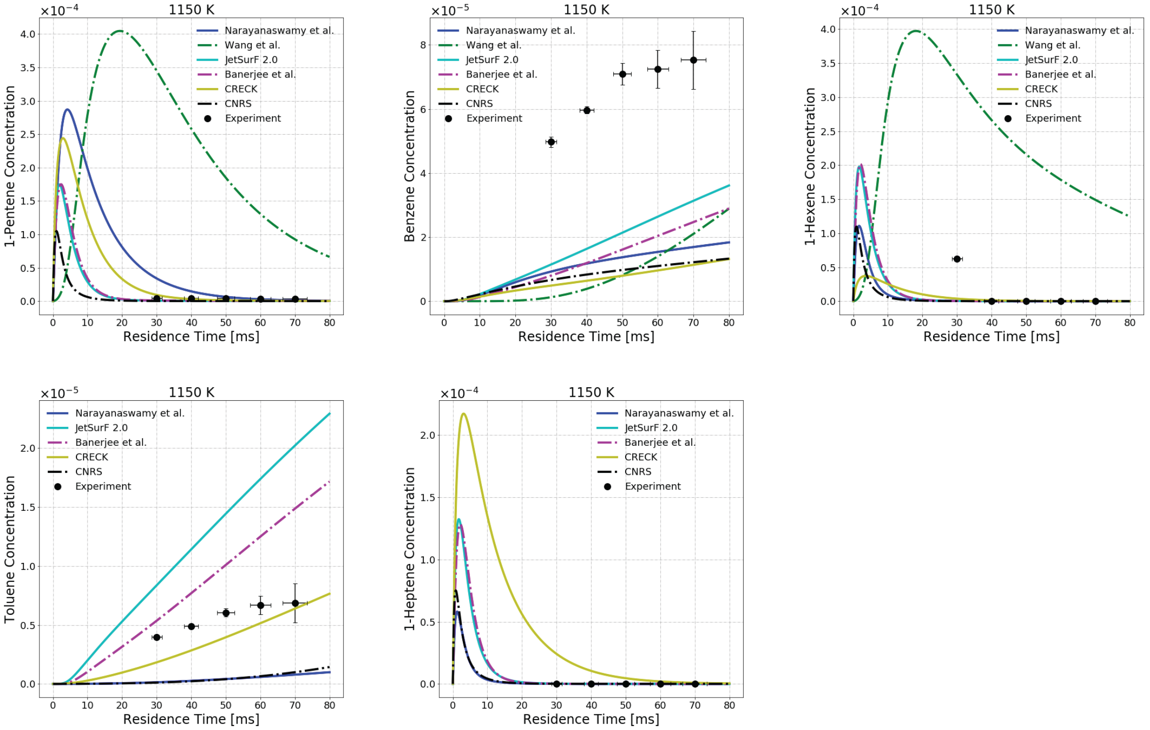

Figure C.2: Measured and predicted mole fractions of 1-pentene (C_5H_{10}), 1-hexene (C_6H_{12}), and 1-heptene (C_7H_{14}), benzene (C_6H_6), and toluene (C_7H_8) during n-dodecane pyrolysis as a function of residence time at T = 1150 K and p = 1 atm. Tested models: Narayanaswamy et al. [95], Wang et al. [96], JetSurF 2.0 [25], Banerjee et al. [27], CRECK [88], and CNRS [89].

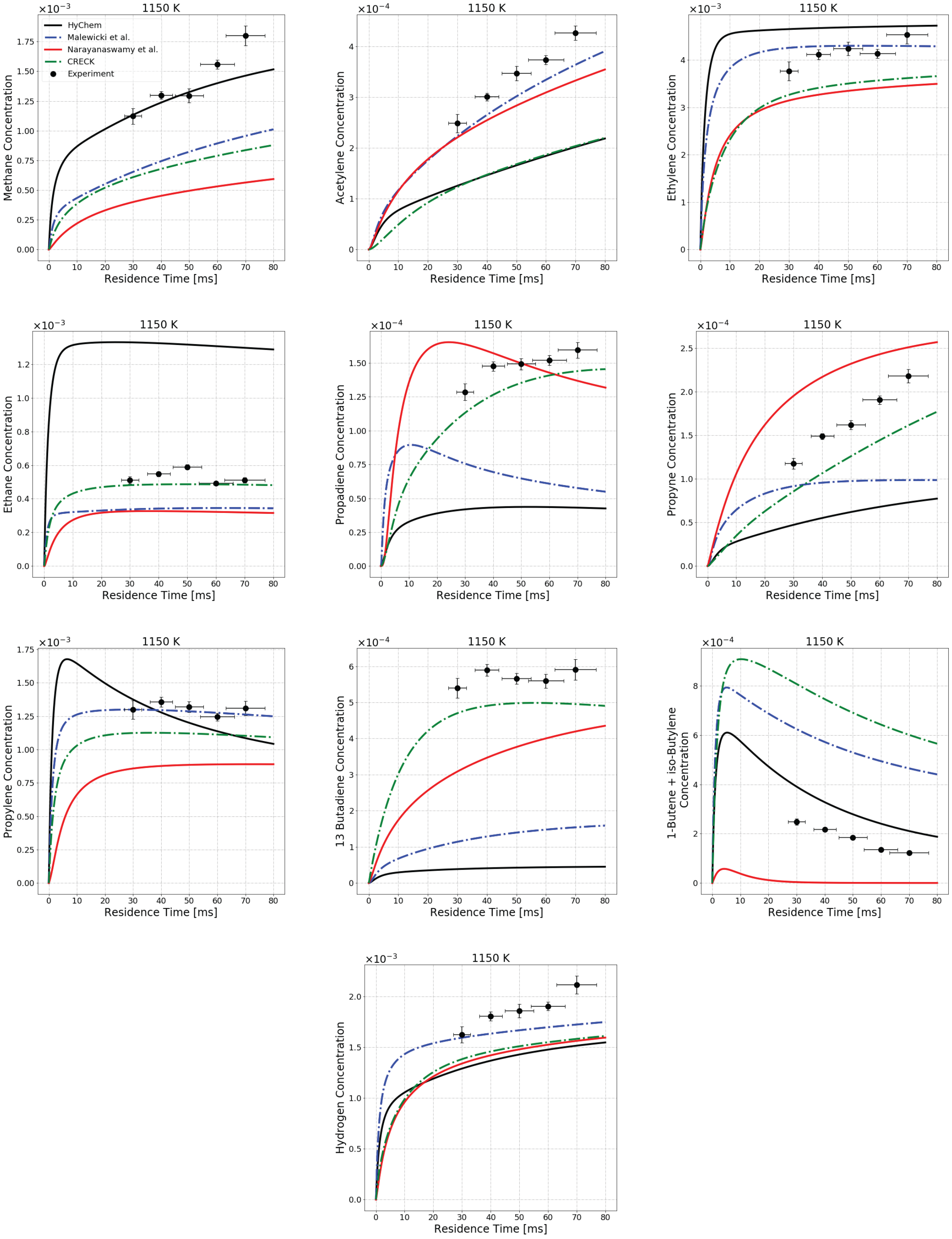

Figure C.3: Measured and predicted mole fractions of H_2 and C_1-C_4 hydrocarbon products from pyrolysis of Jet A as a function of residence time at 1150 K and 1 atm. Tested models are Malewicki et al. [128], Narayanaswamy et al. [130], CRECK [88], and HyChem [133].

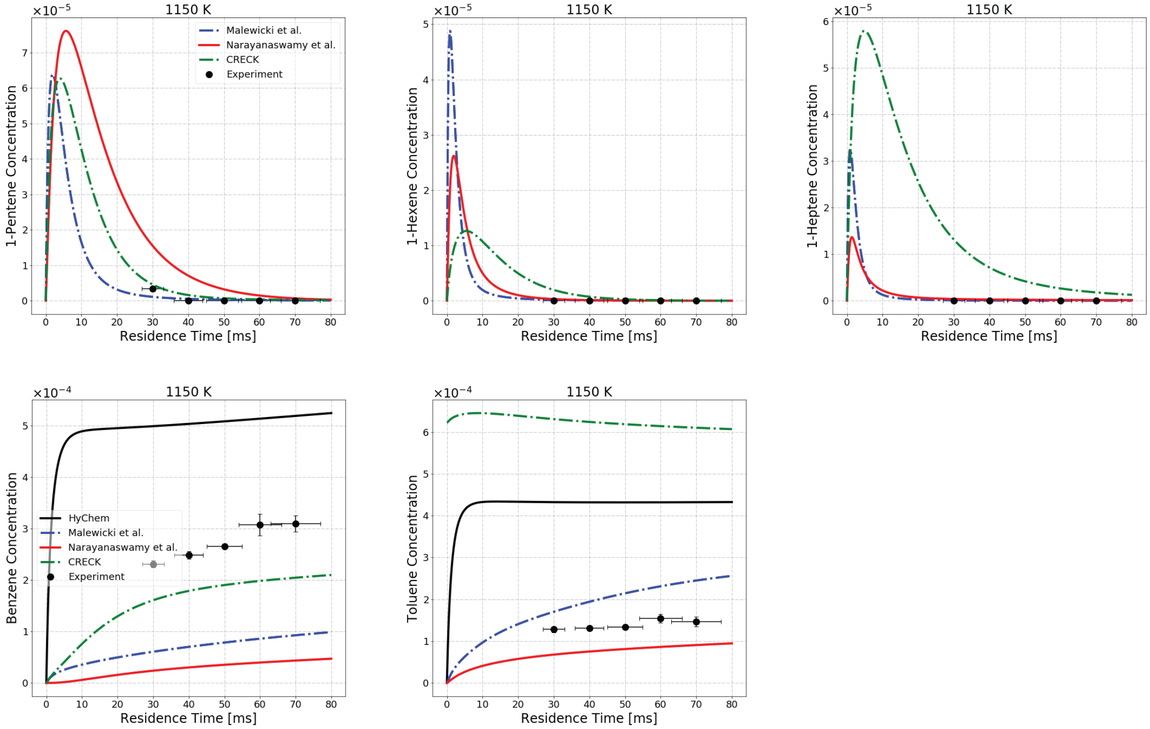

Figure C.4: Measured and predicted mole fractions of hydrocarbon products with more than 4 C atoms from pyrolysis of Jet A as a function of residence time at 1050 K and 1 atm. Tested models are Malewicki et al. [128], Narayanaswamy et al. [130], CRECK [88], and HyChem [133].

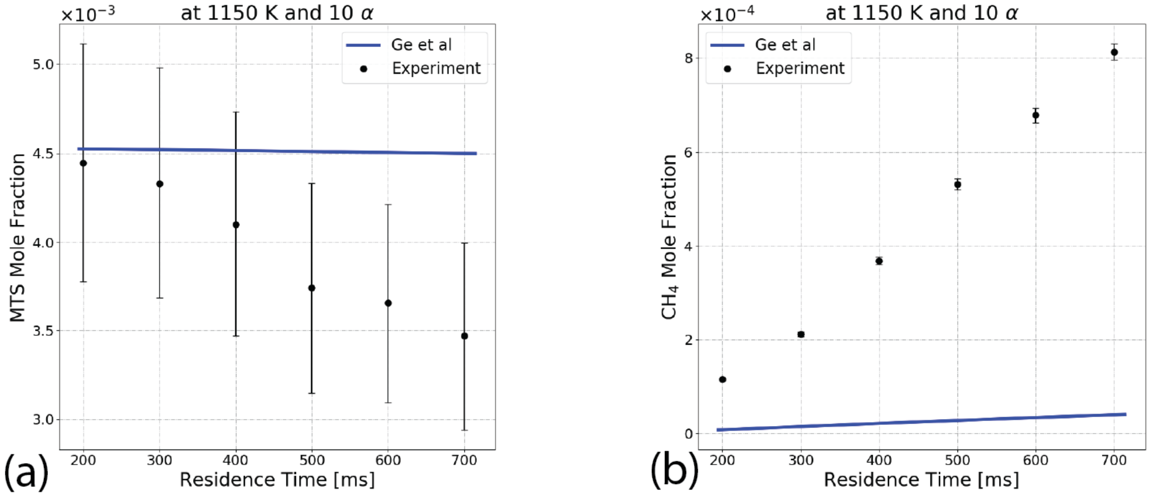

Figure C.5: Measured and predicted concentrations of four species: MTS and CH_4 as a function of nominal residence times at 1150 K and $\alpha = 10$.

Bibliography

[1] International civil aviation organization - future of aviation. `https://www.icao.int`, 2019.

[2] Barbara J Finlayson-Pitts and James N Pitts. Tropospheric air pollution: ozone, airborne toxics, polycyclic aromatic hydrocarbons, and particles. *Science*, 276(5315):1045–1051, 1997.

[3] Tami C Bond, Sarah J Doherty, David W Fahey, Piers M Forster, Terje Berntsen, Benjamin J DeAngelo, Mark G Flanner, S Ghan, Bernd Kärcher, Dorothy Koch, et al. Bounding the role of black carbon in the climate system: A scientific assessment. *Journal of Geophysical Research: Atmospheres*, 118(11):5380–5552, 2013.

[4] Stephan Bakan, Andreas Chlond, Ulrich Cubasch, Johann Feichter, H Graf, Hartmut Grassl, K Hasselmann, Ingo Kirchner, Mojib Latif, Erich Roeckner, et al. Climate response to smoke from the burning oil wells in kuwait. *Nature*, 351(6325):367–371, 1991.

[5] James Haywood and Olivier Boucher. Estimates of the direct and indirect radiative forcing due to tropospheric aerosols: A review. *Reviews of geophysics*, 38(4):513–543, 2000.

[6] Mark Z Jacobson. Strong radiative heating due to the mixing state of black carbon in atmospheric aerosols. *Nature*, 409(6821):695–697, 2001.

[7] Mark Z Jacobson. Effects of externally-through-internally-mixed soot inclusions within clouds and precipitation on global climate. *The Journal of Physical Chemistry A*, 110(21):6860–6873, 2006.

[8] Surabi Menon, James Hansen, Larissa Nazarenko, and Yunfeng Luo. Climate effects of black carbon aerosols in china and india. *Science*, 297(5590):2250–2253, 2002.

[9] James Hansen and Larissa Nazarenko. Soot climate forcing via snow and ice albedos. *Proceedings of the national academy of sciences*, 101(2):423–428, 2004.

[10] JoAnn Slama Lighty, John M Veranth, and Adel F Sarofim. Combustion aerosols: factors governing their size and composition and implications to human health. *Journal of the Air & Waste Management Association*, 50(9):1565–1618, 2000.

[11] Nicole AH Janssen, Gerard Hoek, Milena Simic-Lawson, Paul Fischer, Leendert Van Bree, Harry Ten Brink, Menno Keuken, Richard W Atkinson, H Ross Anderson, Bert Brunekreef, et al. Black carbon as an additional indicator of the adverse health effects of airborne particles compared with pm10 and pm2. 5. *Environmental health perspectives*, 119(12):1691–1699, 2011.

[12] Thomas F Stocker, Dahe Qin, Gian-Kasper Plattner, Melinda Tignor, Simon K Allen, Judith Boschung, Alexander Nauels, Yu Xia, Vincent Bex, Pauline M Midgley, et al. Climate change 2013: The physical science basis. *Contribution of working group I to the fifth assessment report of the intergovernmental panel on climate change*, 1535, 2013.

[13] Yun Qian, Teppei J Yasunari, Sarah J Doherty, Mark G Flanner, William KM Lau, Jing Ming, Hailong Wang, Mo Wang, Stephen G Warren, and Rudong Zhang. Light-absorbing particles in snow and ice: Measurement and modeling of climatic and hydrological impact. *Advances in Atmospheric Sciences*, 32(1):64–91, 2015.

[14] B Kärcher. Aviation-produced aerosols and contrails. *Surveys in geophysics*, 20(2):113–167, 1999.

[15] Brian S Haynes and H Gg Wagner. Soot formation. *Progress in energy and combustion science*, 7(4):229–273, 1981.

[16] Jack B Howard. Carbon addition and oxidation reactions in heterogeneous combustion and soot formation. In *Symposium (International) on Combustion*, volume 23, pages 1107–1127. Elsevier, 1991.

[17] Richard A Dobbins. Hydrocarbon nanoparticles formed in flames and diesel engines. *Aerosol Science and Technology*, 41(5):485–496, 2007.

[18] Gilles Prado, Jacques Lahaye, and Brian S Haynes. Soot particle nucleation and agglomeration. In *Soot in Combustion Systems and Its Toxic Properties*, pages 145–161. Springer, 1983.

[19] Henning Bockhorn. *Soot formation in combustion: mechanisms and models*, volume 59. Springer Science & Business Media, 2013.

[20] Charles S McEnally, Lisa D Pfefferle, Burak Atakan, and Katharina Kohse-Höinghaus. Studies of aromatic hydrocarbon formation mechanisms in flames: Progress towards closing the fuel gap. *Progress in Energy and Combustion Science*, 32(3):247–294, 2006.

[21] Hartwell F Calcote. Mechanisms of soot nucleation in flames—a critical review. *Combustion and Flame*, 42:215–242, 1981.

[22] Klaus-Heinrich Homann. Fullerenes and soot formation—new pathways to large particles in flames. *Angewandte Chemie International Edition*, 37(18):2434–2451, 1998.

[23] Hai Wang. Formation of nascent soot and other condensed-phase materials in flames. *Proceedings of the Combustion institute*, 33(1):41–67, 2011.

[24] Michael Frenklach. Reaction mechanism of soot formation in flames. *Physical chemistry chemical Physics*, 4(11):2028–2037, 2002.

[25] H Wang, E Dames, B Sirjean, D A Sheen, R Tango, A Violi, J Y W Lai, F N Egolfopoulos, D F Davidson, R K Hanson, C T Bowman, C., C K Law, W Tsang, N P Cernansky, D L Miller, and R P Lindstedt. A high-temperature chemical kinetic model of n-alkane (up to n-dodecane), cyclohexane, and methyl-, ethyl-, n-propyl and n-butyl-cyclohexane oxidation at high temperatures, jetsurf version 2.0. http://web.stanford.edu/group/haiwanglab/JetSurF/JetSurF2.0/index.html, September 2010.

[26] Nick M Marinov, William J Pitz, Charles K Westbrook, Antonio M Vincitore, Marco J Castaldi, Selim M Senkan, and Carl F Melius. Aromatic and polycyclic aromatic hydrocarbon formation in a laminar premixed n-butane flame. *Combustion and flame*, 114(1-2):192–213, 1998.

[27] Sayak Banerjee, Rei Tangko, David A Sheen, Hai Wang, and C Tom Bowman. An experimental and kinetic modeling study of n-dodecane pyrolysis and oxidation. *Combustion and Flame*, 163:12–30, 2016.

[28] Alessio Frassoldati, Alberto Cuoci, Tiziano Faravelli, Ulrich Niemann, Eliseo Ranzi, Reinhard Seiser, and Kalyanasundaram Seshadri. An experimental and kinetic modeling study of n-propanol and iso-propanol combustion. *Combustion and Flame*, 157(1):2–16, 2010.

[29] Chong-Wen Zhou, Yang Li, Ultan Burke, Colin Banyon, Kieran P Somers, Shuiting Ding, Saadat Khan, Joshua W Hargis, Travis Sikes, Olivier Mathieu, et al. An experimental and chemical kinetic modeling study of 1, 3-butadiene combustion: Ignition delay time and laminar flame speed measurements. *Combustion and Flame*, 197:423–438, 2018.

[30] G Blanquart, P Pepiot-Desjardins, and H Pitsch. Chemical mechanism for high temperature combustion of engine relevant fuels with emphasis on soot precursors. *Combustion and Flame*, 156(3):588–607, 2009.

[31] John B Homer and GB Kistiakowsky. Oxidation and pyrolysis of ethylene in shock waves. *The Journal of Chemical Physics*, 47(12):5290–5295, 1967.

[32] Gordon B Skinner and Edward M Sokoloski. Shock tube experiments on the pyrolysis of ethylene. *The Journal of Physical Chemistry*, 64(8):1028–1031, 1960.

[33] JH Kiefer, SA Kapsalis, MZ Al-Alami, and KA Budach. The very high temperature pyrolysis of ethylene and the subsequent reactions of product acetylene. *Combustion and Flame*, 51:79–93, 1983.

[34] Koyo Norinaga, Vinod M Janardhanan, and Olaf Deutschmann. Detailed chemical kinetic modeling of pyrolysis of ethylene, acetylene, and propylene at 1073–1373 k with a plug-flow reactor model. *International Journal of Chemical Kinetics*, 40(4):199–208, 2008.

[35] Hai Wang, Rui Xu, Kun Wang, Craig T Bowman, Ronald K Hanson, David F Davidson, Kenneth Brezinsky, and Fokion N Egolfopoulos. A physics-based approach to modeling real-fuel combustion chemistry-i. evidence from experiments, and thermodynamic, chemical kinetic and statistical considerations. *Combustion and Flame*, 193:502–519, 2018.

[36] Hugh O Pierson. *Handbook of chemical vapor deposition: principles, technology and applications*. William Andrew, 1999.

[37] Jan-Otto Carlsson. Processes in interfacial zones during chemical vapour deposition: aspects of kinetics, mechanisms, adhesion and substrate atom transport. *Thin solid films*, 130(3-4):261–282, 1985.

[38] F. Loumagne, F. Langlais, R. Naslain, S. Schamm, D. Dorignac, and J. Sévely. Physicochemical properties of SiC-based ceramics deposited by low pressure chemical vapor deposition from CH3SiCl3H2. *Thin Solid Films*, 254(1-2):75–82, 1995.

[39] Stewart K Griffiths and Robert H Nilson. Optimum conditions for composites fiber coating by chemical vapor infiltration. *Journal of the Electrochemical Society*, 145(4):1263–1272, 1998.

[40] John Y Ofori and Stratis V Sotirchos. Optimal pressures and temperatures for isobaric, isothermal chemical vapor infiltration. *AIChE journal*, 42(10):2828–2840, 1996.

[41] Kenneth Petroski, Shannon Poges, Chris Monteleone, Joseph Grady, Ram Bhatt, and Steven L Suib. Rapid chemical vapor infiltration of silicon carbide minicomposites at atmospheric pressure. *ACS applied materials & interfaces*, 10(5):4986–4992, 2018.

[42] Takahiro Takahashi, Katsunori Hagiwara, Hiroshi Komiyama, and Yasuyuki Egashira. The effects of gas-phase additives nh3, no, and no2 on sih4/o2 chemical vapor deposition. *Journal of The Electrochemical Society*, 145(3):1070, 1998.

[43] David A Masten, Ronald K Hanson, and Craig T Bowman. Shock tube study of the reaction hydrogen atom+ oxygen. fwdarw. hydroxyl+ oxygen atom using hydroxyl laser absorption. *Journal of Physical Chemistry*, 94(18):7119–7128, 1990.

[44] JF Bott and N Cohen. A shock tube study of the reaction of methyl radicals with hydroxyl radicals. *International journal of chemical kinetics*, 23(11):1017–1033, 1991.

[45] Venkatesh Vasudevan, Ronald K Hanson, Craig T Bowman, David M Golden, and David F Davidson. Shock tube study of the reaction of ch with n2: overall rate and branching ratio. *The Journal of Physical Chemistry A*, 111(46):11818–11830, 2007.

[46] Subith S Vasu, David F Davidson, and Ronald K Hanson. Jet fuel ignition delay times: Shock tube experiments over wide conditions and surrogate model predictions. *Combustion and flame*, 152(1-2):125–143, 2008.

[47] Eric L Petersen and Ronald K Hanson. Nonideal effects behind reflected shock waves in a high-pressure shock tube. *Shock Waves*, 10(6):405–420, 2001.

[48] Olivier Herbinet and Guillaume Dayma. Jet-stirred reactors. In *Cleaner combustion*, pages 183–210. Springer, 2013.

[49] PM Marquaire and GM Côme. Non quasi-stationary state pyrolysis. induction period of neopentane pyrolysis. *Reaction Kinetics and Catalysis Letters*, 9(2):165–169, 1978.

[50] Mohammed Hichem Hakka, Pierre-Alexandre Glaude, Olivier Herbinet, and Frédérique Battin-Leclerc. Experimental study of the oxidation of large surrogates for diesel and biodiesel fuels. *Combustion and Flame*, 156(11):2129–2144, 2009.

[51] Olivier Herbinet, Frédérique Battin-Leclerc, Sarah Bax, Hervé Le Gall, Pierre-Alexandre Glaude, René Fournet, Zhongyue Zhou, Liulin Deng, Huijun Guo, Mingfeng Xie, et al. Detailed product analysis during the low temperature oxidation of n-butane. *Physical Chemistry Chemical Physics*, 13(1):296–308, 2011.

[52] Frederick L Dryer, Francis M Haas, Jeffrey Santner, Tanvir I Farouk, and Marcos Chaos. Interpreting chemical kinetics from complex reaction–advection–diffusion systems: Modeling of flow reactors and related experiments. *Progress in energy and combustion science*, 44:19–39, 2014.

[53] MA Mueller, TJ Kim, Richard A Yetter, and FL Dryer. Flow reactor studies and kinetic modeling of the h2/o2 reaction. *International Journal of Chemical Kinetics*, 31(2):113–125, 1999.

[54] Robert H Natelson, Matthew S Kurman, Nicholas P Cernansky, and David L Miller. Low temperature oxidation of n-butylcyclohexane. *Combustion and flame*, 158(12):2325–2337, 2011.

[55] MU Alzueta and JM Hernández. Ethanol oxidation and its interaction with nitric oxide. *Energy & fuels*, 16(1):166–171, 2002.

[56] Zhi Li, Juergen Eckwert, Adam Łapicki, and Scott L Anderson. Low energy, high resolution ion scattering mass spectrometry of strained molecules and their isomers. *International journal of mass spectrometry and ion processes*, 167:269–279, 1997.

[57] Brian Van Devener and Scott L Anderson. Breakdown and combustion of jp-10 fuel catalyzed by nanoparticulate ceo2 and fe2o3. *Energy & fuels*, 20(5):1886–1894, 2006.

[58] Shiju Thomas and Mary J Wornat. Effects of acetylene addition on yields of the c1- c10 hydrocarbon products of catechol pyrolysis. *Energy & fuels*, 22(2):976–986, 2008.

[59] Hisashi Nakamura, Ryu Tanimoto, Takuya Tezuka, Susumu Hasegawa, and Kaoru Maruta. Soot formation characteristics and pah formation process in a micro flow reactor with a controlled temperature profile. *Combustion and flame*, 161(2):582–591, 2014.

[60] Christian Lund Rasmussen, Anja Egede Rasmussen, and Peter Glarborg. Sensitizing effects of nox on ch4 oxidation at high pressure. *Combustion and Flame*, 154(3):529–545, 2008.

[61] U Shrestha, MJ Rahimi, GP Simms, and HK Chelliah. Fuel pyrolysis in a microflow tube reactor–measurement and modeling uncertainties of ethane, n-butane, and n-dodecane pyrolysis. *Combustion and Flame*, 177:10–23, 2017.

[62] John V. Seeley, John T. Jayne, and Mario J. Molina. High pressure fast-flow technique for gas phase kinetics studies. *International Journal of Chemical Kinetics*, 25(7):571–594, 1993.

[63] A. A. Westenberg and N. de Haas. Atom—molecule kinetics at high temperature using esr detection. technique and results for o +h2, o +ch4, and o +c2h6. *The Journal of Chemical Physics*, 46(2):490–501, 1967.

[64] Carleton J. Howard. Kinetic measurements using flow tubes. *The Journal of Physical Chemistry*, 83(1):3–9, 1979.

[65] A.M. Dean, J.E. Hardy, and R.K. Lyon. Kinetics and mechanism of nh3 oxidation. *Symposium (International) on Combustion*, 19(1):97 – 105, 1982. Nineteenth Symposium (International) on Combustion.

[66] Francis M. Haas. *Studies of small molecule reactions foundational to combustion chemistry, including experimental measurements from a novel high pressure flow reactor*. PhD thesis, Princeton University, 2016.

[67] Ujuma Shrestha. *Fuel pyrolysis at atmospheric and elevated pressure conditions in microflow tube reactor*. PhD thesis, Mechanical and Aerospace Engineering, Univerisity of Virginia, 2017.

[68] Greg Simms. *An investigation of pyrolytic cracking of JP-10 in laminar flow reactors with molecular beam mass spectrometry*. PhD thesis, Mechanical and Aerospace Engineering, University of Virginia, 2018.

[69] Andrew Hall Cutler, Michael Jerry Antal Jr, and Maitland Jones Jr. A critical evaluation of the plug-flow idealization of tubular-flow reactor data. *Industrial & engineering chemistry research*, 27(4):691–697, 1988.

[70] Geoffrey Ingram Taylor. Dispersion of soluble matter in solvent flowing slowly through a tube. *Proceedings of the Royal Society of London. Series A. Mathematical and Physical Sciences*, 219(1137):186–203, 1953.

[71] Rutherford Aris. On the dispersion of a solute in a fluid flowing through a tube. *Proceedings of the Royal Society of London. Series A. Mathematical and Physical Sciences*, 235(1200):67–77, 1956.

[72] George D Papasouliotis and Stratis V Sotirchos. Experimental study of atmospheric pressure chemical vapor deposition of silicon carbide from methyltrichlorosilane. *Journal of materials research*, 14(8):3397–3409, 1999.

[73] Yvette Gertrude Roman. *Forced flow chemical vapor infiltration*. PhD thesis, Eindhoven University of Technology, 1994.

[74] Bruce E Poling, John M Prausnitz, John P O'connell, et al. *The properties of gases and liquids*, volume 5. Mcgraw-hill New York, 2001.

[75] Philip D Neufeld, AR Janzen, and RA Aziz. Empirical equations to calculate 16 of the transport collision integrals ω (l, s)* for the lennard-jones (12–6) potential. *The Journal of Chemical Physics*, 57(3):1100–1102, 1972.

[76] Michael Frenklach and Hai Wang. Detailed mechanism and modeling of soot particle formation. In *Soot formation in combustion*, pages 165–192. Springer, 1994.

[77] M Frenklach, WC Gardiner, SE Stein, DW Clary, and T Yuan. Mechanism of soot formation in acetylene-oxygen mixtures. *Combustion science and technology*, 50(1-3):79–115, 1986.

[78] Carl F Melius, James A Miller, and Earl M Evleth. Unimolecular reaction mechanisms involving c3h4, c4h4, and c6h6 hydrocarbon species. In *Symposium (International) on Combustion*, volume 24, pages 621–628. Elsevier, 1992.

[79] Lisa D Pfefferle, German Bermudez, and James Boyle. Benzene and higher hydrocarbon formation during allene pyrolysis. In *Soot Formation in Combustion*, pages 25–49. Springer, 1994.

[80] RD Kern and K Xie. Shock tube studies of gas phase reactions preceding the soot formation process. *Progress in energy and combustion science*, 17(3):191–210, 1991.

[81] Stephen E Stein, James A Walker, Mahendra M Suryan, and Askar Fahr. A new path to benzene in flames. In *Symposium (International) on Combustion*, volume 23, pages 85–90. Elsevier, 1991.

[82] CH Wu and RD Kern. Shock-tube study of allene pyrolysis. *Journal of Physical Chemistry*, 91(24):6291–6296, 1987.

[83] Zoran M Djurisic. *Detailed kinetic modeling of benzene and toluene oxidation at high temperatures*. PhD thesis, University of Delaware, 1999.

[84] Michael Frenklach, David W Clary, William C Gardiner Jr, and Stephen E Stein. Effect of fuel structure on pathways to soot. In *Symposium (International) on Combustion*, volume 21, pages 1067–1076. Elsevier, 1988.

[85] JD Bittner and JB Howard. Composition profiles and reaction mechanisms in a near-sooting premixed benzene/oxygen/argon flame. In *Symposium (International) on Combustion*, volume 18, pages 1105–1116. Elsevier, 1981.

[86] M Frenklach, S Taki, and RA Matula. A conceptual model for soot formation in pyrolysis of aromatic hydrocarbons. *Combustion and Flame*, 49(1-3):275–282, 1983.

[87] M Frenklach, S Taki, MB Durgaprasad, and RA Matula. Soot formation in shock-tube pyrolysis of acetylene, allene, and 1, 3-butadiene. *Combustion and Flame*, 54(1-3):81–101, 1983.

[88] Ranzi, Alessio Frassoldati, Roberto Grana, Alberto Cuoci, Tiziano Faravelli, AP Kelley, and Chung King Law. Hierarchical and comparative kinetic modeling of laminar flame speeds of hydrocarbon and oxygenated fuels. *Progress in Energy and Combustion Science*, 38(4):468–501, 2012.

[89] Amir Mze-Ahmed, Kamal Hadj-Ali, Philippe Dagaut, and Guillaume Dayma. Experimental and modeling study of the oxidation kinetics of n-undecane and n-dodecane in a jet-stirred reactor. *Energy & fuels*, 26(7):4253–4268, 2012.

[90] Tianfeng Lu and Chung K Law. Toward accommodating realistic fuel chemistry in large-scale computations. *Progress in Energy and Combustion Science*, 35(2):192–215, 2009.

[91] Kyle E Niemeyer, Chih-Jen Sung, and Mandhapati P Raju. Skeletal mechanism generation for surrogate fuels using directed relation graph with error propagation and sensitivity analysis. *Combustion and flame*, 157(9):1760–1770, 2010.

[92] Gaetano Esposito. *Reduction and Uncertainty Analysis of Chemical Mechanisms based on Local and Global Sensitivities.* PhD thesis, University of Virginia, 2010.

[93] Perrine Pepiot-Desjardins and Heinz Pitsch. An efficient error-propagation-based reduction method for large chemical kinetic mechanisms. *Combustion and Flame*, 154(1-2):67–81, 2008.

[94] Perrine Pepiot-Desjardins and Heinz Pitsch. An automatic chemical lumping method for the reduction of large chemical kinetic mechanisms. *Combustion Theory and Modelling*, 12(6):1089–1108, 2008.

[95] Krithika Narayanaswamy, Perrine Pepiot, and Heinz Pitsch. A chemical mechanism for low to high temperature oxidation of n-dodecane as a component of transportation fuel surrogates. *Combustion and Flame*, 161(4):866–884, 2014.

[96] Hu Wang, Youngchul Ra, Ming Jia, and Rolf D Reitz. Development of a reduced n-dodecane-pah mechanism and its application for n-dodecane soot predictions. *Fuel*, 136:25–36, 2014.

[97] S Som, DE Longman, Z Luo, M Plomer, and T Lu. Three dimensional simulations of diesel sprays using n-dodecane as a surrogate. In *Fall technical meeting of the eastern states section of the combustion institute*, 2011.

[98] Yuanjiang Pei, Evatt R Hawkes, Sanghoon Kook, Graham M Goldin, and Tianfeng Lu. Modelling n-dodecane spray and combustion with the transported probability density function method. *Combustion and Flame*, 162(5):2006–2019, 2015.

[99] Youngchul Ra and Rolf D Reitz. A combustion model for multi-component fuels using a physical surrogate group chemistry representation (psgcr). *Combustion and Flame*, 162(10):3456–3481, 2015.

[100] Xiaoqing You, Fokion N Egolfopoulos, and Hai Wang. Detailed and simplified kinetic models of n-dodecane oxidation: The role of fuel cracking in aliphatic hydrocarbon combustion. *Proceedings of the Combustion Institute*, 32(1):403–410, 2009.

[101] Eliseo Ranzi, Alessio Frassoldati, Alessandro Stagni, Matteo Pelucchi, Alberto Cuoci, and Tiziano Faravelli. Reduced kinetic schemes of complex reaction systems: fossil and biomass-derived transportation fuels. *International Journal of Chemical Kinetics*, 46(9):512–542, 2014.

[102] Bo Li, Hai Zhang, and Fokion N Egolfopoulos. Laminar flame propagation of atmospheric iso-cetane/air and decalin/air mixtures. *Combustion and flame*, 161(1):154–161, 2014.

[103] Subith S Vasu, David F Davidson, Z Hong, V Vasudevan, and Ronald K Hanson. n-dodecane oxidation at high-pressures: Measurements of ignition delay times and oh concentration time-histories. *Proceedings of the Combustion Institute*, 32(1):173–180, 2009.

[104] Hsi-Ping S Shen, Justin Steinberg, Jeremy Vanderover, and Matthew A Oehlschlaeger. A shock tube study of the ignition of n-heptane, n-decane, n-dodecane, and n-tetradecane at elevated pressures. *Energy & Fuels*, 23(5):2482–2489, 2009.

[105] DF Davidson, DR Haylett, and RK Hanson. Development of an aerosol shock tube for kinetic studies of low-vapor-pressure fuels. *Combustion and Flame*, 155(1-2):108–117, 2008.

[106] DF Davidson, Z Hong, GL Pilla, A Farooq, RD Cook, and RK Hanson. Multi-species time-history measurements during n-dodecane oxidation behind reflected shock waves. *Proceedings of the Combustion Institute*, 33(1):151–157, 2011.

[107] Matthew S Kurman, Robert H Natelson, Nicholas P Cernansky, and David L Miller. Speciation of the reaction intermediates from n-dodecane oxidation in the low temperature regime. *Proceedings of the Combustion Institute*, 33(1):159–166, 2011.

[108] Chunsheng Ji, Enoch Dames, Yang L Wang, Hai Wang, and Fokion N Egolfopoulos. Propagation and extinction of premixed c5–c12 n-alkane flames. *Combustion and Flame*, 157(2):277–287, 2010.

[109] David G. Goodwin, Raymond L. Speth, Harry K. Moffat, and Bryan W. Weber. Cantera: An object-oriented software toolkit for chemical kinetics, thermodynamics, and transport processes. `https://www.cantera.org`, 2018. Version 2.4.0.

[110] K Narayanaswamy, G Blanquart, and H Pitsch. A consistent chemical mechanism for oxidation of substituted aromatic species. *Combustion and Flame*, 157(10):1879–1898, 2010.

[111] S Mani Sarathy, Charles K Westbrook, Marco Mehl, William J Pitz, Casimir Togbe, Philippe Dagaut, Hai Wang, Matthew A Oehlschlaeger, Ulrich Niemann, Kalyanasundaram Seshadri, et al. Comprehensive chemical kinetic modeling of the oxidation of 2-methylalkanes from c7 to c20. *Combustion and flame*, 158(12):2338–2357, 2011.

[112] Nadezhda A Slavinskaya, Uwe Riedel, Seth B Dworkin, and Murray J Thomson. Detailed numerical modeling of pah formation and growth in non-premixed ethylene and ethane flames. *Combustion and Flame*, 159(3):979–995, 2012.

[113] Tomasz Malewicki and Kenneth Brezinsky. Experimental and modeling study on the pyrolysis and oxidation of n-decane and n-dodecane. *Proceedings of the Combustion Institute*, 34(1):361–368, 2013.

[114] Olivier Herbinet, Paul-Marie Marquaire, Frédérique Battin-Leclerc, and René Fournet. Thermal decomposition of n-dodecane: Experiments and kinetic modeling. *Journal of analytical and applied pyrolysis*, 78(2):419–429, 2007.

[115] Meredith Colket, Joshua Heyne, Mark Rumizen, Mohan Gupta, Tim Edwards, William M Roquemore, Gurhan Andac, Randy Boehm, Jeffery Lovett, Randy Williams, et al. Overview of the national jet fuels combustion program. *AiAA Journal*, pages 1087–1104, 2017.

[116] James T Edwards. Reference jet fuels for combustion testing. In *55th AIAA Aerospace Sciences Meeting*, page 0146, 2017.

[117] A Violi, S Yan, EG Eddings, AF Sarofim, Silvia Granata, Tiziano Faravelli, and ELISEO Ranzi. Experimental formulation and kinetic model for jp-8 surrogate mixtures. *Combustion Science and Technology*, 174(11-12):399–417, 2002.

[118] Tim Edwards and Lourdes Q Maurice. Surrogate mixtures to represent complex aviation and rocket fuels. *Journal of Propulsion and Power*, 17(2):461–466, 2001.

[119] Philippe Dagaut and Michel Cathonnet. The ignition, oxidation, and combustion of kerosene: A review of experimental and kinetic modeling. *Progress in energy and combustion science*, 32(1):48–92, 2006.

[120] Corinne Guéret, Michel Cathonnet, Jean-Claude Boettner, and Françoise Gaillard. Experimental study and modeling of kerosene oxidation in a jet-stirred flow reactor. In *Symposium (International) on Combustion*, volume 23, pages 211–216. Elsevier, 1991.

[121] Steven Zabarnick. Chemical kinetic modeling of jet fuel autoxidation and antioxidant chemistry. *Industrial & engineering chemistry research*, 32(6):1012–1017, 1993.

[122] L Maurice, J Blust, K Leung, and R Lindstedt. Emissions from combustion of hydrocarbons in a well-stirred reactor. In *37th Aerospace Sciences Meeting and Exhibit*, page 1038, 1999.

[123] RP Lindstedt and LQ Maurice. Detailed chemical-kinetic model for aviation fuels. *Journal of Propulsion and Power*, 16(2):187–195, 2000.

[124] S Humer, A Frassoldati, S Granata, T Faravelli, E Ranzi, R Seiser, and K Seshadri. Experimental and kinetic modeling study of combustion of jp-8, its surrogates and reference components in laminar nonpremixed flows. *Proceedings of the Combustion Institute*, 31(1):393–400, 2007.

[125] AJ Dean, OG Penyazkov, KL Sevruk, and B Varatharajan. Autoignition of surrogate fuels at elevated temperatures and pressures. *Proceedings of the Combustion Institute*, 31(2):2481–2488, 2007.

[126] Stephen Dooley, Sang Hee Won, Marcos Chaos, Joshua Heyne, Yiguang Ju, Frederick L Dryer, Kamal Kumar, Chih-Jen Sung, Haowei Wang, Matthew A Oehlschlaeger, et al. A jet fuel surrogate formulated by real fuel properties. *Combustion and flame*, 157(12):2333–2339, 2010.

[127] Stephen Dooley, Sang Hee Won, Joshua Heyne, Tanvir I Farouk, Yiguang Ju, Frederick L Dryer, Kamal Kumar, Xin Hui, Chih-Jen Sung, Haowei Wang, et al. The experimental evaluation of a methodology for surrogate fuel formulation to emulate gas phase combustion kinetic phenomena. *Combustion and Flame*, 159(4):1444–1466, 2012.

[128] Tomasz Malewicki, Soumya Gudiyella, and Kenneth Brezinsky. Experimental and modeling study on the oxidation of jet a and the n-dodecane/iso-octane/n-propylbenzene/1, 3, 5-trimethylbenzene surrogate fuel. *Combustion and Flame*, 160(1):17–30, 2013.

[129] Doohyun Kim, Jason Martz, and Angela Violi. A surrogate for emulating the physical and chemical properties of conventional jet fuel. *Combustion and Flame*, 161(6):1489–1498, 2014.

[130] Krithika Narayanaswamy, Heinz Pitsch, and Perrine Pepiot. A component library framework for deriving kinetic mechanisms for multi-component fuel surrogates: Application for jet fuel surrogates. *Combustion and Flame*, 165:288–309, 2016.

[131] Dongil Kang, Vickey Kalaskar, Doohyun Kim, Jason Martz, Angela Violi, and André Boehman. Experimental study of autoignition characteristics of jet-a surrogates and their validation in a motored engine and a constant-volume combustion chamber. *Fuel*, 184:565–580, 2016.

[132] Doohyun Kim and Angela Violi. Hydrocarbons for the next generation of jet fuel surrogates. *Fuel*, 228:438–444, 2018.

[133] Hai Wang, Rui Xu, Kun Wang, Craig T Bowman, Ronald K Hanson, David F Davidson, Kenneth Brezinsky, and Fokion N Egolfopoulos. A physics-based approach to modeling real-fuel combustion chemistry-i. evidence from experiments, and thermodynamic, chemical kinetic and statistical considerations. *Combustion and Flame*, 193:502–519, 2018.

[134] Rui Xu, Kun Wang, Sayak Banerjee, Jiankun Shao, Tom Parise, Yangye Zhu, Shengkai Wang, Ashkan Movaghar, Dong Joon Lee, Runhua Zhao, et al. A physics-based approach to modeling real-fuel combustion chemistry–ii. reaction kinetic models of jet and rocket fuels. *Combustion and Flame*, 193:520–537, 2018.

[135] Yujie Tao, Rui Xu, Kun Wang, Jiankun Shao, Sarah E Johnson, Ashkan Movaghar, Xu Han, Ji-Woong Park, Tianfeng Lu, Kenneth Brezinsky, et al. A physics-based approach to modeling real-fuel combustion chemistry–iii. reaction kinetic model of jp10. *Combustion and Flame*, 198:466–476, 2018.

[136] Kun Wang, Rui Xu, Tom Parise, Jiankun Shao, Ashkan Movaghar, Dong Joon Lee, Ji-Woong Park, Yang Gao, Tianfeng Lu, Fokion N Egolfopoulos, et al. A physics-based approach to modeling real-fuel combustion chemistry–iv. hychem modeling of combustion kinetics of a bio-derived jet fuel and its blends with a conventional jet a. *Combustion and Flame*, 198:477–489, 2018.

[137] R. J. Price. Properties of Silicon Carbide for Nuclear Fuel Particle Coatings. *Nuclear Technology*, 35(2):320–336, 1977.

[138] K. Sasaki, E. Sakuma, S. Misawa, S. Yoshida, and S Gonda. High-temperature electrical properties of 3C-SiC epitaxial layers grown by chemical vapor deposition. *Appl. Phys. Lett*, 45, 1984.

[139] A. Mortensen. *Concise encyclopedia of composite materials*. Elsevier, 2007.

[140] N. P. Bansal and A. R. Boccaccini. *Ceramics and composites processing methods*. Wiley, 2012.

[141] F Loumagne, F Langlais, and R Naslain. Experimental kinetic study of the chemical vapour deposition of sic-based ceramics from ch3sicl3h2 gas precursor. *Journal of crystal growth*, 155(3-4):198–204, 1995.

[142] M. G. So and J. S. Chun. Growth and structure of chemical vapor deposited silicon carbide from methyltrichlorosilane and hydrogen in the temperature range of 1100 to 1400 °C. *Journal of Vacuum Science & Technology A: Vacuum, Surfaces, and Films*, 6(1):5–8, 1988.

[143] C. C. Chiu, S. B. Desu, and C. Y. Tsai. Low pressure chemical vapor deposition (LPCVD) of β-SiC on Si(100) using MTS in a hot wall reactor. 2019.

[144] H. S. Kim and D. J. Choi. The reactant depletion effect on chemically vapor deposited SiC films with pressure and gas ambient. *Thin Solid Films*, 312(1-2):195–201, 1998.

[145] J. H. Oh, B. J. Oh, D. J. Choi, G. H. Kim, and H. S. Song. The effect of input gas ratio on the growth behavior of chemical vapor deposited SiC films. *Journal of Materials Science*, 36:1695–1700, 2001.

[146] Y. Long, A. Javed, I. Shapiro, Z. K. Chen, X. Xiong, and P. Xiao. The effect of substrate position on the microstructure and mechanical properties of SiC coatings on carbon/carbon composites. *Surface and Coatings Technology*, 206(2-3):568–574, 2011.

[147] Mark D Allendorf and Carl F Melius. Theoretical study of thermochemistry of molecules in the silicon-carbon-chlorine-hydrogn system. *The Journal of Physical Chemistry*, 97(3):720–728, 1993.

[148] Thomas H Osterheld, Mark D Allendorf, and Carl F Melius. Unimolecular decomposition of methyltrichlorosilane: Rrkm calculations. *The Journal of Physical Chemistry*, 98(28):6995–7003, 1994.

[149] Mark D Allendorf and Thomas H Osterheld. Modeling the gas-phase chemistry of silicon carbide formation. *MRS Online Proceedings Library Archive*, 363, 1994.

[150] M Ganz, N Dorval, M Lefebvre, M Péalat, F Loumagne, and F Langlais. In situ optical analysis of the gas phase during the deposition of silicon carbide from methyltrichlorosilane. *Journal of the Electrochemical Society*, 143(5):1654–1661, 1996.

[151] D Lespiaux, F Langlais, R Naslain, S Schamm, and J Sevely. Correlations between gas phase supersaturation, nucleation process and physico-chemical characteristics of silicon carbide deposited from si-ch-cl system on silica substrates. *Journal of materials science*, 30(6):1500–1510, 1995.

[152] Y Xu, L Cheng, L Zhang, and W Zhou. Morphology and growth mechanism of silicon carbide chemical vapor deposited at low temperatures and normal atmosphere. *Journal of materials science*, 34(3):551–555, 1999.

[153] Xiang Xiong, Zhao-ke Chen, Bai-yun Huang, Guo-dong Li, Feng Zheng, Peng Xiao, and Hong-bo Zhang. Surface morphology and preferential orientation growth of tac crystals formed by chemical vapor deposition. *Thin Solid Films*, 517(11):3235–3239, 2009.

[154] Dong-Joo Kim, Doo-Jin Choi, and Young-Wook Kim. Effect of reactant depletion on the microstructure and preferred orientation of polycrystalline sic films by chemical vapor deposition. *Thin Solid Films*, 266(2):192–197, 1995.

[155] Michael W Russell, Jaime A Freitas Jr, W James Moore, and James E Butler. Morphological evolution, raman and photoluminescence spectra in optically transparent cubic silicon carbide. *Advanced Materials for Optics and Electronics*, 7(4):195–206, 1997.

[156] Chien C Chiu, Seshu B Desu, Zhi J Chen, and Ching Yi Tsai. Local equilibrium phase diagrams: Sic deposition in a hot wall lpcvd reactor. *Journal of materials research*, 9(8):2066–2071, 1994.

[157] FC Eversteyn, PJW Severin, CHJ vd Brekel, and HL Peek. A stagnant layer model for the epitaxial growth of silicon from silane in a horizontal reactor. *Journal of The Electrochemical Society*, 117(7):925–931, 1970.

[158] Yingbin Ge, Mark S Gordon, Francine Battaglia, and Rodney O Fox. Theoretical study of the pyrolysis of methyltrichlorosilane in the gas phase. 1. thermodynamics. *The Journal of Physical Chemistry A*, 111(8):1462–1474, 2007.

[159] Andrea Lazzeri. Cvi processing of ceramic matrix composites. *Ceramics and composites processing methods*, page 313, 2012.

[160] F Loumagne, F Langlais, and R Naslain. Reactional mechanisms of the chemical vapour deposition of sic-based ceramics from ch3sicl3h2 gas precursor. *Journal of crystal growth*, 155(3-4):205–213, 1995.

[161] Cuiying Lu, Laifei Cheng, Chunnian Zhao, Litong Zhang, and Yongdong Xu. Kinetics of chemical vapor deposition of sic from methyltrichlorosilane and hydrogen. *Applied Surface Science*, 255(17):7495–7499, 2009.

[162] George D Papasouliotis and Stratis V Sotirchos. On the homogeneous chemistry of the thermal decomposition of methyltrichlorosilane thermodynamic analysis and kinetic modeling. *Journal of the Electrochemical Society*, 141(6):1599–1611, 1994.

[163] F De Jong and M Meyyappan. Numerical simulation of silicon carbide chemical vapor deposition. *Diamond and related materials*, 5(2):141–150, 1996.

[164] Yingbin Ge, Mark S Gordon, Francine Battaglia, and Rodney O Fox. Theoretical study of the pyrolysis of methyltrichlorosilane in the gas phase. 2. reaction paths and transition states. *The Journal of Physical Chemistry A*, 111(8):1475–1486, 2007.

[165] Jens Heinrich, Steffen Hemeltjen, and Günter Marx. Analytics of cvd processes in the deposition of sic by methyltrichlorosilane. *Microchimica Acta*, 133(1-4):209–214, 2000.

[166] Weigang G Zhang and Klaus J Hüttinger. Cvd of sic from methyltrichlorosilane. part ii: Composition of the gas phase and the deposit. *Chemical Vapor Deposition*, 7(4):173–181, 2001.

[167] S Hosein Mousavipour, Vahid Saheb, and Shapour Ramezani. Kinetics and mechanism of pyrolysis of methyltrichlorosilane. *The Journal of Physical Chemistry A*, 108(11):1946–1952, 2004.

[168] Yan Yang and Wei-gang Zhang. Chemical vapor deposition of sic at different molar ratios of hydrogen to methyltrichlorosilane. *Journal of Central South University of Technology*, 16(5):730, 2009.

[169] Yasuyuki Fukushima, Noboru Sato, Yuichi Funato, Hidetoshi Sugiura, Kozue Hotozuka, Takeshi Momose, and Yukihiro Shimogaki. Multi-scale analysis and elementary reaction simulation of sic-cvd using ch3sicl3/h2 i. effect of reaction temperature. *ECS Journal of Solid State Science and Technology*, 2(11):492–497, 2013.

[170] S Vajda, P Valko, and Tamas Turanyi. Principal component analysis of kinetic models. *International Journal of Chemical Kinetics*, 17(1):55–81, 1985.

[171] A.E. Lutz, R.J. Kee, and J.A. Miller. Senkin: A fortran program for predicting homogeneous gas phase chemical kinetics with sensitivity analysis. ON: DE88006928(SAND-87-8248), 2 1988.

[172] Rohit Singhal. Soot particle size distribution of a microflow tube reactor : Experimental and sectional modeling investigations. Master's thesis, University of Virginia, 2015.

[173] Shawali Chaudhury. Experimental investigation of soot particle size evolution in micro-flow tube reactor. Master's thesis, University of Virginia, 2016.

[174] Youngchul Ra and Rolf D Reitz. A reduced chemical kinetic model for ic engine combustion simulations with primary reference fuels. *Combustion and Flame*, 155(4):713–738, 2008.